

**DEFORMATION BEHAVIOUR OF BITUMEN
AND BITUMINOUS MIXES**

**E Alexander Ossa
Queens' College**



A dissertation submitted to the University of Cambridge
for the Degree of Doctor of Philosophy

**Cambridge University Engineering Department
September, 2004**

Preface and declaration

The work described in this dissertation was carried out at the Cambridge University Engineering Department between October 2001 and September 2004.

I would like to thank my supervisor Dr David Cebon for his guidance and invaluable discussions. I am greatly in debt with Dr Vikram Deshpande for all his guidance and advice throughout the project.

Special thanks to Mr Simon Bergonioux for his help on the experimental study of polymer-modified bitumen. Also to Mr Alan Heaver and Mr Simon Marshal for helping with the X-ray measurements of asphalt specimens.

Financial support for this project was given to me by the Nottingham Asphalt Research Consortium (NARC).

This dissertation is the result of my own work, except where specific reference has been made to the work of others. No part of the work has been, or is currently being, submitted for any degree, diploma or other qualification. This dissertation is 225 pages in length and contains approximately 44,000 words.

E. A. Ossa
Cambridge
September 2004

DEFORMATION BEHAVIOUR OF BITUMEN AND BITUMINOUS MIXES

E. Alexander Ossa

Summary

The main goal of this dissertation is to develop simple and accurate models for the transient monotonic and cyclic deformation behaviour of bitumen and asphalt mixes. The first part of this dissertation is concerned with an experimental and theoretical investigation of the deformation behaviour of bitumen. The second part is concerned with the deformation of bituminous mixes.

A brief description of the main literature on composition, structure and mechanical behaviour of pure and polymer-modified bitumens is presented in chapter 2.

An extensive experimental study comprising of monotonic, continuous cyclic and pulse loading tensile experiments for two pure and two polymer-modified bitumens is detailed in chapter 3. Based on these experimental findings a simple constitutive phenomenological model including the effects of rate dependent recovery is proposed for bitumen. Comparisons between experiments and model predictions are presented with good agreement.

The spherical indentation behaviour of bitumen under monotonic and cyclic loading conditions is studied in chapter 4. A simple extension to the power-law indentation model of Bower et al. (1993) is proposed for bitumen with good agreement with experimental results.

Chapter 5 presents a review of the main research on continuum and micro-mechanical models for the deformation behaviour of bituminous mixes.

An extensive experimental investigation of the monotonic and cyclic compressive deformation behaviour of bituminous mixes with varying volume fractions of aggregate, for uniaxial and triaxial conditions, is described in chapters 6 and 7, respectively. An extension to the phenomenological model proposed for bitumen is proposed for these mixes. The predictions of the model are compared with the experimental results with good agreement.

In chapter 8, a micro-mechanical constitutive model for the deformation behaviour of asphalt is *assembled* using micro-mechanical theories and experimental observations. The model predictions are compared with uniaxial and triaxial experimental results, showing reasonably good agreement.

Finally, conclusions and recommendations for future work are presented in chapter 9.

Contents

Preface and declaration	1
Summary	2
Contents	4
List of figures	18
List of tables	19
Notation	20
1 Introduction	1
2 Review of previous research	
on bitumen	4
2.1 Introduction	4
2.2 Understanding of bitumen as an engineering material	4
2.3 Composition of pure bitumen	6
2.4 Polymer-modified bitumen	6
2.5 Physical characterisation	7
2.5.1 Quasi-static behaviour	7
2.5.2 Dynamic behaviour	16
2.5.3 Indentation behaviour	18

2.6	Conclusions	19
2.7	Figures	21
3	Deformation behaviour of bitumen	23
3.1	Introduction	23
3.2	Experimental investigation	24
3.2.1	Materials	24
3.2.2	Specimen preparation	24
3.2.3	Test protocol	25
3.3	Experimental results for pure bitumen	28
3.3.1	Monotonic behaviour	28
3.3.2	Creep recovery behaviour	31
3.3.3	Continuous cyclic response	32
3.3.4	Results of pulse train tests	34
3.4	Experimental results for polymer-modified bitumen Cariphalte TS	34
3.4.1	Monotonic loading behaviour	34
3.4.2	Creep recovery behaviour	35
3.4.3	Continuous cyclic loading	36
3.4.4	Pulse train tests	37
3.5	Phenomenological model	37
3.5.1	Comparison with experimental results	39
3.5.2	Extension to 3-dimensional loading	41
3.5.3	An approximate calibration of the model	43
3.6	Discussion	46
3.7	Concluding Remarks	47
3.8	Tables	48

3.9	Figures	49
4	Indentation behaviour of bitumen	65
4.1	Introduction	65
4.2	Indentation behaviour of creeping solids	66
4.3	Indentation model for bitumen	68
4.4	Experimental investigation	69
4.4.1	Material	69
4.4.2	Specimen preparation	70
4.4.3	Test protocol	70
4.5	Experimental results and comparison with model predictions	73
4.5.1	Monotonic indentation behaviour	73
4.5.2	Creep recovery indentation behaviour	74
4.5.3	Continuous cyclic indentation response	75
4.5.4	Pulse train indentation experiments	76
4.6	Discussion	77
4.7	Concluding Remarks	78
4.8	Tables	80
4.9	Figures	81
5	Review of previous research on bituminous mixes	90
5.1	Introduction	90
5.2	Continuum models of bituminous mixes	90
5.2.1	Stiffness representation	90
5.2.2	Creep properties	91
5.2.3	Linear viscoelastic models	92

5.2.4	Non-linear viscoelastic models	93
5.2.5	Viscoelastoplastic models	93
5.2.6	The finite element model	94
5.2.7	Triaxial models	94
5.3	Micromechanical models for bituminous mixes	96
5.3.1	The three phase composite sphere model	96
5.3.2	The bitumen film creep model	96
5.3.3	The discrete element model (DEM)	97
5.4	Review of research on particulate composites	98
5.5	Steady-state constitutive relationship for idealised asphalt mixes	100
5.6	Quasi-static mechanics of granular assemblages	103
5.7	Conclusions	105
5.8	Figures	107
6	Uniaxial deformation behaviour of bituminous mixes	108
6.1	Introduction	108
6.2	Experimental investigation	109
6.2.1	Mix specification	109
6.2.2	Mix preparation	109
6.2.3	Test protocol	112
6.3	Experimental results	114
6.3.1	Monotonic behaviour	114
6.3.2	Creep recovery behaviour	117
6.3.3	Continuous cyclic response	119

6.3.4	Results of pulse train tests	121
6.4	Uniaxial phenomenological model	121
6.5	Effects of particle shape	124
6.6	Concluding Remarks	125
6.7	Tables	128
6.8	Figures	131
7	Triaxial deformation behaviour of bituminous mixes	143
7.1	Introduction	143
7.2	Experimental investigation	144
7.2.1	Description of apparatus	145
7.2.2	Testing procedure	145
7.3	Experimental results	149
7.3.1	Monotonic behaviour	149
7.3.2	Creep recovery behaviour	151
7.3.3	Continuous cyclic response	152
7.3.4	Pulse train triaxial behaviour	154
7.4	Phenomenological constitutive model	154
7.5	Comparison with experimental results	156
7.6	Discussion	158
7.7	Conclusions	159
7.8	Figures	161
8	Micro-mechanical modelling of asphalt deformation	170
8.1	Introduction	170
8.2	Description of the model	172
8.2.1	General loading	172

8.2.2	Axisymmetric loading	178
8.3	Comparison with experimental results	179
8.4	Discussion	182
8.5	Conclusions	183
8.6	Tables	185
8.7	Figures	186
9	Conclusions and Recommendations	192
9.1	Summary of main conclusions	192
9.1.1	Review of previous research on bitumen: Chapter 2.	192
9.1.2	Deformation behaviour of bitumen: Chapter 3	193
9.1.3	Indentation behaviour of bitumen: Chapter 4	194
9.1.4	Review of previous research on bituminous mixes: Chapter 5	195
9.1.5	Uniaxial deformation behaviour of bituminous mixes: Chapter 6	195
9.1.6	Triaxial deformation behaviour of bituminous mixes: Chapter 7	196
9.1.7	Micro-mechanical modelling of asphalt deformation: Chapter 8.	198
9.2	Recommendations for future work	199
9.2.1	Bitumen	199
9.2.2	Bituminous mixes	199
	Bibliography	201

List of Figures

2.1	Deformation-Mechanism Maps for 50 pen bitumen (Cheung and Cebon, (1997))	21
2.2	Spring and Dashpot mechanical viscoelastic analogous representation.	22
3.1	Experimental arrangements for tension tests, Cheung (1995)	49
3.2	(a) Schematic showing the stress and strain time histories in a creep recovery test. (b) Schematic of the applied stress as a function of time in the continuous cyclic tests.(c) Schematic of the stress and strain time histories in the pulse train experiments.	50
3.3	Constant strain-rate tests at four selected values of the applied strain-rate on the 50 pen bitumen at 0°C.	51
3.4	Constant stress creep tests at two selected creep stresses on the 50 pen bitumen at 10°C.	51
3.5	The monotonic and continuous cyclic steady-state behaviour of the 50 pen bitumen at the four temperatures investigated in the current study.	52
3.6	Loading calibration curves $\dot{\epsilon}_{oc}(\epsilon)$ for the 50 and 100 pen bitumens. Curves from a series of five constant strain-rate and creep tests at different temperatures are superimposed.	52
3.7	Creep recovery test results for 50 pen bitumen. (a) $T = 10^\circ\text{C}$, $\sigma = 0.32$ MPa. (b) $T = 0^\circ\text{C}$, $\sigma = 0.2$ MPa.	53

3.8	Summary of the creep recovery experimental results which show a linear relationship between ϵ^r and ϵ^T	54
3.9	Recovery calibration curves $\dot{\epsilon}_{uc}(\hat{\epsilon}^r)$ for the 50 and 100 pen bitumens. Curves from a series of five creep recovery tests at different temperatures are superimposed.	54
3.10	Continuous cyclic stress controlled tests for 50 pen bitumen. (a) $T = 10^\circ\text{C}$, $f = 2$ Hz and $R = 0.15$. (b) $T = 0^\circ\text{C}$, $f = 0.1$ Hz and $R = 0.15$	55
3.11	Continuous cyclic stress controlled tests at 0°C for 50 pen bitumen. (a) Results for three selected values of R with $\sigma_m = 0.095$ MPa and $f = 0.1$ Hz. (b) Results for four selected frequencies f with $\sigma_m = 0.064$ MPa and $R = 0.15$	56
3.12	Pulse loading tests on the 50 pen bitumen. (a) $T = 10^\circ\text{C}$, $\sigma_p = 0.32$ MPa and $\Delta_p = 0.2$ s. (b) $T = 0^\circ\text{C}$, $\sigma_p = 0.16$ MPa, $\Delta_p = 12$ s.	57
3.13	Pulse loading tests on 100 pen bitumen with $T = 0^\circ\text{C}$, $\sigma_p = 0.095$ MPa and $\Delta_p = 12$ s.	58
3.14	Monotonic constant strain-rate tests at three selected values of the applied strain-rate at 0°C on Cariphalte TS.	58
3.15	Monotonic constant stress creep tests on Cariphalte TS at two selected values of the applied stress at 0°C	59
3.16	Monotonic steady-state behaviour of the polymer-modified bitumen Cariphalte TS at the three temperatures investigated in the current study.	59
3.17	Loading calibration curves $\dot{\epsilon}_{oc}(\epsilon)$ for Cariphalte TS and DM bitumens.	60
3.18	Creep recovery tests.(a) Creep recovery test results for Cariphalte TS at $\sigma = 0.64$ MPa and $T = 0^\circ\text{C}$. (b) Summary of creep recovery experimental results which show a linear relationship between ϵ^r and ϵ^T	61

3.19	Recovery calibration curves $\dot{\epsilon}_{uc}(\hat{\epsilon}^r)$ for 50 and 100 pen bitumens and polymer-modified bitumens Cariphalte TS and DM.	62
3.20	Continuous cyclic stress controlled tests for Cariphalte TS at 0°C, R=0.15 and $f=2$ Hz.	62
3.21	Continuous cyclic stress controlled tests at 0°C for Cariphalte TS. (a) Results for three selected values of R with $\sigma_m = 0.36$ MPa and $f = 2$ Hz. (b) Results for four selected frequencies f with $\sigma_m = 0.36$ MPa and $R = 0.3$	63
3.22	Pulse loading tests on Cariphalte TS with $T = 0^\circ\text{C}$, $\sigma_p = 0.4$ MPa and $\Delta_p = 13\text{s}$	64
3.23	Pulse loading tests on Cariphalte DM with $T = 0^\circ\text{C}$, $\sigma_p = 0.4$ MPa and $\Delta_p = 13\text{s}$. Model calibration performed using a set of four simple tension and recovery tests.	64
4.1	Spherical indentation of a half-space. The notation and sign convention is shown.	81
4.2	(a) Schematic showing the stress and strain time histories in a creep recovery test. (b) Schematic of the applied stress as a function of time in the continuous cyclic tests.(c) Schematic of the stress and strain time histories in the pulse train experiments.	82
4.3	(a) Applied indentation force versus indentation depth for two selected values of the applied indentation-rate and (b) indentation depth versus time histories for two selected values of a constant applied indentation force at 0°C with a 40 mm diameter spherical indenter. Experimental measurements and model predictions are included.	83

4.4	(a) Applied indentation force versus indentation depth for two selected values of the applied indentation-rate and (b) indentation depth versus time histories for two selected values of a constant applied indentation force at 5°C with a 40 mm diameter spherical indenter. Experimental measurements and model predictions are included.	84
4.5	Indentation depth versus time history for a constant applied indentation force $F = 35$ N at 0°C. Experimental measurements and model predictions for two indenter diameters $D = 15$ mm and 40 mm are included in the figure.	85
4.6	(a) Indentation creep recovery experimental measurements and model predictions at two selected values of the total indentation depths h^T with $F = 65$ N at 0°C. (b) Summary of the indentation creep recovery experimental measurements. The experimental data for the different levels of indentation force and indenter diameters show a linear relationship between ϵ^r and ϵ^T at the two temperatures investigated.	86
4.7	Continuous cyclic load controlled indentation experimental measurements and model predictions (frequency $f = 2$ Hz and load ratio $R = 0.7$) for two applied mean loads F_m at 0°C with a 40 mm diameter spherical indenter.	87
4.8	Continuous cyclic load controlled indentation test results at 0° C with 40 mm diameter spherical indenter. Experimental measurements and model predictions for (a) a fixed mean load $F_m = 100$ N and a frequency $f = 5.0$ Hz at three selected values of the load ratio $R = 0.3, 0.5$ and 0.7 and (b) $F_m = 150$ N and $R = 0.7$ for three selected values of $f = 0.5, 5.0$ and 10 Hz.	88

4.9	Cyclic load controlled pulse train indentation experimental measurements and model predictions with $F_p = 75\text{N}$ and $\Delta_p = 4.0\text{s}$ for two selected values of the pulse gap Δ_g at (a) 0°C and (b) 5°C	89
5.1	Steady-State Deformation Behaviour of idealised mixes with 40, 52, 75, and 85% by Volume Aggregate (Deshpande and Cebon, 2000) . . .	107
6.1	Density profiles for three different specimen making techniques studied on mix C (64%).	131
6.2	Constant strain-rate tests at two selected values of the applied strain-rate for mix DS (75%) at 20°C	132
6.3	Constant stress creep tests at two selected creep stresses on mix DS (75%) at 20°C	132
6.4	Monotonic and continuous cyclic steady-state behaviour at two different temperatures for mix DS (75%). Also shown is the steady-state response of pure bitumen	133
6.5	Constant strain rate tests for mixes CS (64%) and DS (75%) at 20°C and 0.0015s^{-1}	133
6.6	Variation of loading stiffening S^l factor with volume fraction of sand. The error bars show the experimental scatter of the results.	134
6.7	Variation of nominal axial strain to reach steady-state with volume fraction of sand. The error bars show the experimental scatter of the results.	134
6.8	Creep recovery test results for mix DS (75%) at 20°C , $\sigma = 0.270\text{MPa}$	135
6.9	Summary of the creep recovery experimental results for mix DS (75%) showing a linear relationship between ϵ^r and ϵ^T	135

6.10	Variation of recovery constant with volume fraction of sand. The error bars show the experimental scatter of the results.	136
6.11	Recovery calibration curves $\dot{\epsilon}_{uc}(\hat{\epsilon}^r)$ for 50 pen bitumen and mix DS (75%).	136
6.12	Variation of “recovery stiffening factor” with volume fraction of sand. The error bars show the experimental scatter of the results.	137
6.13	Variation of volumetric strain with distortional strain for mix DS (75%). Creep recovery test result, $\sigma = 0.470$ MPa at 10°C	137
6.14	Continuous cyclic stress controlled tests for mix DS (75%) at 20°C , $f = 5\text{Hz}$ and $R = 0.5$	138
6.15	Continuous cyclic stress controlled tests at 20°C for mix DS (75%). (a) Results for three selected values of R with $\sigma_m = 0.245$ MPa and $f = 2.0$ Hz. (b) Results for three selected frequencies f with $\sigma_m = 0.245$ MPa and $R = 0.7$	139
6.16	Pulse loading tests for mix DS (75%). (a) At 20°C , $\sigma_p = 0.13\text{MPa}$ and $\Delta_p = 4\text{s}$. (b) At 0°C , $\sigma_p = 1.3\text{MPa}$ and $\Delta_p = 16\text{s}$	140
6.17	Pulse loading tests for mix CS (64%). (a) At 20°C , $\sigma_p = 0.3\text{MPa}$ and $\Delta_p = 10\text{s}$. (b) At 0°C , $\sigma_p = 1.3\text{MPa}$ and $\Delta_p = 16\text{s}$	141
6.18	Pulse loading tests for mixes with 85% volume fraction of aggregate. (a) Mix ES at 20°C , $\sigma_p = 0.26\text{MPa}$, $\Delta_p = 20\text{s}$ and $\Delta_g = 60\text{s}$. (b) Mix EA at 20°C , $\sigma_p = 0.26\text{MPa}$, $\Delta_p = 20\text{s}$ and $\Delta_g = 60\text{s}$	142
7.1	Schematic showing the triaxial test coordinate system and test sequences. (a) Stresses on the cylindrical specimen and definition of stress ratio η . (b) Recovery test. (c) Continuous cyclic test sequence. (d) Pulse train test sequence.	161

7.2	Monotonic constant stress creep triaxial tests on mix DS (75%) at two selected values of the applied deviatoric stress, at 20°C with the same stress ratio ($\eta = 0.6$) in both cases.	162
7.3	Triaxial steady state behaviour on mix DS (75%) at various stress ratios η for monotonic and continuous cyclic loading at 20°C.	162
7.4	Effect of stress ratio on deformation behaviour of mixes with varying volume fractions of aggregate.	163
7.5	Creep recovery triaxial test results for mix DS (75%). Results for two selected values of Σ with $\eta = 1.0$ in both cases.	164
7.6	Summary of the creep recovery triaxial test results for mix DS (75%) at different stress ratios η	164
7.7	Recovery calibration curves $\dot{\epsilon}_{uc}(\hat{\mathcal{E}}_{33}^r)$ for pure bitumen and mix DS (75%) with $\eta = 0.6$	165
7.8	Continuous cyclic triaxial tests for mix DS (75%). Results for 2 selected values of Σ_{mean} , with $f = 0.5 \text{ Hz}$, $\eta_m \approx 0.6$ and $R = 0.7$	165
7.9	Continuous cyclic triaxial tests for mix DS (75%). (a) Results for three selected values of f with $\Sigma_{mean} = 0.52 \text{ MPa}$, $\eta_m = 0.6$ and $R = 0.7$. (b) Results for three selected values of R with $\Sigma_{mean} = 0.18 \text{ MPa}$, $\eta_m = 0.6$ and $f = 0.5 \text{ Hz}$	166
7.10	Triaxial pulse test results at 20° C for mix DS (75%) with $\Sigma_p = 0.3 \text{ MPa}$, $\Delta_p = 8 \text{ s}$, $\Delta_g = 30 \text{ s}$ at two different stress ratios η_p	167
7.11	Triaxial pulse test results at 20° C for 85% volume fraction of aggregate with round and angular stones. (a) Mix ES (Round stones) with $\Sigma_p = 0.52 \text{ MPa}$, $\Delta_p = 20 \text{ s}$, $\Delta_g = 60 \text{ s}$. (b) Mix EA (Angular stones) with $\Sigma_p = 0.52 \text{ MPa}$, $\Delta_p = 20 \text{ s}$, $\Delta_g = 60 \text{ s}$	168

7.12	Error between experiments and model for pulse loading tests for all specimens tested. The time period ratio and temperature (Δ_p/Δ_g , T) are shown for each experimental point. Solid lines represent the standard deviation error of the steady-state experimental results for each mix. The mean modelling error is represented by dashed line.	169
8.1	Flow diagram showing the procedure of calculation of the deformation behaviour of mixes using the constitutive model.	186
8.2	Monotonic creep recovery triaxial test on mix ES (85%) at 20°C with $\Sigma = 0.78 \text{ MPa}$ and $\eta = 0.6$. The dotted lines represent the model predictions with the two limits of the experimentally measured dilation gradient s . The dashed line represent the model prediction with $s = 0.43$ calculated using eq. (5.17).	187
8.3	Evolution of stiffening factor (a), and volume fractions of aggregate and voids (b), for creep recovery simulation shown in fig. 8.2, with $s = 0.43$	188
8.4	Effect of stress ratio on deformation behaviour of mixes with varying volume fractions of sub-spherical aggregate. The values of S^{-1} calculated by the model are plotted along with the experimental error bars of S^{-1}	189
8.5	Triaxial pulse test results at 20° C for Mix ES (85% volume fraction of sub-spherical aggregate) with $\Sigma_p = 0.52 \text{ MPa}$, $\Delta_p = 20 \text{ s}$, $\Delta_g = 60 \text{ s}$, $s = 0.43$. (a) Model prediction with evolution of c and v . (b) Percentage of variation of c , v and S during mix evolution.	190
8.6	Triaxial pulse test results at 20° C for Mix ES (85% volume fraction of sub-spherical aggregate) with $\Sigma_p = 0.52 \text{ MPa}$, $\Delta_p = 20 \text{ s}$, $\Delta_g = 60 \text{ s}$, $s = 0.43$. Model prediction ignoring evolution of the mix.	191

- 8.7 Triaxial pulse test results at 20° C for Mix EA (85% volume fraction of angular aggregate) with $\Sigma_p = 0.52 \text{ MPa}$, $\Delta_p = 20 \text{ s}$, $\Delta_g = 60 \text{ s}$, $s = 0.9$ at two different stress ratios. Model prediction with mix evolution. . . 191

List of Tables

3.1	Pure bitumens parameters.	48
3.2	Polymer-modified bitumens parameters.	48
4.1	Indentation model parameters α and ϕ as a function of the power-law exponent n . (Reproduced from Bower et al. (1993)).	80
6.1	Description of mixes studied.	128
6.2	Description of mixes studied for aggregate shape effects.	129
6.3	Dilation gradient for the mixes studied	129
6.4	Experimental results for mixes studied for aggregate shape effects. . .	130
8.1	Comparison between Young's modulus and dilation gradient measured and predicted by the 2-D model (eq. 5.17) for fully dense mixes. Numbers in bold indicate where models are expected to be valid	185

Notation

The following general physics notation will be used throughout this dissertation, unless otherwise specified within the text.

$G(t)$	Relaxation Modulus
G^*	Complex relaxation Modulus
$J(t)$	Creep compliance
J^*	Complex compliance
t	Time
Q	Activation energy
R	Universal gas constant
T	Temperature
T_g	Glass transition temperature
E	Young's modulus
ν	Poisson's ratio
μ	Shear modulus
k	Bulk modulus
c	Volume fraction of rigid inclusions
v	Volume fraction of air voids
f	Frequency
η	Stress ratio
ϵ_{ij}	Microscopic strain tensor
$\dot{\epsilon}_{ij}$	Microscopic strain rate tensor
ϵ_e	Microscopic Von mises effective strain

\mathcal{E}_{ij}	Macroscopic strain tensor
$\dot{\mathcal{E}}_e$	Macroscopic Von mises equivalent strain rate tensor
H	Volumetric strain
σ_{ij}	Microscopic stress tensor
σ'_{ij}	Deviatoric stress
σ_e	Microscopic Von mises effective stress
Σ_{ij}	Macroscopic stress tensor
Σ_e	Macroscopic Von mises effective stress
Σ_m	Mean or hydrostatic stress
δ_{ij}	Kronecker delta

Chapter 1

Introduction

Pavements are intended to provide a durable and smooth running surface with adequate skid resistance in an economic way, throughout their design life (Deshpande, 1997). To fulfill these requirements the sub-grade is protected from traffic and environmental effects by ensuring that the surface material does not suffer unacceptable deterioration. There are several ways in which a flexible (asphalt) pavement can fail. The most common are fatigue cracking, permanent deformation (rutting), reduced skid resistance, low temperature cracking and reflection cracking of composite constructions (Cebon, 1993).

During the last decade, several projects have been completed in the Cambridge University Engineering Department (CUED) as part of an overall effort to understand the rutting and cracking of flexible pavements.

The development of a reliable and easy-to-implement model for predicting rutting during road design stages requires an understanding of the influence of the mix components and their interactions. Therefore, the approach is to try to predict the deformation properties of asphalt theoretically from the characteristics of its constituents. These deformation models can then be used in an analytical pavement

rutting model implemented in Finite Elements codes.

Cheung (1995) performed monotonic tests on pure bitumen over a wide range of loading and temperature conditions and developed steady-state constitutive laws, summarised using Deformation Mechanism maps. He also studied experimentally and theoretically the thin film behaviour of pure bitumen with good results.

Deshpande (1997) performed monotonic tests on idealised bituminous mixes over a wide range of loading conditions, stress ratios and temperatures. He developed a steady-state model for mixes using the constitutive laws for pure bitumen developed by Cheung, along with theories of composite mechanics. Deshpande's model showed good agreement with experimental results for uniaxial and triaxial stress states.

As a first step towards understanding asphalt cracking, Harvey (2000) and Genin and Cebon (2000) studied experimentally and theoretically the crack opening behaviour of bitumen films for various loading and temperature conditions.

Following-on from the work of Cheung and Deshpande, the logical next step is to develop a model for the transient monotonic and cyclic behaviour of bitumen and asphalt mixes. This is the topic of the work described in this dissertation. Such models are essential for understanding the permanent deformation of asphalt road surfaces.

A review of relevant literature concerning the deformation behaviour of bitumen is presented in chapter 2.

An extensive experimental study of the uniaxial tensile monotonic and cyclic behaviour of 2 pure and 2 polymer-modified bitumens under a wide range of loading and temperature conditions is described in chapter 3. A simple phenomenological constitutive model for bitumen is proposed based on these observations.

The constitutive model for bitumen is validated under spherical indentation condi-

tions in chapter 4. An extension to the indentation model for creeping solids developed by Bower et al. (1993) is proposed. An extensive set of monotonic and cyclic indentation tests are detailed and the results compared with the predictions of the extended Bower et al. model.

A review of previous research on continuum and micro-mechanical models for bituminous mixes is given in chapter 5.

An extensive uniaxial and triaxial experimental investigation of the monotonic and cyclic compressive deformation behaviour of bituminous mixes with various volume fractions of aggregate is described in chapters 6 and 7, respectively. An extension to the phenomenological model proposed for bitumen is also proposed for these mixes. The predictions of the model are compared with the experimental results.

Using the constitutive law developed in chapter 3 for bitumen, and the steady-state constitutive law for asphalt developed by Deshpande (1997), a micro-mechanical model for asphalt is assembled in chapter 8. This model uses the properties of bitumen and aggregate to predict the macroscopic behaviour of the mix. Comparisons between experimental results from chapters 6 and 7 and model predictions are provided.

Finally, conclusions and recommendations for future work are given in chapter 9.

Chapter 2

Review of previous research on bitumen

2.1 Introduction

A brief description of the main literature on composition, structure and mechanical behaviour of pure and polymer-modified bitumens is presented in this chapter. Detailed reviews can be found elsewhere (SHRP-A-631, 1993; Cheung, 1995; Harvey, 2000).

2.2 Understanding of bitumen as an engineering material

Natural bitumen was used as an adhesive and waterproofing material as early as 3800 B.C. (Whiteoak, 1990). The use of bitumen in pavement construction started in the early nineteenth century (Abraham, 1960; Cebon, 1993). It was not, however, until the 1920's when systematic research was performed by oil companies to

understand bitumen as an engineering material. The first attempt to understand the behaviour of bitumen was the source of the colloidal model developed by Nellensteyn (Nellensteyn, 1924; Nellensteyn, 1927) which was widely accepted by 1950. At the same time, mechanical tests were conducted on bitumen by Lee and Warren (1940), Lethersich (1942), Saal and coworkers (Saal and Labout, 1940; Saal, 1950) and Traxler and coworkers (Traxler and Coombs, 1936; Traxler et al., 1944; Traxler, 1947; Romberg and Traxler, 1947) to experimentally corroborate the colloidal model. A few years later, Van der Poel (van der Poel, 1954a; van der Poel, 1954b; Van der Poel, 1955) succeeded in correlating the *stiffness*¹ of bitumen with two experimental parameters, namely the *penetration*² and the ring and ball *softening point*³, obtained by routine tests for bitumen. Van der Poel summarised the mechanical behaviour as a function of temperature and loading time in the well known Van der Poel nomograph (van der Poel, 1954b). After 1960 bitumen research was increased due to the availability of a wide range of experimental tools to study composition (Differential scanning Calorimetry, Fourier Transform Infrared Spectroscopy, High pressure gel permeation chromatography, etc) and mechanical behaviour (shear viscometry for quasi-static and dynamic tests). Due to the improvement in testing facilities, a number of theories originating from materials science and soil mechanics were applied to model experimental data for bitumen. Some of those theories were developed from constitutive relations for other materials which do not have the amorphous nature of bitumen.

¹The *stiffness* for a visco-elastic material S_t , is defined as the ratio between the applied stress and the resulting strain at loading time t (Whiteoak, 1990).

²The *penetration* is the distance measured in decimeters travelled into a bitumen sample by a standard needle under a load of 100g in a time of 5s (BS2000-49, 1983).

³the ring and ball *softening point* is the temperature at which a bitumen disc contained in a brass ring under the loading of a steel ball will touch a base plate 25 mm below the ring when the sample temperature is raised at 5°C per minute (BS2000-58, 1983).

2.3 Composition of pure bitumen

Bitumen is a complex polymeric system consisting of asphaltenes and maltenes. Its properties are dependent on:

1. The properties of the *asphaltenes*⁴, including the quantities, sizes and shapes, as well as chemical properties such as composition, presence of functional groups or heterocompounds and reactivity.
2. The chemical nature of the *maltenes*⁵. These include a collection of characteristics which includes the peptizing power of the resins (Brule et al., 1986).
3. The prominent functional groups present in the bitumen.
4. The nature of the aromatics and saturates, which in turn determine the glass transition.
5. The crystallisation behaviour of the system.

Quantification of the effects of individual components and the collective effects of combinations of components is not well developed.

2.4 Polymer-modified bitumen

Since the 1980's bitumens have commonly been modified by addition of polymers, to decrease the susceptibility of pavements to high temperature rutting and low temperature cracking.

A variety of polymers have been employed to improve the properties of bitumen, these include low and high density polyethylene (LDPE and HDPE) and elastomers

⁴The chemical definitions of the components can be found elsewhere, e. g. (Petersen, 1984).

⁵Resins, aromatics and saturates are collectively called maltenes.

such as ethylene-propylene-diene (EPDM). Copolymers such as styrene-butadiene-styrene (SBS) triblock are most commonly used in commercially available polymer modified bitumens. Various studies have confirmed that bitumens modified with SBS have superior performance to pure bitumens. For example Qi et al. (1995) and Martinez-Boza et al. (2001) showed that SBS improves the thermal susceptibility of bitumen, while experiments by Elseifi et al. (2003) demonstrated that SBS increases the rutting and fatigue resistance of bitumen.

Chen et al. (2002) attempted to model modified bitumen as a two phase material and employed Kerner's theory for a two phase composite to quantify the effects of composition on the viscosity of polymer modified bitumens. While such model give some insights into the origins of the enhanced performance, they are unable to capture the complex viscoelastic behaviour of the polymer modified bitumens under realistic loading conditions and thus have limited applicability in predictive design.

Despite the effort to predict the behaviour of modified bitumens from the properties of the base bitumen and the added polymer, the main methods of characterisation developed for pure bitumens are commonly used to characterise the modified bitumens. For example, Zeng et al. (2001) extended the models proposed under SHRP-A-369 (1994) to characterise polymer modified bitumens, with the consequent limitations of these models.

2.5 Physical characterisation

2.5.1 Quasi-static behaviour

Bitumens are visco-elastic materials and their deformation under stress is a function of temperature, strain and loading time. At high temperatures or long times of loading they behave as viscous liquids, whereas at low temperatures (below glass transition

temperature T_g) or short times of loading they behave as elastic (brittle) solids. The intermediate range of temperature and loading times results in visco-elastic behaviour (Whiteoak, 1990). Cheung and Cebon (1997a) summarised a wide range of deformation behaviour of bitumen (see fig. 2.1) using the concept of deformation mechanism maps developed by Frost and Ashby (1982). The map in fig. 2.1 shows a range of deformation mechanisms characterised by power-law and linear viscous relationships at high strain rates and Eyring plasticity at very low strain rates. The temperature dependence is discussed later.

Several theories for quasi-static deformation behaviour of bitumen can be found in the literature, some of the more relevant will be briefly discussed in the following sections. The reader is referred to the works of Ward (1971), Ferry (1980), SHRP-A-369 (1994), Cheung (1995) and Harvey (2000) for more comprehensive reviews of this subject.

Time-dependent modulus

A time dependent modulus is a generalised version of the elastic modulus in elastic solids. When a fixed strain ϵ_o is applied to a visco-elastic material at time $t \geq 0$, the resulting stress response $\sigma(t)$ of the material is a function of time, and the *relaxation modulus* $G(t)$ can be defined as:

$$G(t) = \frac{\sigma(t)}{\epsilon_o}. \quad (2.1)$$

In a similar way, in a creep test in which a stress σ_o is applied at time $t \geq 0$, the resulting strain response $\epsilon(t)$ of the material is a function of time, and the *creep compliance* $J(t)$ can be defined as:

$$J(t) = \frac{\sigma_o}{\epsilon(t)}. \quad (2.2)$$

As an extension of equation 2.1, hereditary integrals can be used to take into account the contributions of the loading history on the total stress of the material, according to:

$$\sigma(t) = \int_{-\infty}^t G(t - \xi) \frac{d\epsilon(\xi)}{d\xi} d\xi, \quad (2.3)$$

where ξ is a dummy integration variable which is used to differentiate the current time t from all previous times ξ . Some models of viscoelastic behaviour are based on elastic constitutive equations in which the elastic modulus is replaced by the relaxation modulus (Williams, 1972). Other similar models use a time averaged modulus defined as:

$$\bar{G} = \frac{1}{t} \int_{-\infty}^t G(t - \xi) \frac{d\epsilon(\xi)}{d\xi} d\xi. \quad (2.4)$$

This averaged modulus is based in the summation of contributions of each value of the relaxation modulus over the loading history.

Correspondence principles

The Boltzmann (1876) correspondence principle is the first mathematical statement of linear viscoelastic behaviour. Boltzmann proposed that the creep in a specimen is a function of the entire loading history, and that each loading step makes an independent contribution to the final deformation, and therefore, the final deformation can be obtained by addition of each individual contribution.

Schapery (1984), developed a nonlinear viscoelastic correspondence principle, in which constitutive equations for nonlinear viscoelastic materials, in which stress-independent relaxation or creep functions in single integrals serve to characterise the hereditary behaviour, can be written in a form that is identical to those for the nonlinear elastic case, but the strains and stresses are not necessarily physical quantities in the viscoelastic body. Instead, they are *pseudo strains* and *pseudo stresses*

which are in the form of convolution or hereditary integrals as:

$$\epsilon_i^R = \frac{1}{E_R} \int_0^t G(t - \xi) \frac{\partial \epsilon_i}{\partial \xi} d\xi \quad (2.5)$$

$$\sigma_{ij}^R = E_R \int_0^t J(t - \xi) \frac{\partial \sigma_{ij}}{\partial \xi} d\xi, \quad (2.6)$$

where σ_{ij} and ϵ_i are physical stresses and physical strains, σ_{ij}^R and ϵ_i^R are pseudo stresses and pseudo strains; $G(t)$ and $J(t)$ are relaxation modulus and creep compliance; and E_R is the reference modulus, which is an arbitrary constant. Thus, for a given stress history, pseudo strains can be calculated by elastic laws, and viscoelastic strains can be deduced using equation 2.5.

Molecular theory

The molecules inside a polymer structure are in constant oscillation about a potential energy barrier. Their frequency of oscillation f_m is given by:

$$f_m = f_{m_0} \exp\left(-\frac{\Delta Q}{RT}\right), \quad (2.7)$$

where ΔQ is the activation energy, R is the universal gas constant, and T is the absolute temperature. f_{m_0} is a reference frequency value. When a stress σ is applied, the energy barrier is affected, generating a shift $\beta\sigma$ in the position of the molecules. If this shift is large enough, it becomes improbable that the molecules will return to their original positions, and so the deformation is permanent. Assuming viscous flow to occur in that way, the strain rate can be deduced to be:

$$\dot{\epsilon} = \dot{\epsilon}_o \exp\left(-\frac{\Delta Q}{RT}\right) \sinh\left(\frac{\beta\sigma}{RT}\right), \quad (2.8)$$

where β is an activation volume for the molecular event. Equation 2.8 defines an activated non-Newtonian viscosity, and is better known as the Eyring viscous model.

Cheung (1995) found that this model can be applied to pure bitumen below the glass transition temperature T_g (see figure 2.1).

Mechanical analogs

Mechanical analog models based on springs⁶ and dashpots⁷ in series (Maxwell model), in parallel (Kelvin or Voigt model) or combinations of both, are commonly used to represent the viscoelastic behaviour in conjunction with the Boltzmann correspondence principle (Ward, 1971).

In the case of the Maxwell model (figure 2.2a), the quantity $\tau = \eta/E$ is known as the *relaxation time constant* and can be regarded as a measure of the time required for stress relaxation. For the Kelvin model (fig 2.2b), the same quantity is known as the *retardation time constant* and is a measure of the time required for the extension of the spring to return to its equilibrium length when the load is removed, while retarded by the dashpot. A group of n Maxwell elements in parallel can be used to represent a discrete spectrum of relaxation times, resulting with the relaxation modulus:

$$G(t) = \sum_{i=1}^n E_i \exp\left(-\frac{t}{\tau_i}\right). \quad (2.9)$$

In the case of n Voigt elements in series, a discrete spectrum of retardation times can be found. The creep compliance is then given by:

$$J(t) = \sum_{i=1}^n \frac{1}{E_i} \left\{ 1 - \exp\left(-\frac{t}{\tau_i}\right) \right\}. \quad (2.10)$$

In the general case, where continuous spectra of relaxation times and retardation

⁶Elastic elements which obey Hooke's Law.

⁷Viscous elements which obey Newton's Law of viscosity.

times are employed, $G(t)$ and $J(t)$ are given by:

$$G(t) = \int_0^{\infty} H(\tau) \exp\left(-\frac{t}{\tau}\right) d\tau \quad (2.11)$$

$$J(t) = \int_0^{\infty} L(\tau) \left\{ 1 - \exp\left(-\frac{t}{\tau}\right) \right\} d\tau, \quad (2.12)$$

where $H(\tau)$ and $L(\tau)$ are called *relaxation spectrum* and *retardation spectrum* respectively.

Some of these models, or combinations of them, have been used by researchers to model the viscoelastic behaviour of bitumen and other materials (e. g. van der Poel (1954a), Bland and Lee (1956), Jeng and Perng (1991), Toth (1996), Francken (1998), Dietrich and Lekszycki (1998) and Harvey (2000)), yielding reasonable agreement with experimental results for specific conditions, at low strain and stress levels.

Steady state behaviour

At small strains, linear behaviour is usually observed in the properties of pure bitumen, nonetheless non-linear behaviour is observed at large strains. Researchers including Saal and Labout (1940), Lethersich (1942), Saal (1950) and Brown and Sparks (1958), observed linear behaviour for low stress levels (2 kPa or below), which they modelled by the theories of linear viscoelasticity. However, some researchers stated that non linearities become more noticeable at higher stress levels (Lethersich, 1942). This observation was confirmed by experimental studies at higher stresses in the range 100 kPa to 1 MPa , (Gaskins et al., 1960; Sisko, 1965; Welborn et al., 1966; Moavenzadeh and carnaghi, 1966; Khong et al., 1978) where bitumen was found to behave as a power law material.

One of the approaches used to model power law materials is to use linear viscoelastic models and employ an extrapolated zero-strain-rate viscosity as the steady-state

equivalence of a linear material. The deviation from linear behaviour is then known as the *shear susceptibility* which is the slope of either the stress strain-rate or the viscosity strain-rate relationship.

Another approach is to model the transition from linear behaviour to power law behaviour empirically (Sisko, 1965; Welborn et al., 1966; Garrick, 1992). This approach fits experimental data well, but no theoretical basis for its use has been presented.

Cross (1965), published a pseudo-plastic flow equation based on the formation and rupture of structural linkages. He argued that if a system contains elements which are capable of assuming some structural formation which is wholly or partially disrupted by shear, a viscosity-shear rate dependence of the pseudo-plastic flow nature would be expected. Cross (1965) applied the principles of reaction kinetics to the formation and rupture of linkages between particles, and assumed the rate of linkage rupture to be a combination of Brownian movement and shearing action, given by $k_o + k_1\dot{\gamma}^m$, where k_o, k_1 and m are all constants. He was able to show that at equilibrium:

$$\bar{\eta} = \bar{\eta}_\infty + \frac{\bar{\eta}_o - \bar{\eta}_\infty}{1 + \alpha\dot{\gamma}^m}, \quad (2.13)$$

where $\bar{\eta}_\infty$ is the shear viscosity when $\dot{\gamma} \rightarrow \infty$, $\bar{\eta}_o$ is the shear viscosity when $\dot{\gamma} \rightarrow 0$ and $\alpha = k_1/k_o$.

Cheung (1995) and Cheung and Cebon (1997a), combined the Cross model with an empirical equation proposed by Sisko (1965) to describe the steady state behaviour of pure bitumen over a wide range of stress levels at temperatures above T_g as:

$$\frac{\sigma}{\sigma_o} = \frac{\dot{\epsilon}}{\dot{\epsilon}_p} \left\{ \frac{1}{1 + \left(\frac{\dot{\epsilon}}{\dot{\epsilon}_p}\right)^m} \right\}, \quad (2.14)$$

where σ is the applied stress, $\dot{\epsilon}$ is the strain rate, σ_o is the failure strength of structural linkages which can be regarded as the “*yield stress*” or linear limit of the material, m and $\dot{\epsilon}_p$ are material parameters for bitumen. Equation 2.14, which Cheung and

Cebon (1997a) named the Modified Cross Model (MCM) reduces to a linear viscous law for low values of $\dot{\epsilon}$ and a nonlinear viscous law with a power law exponent of $n = 1/(1 - m)$ for high values of $\dot{\epsilon}$. They found that the MCM fitted their experimental measurements on the steady-state behaviour of pure bitumen very well and it also fitted a considerable body of other experimental data found in the literature on bitumen.

Cheung and Cebon (1997a) summarised the steady-state deformation behaviour of bitumen over a wide range of temperatures on deformation mechanism maps as shown in figure 2.1. They found that the temperature dependence of the material can be divided in three main regions, governed by different deformation models: i) below T_g (the glass transition temperature); ii) immediately above T_g ; and iii) well above T_g . T_g for bitumen has been reported to lie in the range $-40^\circ\text{C} < T_g < 0^\circ\text{C}$ (Cheung and Cebon, 1997a).

For temperatures well below the glass transition temperature ($T \ll T_g$) the Eyring Plasticity Model (EPM) can be used to model the transient behaviour as a function of time t :

$$\frac{\dot{\epsilon}(t)}{\dot{\epsilon}_e} = 2 \exp\left(-\frac{Q_e}{RT}\right) \sinh\left(\frac{\tau\nu_s - P\nu_p}{RT}\right) \left(\frac{t}{t_o}\right)^{m_e}, \quad (2.15)$$

where $\dot{\epsilon}$ is the strain rate, τ is the shear stress, P is the pressure, $\dot{\epsilon}_e$ is a constant, Q_e is the activation energy for the flow process, R is the universal gas constant, ν_s is the shear activation volume, ν_p is the pressure activation volume, t_o is a reference time, and m_e is a time hardening constant.

For temperatures immediately above T_g ($T > T_g$) the material follows *Arrhenius* type “diffusion-controlled” behaviour, and $\dot{\epsilon}_p$ in equation 2.14 is written as:

$$\dot{\epsilon}_p = \dot{\epsilon}_{pc} e^{-k\left(\frac{1}{T} - \frac{1}{273}\right)}, \quad (2.16)$$

where k is the Arrhenius constant which is the ratio of the thermal activation energy

to the universal gas constant, and $\dot{\epsilon}_{pc}$ is the reference strain rate at $T = 0^\circ C$ or $273 K$.

For temperatures well above T_g ($T \gg T_g$) the behaviour is controlled by “free volume”. $\dot{\epsilon}_p$ is then given by:

$$\dot{\epsilon}_p = \dot{\epsilon}_{pc} \exp\left(\frac{2.303c_1^s(T - T_s)}{c_2^s + (T - T_s)}\right), \quad (2.17)$$

where T_s is a reference temperature and c_1^s , c_2^s are “universal” constants. Equation 2.17 is known as the *WLF* equation and is often used to characterise the temperature dependence of a wide range of polymers.

Transient behaviour

Various models can be found in the literature to describe the transient behaviour of pure bitumen. Almost all of them were developed using linear viscoelastic theory based on springs and dashpots, as described in previous sections. Another method employed to estimate the transient creep strain of bitumen is using the Van der Poel Nomograph (van der Poel, 1954a). A more elaborate method was reported by the Strategic Highway Research Program (SHRP-A-369, 1994) in which creep data in bending for short duration of tests ($< 240s$) was correlated with corresponding relaxation data.

Cheung (1995) adopted a transient creep model developed by Webster et al. (1969) and Amin et al. (1970) to fit the transient creep behaviour of bitumen at stresses above the linear regime and temperatures above T_g . It is given by:

$$\dot{\epsilon}_c = \dot{\epsilon}_{ss}[1 + \Lambda_1\epsilon_{T1} \exp(\Lambda_1\dot{\epsilon}_{ss}t) + \Lambda_2\epsilon_{T2} \exp(\Lambda_2\dot{\epsilon}_{ss}t)], \quad (2.18)$$

where $\dot{\epsilon}_{ss}$ is the steady state creep rate, Λ_i are dimensionless constants, ϵ_T is the total transient strain which is dependent on the stress and temperature and $\dot{\epsilon}_c$ is the creep strain rate. Equation 2.18 is known as the Transient Creep Model (TCM) with

two time constants. To obtain the TCM parameters, eq. (2.18) must be fitted to experimental results.

Researchers like Lin and Wang (1998), Geist (1998), Poh (1998), Fafard et al. (2001), Houlsby and Puzrin (2002), Saleeb et al. (2002) and Saleeb et al. (2003) developed transient models for creeping materials based on curve fitting and thermodynamics approaches. These models have two major drawbacks. First, they require a large number of experiments to obtain the calibration parameters. Second, the fitting of experimental results often requires complex mathematical procedures and specialised software.

2.5.2 Dynamic behaviour

When a linear viscoelastic material is subjected to a sinusoidally varying strain $\epsilon = \bar{\epsilon} \exp(i\omega t)$, the resulting stress response will vary sinusoidally with amplitude $\bar{\sigma}$, and will be out of phase with the strain by a phase angle θ as:

$$\sigma = \bar{\sigma} \exp\{i(\omega t + \theta)\}. \quad (2.19)$$

The *Storage Modulus*⁸, G_1^* and the *Loss Modulus*⁹, G_2^* are defined as:

$$G^* = \frac{\sigma}{\epsilon} = \frac{\bar{\sigma}}{\bar{\epsilon}} \exp(i\theta) = G_1^* + iG_2^*, \quad (2.20)$$

where:

$$G_1^* = \frac{\bar{\sigma}}{\bar{\epsilon}} \cos \theta \quad (2.21)$$

$$G_2^* = \frac{\bar{\sigma}}{\bar{\epsilon}} \sin \theta. \quad (2.22)$$

⁸The *Storage Modulus* is the real part of the modulus, associated with the energy stored in the specimen due to the applied strain (Ward, 1971).

⁹The *Loss Modulus* is the imaginary part of the modulus associated with the dissipation of energy (Ward, 1971).

The phase angle θ is given by:

$$\frac{G_2^*}{G_1^*} = \tan \theta. \quad (2.23)$$

The magnitude of the complex relaxation modulus is given by:

$$|G^*| = \left| \frac{\bar{\sigma}}{\bar{\epsilon}} \right| = \sqrt{G_1^{*2} + G_2^{*2}}. \quad (2.24)$$

If the continuous relaxation spectrum $H(\tau)$ is known (eq. 2.12), the storage modulus and the loss modulus can be obtained as (Ferry, 1980):

$$G_1^*(\omega) = \int_0^{\infty} H(\tau) \frac{\omega^2 \tau^2}{1 + \omega^2 \tau^2} d\tau \quad (2.25)$$

$$G_2^*(\omega) = \int_0^{\infty} H(\tau) \frac{\omega \tau}{1 + \omega^2 \tau^2} d\tau. \quad (2.26)$$

Similarly, data from dynamic tests can be expressed in terms of a complex compliance $J^* = J_1^*(\omega) - iJ_2^*(\omega)$.

Dynamic shear viscometry has been extensively used since the 1960's to study the dynamic behaviour of bitumen. Almost all the researchers¹⁰ employed the theories of linear viscoelasticity to analyse the results of these tests, which were usually performed over a range of frequencies and temperatures under strain control. Linear behaviour was usually found if the maximum strain applied was smaller than a limiting value. This value is 0.1 according to Jongepier and Kuilman (1969), and 0.04 according to Dickinson and Witt (1974). SHRP-A-369 (1994) proposed that this limiting value is dependent on the magnitude of the complex modulus, ranging from 0.01 at high modulus ($> 10^7 Pa$) to values larger than 0.1 at low modulus ($> 10^5 Pa$). Using data at various frequencies and temperatures, two characteristic curves can be constructed, one describing the dependence of the modulus on frequency and the other

¹⁰An extensive literature review on this topic can be found in Cheung (1995)

expressing the time-temperature “shift factor” as a function of temperature. Some researchers including Jongepier and Kuilman (1969), Dobson (1969), Dobson (1972), Dickinson and Witt (1974), Gilbert et al. (1986), Anderson et al. (1991), Christensen and Anderson (1992) and Marasteanu and Anderson (1999) have attempted to model these master curves, to correlate the results to those from other tests and to explain the results in terms of the composition of the material. Some good results have been reported. The limitation of these approaches is that they are only valid below the limiting strain value and cannot be used to model behaviour at higher strains.

2.5.3 Indentation behaviour

Indentation tests have been pursued as a cheap and easy method to measure the mechanical properties of materials for over a century. Many researchers have attempted to deduce the uniaxial stress versus strain behaviour of the indented material from the results of indentation tests. For instance, Tabor (1951) proposed empirical relations to correlate the results of indentation tests on rate independent materials with uniaxial test results. Later, more rigorous theoretical works were conducted on creeping solids. Notable among those are the works of Mulhearn and Tabor (1960), Atkins et al. (1966), Wilkinson and Ashby (1975), Mayo and Nix (1988), Hill et al. (1989), Sargent and Ashby (1992) and Bower et al. (1993). All those studies were based on steady-state models of the indentation behaviour. Ogbonna (1994) and Ogbonna et al. (1995) also studied the transient behaviour of creeping solids in the time domain, based on the steady state model of Bower et al. (1993). They found that neglecting the transient primary creep regime is a major source of error in the interpretation of creep properties from indentation tests.

Early work by van der Poel (1954a) indicated that the “stiffness” of bitumen at low strains could be correlated with the *penetration index* (measured with a nee-

dle, see section 2.2) and *softening point* of the bitumen (Whiteoak, 1990). van der Poel summarised this behaviour in the well-known van der Poel nomograph (van der Poel, 1954b). Under the *Strategic Highway Research Program* (SHRP-A-369, 1994) indentation tests were conducted on bitumen using a spherical indenter, in order to extend the test results to the linear viscoelastic models developed under the same programme. The results were promising but the researchers did not propose a complete model of the indentation process.

2.6 Conclusions

1. The colloidal model (developed in the 1950's) explains the influence of composition on the mechanical behaviour of bitumen.
2. A bitumen can be characterised by the properties of its two main components, the asphaltenes and the maltenes.
3. Since the 1980's bitumens have been commonly modified by addition of polymers to decrease the susceptibility of pavements to high temperature rutting and low temperature cracking. Despite the efforts to predict the behaviour of modified bitumens from the properties of the base bitumen and the added polymer, the main methods of characterisation developed for pure bitumens are commonly used to characterise the modified bitumens.
4. The quasi-static behaviour of bitumen has been studied by many researchers using approaches such as the time dependent modulus, non linear correspondence principles, molecular theories and mechanical analogies. Almost all have concentrated on small strains in which the bitumen behaviour is nearly linear. A few had studied the behaviour at higher strains where the nonlinearities are

more noticeable. However, these models are too complex to be used in common engineering practice.

5. The Modified Cross Model developed by Cheung and Cebon provides a good representation of the steady state behaviour of bitumen at temperatures above the glass transition (T_g). For temperatures below T_g the Eyring Plasticity Model can be used to model bitumen behaviour.
6. Some researchers have attempted to model the transient behaviour of creeping materials based on curve fitting and thermodynamics principles. They have achieved good agreement with experimental results in some cases. However, these models are complex and usually require specialised software to carry the model fitting with experimental results.
7. The dynamic behaviour of bitumen at small strains, where the behaviour is nearly linear, is well understood. Nonetheless, the models proposed for the dynamic behaviour in the non-linear regime are prohibitive in terms of the complexity and number of tests needed for calibration.
8. No conclusive information could be found about the indentation behaviour of bitumen for large strains, despite the promising results observed by some researchers for small strains.

2.7 Figures

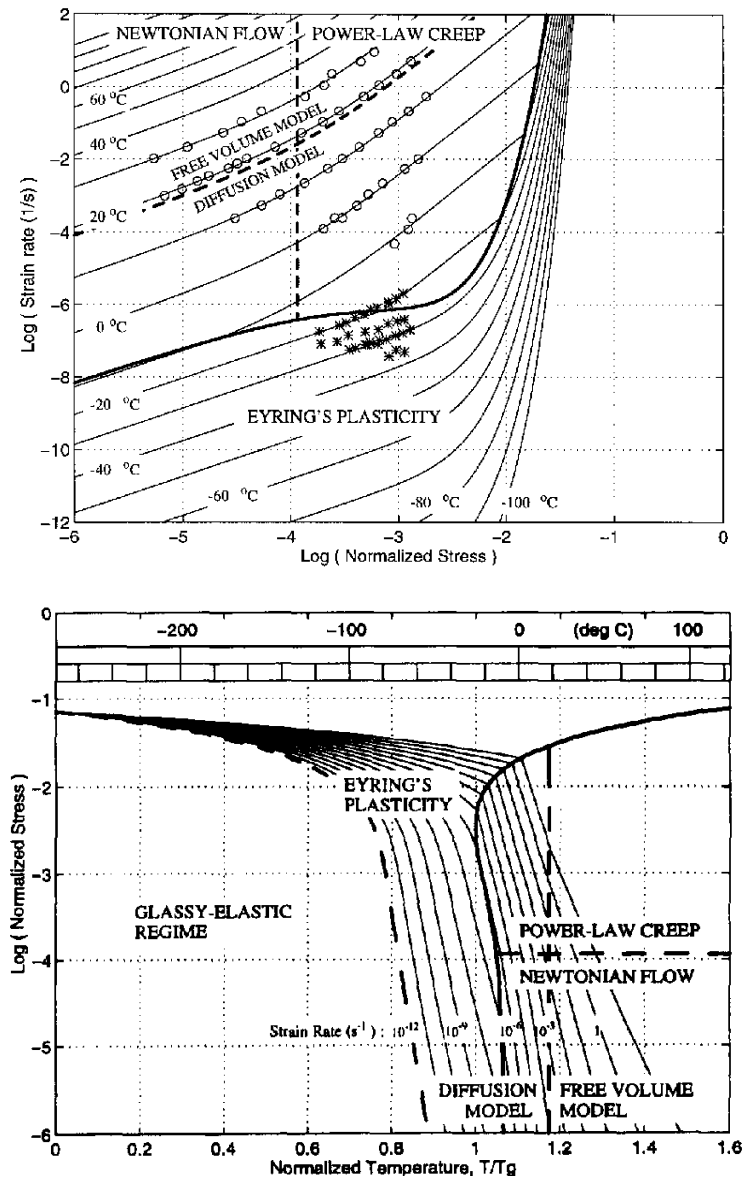


Figure 2.1: Deformation-Mechanism Maps for 50 pen bitumen (Cheung and Cebon, (1997))

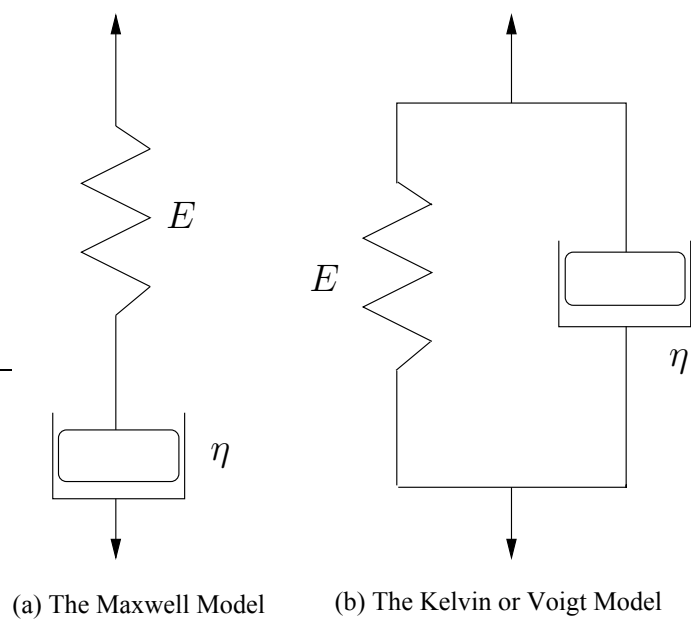


Figure 2.2: Spring and Dashpot mechanical viscoelastic analogous representation.

Chapter 3

Deformation behaviour of bitumen

3.1 Introduction

A large number of experimental investigations have attempted to characterise the monotonic and cyclic behaviour of bitumen with the aim of improving the understanding of the *rutting* or permanent deformation behaviour of pavements, as discussed in chapter 2. However, despite the efforts, these models use (i) Linear viscoelastic theories which showed good results at low strains but fail at higher strains, or (ii) Non-linear viscoelastic or visco-plastic theories which are too complex to be used in day to day engineering design.

In this chapter an extensive experimental study comprising of monotonic, continuous cyclic and pulse loading tensile experiments for two pure bitumens and two polymer-modified bitumens is detailed. Based on these experimental findings a viscous model including the effects of rate dependent recovery is proposed. In this model, the total strain-rate is decomposed into rate dependent permanent and recoverable components. By contrast to the visco-elastic models discussed in chapter 2, the “viscosity” of the bitumen is assumed to be dependent on strain and thus the relaxation

spectra are not explicitly required.

3.2 Experimental investigation

3.2.1 Materials

Four different bitumens were tested in this study:

1. Two pure bitumens, a 50 penetration grade (pen) and a 100 pen bitumens.
2. Two commercial polymer-modified bitumens, subsequently referred to as Cariphalte TS and Cariphalte DM. These bitumens have been modified using the styrene-butadiene-styrene triblock copolymer (SBS), Kraton D-1101CS.

The glass transition temperature of these materials are in the range $-40^{\circ}\text{C} < T_g < -15^{\circ}\text{C}$ (see Welborn et al. (1966) and Cheung and Cebon (1997a)). These bitumens are commonly used in hot rolled asphalt paving mixtures as well as in coated Macadam paving mixtures in the U.K. (Whiteoak, 1990). While most of the experimental results are presented for the 50 pen and Cariphalte TS bitumens, the generality of the model developed is demonstrated via spot comparisons with tests on the 100 pen bitumen. Further, the model for the Cariphalte DM bitumen is calibrated by performing a simple calibration procedure which requires only four monotonic tests, and the predictions of the model compared with pulse train experiments on this polymer-modified bitumen.

3.2.2 Specimen preparation

Dumbbell-shaped tensile bitumen specimens were cast in split silicon rubber moulds, see Cheung and Cebon (1997b) for details. The specimens were designed to have

a thick gripping section and an uniform central gage section of length 80 mm and diameter 20 mm (see fig. 3.1).

About 110 g of bitumen granules were taken from the freezer and melted at 160°C for approximately 2 hours to remove all the air bubbles. The bitumen was then poured into the pre-heated mould¹. Once the mould was filled with bitumen, it was allowed to cool to room temperature for 3 hours before half of the mould was removed. The half-mould with the specimen still in place was put into the freezer at -20°C for 6 hours. The hard specimen was then removed from the half-mould and stored in the freezer ready to be tested.

3.2.3 Test protocol

Tensile tests on the dumbbell shaped specimens were performed in a hydraulic testing machine. The load measured with a 2 kN load cell was used to define the nominal stress in the specimen while the load line displacement was employed to define the nominal strain. The specimen grips were diametrically split cups whose inner surfaces were shaped to match the head of the dumbbell specimens. The inner surfaces of the grips were lubricated with a mixture of soap and glycerine in order to prevent the specimen from adhering to the grips. The test temperature was controlled by an environmental chamber with a resolution of $\pm 0.5^\circ\text{C}$ and the rates of loading employed in this study were too slow for adiabatic heating effects to be significant. Prior to testing, all specimens were kept in the environmental chamber for about 2 hours to allow the specimens to attain the test temperature. Experimental results from tests at -5°C , 0°C , 10°C and 20°C are reported here, which are representative of operating temperatures in the U.K. It is worth mentioning here that a number of spot repeat

¹The mould was pre-heated to 90°C for 15 minutes, to avoid thermal contraction that could generate bubbles or residual stresses in the final specimen after casting.

tests confirmed the repeatability of the test results reported here. For the sake of brevity, these results are not presented here.

Monotonic tests

Constant strain-rate and constant stress creep tests were employed to characterize the monotonic stress versus strain behaviour of the material. In the constant strain-rate tests, a specified uniaxial tensile strain-rate $\dot{\epsilon}$ was applied to the specimen and the resulting nominal tensile stress σ and strain ϵ recorded. In the constant stress creep tests, a constant nominal tensile stress was applied “instantaneously” to the specimen and the nominal tensile strain ϵ recorded as a function of time t .

Creep recovery tests

The creep recovery behaviour of pure bitumen was investigated by performing a series of single load/unload tests as shown in Fig. 3.2a. A stress σ was applied rapidly to the specimen and then held constant. The material was allowed to creep to a specified total nominal tensile strain ϵ^T . At this strain, the loading stress was released and the tensile strain monitored until the strain rate was zero $\dot{\epsilon} \approx 0$. The strain at this point $\epsilon^{pl} = \epsilon^T - \epsilon^r$ is the irrecoverable strain, as shown schematically in Fig. 3.2a. Such tests were repeated for a series of strains ϵ^T and creep stresses, σ .

Cyclic tests

Continuous cyclic and pulse train tests were performed to characterise the cyclic or repeated loading behaviour of the bitumen.

Continuous cyclic tests.

In the continuous cyclic tests, the nominal tensile stress σ was varied between σ_{\min}

and σ_{\max} as shown schematically in Fig. 3.2b, with

$$R = \frac{\sigma_{\min}}{\sigma_{\max}}, \quad (3.1)$$

and

$$\sigma_m = \frac{\sigma_{\min} + \sigma_{\max}}{2}, \quad (3.2)$$

defining the load levels and the frequency f of the triangular waveform defining the loading rate. The nominal tensile strain was measured as a function of time and tests repeated for a series of values of R , σ_m and f . Strain controlled cyclic tests were not performed in this study because the strain controlled cyclic behaviour is not expected to be important in understanding the “rutting” problem wherein the ratcheting of strain gives rise to the permanent deformation.

Pulse train tests.

Tests comprising intermittent identical tensile stress pulses with a trapezoidal shape in the time domain, as shown in Fig. 3.2c, were performed in order to simulate a load history similar to that experienced in a pavement. The aim here was to investigate the relation between the single load/unload behaviour analysed via the creep and creep recovery tests and the gradual ratcheting of strain due to the application of a continuous train of discrete stress pulses as shown schematically in Fig. 3.2c.

The constant maximum stress σ_p in each trapezoidal stress pulse was applied for a time period $\Delta_p/2$ with a loading and unloading rate $\dot{\sigma} = 4\sigma_p/\Delta_p$. A series of tests at each test temperature were performed with varying time period Δ_g between consecutive trapezoidal pulses at a fixed σ_p .

3.3 Experimental results for pure bitumen

3.3.1 Monotonic behaviour

Constant strain-rate tests were performed over a wide range of strain-rates and temperatures. Figure 3.3 shows the nominal stress versus nominal strain response of the 50 pen bitumen at 0°C for four selected values of the applied strain-rate $\dot{\epsilon}$ (similar results were also obtained at other temperatures). In each test, the stress increases progressively until a maximum value is reached. This value is defined as the steady-state stress σ_{ss} , following the procedure proposed by Ward (1971) and Cheung and Cebon (1997b). With increasing applied strain-rate, the steady-state stress increases and at strain-rates $\dot{\epsilon} > 0.5 \text{ s}^{-1}$, a brittle fracture mode dominates. This very high strain-rate regime is not investigated in this study.

Constant stress creep tests were also performed over a range of stresses and temperatures. Figure 3.4 shows the monotonic creep response of the 50 pen bitumen at 0°C for two selected stress values. The slope of the secondary creep region, in which the strain varies linearly with time is defined as the steady-state strain-rate $\dot{\epsilon}_{ss}$ at the prescribed stress, in line with the prescription of Ward (1971) and Cheung and Cebon (1997b).

Figure 3.5 summarises the monotonic steady-state behaviour of the 50 pen bitumen over a range of stresses, strain-rates and temperatures on a log-log scale with axes of $\dot{\epsilon}_{ss}$ and σ_{ss} . The steady-state results from the constant stress and constant strain-rate tests are seen to be complementary, with results of both types of tests overlapping at intermediate values of σ_{ss} and $\dot{\epsilon}_{ss}$. This behaviour enables the use of constant stress tests at low strain-rates, and constant strain-rate tests at the higher stresses and strain-rates at which creep tests are impractical.

The Modified Cross model (2.14), with the constants listed in Table 3.1 was fitted

to the steady-state experimental data of the 50 pen bitumen in Fig. 3.5. Similar to the observations of Cheung and Cebon (1997b), the bitumen exhibits nonlinear viscous behaviour with $\dot{\epsilon}_{ss} \propto \sigma_{ss}^{2.6}$ ($m = 0.615$) at high stresses and linear behaviour with $\dot{\epsilon}_{ss} \propto \sigma_{ss}$ at low stress levels. Further, the temperature dependence ($-5^\circ\text{C} \leq T \leq 20^\circ\text{C}$) of the steady-state behaviour of the bitumen is well characterised by the Arrhenius relation (2.16). It is worth mentioning here that at temperatures outside this range, the thermal sensitivity of bitumen is expected to follow other scalings, for example the WLF relation as discussed by Cheung and Cebon (1997b) (see chapter 2). A similar series of tests were also performed on the 100 pen bitumen and steady-state behaviour was again found to be well characterised by the Modified Cross model with $m = 0.60$ and the Arrhenius relation capturing the temperature dependence: the material constants for the 100 pen are also listed in Table 3.1. Outside the temperature range investigated here, it is expected that the temperature sensitivity of the pure bitumens is well captured by the models proposed by Cheung and Cebon (1997b).

The constant strain-rate and creep tests reveal that the steady-state stress and strain-rate, respectively of the pure bitumen occurs at a strain $\epsilon \approx 0.15$. Thus, the steady-state Modified Cross model described above can be viewed as the relation between stress and strain-rate at a strain level $\epsilon = 0.15$ with $\dot{\epsilon}_{pc}$ as given in Table 3.1 being the calibration constant for a strain $\epsilon = 0.15$. Thus, it is expected that the Cross model can be extended to give the relation between the stress and strain-rate at any value of strain ϵ by replacing the constant $\dot{\epsilon}_{pc}$ with a reference strain-rate $\dot{\epsilon}_o(\epsilon)$ that is a function of strain ϵ . Equations (2.14) and (2.16) can then be re-written as:

$$\frac{\sigma}{\dot{\epsilon}} = \frac{\sigma_o}{\dot{\epsilon}_o(\epsilon)} \frac{1}{1 + \left(\frac{\dot{\epsilon}}{\dot{\epsilon}_o(\epsilon)}\right)^m}, \quad (3.3)$$

where

$$\dot{\epsilon}_o(\epsilon) = \dot{\epsilon}_{oc}(\epsilon) e^{-k\left(\frac{1}{T} - \frac{1}{273}\right)}, \quad (3.4)$$

with the Arrhenius constant k assumed to remain unchanged from that given in Table 3.1. Note that it has been employed a reference temperature of 273 K (0°C) rather than the glass transition temperature T_g . This is because T_g of these bitumens lies outside the range of temperatures tested here and that the applicability of the model at that rather low temperature is unclear.

To test this hypothesis, the function $\dot{\epsilon}_{oc}(\epsilon)$ was extracted from the constant strain-rate and creep responses of the bitumen at a temperature T as follows. Given the stress versus strain curve for a constant strain-rate test at an applied strain rate $\dot{\epsilon}$, Eqn. (3.3) was solved for $\dot{\epsilon}_o(\epsilon)$ with σ given by the experimentally measured value of stress at the strain $\epsilon > 0.005^2$. This procedure was repeated at selected values of ϵ to get $\dot{\epsilon}_o(\epsilon)$ as a function of ϵ . Similarly, from creep tests, (3.3) was solved at selected values of ϵ to give $\dot{\epsilon}_o(\epsilon)$, with $\dot{\epsilon}$ at each value of ϵ given by the experimentally measured value of the strain-rate at that strain ϵ . The calibration function $\dot{\epsilon}_{oc}(\epsilon)$ was then obtained from (3.4) with the constant k as given in Table 3.1 and T , the temperature of the test used to obtain the function $\dot{\epsilon}_o(\epsilon)$.

The calibration curves, $\dot{\epsilon}_{oc}(\epsilon)$ versus ϵ , obtained from a series of three constant strain-rate and creep tests on the 50 pen bitumen at 0°C and 10°C are shown in Fig. 3.6: all the curves overlap to within experimental error, demonstrating the validity of the extension (3.3) to the Modified Cross model. Calibration curves, $\dot{\epsilon}_{oc}(\epsilon)$ versus ϵ , obtained for the 100 pen bitumen from two constant strain-rate tests at 0°C are also shown in Fig. 3.6. These curves also overlap to within experimental error, which confirms that the extension to the Modified Cross model holds for the 100 pen bitumen as well.

²At $\epsilon = 0$, $\dot{\epsilon}_o(0) = \infty$ as the stress $\sigma = 0$. Thus, the calibration calculation is performed for strain values $\epsilon > 0$. The Modified Cross model is not expected to be accurate at very small strains when the rate-independent elastic response of the bitumen is not negligible and thus this approximation for calibrating the model suffices.

3.3.2 Creep recovery behaviour

Creep recovery tests on the 50 pen bitumen were performed at -5°C , 0°C and 10°C and the recovery behaviour investigated for unloading from total creep strains ϵ^{T} in the range $0.02 \leq \epsilon^{\text{T}} \leq 0.2$, for five levels of the constant creep stress σ . The creep recovery response at 10°C of the 50 pen bitumen with $\sigma = 0.32$ MPa is shown in Fig. 3.7a, with strain ϵ plotted as a function of time t , for three selected values of $\epsilon^{\text{T}} = 0.06, 0.12$ and 0.22 . Similarly, the creep recovery response of the 50 pen bitumen at 0°C with $\sigma = 0.2$ MPa is shown in Fig. 3.7b for two selected values of $\epsilon^{\text{T}} = 0.097$ and 0.16 . In all cases, the recovered strain ϵ^{r} is seen to increase with increasing ϵ^{T} .

The results from all the creep recovery tests performed are summarised in Fig. 3.8 where the recovered strain ϵ^{r} (defined in Section 3.2.3) is plotted as a function of the total strain ϵ^{T} prior to unloading. The figure reveals that, to within experimental error, $\epsilon^{\text{r}} = \psi \epsilon^{\text{T}}$ with the slope ψ ($0 \leq \psi \leq 1$) of the line in Fig. 3.8 independent of the stress and temperature for a given bitumen. In the following this slope shall be referred to as the “recovery constant” ψ . ψ was found to be 0.70 and 0.47 for the 50 and 100 pen bitumens, respectively.

Given that the monotonic loading response of the bitumen is captured by the extended Cross model in which the reference strain rate $\dot{\epsilon}_{oc}(\epsilon)$ is a unique function of strain ϵ , it is expected that the recovery strain versus time history could also be captured by a unique unloading calibration curve. The recovery strain-rate $\dot{\epsilon}^{\text{r}}$ is a maximum immediately after the removal of the stress and reduces to zero as the strain $\epsilon \rightarrow \epsilon^{\text{pl}}$. Thus, the recoverable strain is parametrised by

$$\hat{\epsilon}^{\text{r}} \equiv \left(\frac{\epsilon}{\epsilon^{\text{pl}}} - 1 \right) \frac{1 - \psi}{\psi}, \quad (3.5)$$

with $\hat{\epsilon}^{\text{r}} = 1$ at the instant of unloading and $\hat{\epsilon}^{\text{r}} = 0$ when the strain $\epsilon = \epsilon^{\text{pl}}$, ie. when the recoverable strain is zero. It is hypothesised that the recovery rate $\dot{\epsilon}^{\text{r}}$ at temperature

T is described by a unique function $\dot{\epsilon}_{uc}(\hat{\epsilon}^r)$ such that

$$\dot{\epsilon}^r = -\dot{\epsilon}_u(\hat{\epsilon}^r), \quad (3.6)$$

where

$$\dot{\epsilon}_u(\hat{\epsilon}^r) = \dot{\epsilon}_{uc}(\hat{\epsilon}^r)e^{-k\left(\frac{1}{T}-\frac{1}{273}\right)}. \quad (3.7)$$

The above equations imply that the recovery rate $\dot{\epsilon}^r$ is (i) a unique function of $\hat{\epsilon}^r$, (ii) independent of loading history, and (iii) scales with temperature according to same Arrhenius relation that governs the loading temperature dependence.

The function $\dot{\epsilon}_{uc}(\hat{\epsilon}^r)$ is calculated as follows. With the recovery constant ψ known for the bitumen, the recovery rate $\dot{\epsilon}^r$ is calculated as a function of $\hat{\epsilon}^r$ from recovery experiments such as those shown in Fig. 3.7 and set equal to $-\dot{\epsilon}_u$. The reference recovery strain-rate $\dot{\epsilon}_{uc}$ is then calculated via (3.7) with the Arrhenius constant k given in Table 3.1 for the two bitumens under consideration. This reference strain rate $\dot{\epsilon}_{uc}$ is plotted in Fig. 3.9 as a function of $\hat{\epsilon}^r$ for the 50 pen bitumen from a series of three recovery tests at 0°C and 10°C, similar to those shown in Fig. 3.7. To within experimental error, all the curves for the 50 pen overlap each other. This confirms that the recovery behaviour can be captured by a unique calibration curve $\dot{\epsilon}_{uc}(\hat{\epsilon}^r)$. Similar results were also found for the 100 pen bitumen, with $\dot{\epsilon}_{uc}$ calculated from series of two recovery tests on the 100 pen bitumen included in Fig. 3.9. Intriguingly the $\dot{\epsilon}_{uc}(\hat{\epsilon}^r)$ versus $\hat{\epsilon}^r$ curves for both bitumens are very similar.

3.3.3 Continuous cyclic response

Continuous stress controlled cyclic tests were performed to investigate the effect of the mean stress σ_m , load ratio R , frequency f and temperature on the cyclic strain versus time response of the bitumen.

The strain versus time response of the 50 pen bitumen with $R = 0.15$ is shown

in Figs. 3.10a and 3.10b at 10°C and 0°C, respectively for two selected values of the mean stress σ_m in each case. The cyclic stress-controlled response is seen to be similar in form to the monotonic creep response with primary, secondary and tertiary regimes of behaviour. The cyclic steady-state strain-rate is defined as the mean gradient of the strain versus time history in the secondary regime of behaviour. Fig. 3.10 shows that this steady-state strain-rate increases with increasing mean stress σ_m for a fixed R .

Next, consider the influence of the load ratio R and frequency f on the cyclic stress controlled response. The strain versus time history of the 50 pen bitumen at 0°C with $\sigma_m = 0.095$ MPa and $f = 0.1$ Hz is shown in Fig. 3.11a for three selected values of R and in Fig. 3.11b with $\sigma_m = 0.064$ MPa and $R = 0.15$ for four selected frequencies f . Both these figures demonstrate that the load ratio R and frequency f have a negligible effect on the cyclic stress controlled strain versus time response of the 50 pen bitumen. A series of similar experiments on both the 50 pen and 100 pen bitumens confirmed this result over the range of temperatures and stresses investigated here.

Given that the cyclic stress controlled behaviour of bitumen is governed by the mean stress, it is worth examining the relation of the *cyclic* steady-state strain rate and the *monotonic* steady-state creep strain-rate. The cyclic steady-state strain-rate from a series of tests on the 50 pen bitumen (with varying values of f , R and temperature T) are also plotted in Fig. 3.5 as a function of the mean stress σ_m , alongside the monotonic steady-state data. A comparison between the cyclic and monotonic steady-state data reveals that the cyclic steady-state behaviour follows the monotonic steady-state response, with the creep stress σ_{ss} interpreted as the cyclic mean stress σ_m .

3.3.4 Results of pulse train tests

Cyclic stress controlled pulse tests were performed for a range of temperatures, pulse stresses σ_p and time period ratios Δ_p/Δ_g (see fig. 3.2c). Representative results for tests on the 50 pen bitumen at 10°C and 0°C are shown in Figs. 3.12a and 3.12b, respectively for Δ_p/Δ_g in the range 0.04 to 0.4. Similar tests on the 100 pen bitumen at 0°C with $\Delta_p/\Delta_g = 0.2$ and 0.4 are shown in Fig. 3.13. The results clearly show that for a fixed value of σ_p , the accumulated permanent strain decreases with decreasing Δ_p/Δ_g , because larger fractions of the creep strain are recovered in the zero-load gaps between the pulses. In fact, as $\Delta_g \rightarrow 0$, the pulse train tests converge to the continuous cyclic loading tests, with no recovery of the accumulated strain.

3.4 Experimental results for polymer-modified bitumen Cariphalte TS

3.4.1 Monotonic loading behaviour

Constant strain-rate tests were performed over a wide range of strain-rates at three different temperatures, 0°C, 10°C and 20°C. Figure 3.14 shows the nominal stress versus nominal strain response of Cariphalte TS at 0°C for three selected values of the applied strain-rate $\dot{\epsilon}$ (similar results were obtained at other temperatures). In each test, the tensile stress increases progressively until a maximum value is reached, as for pure bitumen. This value is defined as the steady-state stress σ_{ss} , following the procedure described for pure bitumen. With increasing applied strain-rate, the steady-state stress increases.

Constant stress creep tests were also performed over a range of stresses and temperatures and selected results at 0°C are plotted in Fig. 3.15. The creep response

is seen to be similar to that of pure bitumen and therefore the creep strain-rate in the secondary creep region (in which the strain varies linearly with time) is defined as the steady-state strain-rate $\dot{\epsilon}_{ss}$ at the applied stress.

The steady-state behaviour of Cariphalte TS, is summarised in Fig. 3.16 for three test temperatures tested with the steady state strain-rate $\dot{\epsilon}_{ss}$ plotted against the steady-state stress σ_{ss} . The modified Cross model (2.14) with constants listed in Table 3.2 along with the Arrhenius relation for temperature-dependence is seen to describe the steady-state response of the Cariphalte TS bitumen with reasonable accuracy over the range of temperatures, stresses and strain-rates tested.

Following a similar procedure to that followed for pure bitumen in section 3.3.1, calibration curves, $\dot{\epsilon}_{oc}$ versus ϵ , were obtained from constant strain-rate and creep tests at various test conditions. These calibration curves are shown in Fig. 3.17: all the curves for Cariphalte TS overlap to within experimental error suggesting that the model proposed for pure bitumen in section 3.3.1 is also applicable to this polymer-modified bitumen.

3.4.2 Creep recovery behaviour

Creep recovery experiments were performed at 0°C and 10°C at selected stress levels and for unloading from total strains ϵ^T in the range $0.02 \leq \epsilon^T \leq 0.9$. Typical results at 0°C for an applied stress level $\sigma = 0.64$ MPa and $\epsilon^T \approx 0.04$ and 0.14 are shown in Fig. 3.18a. Similar to the case of the pure bitumen, the Cariphalte TS exhibits strain recovery with the recovered strain ϵ^r increasing with total strain ϵ^T , before load release.

The results from all the creep recovery tests performed are summarised in Fig. 3.18b where the recovered strain ϵ^r (defined in section 3.2.3) is plotted as a function of the total strain ϵ^T prior to unloading. The figure reveals that, to within experimental

error, $\epsilon^r = \psi \epsilon^T$ with the slope ψ ($0 \leq \psi \leq 1$) of the line in Fig. 3.18b independent of the stress and temperature as for pure bitumen. The “recovery constant” is $\psi \approx 0.65$ for the Cariphalte TS.

The recovery calibration curve $\dot{\epsilon}_{uc}(\dot{\epsilon}^r)$ for the Cariphalte TS bitumen was calculated following the same procedure described in section 3.3.2 for pure bitumen. For the sake of clarity only one recovery calibration curve is shown in Fig. 3.19 for the Cariphalte TS bitumen. The recovery calibration curves extracted from a series of tests were found to overlap this curve to within experimental error.

3.4.3 Continuous cyclic loading

The strain versus time response of the Cariphalte TS bitumen with $R = 0.15$ is shown in Fig. 3.20 at 0°C , for two selected values of the mean stress σ_m . The cyclic stress-controlled response is similar in form to the monotonic creep response (fig. 3.15), with primary, secondary and tertiary regimes of behaviour (the tertiary regime occurs for longer loading times than those shown in the figure). The cyclic steady-state strain-rate is defined as the mean gradient of the strain versus time history in the secondary regime of behaviour, as for pure bitumen. Fig. 3.20 shows that this steady-state strain-rate increases with increasing mean stress σ_m for a fixed R .

Next, consider the influence of the load ratio R and frequency f on the cyclic stress controlled response. The strain versus time history at 0°C with $\sigma_m = 0.36$ MPa and $f = 2$ Hz is shown in Fig. 3.21a for three selected values of R . The response for loading with $\sigma_m = 0.36$ MPa and $R = 0.3$ is shown in Fig. 3.21b for four selected frequencies f . Both these figures demonstrate that the load ratio R and frequency f have a minimal effect on the strain versus time response for cyclic stress-controlled tests, as was the case for pure bitumen.

It is worth mentioning here that, similar to the pure bitumens studied, the mean

steady-state stress versus strain-rate responses of the Cariphalte TS bitumen measured in cyclic tests is well represented by the Modified Cross model (2.14), with constants unchanged from the monotonic case (and listed in Table 3.2). This further confirms the observation that the continuous cyclic response is only a function of the mean stress and essentially independent of the stress amplitude or frequency.

3.4.4 Pulse train tests

Cyclic stress controlled pulse tests were performed for a range of temperatures, pulse stresses σ_p and time periods Δ_p/Δ_g (see Fig. 3.2c). Representative results for tests at 0°C are shown in Fig. 3.22 for $\Delta_p = 13$ s and $\sigma_p = 0.4$ MPa at two selected values of the gap period Δ_g for the Cariphalte TS bitumen. The results clearly show that for a fixed value of σ_p , the accumulated permanent strain decreases with increasing Δ_g , as for pure bitumen.

3.5 Phenomenological model

A phenomenological uniaxial constitutive model for bitumen is proposed here. It captures the monotonic, creep recovery, continuous cyclic and pulse loading behaviour described in the previous sections for both pure and polymer-modified bitumens. The model is motivated by the following experimental observations:

1. The monotonic response is adequately described by the extended Cross model with the reference strain-rate $\dot{\epsilon}_{oc}$ a function of the strain ϵ .
2. The recovery response is captured by an unloading reference strain-rate $\dot{\epsilon}_{uc}$ which is a function of the recoverable strain as parametrised by $\hat{\epsilon}^r$.
3. The continuous cyclic response follows the monotonic response with the mean

stress σ_m interpreted as the creep stress σ . This indicates that recovery is negligible in these continuous cyclic tests.

4. The loading and recovery temperature dependence of the bitumen is adequately described by the Arrhenius relation over the range of temperatures, $-5^\circ\text{C} \leq T \leq 20^\circ\text{C}$, investigated here.

The total strain-rate $\dot{\epsilon}$ is written as the sum of the viscous strain-rate $\dot{\epsilon}^v$, which is active during loading ($\sigma \neq 0$) and the recovery strain-rate $\dot{\epsilon}^r$, which is only active when the stress $\sigma = 0$. Thus for an arbitrary loading history,

$$\dot{\epsilon} = \dot{\epsilon}^v + \dot{\epsilon}^r. \quad (3.8)$$

The viscous response of the bitumen to an applied load is given by the implicit equation of the extended Cross model

$$\dot{\epsilon}^v = \frac{\dot{\epsilon}^{\text{pl}}}{1 - \psi} = \frac{\sigma \dot{\epsilon}_o(\epsilon)}{\sigma_o} \left[1 + \left(\frac{\dot{\epsilon}^v}{\dot{\epsilon}_o(\epsilon)} \right)^m \right], \quad (3.9a)$$

where $\dot{\epsilon}^{\text{pl}}$ is the irrecoverable fraction of the viscous strain-rate as discussed in Section 3.3.2. Note that in the high loading rate limit ($\dot{\epsilon} \gg \dot{\epsilon}_o$), the viscous strain-rate can be written in terms of the power-law relation

$$\dot{\epsilon}^v = \frac{\dot{\epsilon}^{\text{pl}}}{1 - \psi} = \dot{\epsilon}_o(\epsilon) \left(\frac{\sigma}{\sigma_o} \right)^n, \quad (3.9b)$$

where $n = 1/(1 - m)$.

The recovery rate follows from the discussion in Section 3.3.2 as

$$\dot{\epsilon}^r = -\text{sign}(\epsilon) [1 - \text{sign}(|\sigma|)] \dot{\epsilon}_u(\hat{\epsilon}^r). \quad (3.10)$$

Here $\text{sign}(0)$ is defined to be zero and $-\text{sign}(\epsilon)$ ensures that the recovery rate $\dot{\epsilon}^r$ reduces the strain ϵ . Note that the calibration functions $\dot{\epsilon}_o(\epsilon)$ and $\dot{\epsilon}_u(\hat{\epsilon}^r)$ at the temperature T under consideration are given by (3.4) and (3.7), respectively with $\dot{\epsilon}_{oc}$ and $\dot{\epsilon}_{uc}$ the

reference strain-rates as shown in Figs. 3.6 and 3.9, respectively for pure bitumen and in Figs. 3.17 and 3.19, respectively for polymer-modified bitumen.

It is necessary to integrate equations (3.8)-(3.10) with respect to time to obtain the strain resulting from an applied stress history.

3.5.1 Comparison with experimental results

In this section the predictions of the phenomenological model are compared with the monotonic, recovery, continuous cyclic and pulse loading experimental results. Detailed comparisons are made for the 50 pen and Cariphalte TS bitumens while for the sake of brevity, only comparisons for the more realistic pulse loading tests are shown for the 100 pen bitumen. The material constants employed in these comparisons are listed in Tables 3.1 and 3.2 for the bitumens investigated with the loading and recovery calibration curves, $\dot{\epsilon}_{oc}(\epsilon)$ and $\dot{\epsilon}_{uc}(\hat{\epsilon}^r)$ shown in Figs. 3.6 and 3.9, respectively for pure bitumen and in Figs. 3.17 and 3.19, respectively for polymer-modified bitumen.

Pure bitumen

Comparisons between the model predictions and experimental data for monotonic constant strain-rate and constant stress creep tests are shown in Figs. 3.3 and 3.4, respectively with the dotted lines corresponding to the model predictions. Excellent agreement is seen with both the constant strain-rate tests at 0°C and the creep tests at 10°C over a range of stresses and strain-rates. Similarly, good agreement is seen between the model predictions and the creep-recovery experimental results for the 50 pen bitumen at 0°C and 10°C as shown in Figs. 3.7a and 3.7b, respectively. It is worth emphasising here that the tests used to calibrate $\dot{\epsilon}_{oc}(\epsilon)$ and $\dot{\epsilon}_{uc}(\hat{\epsilon}^r)$ were different from those employed to demonstrate the accuracy of the model in Figs. 3.3, 3.4 and 3.7 : the model is, of-course, in perfect agreement with the calibration tests.

The model captures to within reasonable accuracy the continuous cyclic response of the 50 pen bitumen as shown in Fig. 3.10 for tests at 0°C and 10°C. A rate-independent elastic strain component is not included in the model and thus particularly for the tests at 10°C, the model does not capture the reduction in strain during the unloading part of each cycle. However, the total accumulated strain is predicted to within reasonable accuracy. As per experimental observations, the model correctly predicts a negligible dependence of the response on the load ratio R and frequency f as seen in the comparisons made in Fig. 3.11.

A key judge of the accuracy of the model lies in its ability to predict the response of the bitumen in the pulse loading tests: in these tests both the creep response of the bitumen under loads and its recovery behaviour is combined in a complicated manner and the response of the model is integrated over many cycles, enabling modelling errors to build-up. Such comparisons for pulse loading tests on the 50 pen bitumen at 0°C and 10°C are shown in Fig. 3.12 and in Fig. 3.13 for the 100 pen bitumen at 0°C. The model in all these cases is seen to accurately predict the total accumulated strains. However, the model under-predicts the strain recovery during the zero-load section of the loading history. This is due to the fact that the model assumes no history dependence, ie. the bitumen loading and unloading behaviour is assumed to remain unchanged from cycle to cycle with the first cycle identical to the n^{th} cycle. The experimental results show that this is clearly not the case. However, the current simple model does succeed in capturing the total accumulated strain and the steady-state slopes to within reasonable accuracy: and are the relevant parameters in predicting the rutting response of a pavement.

Polymer-modified bitumen

Comparisons between the model predictions and experimental data for monotonic constant strain-rate and constant stress creep tests for Cariphalte TS bitumen are

shown in Figs. 3.14 and 3.15, respectively with the dotted lines corresponding to the model predictions. Excellent agreement is seen with both the constant strain-rate tests and the creep tests at 0°C over a range of stresses and strain-rates. Similarly, good agreement is seen between the model predictions and the creep-recovery experiments at 0°C shown in Fig. 3.18a. Similarly, the model captures, to within reasonable accuracy, the continuous cyclic response shown in Fig. 3.20 for tests at 0°C, and predicts negligible dependence of the strain versus time history on the stress ratio R or frequency f in line with the experimental data plotted in Figs. 3.21a and 3.21b.

Comparisons between model and experimental results for pulse loading at 0°C are shown in Fig. 3.22. The model is seen to predict the total accumulated strains quite accurately for the two cases shown. However, the model under-predicts the strain recovery during the zero-load section of the loading history, as for pure bitumen.

3.5.2 Extension to 3-dimensional loading

The constitutive model detailed above was developed for uniaxial loading. This model can be generalised for 3D loading by noting that for all practical purposes the response of the bitumen is independent of the mean or hydrostatic stress with the bitumen behaving like a rate-dependent von-Mises solid (Cheung and Cebon, 1997b). Adopting cartesian tensor notation, a 3D phenomenological constitutive model can then be written as

$$\dot{\epsilon}_{ij} = \dot{\epsilon}_{ij}^v + \dot{\epsilon}_{ij}^r. \quad (3.11)$$

Noting that the viscous strain-rate is independent of the hydrostatic stress, a 3D generalisation of the extended Cross model (eq. 3.9a) based on the von-Mises effective stress is given by

$$\dot{\epsilon}_{IJ}^v = \frac{\dot{\epsilon}_{IJ}^{\text{pl}}}{1 - \psi} = \frac{\sigma_e}{k} \dot{\epsilon}_o(\epsilon_e) \left[1 + \left(\frac{\dot{\epsilon}_{IJ}^v k}{\dot{\epsilon}_o(\epsilon_e)} \right)^m \right], \quad (3.12a)$$

where

$$k = \frac{2}{3} \frac{\sigma_e}{\sigma'_{IJ}}. \quad (3.12b)$$

Here $\sigma_e = \sqrt{\frac{3}{2} \sigma'_{ij} \sigma'_{ij}}$ is the von-Mises effective stress, and $\epsilon_e = \sqrt{\frac{2}{3} \epsilon^v_{ij} \epsilon^v_{ij}}$ the von-Mises effective strain, with the prime denoting deviatoric quantities. Capital letters have been employed in the indices of the above equation to emphasise no summation over repeated indices.

A multi-axial generalisation of the uniaxial power-law model (3.9b) based on the von-Mises effective stress is given as

$$\dot{\epsilon}^v_{ij} = \frac{\dot{\epsilon}^{\text{pl}}_{ij}}{1 - \psi} = \frac{3\dot{\epsilon}_o(\epsilon_e)}{2} \left(\frac{\sigma_e}{\sigma_o} \right)^{n-1} \frac{\sigma'_{ij}}{\sigma_o}. \quad (3.12c)$$

Note that in a uniaxial test with the axial stress and strain σ and ϵ , respectively, $\sigma_e = |\sigma|$ while $\epsilon_e = |\epsilon|$ for an incompressible solid. Consistent with the uniaxial observations, strain recovery is assumed to occur when $\sigma_e = 0$. Thus, the recovery rate (eq. 3.10) is given by

$$\dot{\epsilon}^r_{ij} = - [1 - \text{sign}(\sigma_e)] \dot{\epsilon}_u(\dot{\epsilon}_e^r) \frac{\epsilon'_{ij}}{\epsilon_e}, \quad (3.13)$$

and (3.5) becomes

$$\dot{\epsilon}_e^r \equiv \left(\frac{\epsilon_e}{\epsilon_e^{\text{pl}}} - 1 \right) \frac{1 - \psi}{\psi}. \quad (3.14)$$

The term $\frac{\epsilon'_{ij}}{\epsilon_e}$ ensures that (3.13) reduces to the uniaxial model and that volume constancy is maintained, ie. $\dot{\epsilon}^r_{kk} = 0$.

The rate dependent part of the response is now fully specified. In order to complete the constitutive description, the elastic or rate independent contribution can be added. For this, the bitumen is assumed to be a linear isotropic material with Young's modulus E and Poisson's ratio ν . The elastic strain-rate $\dot{\epsilon}^e_{ij}$ is then given by

$$\dot{\epsilon}^e_{ij} = \frac{1 + \nu}{E} \dot{\sigma}_{ij} - \frac{\nu}{E} \dot{\sigma}_{kk} \delta_{ij}, \quad (3.15)$$

where δ_{ij} is the Kronecker delta. This elastic component is negligible for most practical purposes and is added in here to complete the specification of the phenomenological model for implementation in a finite element program. A reasonably high value of E can be chosen so as to not affect the results but ensure numerical stability of the finite element code.

3.5.3 An approximate calibration of the model

Six parameters, $m, \sigma_o, k, \dot{\epsilon}_{oc}(\epsilon_e), \dot{\epsilon}_{uc}(\dot{\epsilon}_e^r)$ and ψ uniquely characterise the deformation behaviour of bitumen in the phenomenological model proposed. A five-step procedure to calibrate the model in an approximate manner with a minimum of four uniaxial tensile experiments is described and applied to the second polymer-modified bitumen, Cariphalte DM, in order to validate this approximate calibration method. Note that in uniaxial tension, the von-Mises effective strain ϵ_e is approximately equal to the tensile strain ϵ : volume constancy is assumed to be approximately maintained in these large deformation tests where elastic effects are negligible. Thus, ϵ_e can be interpreted as the tensile strain ϵ .

Step 1: The first step is to characterise the monotonic steady-state response at the reference temperature of 0°C which involves determining the constants m and σ_o . Note that the Cross model (2.14) reduces to a nonlinear viscous relation of the form

$$\frac{\sigma_{ss}}{\sigma_o} = \left(\frac{\dot{\epsilon}_{ss}}{\dot{\epsilon}_p} \right)^{(1-m)}, \quad (3.16)$$

at $\dot{\epsilon}_{ss}/\dot{\epsilon}_p \gg 1$. Two constant strain rate tests were conducted at 0°C employing strain-rates $\dot{E}_{n1} = 0.015 \text{ s}^{-1}$ and $\dot{E}_{n2} = 0.05 \text{ s}^{-1}$. With the peak stresses in these two tests denoted by Σ_{n1} and Σ_{n2} , respectively, the power-law exponent m in the modified Cross model was calculated using

$$m = 1 - \frac{\log(\Sigma_{n1}/\Sigma_{n2})}{\log(\dot{E}_{n1}/\dot{E}_{n2})}. \quad (3.17)$$

Step 2: Next consider the low strain-rate limit when $\dot{\epsilon}_{ss}/\dot{\epsilon}_p \ll 1$. In this case the Modified Cross model (2.14) reduces to a linear viscous relation

$$\frac{\sigma_{ss}}{\sigma_o} = \left(\frac{\dot{\epsilon}_{ss}}{\dot{\epsilon}_p} \right). \quad (3.18)$$

A constant stress creep-recovery test was conducted at 0°C with an applied creep stress $\Sigma_{l1} = 0.06$ MPa. The specimen was strained to $\epsilon^T = 0.2$ and then the stress removed. The strain was monitored as a function of time until no further strain recovery was observed. The strain-rate \dot{E}_{l1} in the secondary creep region was used to obtain the stress σ_o at which the bitumen behaviour transitions from linear to nonlinear viscous behaviour:

$$\sigma_o = \left(\frac{\dot{E}_{l1}}{\dot{E}_{n1}} \right)^{(1-m)/m} \left(\frac{\Sigma_{n1}}{\Sigma_{l1}} \right)^{1/m} \Sigma_{l1}. \quad (3.19)$$

Step 3: Next, the calibration curve $\dot{\epsilon}_{oc}(\epsilon_e)$ for the monotonic transient behaviour can be obtained from the constant strain-rate test conducted at the strain-rate \dot{E}_{n1} by writing

$$\dot{\epsilon}_o(\epsilon_e) = \dot{E}_{n1} \left(\frac{\sigma_o}{\sigma(\epsilon_e)} \right)^{1/(1-m)}, \quad (3.20)$$

where $\sigma(\epsilon_e)$ is the tensile stress at axial strain ϵ . Note that this calibration is typically performed for strain $\epsilon > 0.005$ in order to avoid the singularity at $\epsilon = 0$ as explained in Section 3.3.1. This calibration curve is plotted in Fig. 3.17.

Step 4: The parameters used to characterise the loading behaviour of the bitumen at 0°C have been found. The unloading calibration curve $\dot{\epsilon}_u(\hat{\epsilon}_e)$ and the recovery constant ψ can now be extracted from the creep recovery test conducted in step 2. With ϵ^T the strain prior to unloading and ϵ^{pl} the permanent strain accumulated in the creep recovery test described above, the recovery constant ψ is given by

$$\psi = 1 - \frac{\epsilon^{pl}}{\epsilon^T}. \quad (3.21)$$

The recovery calibration curve $\dot{\epsilon}_u(\hat{\epsilon}_e^r)$ (with $\hat{\epsilon}_e^r = \hat{\epsilon}^r$) can be obtained from the unloading section of the creep recovery test using the procedure detailed in Section 3.3.2. This curve is plotted in Fig. 3.19, along with the recovery calibration curves of the Cariphalte TS polymer modified bitumen and the 50 pen and 100 pen pure bitumens. Note that all these recovery calibration curves are the same to within experimental error. Further investigations need to be conducted to understand whether $\dot{\epsilon}_{uc}(\hat{\epsilon}^r)$ is a universal function for all bitumens.

Step 5: The phenomenological model is now completely calibrated at 0°C and it remains to determine the Arrhenius constant k in order to quantify the temperature dependence of the bitumen. A creep test was conducted at a temperature $T_2 = 10^\circ\text{C}$ and creep stress $\Sigma_{l2} = 0.17$ MPa. The measured steady-state strain rate is denoted by \dot{E}_{l2} . The Arrhenius constant k was then obtained using

$$k = \frac{\ln \left[\frac{\Sigma_{l2} \dot{E}_{l1}}{\Sigma_{l1} \dot{E}_{l2}} \right]}{1/T_2 - 1/T_1}, \quad (3.22)$$

where $T_1 = 273\text{K}$ and $T_2 = 273 + 10 = 283\text{K}$.

The modified Cross model parameters for the Cariphalte DM bitumen, obtained employing the above procedure are listed in Table 3.1 and the loading and unloading calibration curves plotted in Figs. 3.17 and 3.19, respectively. Using these parameters the predictions of the model are compared with experimental measurements from pulse train tests ($\sigma_p = 0.4$ MPa and $\Delta_p = 13$ s) for two choices of the load gap Δ_g in Fig. 3.23. With this approximate calibration the model captures the pulse loading behaviour with reasonable accuracy: conducting a more comprehensive set of calibration tests as done for the other bitumens would improve the agreement between the model and the experimental measurements.

3.6 Discussion

A general 3D phenomenological model for bitumen has been developed. Four simple uniaxial tests suffice to calibrate the model which is capable of predicting the response of pure and polymer-modified bitumen for a variety of monotonic and cyclic loadings and over a range of temperatures.

Most models for the cyclic behaviour of bitumen, such as those discussed in chapter 2, treat bitumen as either a linear or nonlinear visco-elastic solid. In such cases the creep and relaxation behaviour is captured by a relaxation spectrum in the linear visco-elastic case and by the multiple integral representation of Ward and Onat (1963) in the nonlinear case. In contrast to the simple phenomenological model proposed here, an extensive set of experiments is needed to calibrate these visco-elastic models. In the model proposed here, a different approach is adopted wherein the response is not considered as a superposition of relaxation moduli. Rather, the “viscosity”, as parametrised by $\dot{\epsilon}_{oc}(\epsilon)$ and $\dot{\epsilon}_{uc}(\hat{\epsilon}^r)$, is taken to be a function of strain. This is similar to some metal plasticity theories where the yield strength is taken to be strain dependent. Physically this can be rationalised by recalling that the asphaltenes in the bitumen re-arrange with deformation and thus the “viscosity” is expected to be a function of strain just as the yield strength of metals is a function of accumulated plastic strain due to the evolution of the dislocation structure. Comparisons with a range of experiments show that such an approach provides a sufficiently accurate model for most practical loading histories.

The current model has been shown to be valid for most operating temperatures encountered in the U.K. (-5°C to 20°C). At extremely low temperatures (less than approximately -15°C) the behaviour of bitumen is no longer viscous with brittle fracture and Eyring plasticity becoming the dominant deformation mechanisms (Cheung and Cebon, 1997b). This domain is not addressed in the current study.

3.7 Concluding Remarks

1. The monotonic constant strain-rate and creep behaviour of four bitumens (2 pure and 2 polymer-modified) have been measured over a range of temperatures. The monotonic response under both these loading conditions was found to be adequately described by an extended Cross model wherein the “viscosity” as parametrised by $\dot{\epsilon}_{oc}(\epsilon)$ is a function of strain.
2. The recoverable strain is directly proportional to the strain prior to unloading with the recovery rate a unique function of the recoverable strain $\tilde{\epsilon}$.
3. Both the loading and recovery responses were observed to be temperature dependent with the Arrhenius relation capturing the temperature dependence over the range of temperatures tested, $-5^{\circ}\text{C} \leq T \leq 20^{\circ}\text{C}$.
4. Two types of cyclic loading tests were conducted, (i) continuous cyclic and (ii) pulse train tests to simulate vehicle loading in a pavement. While the continuous cyclic response was similar to the monotonic response with only the mean stress governing the behaviour, significant strain recovery was observed during the rest periods in the pulse train experiments.
5. A simple phenomenological model which can be calibrated by a minimum of four uniaxial tensile experiments was proposed. This model is seen to capture the monotonic, continuous cyclic and pulse loading response of the four bitumens with reasonable accuracy.
6. An extension of the model to fully 3D loading is also proposed based on a von-Mises criterion. This makes the simple model amenable for implementation in a finite element program that can be used to predict the behaviour of the bitumen under more complex loading conditions.

3.8 Tables

Parameter	50 pen Bitumen	100 pen Bitumen
Penetration grade	53 dmm	100 dmm
Softening point	53.5°C	—
$\dot{\epsilon}_{pc}$	$1.44 \times 10^{-4} \text{ s}^{-1}$	$2.66 \times 10^{-4} \text{ s}^{-1}$
ψ	0.70	0.47
k	$22.8 \times 10^3 \text{ K}$	$23.0 \times 10^3 \text{ K}$
m	0.615	0.605
σ_o	0.20 MPa	0.15 MPa

Table 3.1: Pure bitumens parameters.

Parameter	Cariphalte TS	Cariphalte DM
Penetration grade	76 dmm	100 dmm
Softening point	82.0°C	93.6°C
$\dot{\epsilon}_{pc}$	$1.2 \times 10^{-4} \text{ s}^{-1}$	$8.0 \times 10^{-4} \text{ s}^{-1}$
ψ	0.65	0.61
k	$30.5 \times 10^3 \text{ K}$	$25.5 \times 10^3 \text{ K}$
m	0.50	0.34
σ_o	0.20 MPa	0.39 MPa

Table 3.2: Polymer-modified bitumens parameters.

3.9 Figures

Figure 3.1: Experimental arrangements for tension tests, Cheung (1995)

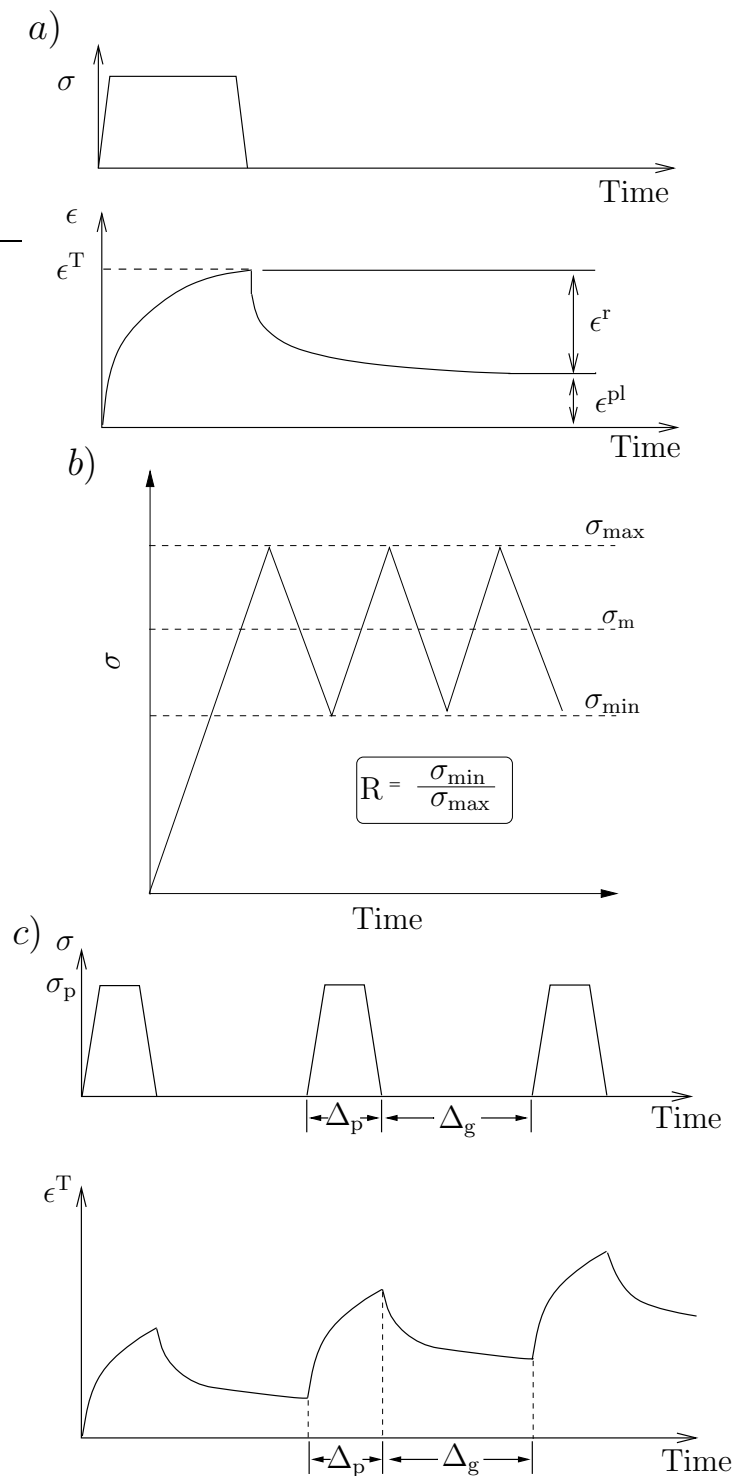


Figure 3.2: (a) Schematic showing the stress and strain time histories in a creep recovery test. (b) Schematic of the applied stress as a function of time in the continuous cyclic tests. (c) Schematic of the stress and strain time histories in the pulse train experiments.

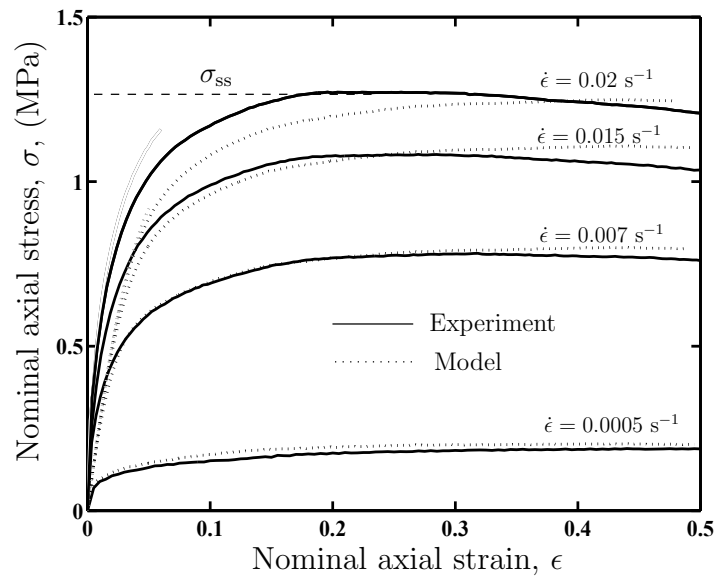


Figure 3.3: Constant strain-rate tests at four selected values of the applied strain-rate on the 50 pen bitumen at 0°C.

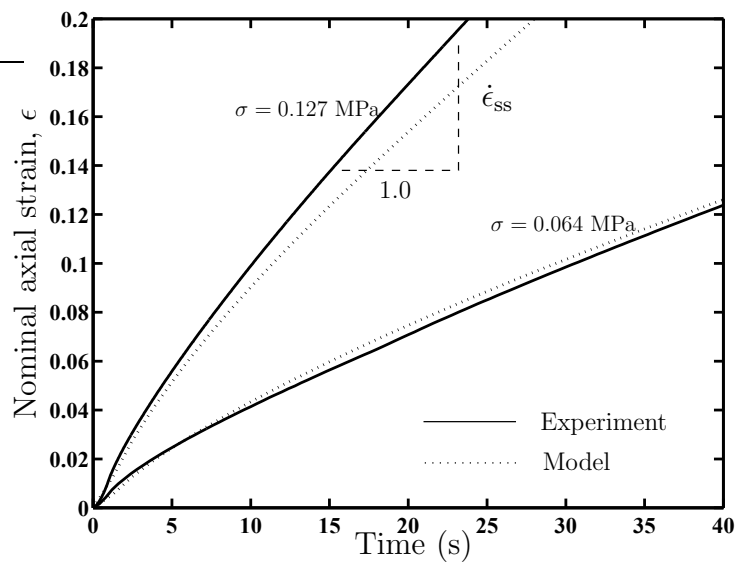


Figure 3.4: Constant stress creep tests at two selected creep stresses on the 50 pen bitumen at 10°C.

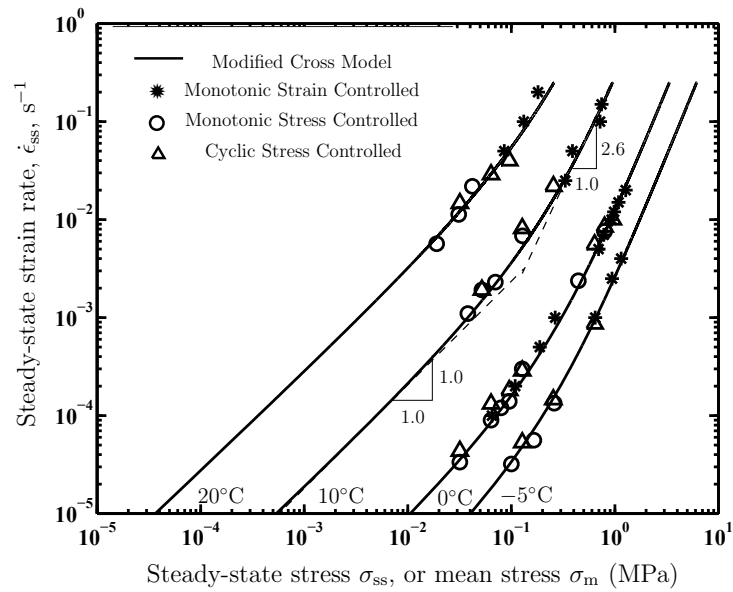


Figure 3.5: The monotonic and continuous cyclic steady-state behaviour of the 50 pen bitumen at the four temperatures investigated in the current study.

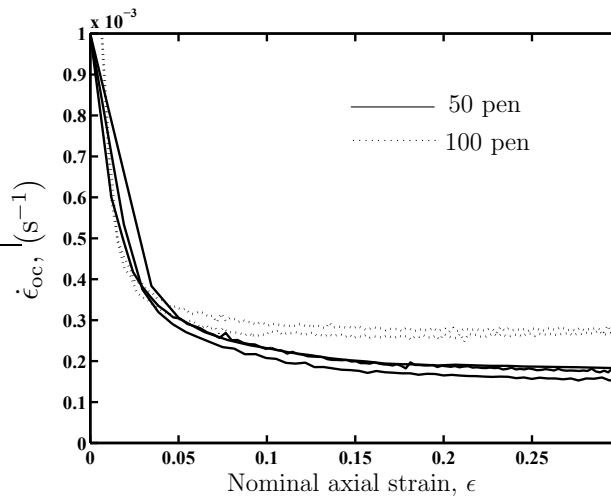


Figure 3.6: Loading calibration curves $\dot{\epsilon}_{oc}(\epsilon)$ for the 50 and 100 pen bitumens. Curves from a series of five constant strain-rate and creep tests at different temperatures are superimposed.

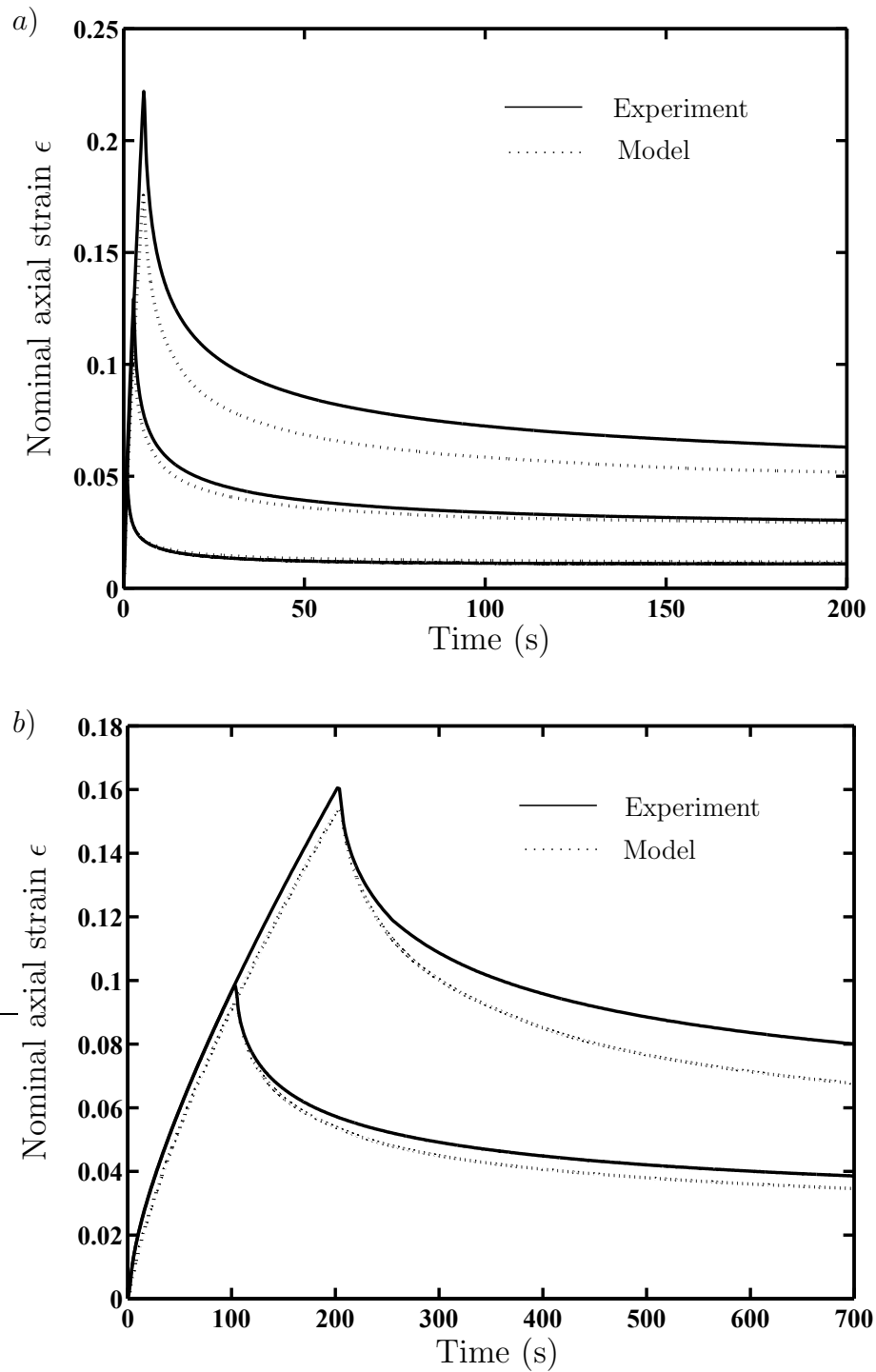


Figure 3.7: Creep recovery test results for 50 pen bitumen. (a) $T = 10^\circ\text{C}$, $\sigma = 0.32$ MPa. (b) $T = 0^\circ\text{C}$, $\sigma = 0.2$ MPa.

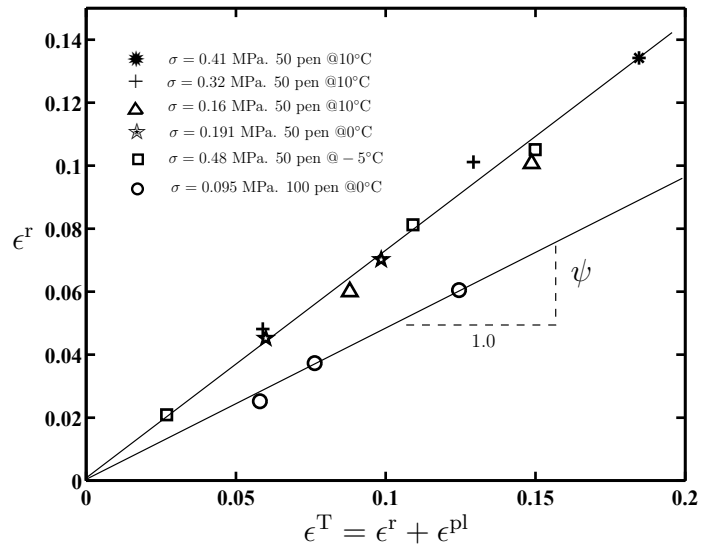


Figure 3.8: Summary of the creep recovery experimental results which show a linear relationship between ϵ^r and ϵ^T .

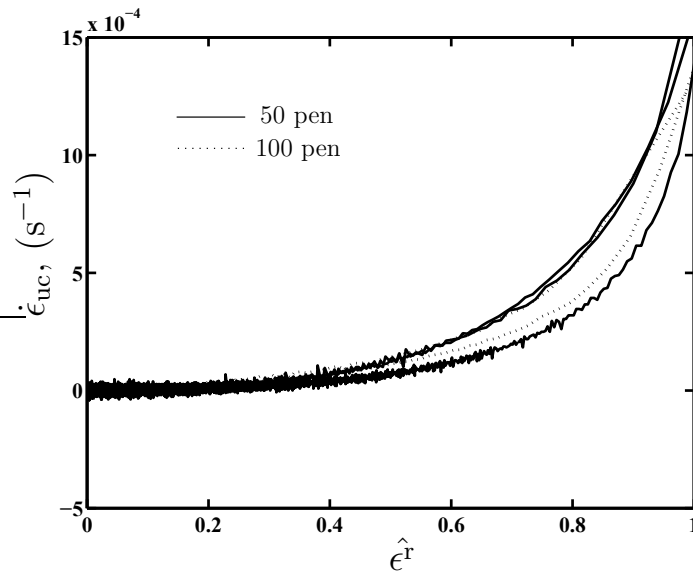


Figure 3.9: Recovery calibration curves $\dot{\epsilon}_{uc}(\hat{\epsilon}^r)$ for the 50 and 100 pen bitumens. Curves from a series of five creep recovery tests at different temperatures are superimposed.

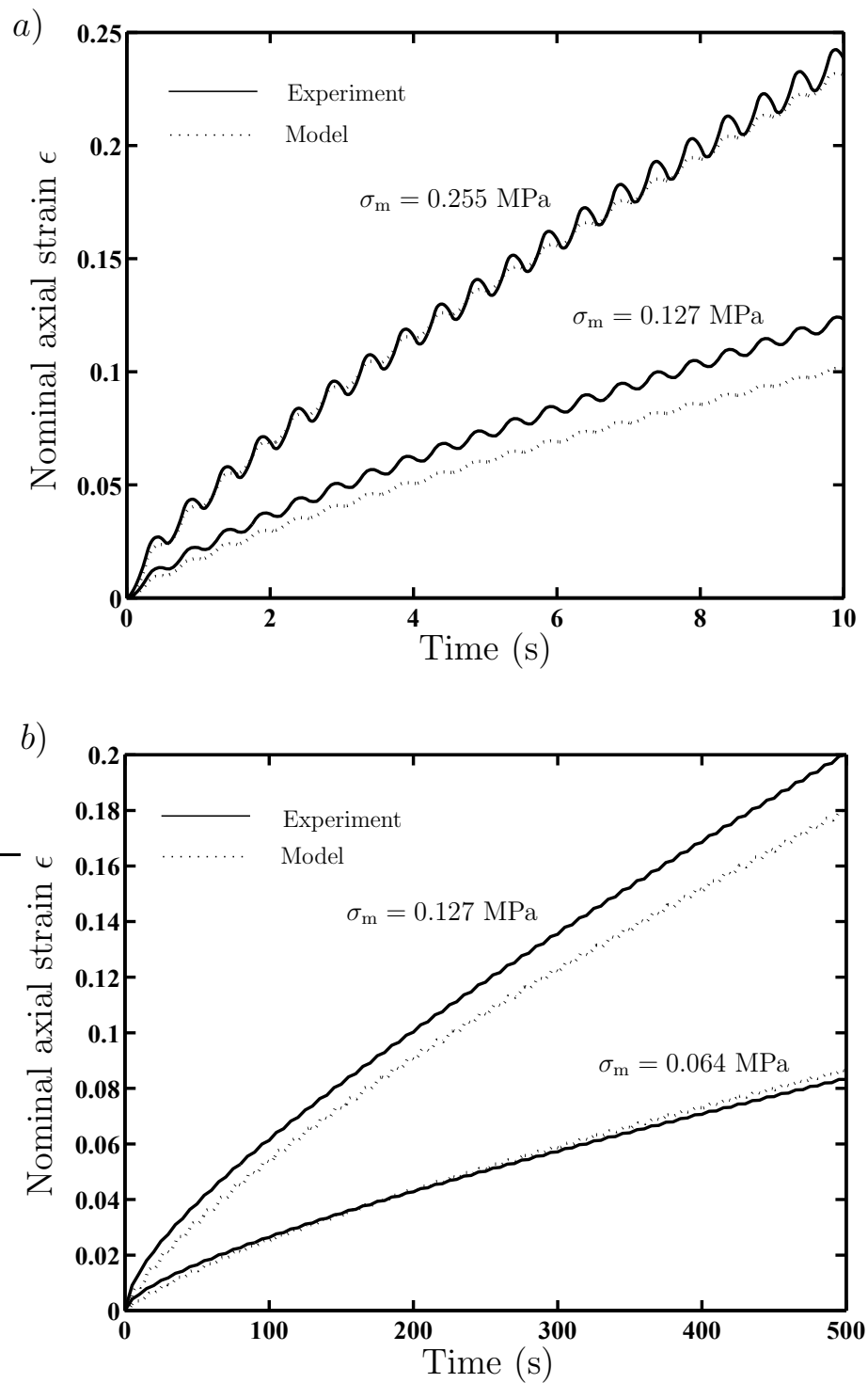


Figure 3.10: Continuous cyclic stress controlled tests for 50 pen bitumen. (a) $T = 10^\circ\text{C}$, $f = 2\text{ Hz}$ and $R = 0.15$. (b) $T = 0^\circ\text{C}$, $f = 0.1\text{ Hz}$ and $R = 0.15$.

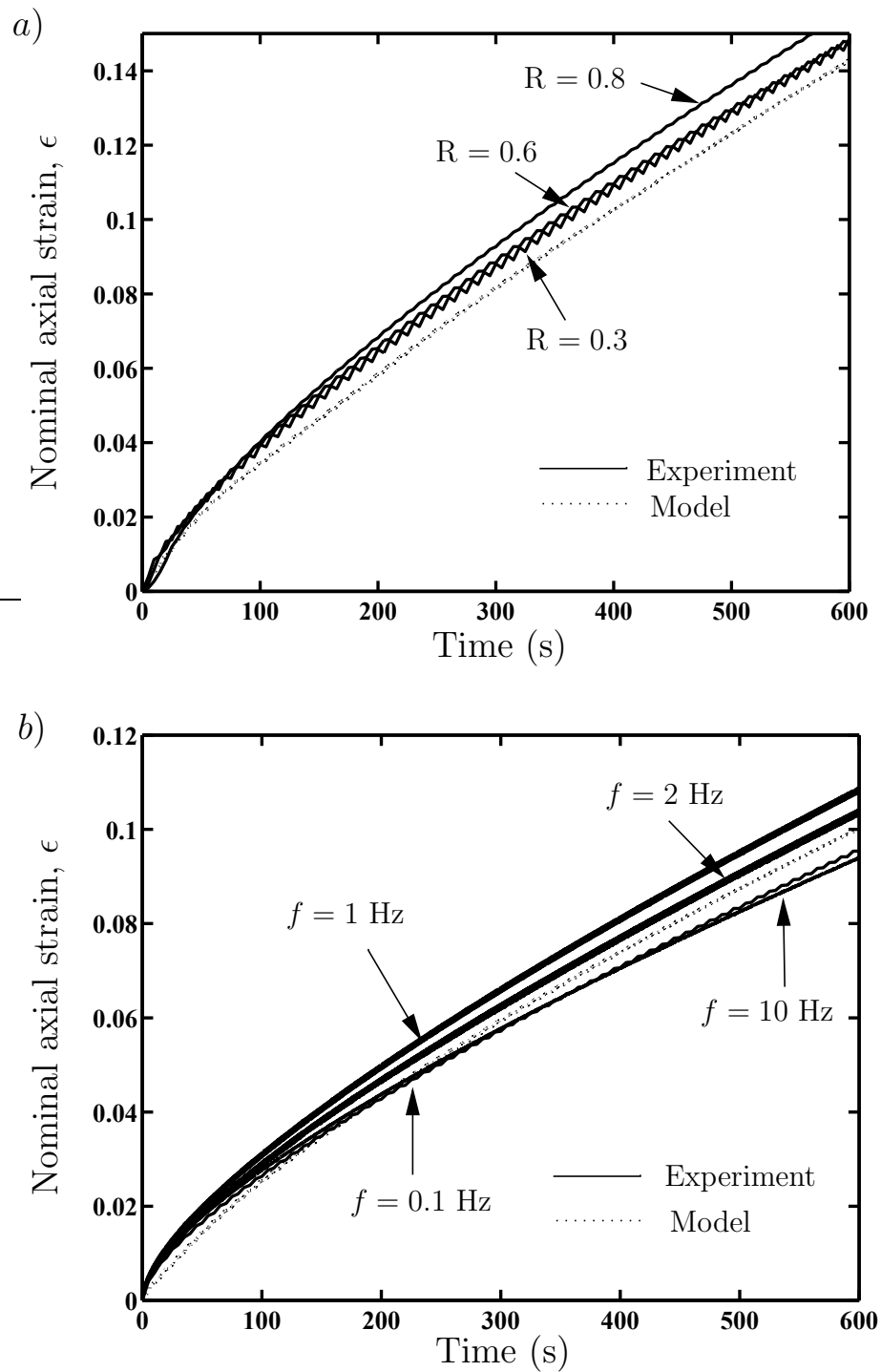


Figure 3.11: Continuous cyclic stress controlled tests at 0° C for 50 pen bitumen. (a) Results for three selected values of R with $\sigma_m = 0.095$ MPa and $f = 0.1$ Hz. (b) Results for four selected frequencies f with $\sigma_m = 0.064$ MPa and $R = 0.15$.

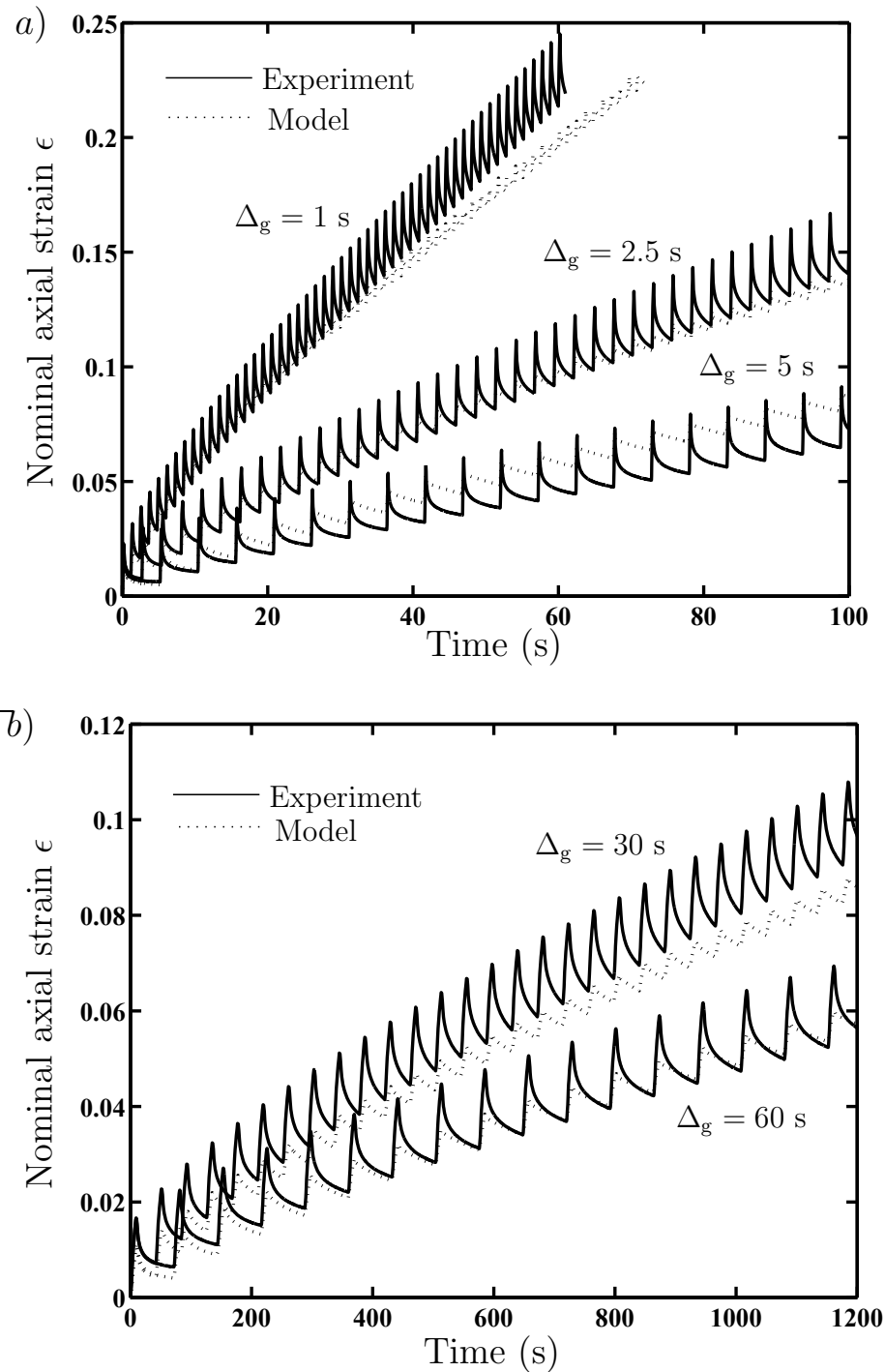


Figure 3.12: Pulse loading tests on the 50 pen bitumen. (a) $T = 10^\circ\text{C}$, $\sigma_p = 0.32$ MPa and $\Delta_p = 0.2$ s. (b) $T = 0^\circ\text{C}$, $\sigma_p = 0.16$ MPa, $\Delta_p = 12$ s.

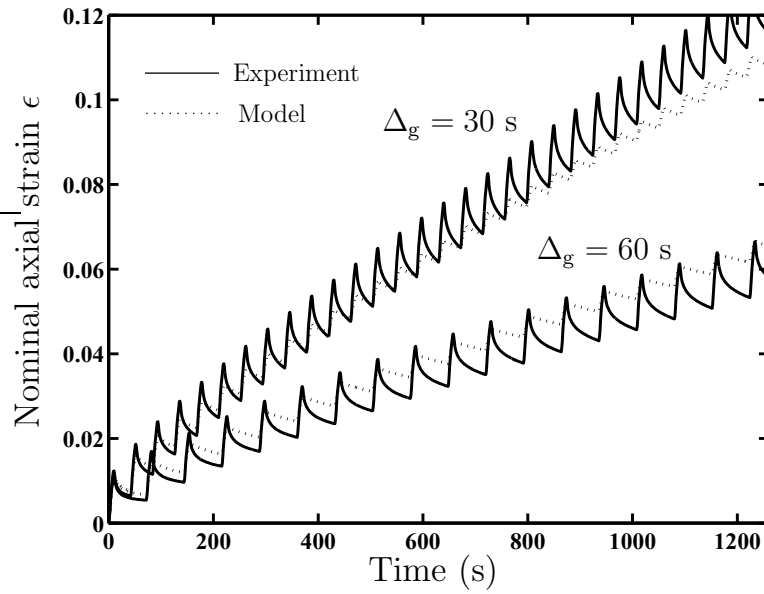


Figure 3.13: Pulse loading tests on 100 pen bitumen with $T = 0^\circ\text{C}$, $\sigma_p = 0.095\text{ MPa}$ and $\Delta_p = 12\text{ s}$.

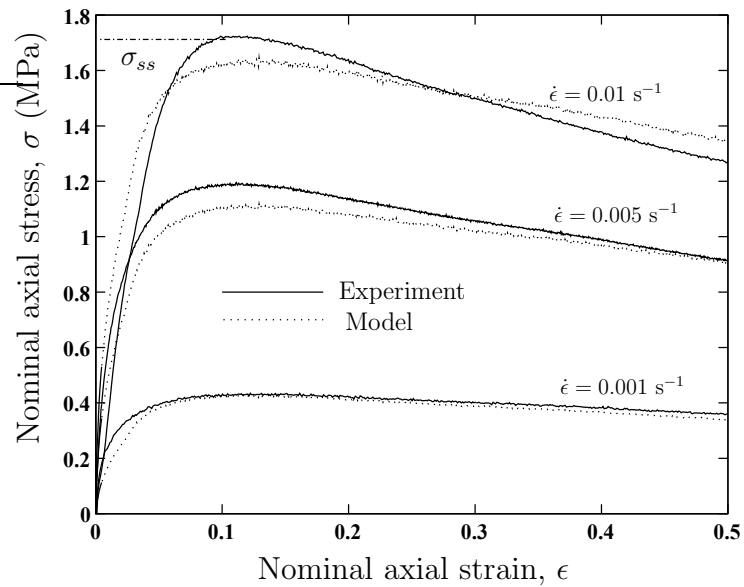


Figure 3.14: Monotonic constant strain-rate tests at three selected values of the applied strain-rate at 0°C on Cariphalte TS.

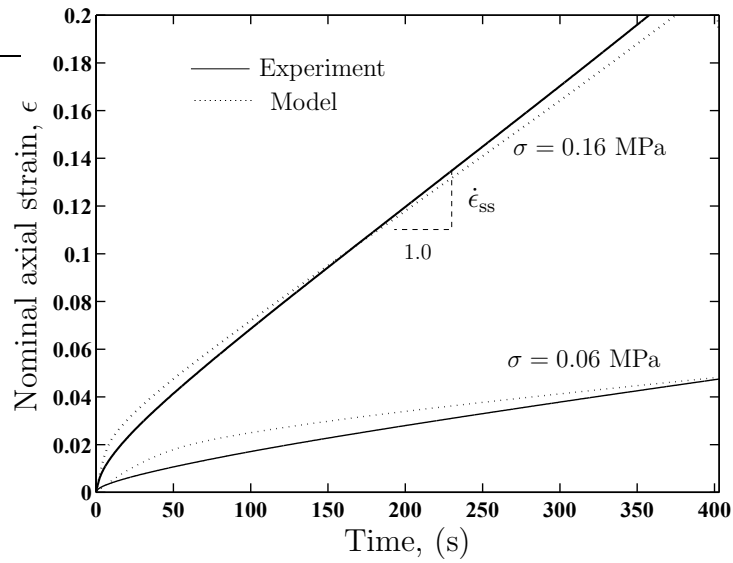


Figure 3.15: Monotonic constant stress creep tests on Cariphalte TS at two selected values of the applied stress at 0°C.

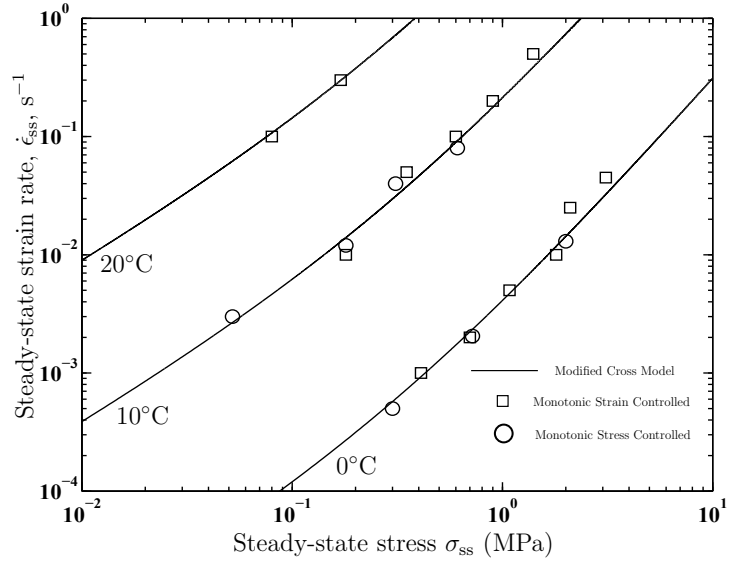


Figure 3.16: Monotonic steady-state behaviour of the polymer-modified bitumen Cariphalte TS at the three temperatures investigated in the current study.

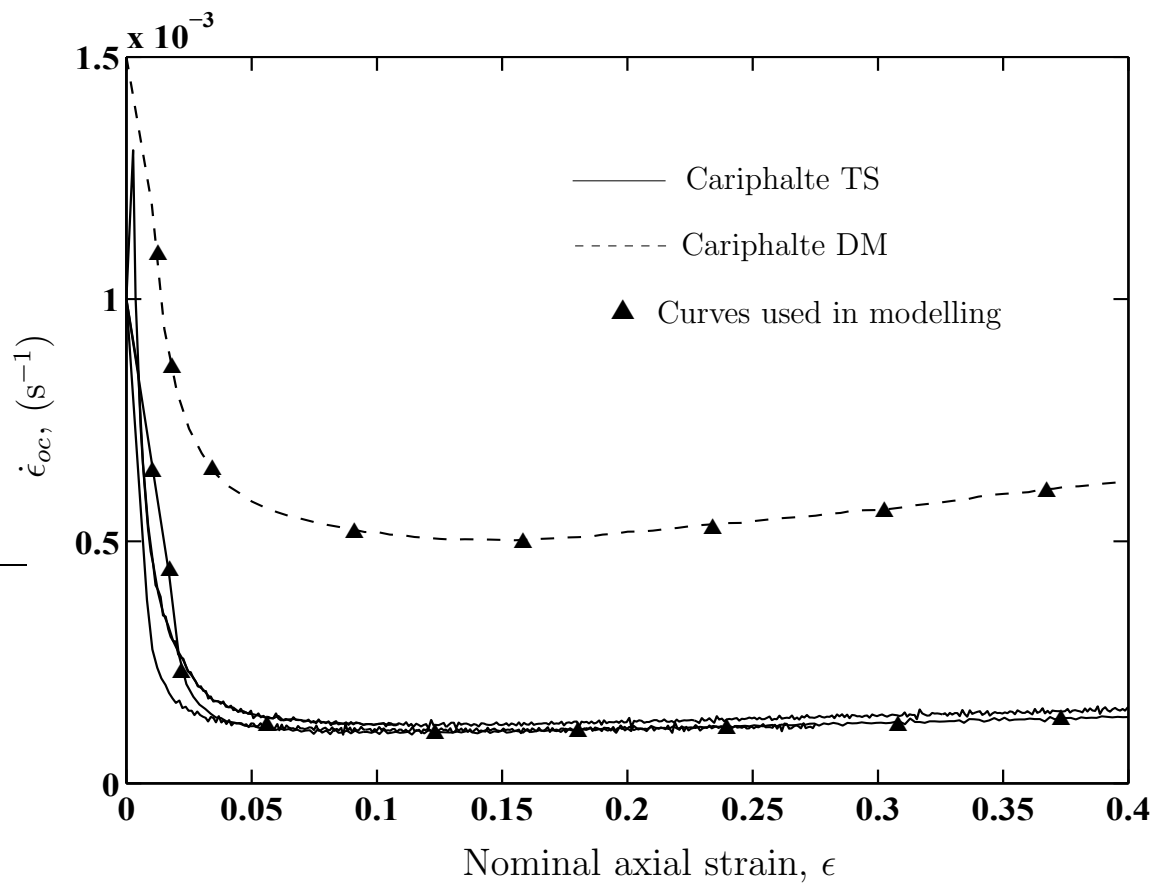


Figure 3.17: Loading calibration curves $\dot{\epsilon}_{oc}(\epsilon)$ for Cariphalte TS and DM bitumens.

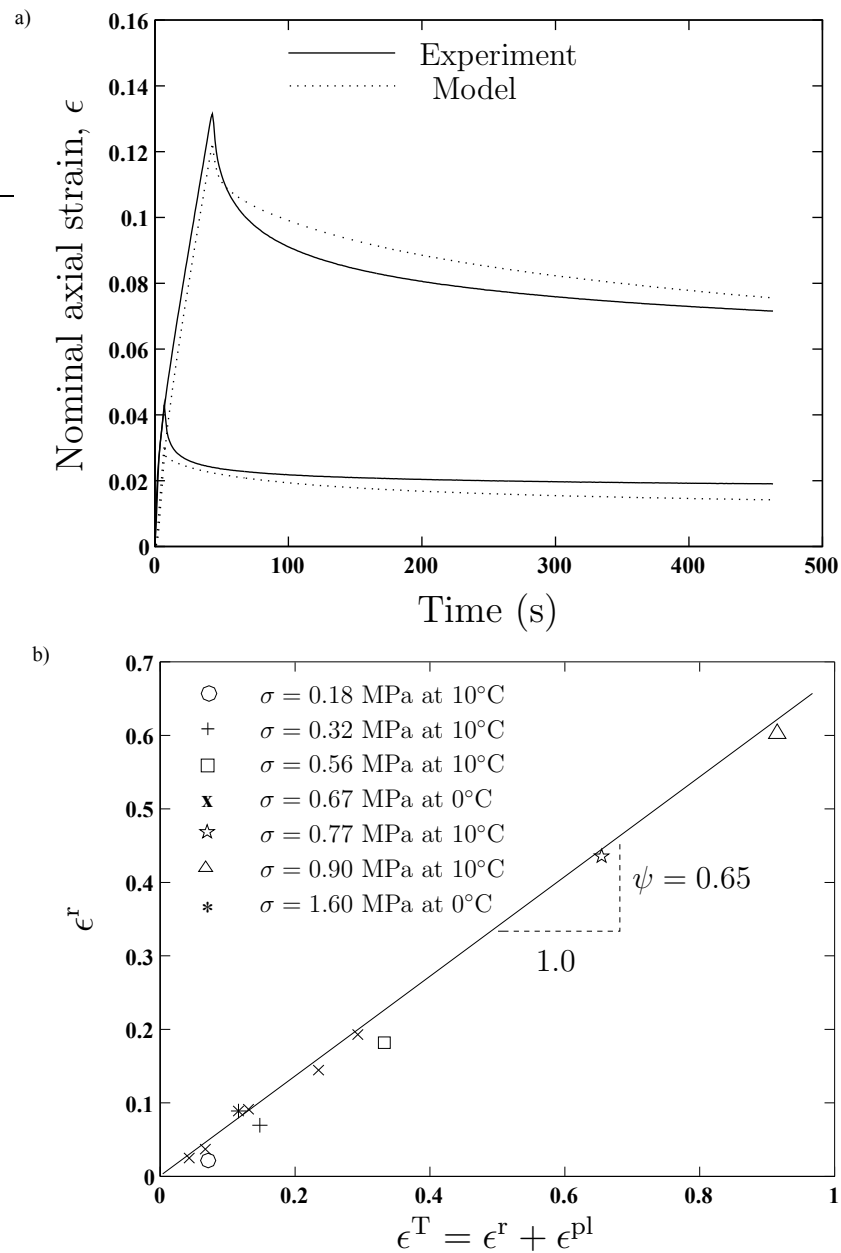


Figure 3.18: Creep recovery tests. (a) Creep recovery test results for Cariphalte TS at $\sigma = 0.64$ MPa and $T = 0^\circ\text{C}$. (b) Summary of creep recovery experimental results which show a linear relationship between ϵ^r and ϵ^T .

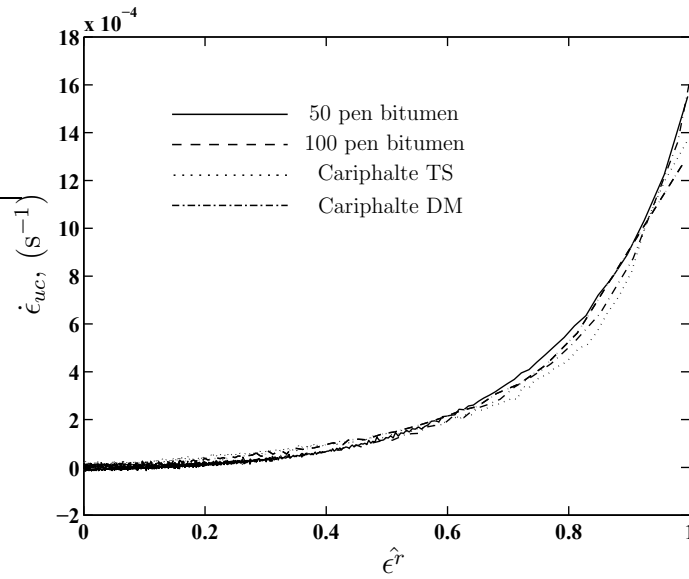


Figure 3.19: Recovery calibration curves $\dot{\epsilon}_{uc}(\hat{\epsilon}^r)$ for 50 and 100 pen bitumens and polymer-modified bitumens Cariphalte TS and DM.

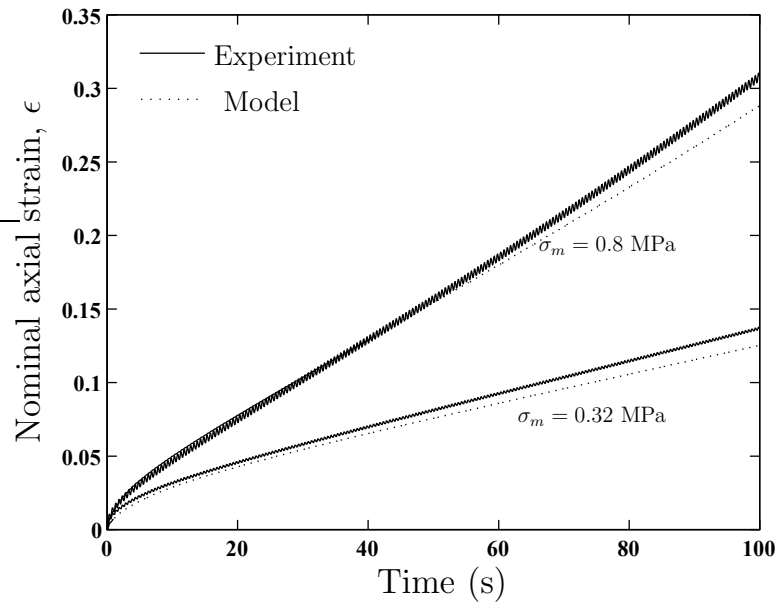


Figure 3.20: Continuous cyclic stress controlled tests for Cariphalte TS at 0°C, $R=0.15$ and $f=2$ Hz.

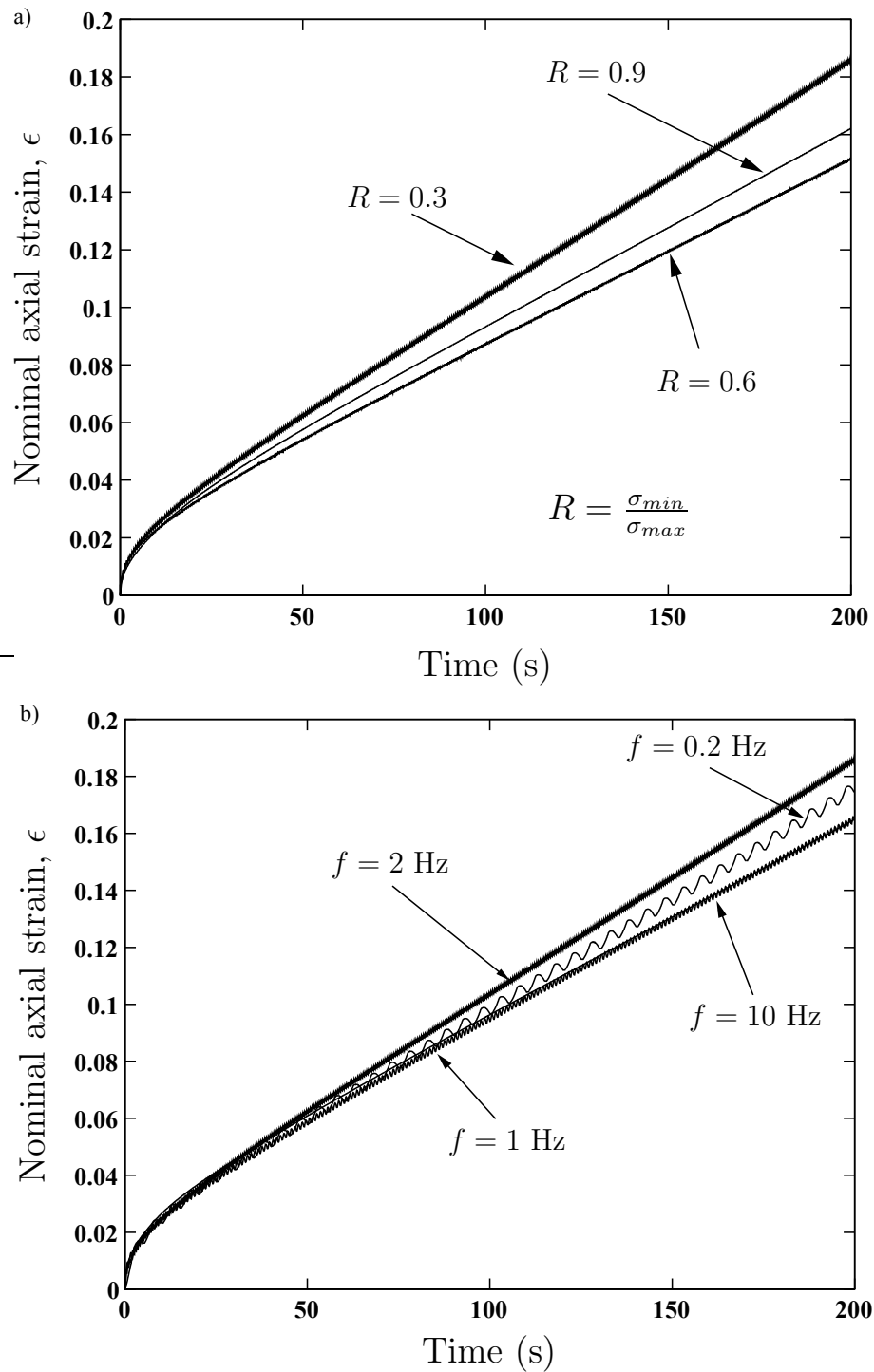


Figure 3.21: Continuous cyclic stress controlled tests at 0°C for Cariphalte TS. (a) Results for three selected values of R with $\sigma_m = 0.36$ MPa and $f = 2$ Hz. (b) Results for four selected frequencies f with $\sigma_m = 0.36$ MPa and $R = 0.3$.

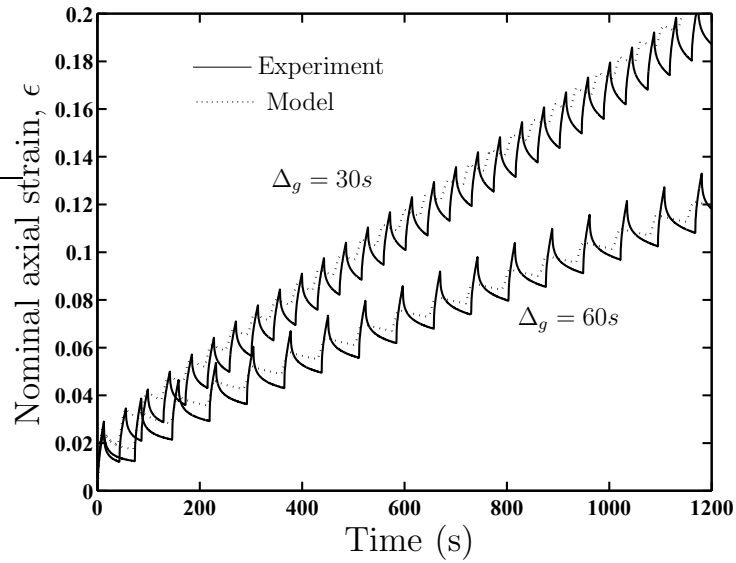


Figure 3.22: Pulse loading tests on Cariphalte TS with $T = 0^{\circ}\text{C}$, $\sigma_p = 0.4 \text{ MPa}$ and $\Delta_p = 13\text{s}$.

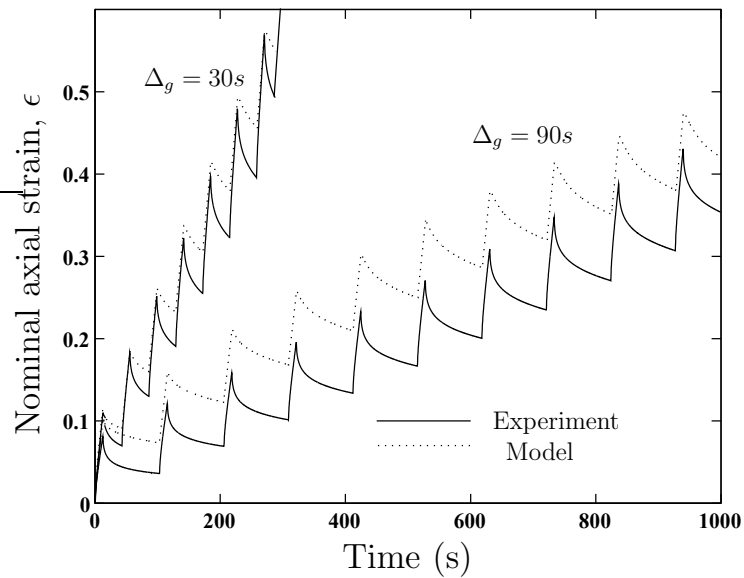


Figure 3.23: Pulse loading tests on Cariphalte DM with $T = 0^{\circ}\text{C}$, $\sigma_p = 0.4 \text{ MPa}$ and $\Delta_p = 13\text{s}$. Model calibration performed using a set of four simple tension and recovery tests.

Chapter 4

Indentation behaviour of bitumen

4.1 Introduction

Indentation tests provide a cheap and easy method to measure the mechanical properties of materials and also serve to validate multi-axial constitutive models of materials. The focus of this chapter is to investigate the monotonic and cyclic spherical indentation response of bitumen with the aim of (i) validating the multi-axial constitutive model for bitumen developed in chapter 3 and (ii) investigating the repeated indentation response of bitumen which serves as a unit problem for road surfaces under vehicle loads.

The standard indentation test on creeping solids involves either applying a constant load and measuring the indentation creep with time or by pressing the indenter into the material at a prescribed rate and measuring the load as a function of time. To interpret these results many researchers have developed models to relate the indentation pressure to the constitutive response of the materials. Notably, Tabor (1951) proposed empirical relations to correlate the indentation pressure for rate independent strain hardening solids to the uniaxial tensile response of the material, while

Mulhearn and Tabor (1960) extended these empirical relations to power-law creeping materials. Using the similarity transformations for the indentation of metals developed by Hill et al. (1989), Bower et al. (1993) provided a rigorous theoretical basis for the empirical relations developed by Mulhearn and Tabor (1960) for rate dependent solids. A source of error in the interpretation of creep properties from indentation tests is the neglect of the primary creep response (or the strain hardening behaviour) of rate dependent materials in the above analyses. Ogbonna et al. (1995) extended the scaling procedure of Hill et al. (1989) and Bower et al. (1993) to a class of creep constitutive laws that account for strain hardening. Such analyses provides the basis for the investigation of the indentation response of bitumen reported in this chapter.

In this chapter, the indentation model for power-law creeping solids of Bower et al. (1993) is summarised and then extended to the constitutive model for bitumen described in chapter 3. Then, an extensive experimental study of the monotonic, recovery and cyclic spherical indentation behaviour of bitumen is reported for a range of temperatures. Finally, the predictions of the model are compared with experimental measurements.

4.2 Indentation behaviour of creeping solids

Consider a half-space, occupying the region $x_3 \geq 0$ and loaded by a frictionless spherical rigid indenter of diameter D , as sketched in Fig. 4.1. The material in the half-space is assumed to deform according to a power-law creep law of the form

$$\frac{\dot{\epsilon}_{ij}}{\dot{\epsilon}_o} = \frac{3}{2} \left(\frac{\sigma_e}{\sigma_o} \right)^{n-1} \frac{\sigma'_{ij}}{\sigma_o}, \quad (4.1)$$

where σ_o , $\dot{\epsilon}_o$ and n are material constants.

Bower et al. (1993) solved the problem of the plane strain and axisymmetric indentation of a half-space comprising a power-law creeping solid (4.1), using the similarity

transformations suggested by Hill et al. (1989). These transformations are based on the observation that at any given instant, the velocity, strain rate and stress fields in the half-space only depend on the size of the contact a and the indentation rate \dot{h} , and are independent of the loading history. Thus, the general indentation problem is reduced to calculating stresses and displacements in a nonlinear elastic solid, indented to a unit depth by a rigid flat punch of unit radius (in the axisymmetric problem). For indentation by a frictionless spherical indenter, the similarity solutions dictate that the contact radius a is related to the indentation depth h by

$$h = \frac{1}{\phi^2} \frac{a^2}{D}, \quad (4.2)$$

where the constant ϕ , is only a function of the material constant n and may be thought of as the ratio of the true to nominal contact radius, where the nominal contact radius is \sqrt{hD} . Similarly, the applied load F is related to the indentation rate \dot{h} via

$$\frac{F}{\pi a^2 \sigma_o} = \alpha \left(\frac{\dot{h}}{a \dot{\epsilon}_o} \right)^{1/n} = \alpha \left(\frac{2\dot{a}}{\dot{\epsilon}_o \phi^2 D} \right)^{1/n}, \quad (4.3)$$

where the constant α is again only a function of the power-law exponent n . Values of ϕ and α for selected values of n , were deduced by Bower et al. (1993) from a series of finite element calculations and are listed in Table 4.1.

Equations (4.2) and (4.3) can be written in terms of the *effective* stress and *effective* strain under the indenter. The effective stress σ^{eff} under the indenter is defined as

$$\sigma^{\text{eff}} = \frac{F}{\pi a^2}, \quad (4.4)$$

while the effective strain rate and strain under the indenter are specified as

$$\dot{\epsilon}^{\text{eff}} = \frac{\dot{a}}{D} = \frac{\phi \dot{h}}{2\sqrt{hD}}, \quad (4.5a)$$

and

$$\epsilon^{\text{eff}} = \phi \sqrt{\frac{h}{D}}, \quad (4.5b)$$

respectively. Substituting these definitions in (4.2) and (4.3) gives the empirical results of Mulhearn and Tabor (1960) result

$$\sigma^{\text{eff}} = \alpha \sigma_o \left(\frac{2\epsilon^{\text{eff}}}{\phi^2 \epsilon_o} \right)^{1/n}, \quad (4.6)$$

for the pressure under an indenter in a power-law creeping solid.

4.3 Indentation model for bitumen

A model for both the monotonic and cyclic spherical indentation response of bitumen is proposed in this section. The model is based on the concepts of *effective stress* σ^{eff} (4.4) and *effective strain* ϵ^{eff} (4.5b) under a spherical indenter, introduced by Mulhearn and Tabor (1960) and justified theoretically by Bower et al. (1993).

As discussed in Section 3.5, the response of bitumen to load can be characterised by the generalised power-law relation (3.12c) that accounts for the “strain hardening” or the primary creep response of bitumen. Ogbonna et al. (1995) extended the similarity relations of Bower et al. (1993), developed for the “steady-state” indentation of a power-law creeping solid to the indentation of a rate dependent strain hardening solid characterised by the Derby and Ashby (1987) constitutive relation. The finite element calculations of Ogbonna et al. (1995) showed that the steady-state analysis of Bower et al. (1993) provides an upper limit for the load factor α and the ratio of the actual to nominal contact radius ϕ with strain hardening not substantially affecting the values of these factors. Therefore, the simpler Bower et al. (1993) analysis is chosen here for the indentation of bitumen and extend it to account for the recovery behaviour.

The indentation rate \dot{h} is written as the sum of the viscous indentation rate \dot{h}^v , which is active during loading (indentation force $F \neq 0$) and the recovery rate \dot{h}^r , which is only active when $F = 0$. For an arbitrary loading history, the strain rate $\dot{\epsilon}$

under the indenter is written as

$$\dot{\epsilon} = \dot{\epsilon}^v + \dot{\epsilon}^r = \frac{\phi}{2\sqrt{hD}}\dot{h} = \frac{\phi}{2\sqrt{hD}}(\dot{h}^v + \dot{h}^r), \quad (4.7)$$

where the viscous indentation and strain rates are related to the indentation force via

$$\dot{h}^v = \frac{2\dot{\epsilon}^v}{\phi}\sqrt{hD} = \left(\frac{F}{\pi a^2 \sigma_o \alpha}\right)^n a \dot{\epsilon}_o(\epsilon), \quad (4.8)$$

and $\dot{\epsilon}_o$ in (4.3) has been replaced by the strain dependent function $\dot{\epsilon}_o(\epsilon)$. It now remains to specify the recovery indentation rate. Assume here that the Mulhearn and Tabor (1960) definition of strain rate (4.5a) under the indenter is still applicable under unloading conditions, with recovery occurring in a self-similar manner; that is, the ratio of the actual to nominal contact radius remaining constant at ϕ as specified by the Bower et al. (1993) model. Thus, the indentation recovery rate is given by

$$\dot{h}^r = \frac{2\dot{\epsilon}^r}{\phi}\sqrt{hD} = -\frac{2\sqrt{hD}}{\phi} [1 - \text{sign}(|F|)] \dot{\epsilon}_u(\dot{\epsilon}^r), \quad (4.9)$$

where $\dot{\epsilon}^r$ is specified by (3.5) with the irrecoverable strain rate $\dot{\epsilon}^{\text{pl}}$ related to the viscous strain rate via the recovery constant ψ

$$\dot{\epsilon}^{\text{pl}} = (1 - \psi)\dot{\epsilon}^v. \quad (4.10)$$

Equations (4.7) to (4.9) completely specify the monotonic and cyclic spherical indentation behaviour of bitumen: time integration of these equations provides the complete history of the indentation depth as a function of time for any specified loading.

4.4 Experimental investigation

4.4.1 Material

The same 50 pen bitumen studied in chapter 3 was used for the spherical indentation study. The material parameters for this 50 pen bitumen are listed in Table 3.1 and

the loading calibration curve $\dot{\epsilon}_{oc}(\epsilon)$ and recovery calibration curve $\dot{\epsilon}_{uc}(\epsilon^r)$, are plotted in Figs. 3.6 and 3.9, respectively.

4.4.2 Specimen preparation

About 100 g of bitumen granules were taken from the freezer and melted at 160°C for approximately 2 hours to remove all the air bubbles. The bitumen was then poured into the pre-heated cylindrical mould¹ 60 mm in diameter and 50 mm in height. It was then allowed to cool to room temperature.

4.4.3 Test protocol

Spherical indentation tests on the specimens were performed in a hydraulic testing machine. The indentation load F was measured using a 1 kN load cell, while the load line displacement was employed to obtain the indentation depth h . The spherical indenter of diameter 15 or 40 mm was lubricated with a thin layer of a mixture of soap and glycerine in order to prevent the specimen from adhering to it, allowing nearly frictionless indentation. Typically indents to a depth $h \leq 2$ mm were performed with the indent affected zone much smaller than the cylindrical mould dimensions. Thus, for all practical purposes, the tests may be regarded as indentation of a half-space of bitumen. The test temperature was controlled by performing the tests in an environmental chamber fitted on the test machine. The environmental chamber has a resolution of $\pm 0.5^\circ\text{C}$ and the rates of loading employed in this study were slow enough for adiabatic heating effects to be negligible. Prior to testing, all specimens were kept in the environmental chamber for about 2 hours to allow them to attain the test temperature. Unless otherwise specified, a 40 mm diameter spherical indenter

¹The mould was pre-heated to 90°C for 15 minutes, to avoid thermal contraction that could generate bubbles or residual stresses in the final specimen.

was employed in this study. A few tests were conducted with a 15 mm diameter indenter in order to confirm the predicted dependence of the indentation response on the indenter diameter. It is worth mentioning here that a number of spot repeat tests confirmed the reproducibility of the test results reported here. For the sake of brevity, these results are not presented.

Monotonic indentation tests

Constant indentation-rate and constant load creep indentation tests were employed to characterise the monotonic indentation response of the bitumen. In the constant indentation-rate tests, a specified indentation-rate \dot{h} was applied by the indenter and the resulting load F and indentation depth h recorded. In the constant load creep indentation tests, a constant indentation load F was applied “instantaneously” by the indenter and the indentation depth h recorded as a function of time t .

Creep recovery indentation tests

The creep recovery indentation behaviour of bitumen was investigated by performing a series of single load/unload indentation tests as sketched in Fig. 4.2a. A load F was applied rapidly by the indenter to the specimen and then held constant. The material was allowed to creep to a specified total indentation depth h^T . At this indentation depth, the load was released and the indentation depth monitored until the indentation rate $\dot{h} \approx 0$. The indentation depth at this point $h^{pl} = h^T - h^f$ is the irrecoverable indentation depth (Fig. 4.2a). Such tests were repeated for a series of indentation depths h^T , loads F , and temperatures.

Cyclic indentation tests

Continuous cyclic and pulse train indentation tests were performed to characterise the cyclic or repeated indentation behaviour of bitumen.

Continuous cyclic indentation tests.

In the continuous cyclic indentation tests, the indentation load F was varied between F_{\min} and F_{\max} as sketched in Fig. 4.2b, with

$$R = \frac{F_{\min}}{F_{\max}}, \quad (4.11)$$

and

$$F_m = \frac{F_{\min} + F_{\max}}{2}, \quad (4.12)$$

defining the load levels while the frequency f of the triangular waveform defines the loading rate. The indentation depth was measured as a function of time and tests repeated for a series of values of R , F_m and f .

Pulse train indentation tests.

Tests comprising intermittent identical indentation load pulses with a trapezoidal shape in the time domain, as shown in Fig. 4.2c, were performed in order to simulate a load history similar to that experienced in a pavement. The aim here was to investigate the relation between the single load/unload behaviour analysed via the creep and creep recovery indentation tests and the gradual ratcheting of indentation depth due to the application of a continuous train of discrete load pulses as shown schematically in Fig. 4.2c.

The constant maximum indentation load F_p in each trapezoidal load pulse was applied for a time period $\Delta_p/2$ with a loading and unloading rate $\dot{F} = 4F_p/\Delta_p$. A series of tests was performed by varying the time period Δ_g between consecutive trapezoidal pulses at a fixed F_p at two selected temperatures.

4.5 Experimental results and comparison with model predictions

The monotonic, recovery, continuous cyclic and pulse indentation experimental results are described in this section and the results compared with the predictions of the indentation model described in section 4.3. The material parameters employed in modelling the indentation behaviour are listed in Table 3.1 with the loading and recovery calibration curves plotted in Figs. 3.6 and 3.9, respectively. Unless otherwise specified, the experiments reported were conducted at 0°C employing the 40 mm diameter spherical indenter.

4.5.1 Monotonic indentation behaviour

The measured indentation load F versus indentation depth h response of the bitumen for two selected values of the applied indentation rate $\dot{h} = 0.07 \text{ mm s}^{-1}$ and 0.15 mm s^{-1} are plotted in Fig 4.3a. In both cases, the indentation load F increases monotonically with indentation depth and the slope of the F versus h curve increases with increasing indentation rate \dot{h} .

Results from two constant load creep indentation tests ($F = 40 \text{ N}$ and 100 N) are plotted in Fig. 4.3b. The indentation depth h versus time response is seen to comprise two regimes: a primary creep regime where \dot{h} decreases with time, followed by a secondary or steady-state creep regime, where \dot{h} remains approximately constant. Increasing the indentation load F increases \dot{h} over the full range of indentation depths considered here.

The monotonic indentation responses at 5°C employing the same loading parameters as in Fig. 4.3 are shown in Fig. 4.4. Comparing Fig. 4.3 and 4.4 it can be seen that while the qualitative behaviour remains unchanged, increasing the temperatures

results in an smaller indentation force for a given indentation rate and a higher indentation creep rate for a given indentation force. Predictions of the model are included in Figs. 4.3 and 4.4 and show reasonably good agreement with the experimental measurements at small times or indentation depths. However, the model generally predicts a “stiffer” response, that is, a lower indentation rate for a given indentation force or a higher force for a given applied indentation rate. This error arises from the approximation of the modified Cross model (2.14) by a power-law relationship: the power-law relationship over-predicts the creep resistance of bitumen, especially at stresses $\sigma \leq \sigma_o$.

The effect of the indenter diameter on the indentation response is illustrated in Fig. 4.5 where the indentation creep response at 0°C for an indentation force $F = 35$ N is plotted for the two diameters of the spherical indenter $D = 40$ mm and $D = 15$ mm. In line with the predictions of the model the indentation creep rate \dot{h} increases with decreasing D and good agreement between the model and the experimental measurements is seen.

4.5.2 Creep recovery indentation behaviour

Creep recovery indentation tests on bitumen were performed at 0°C and 5°C and the recovery behaviour investigated for unloading from total effective strains $\epsilon^T = \phi \sqrt{\frac{h^T}{D}}$ in the range $0.05 \leq \epsilon^T \leq 0.14$. Experiments were performed for indentation loads of $F = 65$ N, 100N and 170N for the 40 mm diameter indenter, and $F = 30$ N for the 15 mm diameter indenter. The creep recovery indentation response of bitumen at 0°C with $F = 65$ N is shown in Fig. 4.6a, where the indentation depth h is plotted as a function of time t , for the two selected values of $h^T = 0.7$ mm and 0.4 mm. The recovered indentation h^r is higher for the larger h^T . This result is consistent with the observations for bitumen in uniaxial tension where it was shown that a larger initial

tensile strain results in a larger recovered strain. A comparison between the model predictions and experimental measurements is included in Fig. 4.6a and indicates that the model captures both the loading and unloading indentation response of the bitumen reasonably accurately.

Results from all the creep recovery indentation tests performed are summarised in Fig. 4.6b where the recovered effective strain $\epsilon^r = \phi \sqrt{\frac{h^r}{D}}$ is plotted as a function of the total effective strain ϵ^T prior to unloading. The figure reveals that, to within experimental error, the data is well represented by the line $\epsilon^r = \psi \epsilon^T$ with ψ ($0 \leq \psi \leq 1$) independent of the applied indentation load (effective stress), temperature and indenter diameter. Moreover, $\psi \approx 0.7$ as measured from these indentation experiments is approximately equal to that found from uniaxial tensile experiments on the same bitumen in chapter 3. This was a key assumption made in the model detailed in Section 4.3 and is confirmed here through a wide range of experiments.

4.5.3 Continuous cyclic indentation response

Continuous load controlled cyclic indentation tests were performed to investigate the effect of the mean indentation load F_m , load ratio R and frequency f on the cyclic indentation depth response of bitumen.

The cyclic indentation depth h versus time response of bitumen with $R = 0.7$ is shown in Fig. 4.7, for $F_m = 100\text{N}$ and 150N at 0°C . The cyclic load-controlled indentation response is similar in form to the monotonic creep indentation response with primary and secondary regimes of behaviour. Next, consider the influence of the load ratio R and frequency f on the cyclic load-controlled response. The indentation depth versus time history of bitumen with $F_m = 100\text{ N}$ and $f = 5.0\text{ Hz}$ is shown in Fig. 4.8a for three selected values of R and in Fig. 4.8b with $F_m = 150\text{ N}$ and $R = 0.7$ for three selected frequencies f . Both these figures demonstrate that the load ratio

R and frequency f have a negligible effect on the cyclic load-controlled indentation depth versus time response of bitumen. Thus, similar to the findings of chapter 3 for bitumen subjected to uniaxial tension, the continuous cyclic indentation response is also seen to be primarily a function of the mean load F_m .

Predictions of the indentation model are included in Figs. 4.7 and 4.8. Again, the model is seen to agree reasonably well with the experimental measurements and correctly predicts the negligible dependence of the response on the load ratio R and frequency f . Consistent with the monotonic response, the model predicts a stiffer response due to the approximation of the modified Cross relation (2.14) by a power-law model.

4.5.4 Pulse train indentation experiments

The indentation response at 0°C and 5°C is plotted in Figs. 4.9a and 4.9b, respectively for cyclic load controlled pulse indentation tests with $F_p = 75\text{N}$ and $\Delta_p = 4.0\text{s}$ for two selected values of the pulse gap Δ_g (see Fig. 4.2c for definitions of F_p , Δ_p and Δ_g). The results clearly show that for a fixed value of F_p , the accumulated permanent indentation depth decreases with increasing Δ_g , because larger fractions of the creep strain are recovered in the zero-load gaps between the pulses. In fact, as $\Delta_g \rightarrow 0$, the pulse train tests converge to the continuous cyclic loading indentation tests, with no recovery of the accumulated strain.

A key measure of the accuracy of the model lies in its ability to predict the accumulated strain response of the bitumen in the pulse loading indentation tests. In these tests both the creep response of the bitumen under loads and its recovery behaviour is combined in a complicated manner and the response is integrated over many cycles resulting in the build-up of modelling errors. Such comparisons for pulse loading indentation tests are included in Fig. 4.9. The model under-predicts the to-

tal accumulated strain at large times similar to that observed in the monotonic and continuous cyclic loading cases. However, the errors in accumulated strain are only of the order of 10 % and hence this simple model is considered adequate for practical purposes.

4.6 Discussion

The spherical indentation response of bitumen was investigated in this chapter and an extension to the model of Bower et al. (1993) proposed to analyse the monotonic and cyclic indentation response of bitumen. The analysis of Bower et al. (1993) is based on the observation that the fields under the indenter in a power-law creeping solid are self-similar, which reduces the analysis to calculating stresses and displacements in a nonlinear elastic solid, indented to a unit depth by a rigid flat punch. In fact, Bower et al. (1993) presented a general analysis which is applicable to either plane strain or axisymmetric indenters of arbitrary geometries including conical and cylindrical indenters. The extension to the Bower et al. (1993) model presented here could also be generalised to these cases on lines similar to that presented in Section 4.3.

The self-similar analysis of Bower et al. (1993) is strictly valid for effective strains under the indenter $\epsilon^{\text{eff}} \leq 0.2$: beyond these strain levels, finite strain effects play a significant role and the simple model presented here is expected to be unable to capture the indentation response. Full finite element solutions of the field equations would be necessary to obtain the indentation response in such cases.

In the present study, the frictionless indentation limit was investigated by coating the indenters with a mixture of soap and glycerine. A few spots tests were conducted with non-lubricated indenters in order to gauge the effect of adhesion on the indentation behaviour. These tests revealed that the indentation recovery behaviour is substantially affected by the adhesion of the bitumen to the indenter. Further inves-

tigation into the effects of adhesion between the indenter and bitumen is proposed as a topic of future study.

4.7 Concluding Remarks

1. The similarity solution developed by Bower et al. (1993) for the indentation of a power-law creeping solid has been extended to the constitutive model for the monotonic and cyclic response of bitumen developed in chapter 3. Under non-zero applied loads, bitumen behaves as a power-law creeping solid and the analysis of Bower et al. (1993) is applicable. During unloading, the bitumen is assumed to recover in a self-similar manner and the effective strain rate under the indenter continues to be related to the indentation depth by (4.5a). Employing this strain measure in the constitutive relation for unloading bitumen it is possible to characterise the indentation behaviour of bitumen under both monotonic and cyclic loading conditions.
2. Monotonic, continuous cyclic and cyclic pulse loading experiments were conducted over a range of temperatures. Similar to the uniaxial tensile behaviour of bitumen, the continuous cyclic response was observed to depend mainly on the mean applied indentation load while the cyclic pulse loading behaviour depended strongly on the recovery behaviour of bitumen and hence was affected by the rest periods in the loading history.
3. The proposed indentation model is seen to capture the experimentally observed indentation response accurately over a wide range of loading conditions. Moreover, the model is also successful in predicting the temperature dependence of the indentation response and the effect of the indenter diameter.
4. The monotonic and repeated indentation behaviour investigated here is the unit

problem for understanding the behaviour of pavements under vehicle loads and is thus of intrinsic interest. Moreover, the indentation study has helped validate the multi-axial constitutive model for bitumen developed in chapter 3.

4.8 Tables

n	α	ϕ
1.00	0.849	0.707
1.11	1.085	0.747
1.25	1.332	0.788
1.43	1.602	0.831
1.66	1.886	0.875
2.00	2.176	0.920
2.50	2.465	0.966
3.33	2.734	1.013
5.00	2.973	1.065
10.00	3.110	1.128
100.00	3.051	1.201

Table 4.1: Indentation model parameters α and ϕ as a function of the power-law exponent n . (Reproduced from Bower et al. (1993)).

4.9 Figures

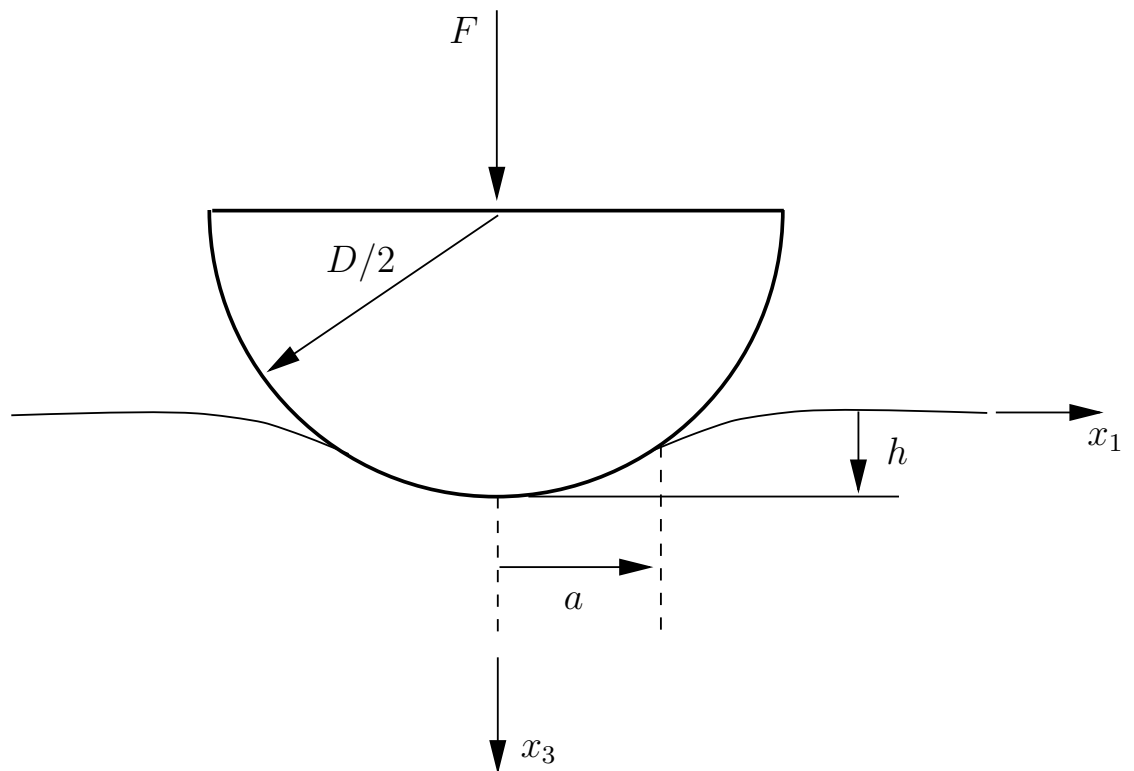


Figure 4.1: Spherical indentation of a half-space. The notation and sign convention is shown.

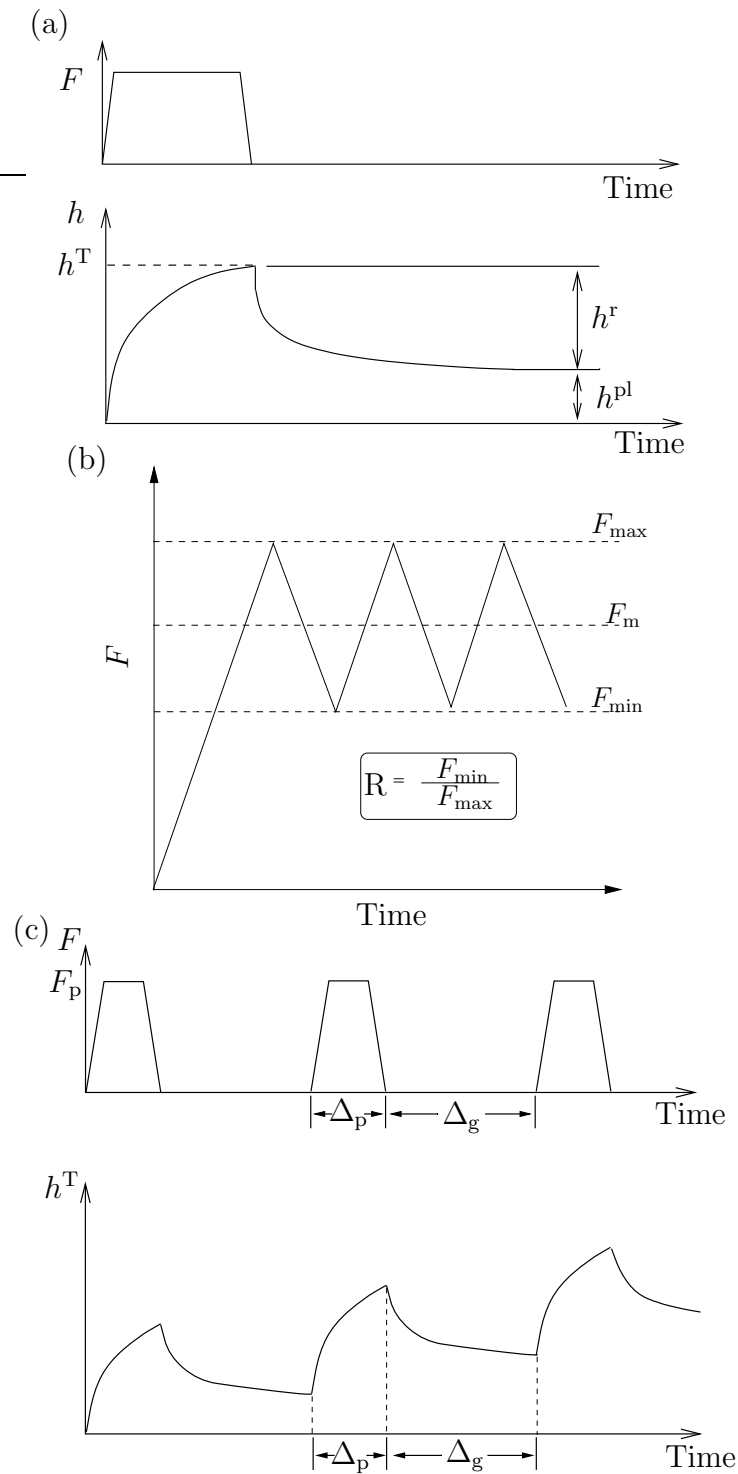


Figure 4.2: (a) Schematic showing the stress and strain time histories in a creep recovery test. (b) Schematic of the applied stress as a function of time in the continuous cyclic tests. (c) Schematic of the stress and strain time histories in the pulse train experiments.

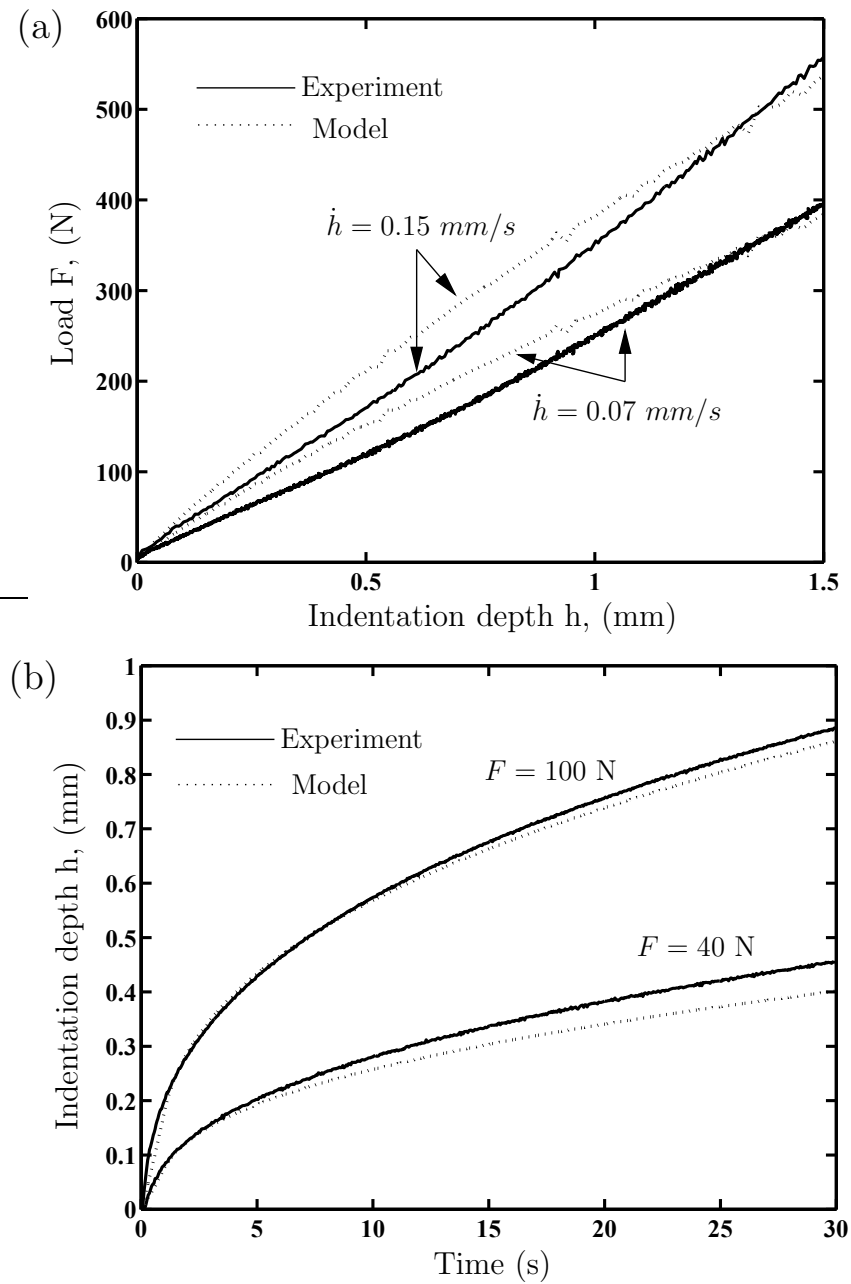


Figure 4.3: (a) Applied indentation force versus indentation depth for two selected values of the applied indentation-rate and (b) indentation depth versus time histories for two selected values of a constant applied indentation force at 0°C with a 40 mm diameter spherical indenter. Experimental measurements and model predictions are included.

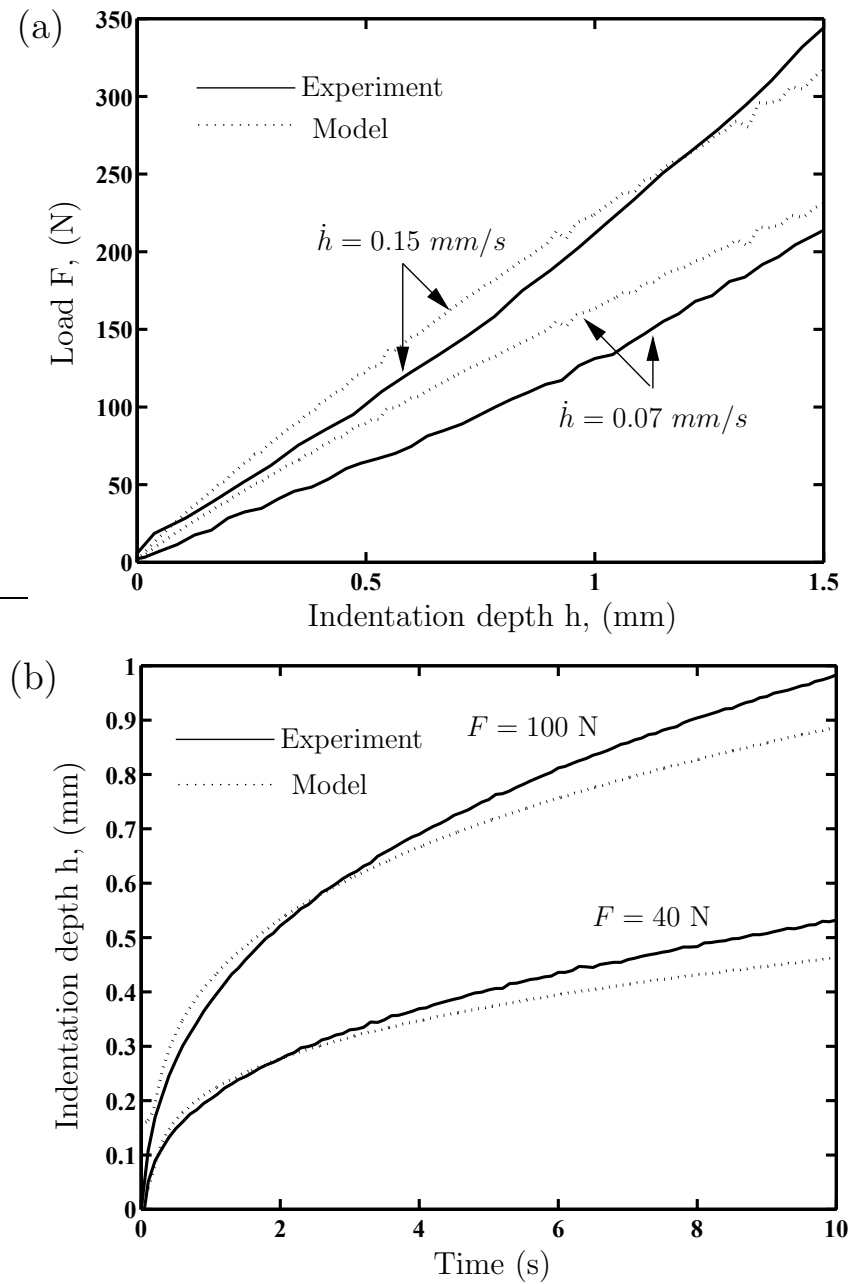


Figure 4.4: (a) Applied indentation force versus indentation depth for two selected values of the applied indentation-rate and (b) indentation depth versus time histories for two selected values of a constant applied indentation force at 5°C with a 40 mm diameter spherical indenter. Experimental measurements and model predictions are included.

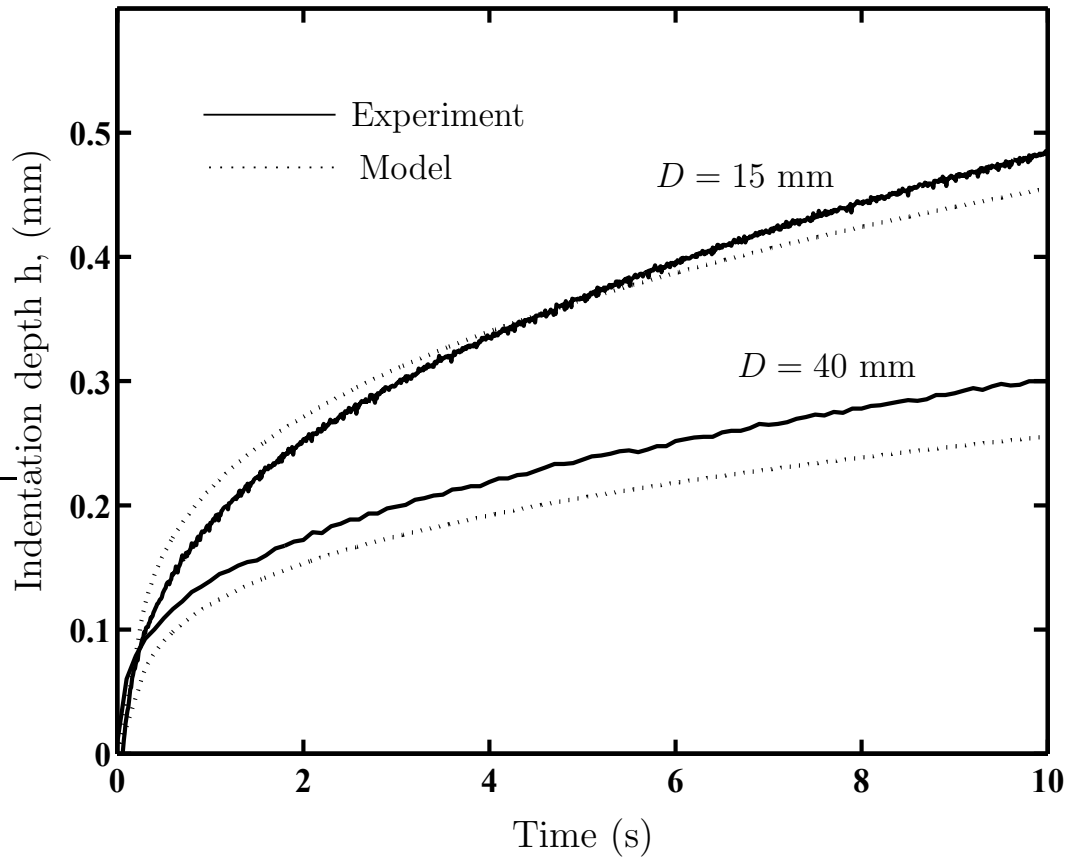


Figure 4.5: Indentation depth versus time history for a constant applied indentation force $F = 35$ N at 0°C . Experimental measurements and model predictions for two indenter diameters $D = 15$ mm and 40 mm are included in the figure.

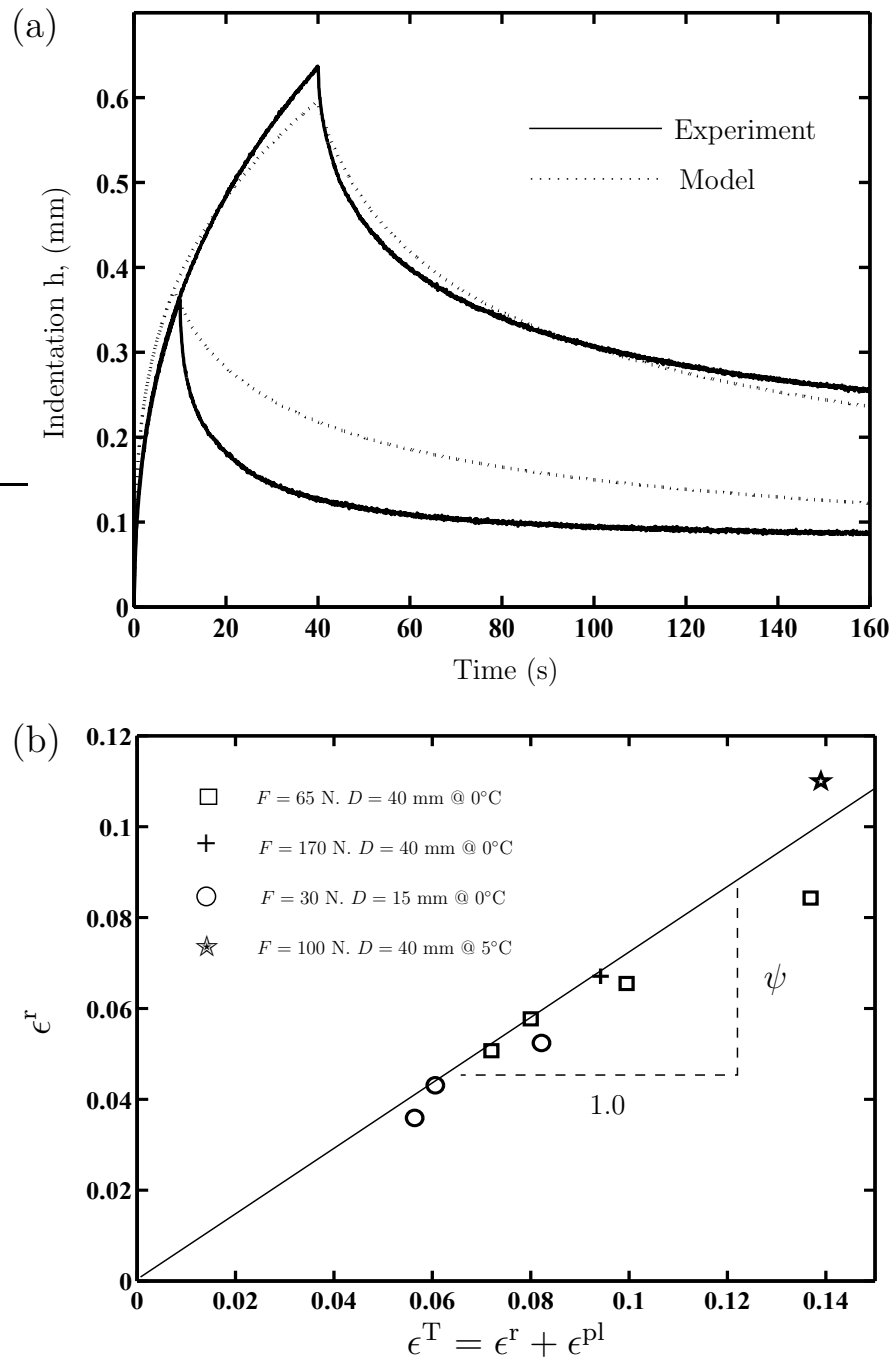


Figure 4.6: (a) Indentation creep recovery experimental measurements and model predictions at two selected values of the total indentation depths h^T with $F = 65$ N at 0°C . (b) Summary of the indentation creep recovery experimental measurements. The experimental data for the different levels of indentation force and indenter diameters show a linear relationship between ϵ^r and ϵ^T at the two temperatures investigated.

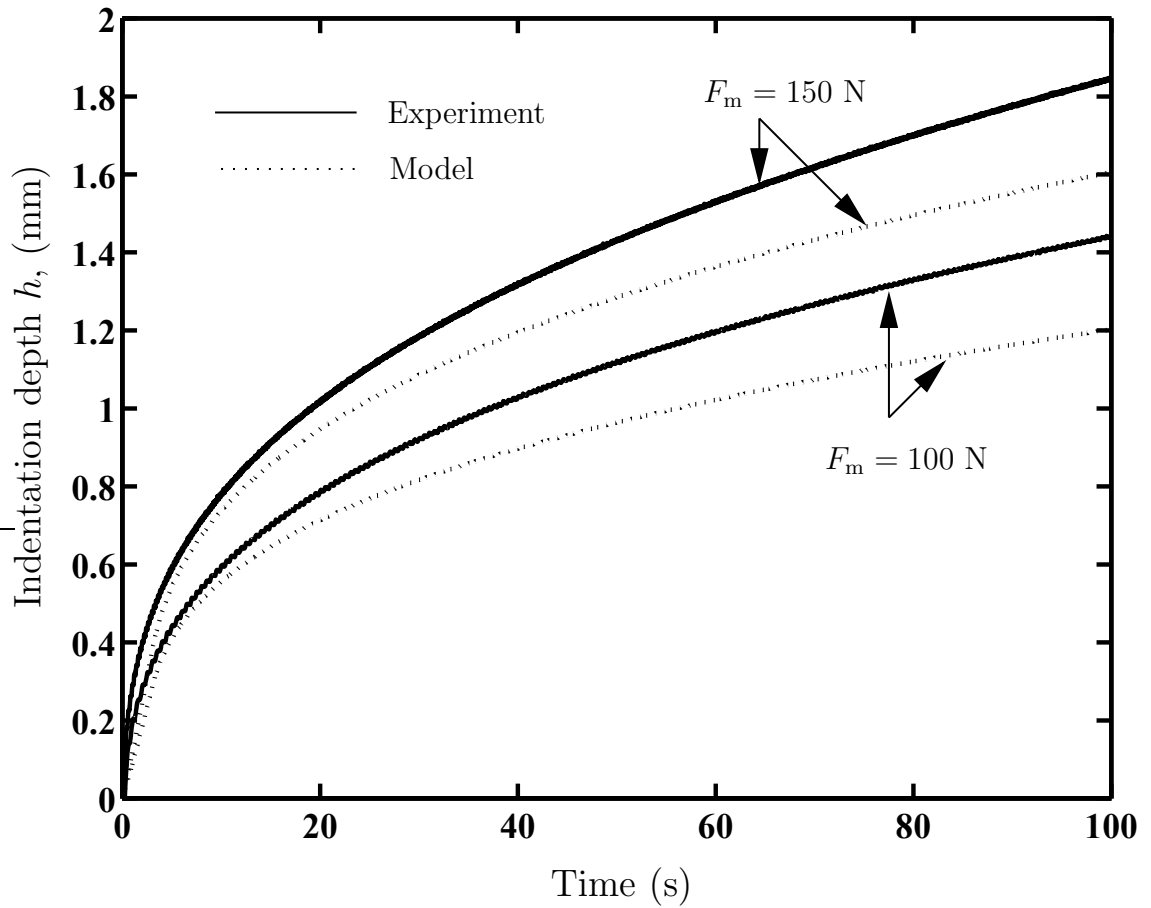


Figure 4.7: Continuous cyclic load controlled indentation experimental measurements and model predictions (frequency $f = 2$ Hz and load ratio $R = 0.7$) for two applied mean loads F_m at 0°C with a 40 mm diameter spherical indenter.

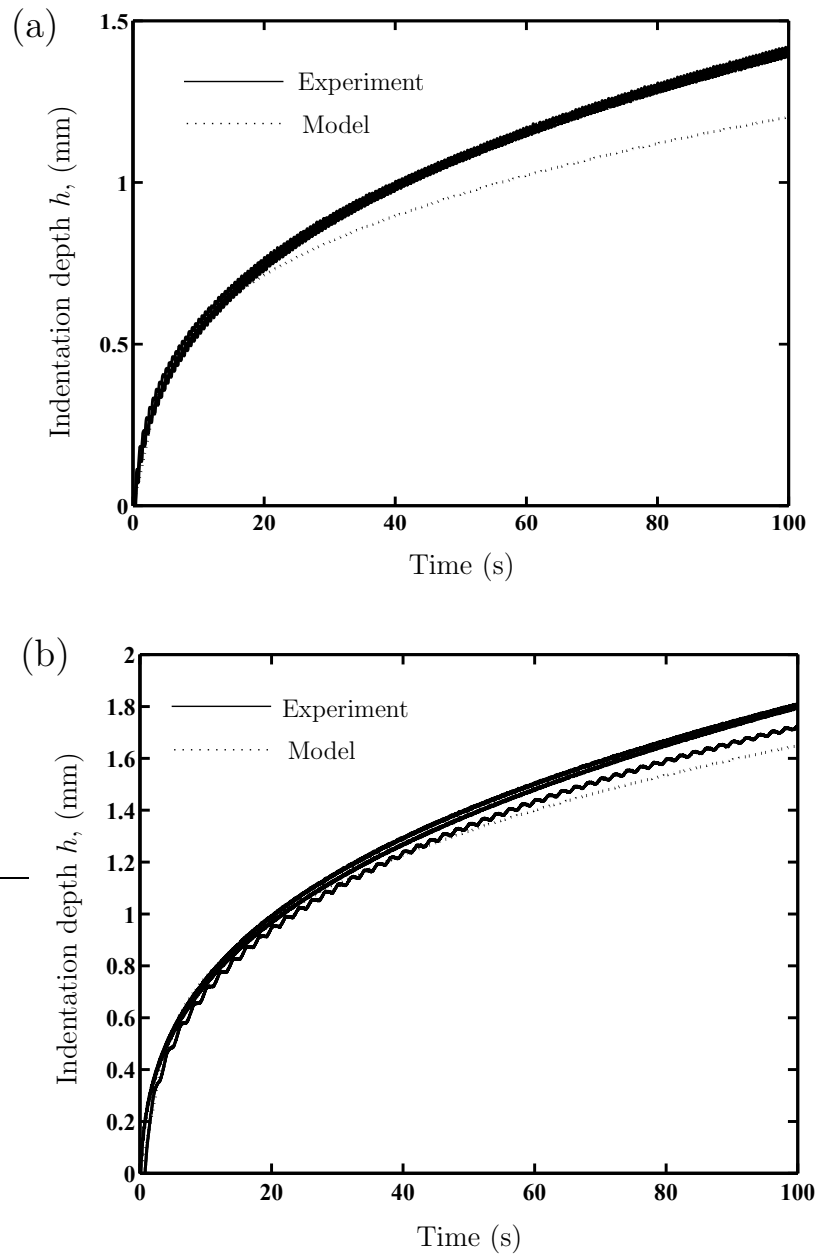


Figure 4.8: Continuous cyclic load controlled indentation test results at 0° C with 40 mm diameter spherical indenter. Experimental measurements and model predictions for (a) a fixed mean load $F_m = 100$ N and a frequency $f = 5.0$ Hz at three selected values of the load ratio $R = 0.3, 0.5$ and 0.7 and (b) $F_m = 150$ N and $R = 0.7$ for three selected values of $f = 0.5, 5.0$ and 10 Hz.

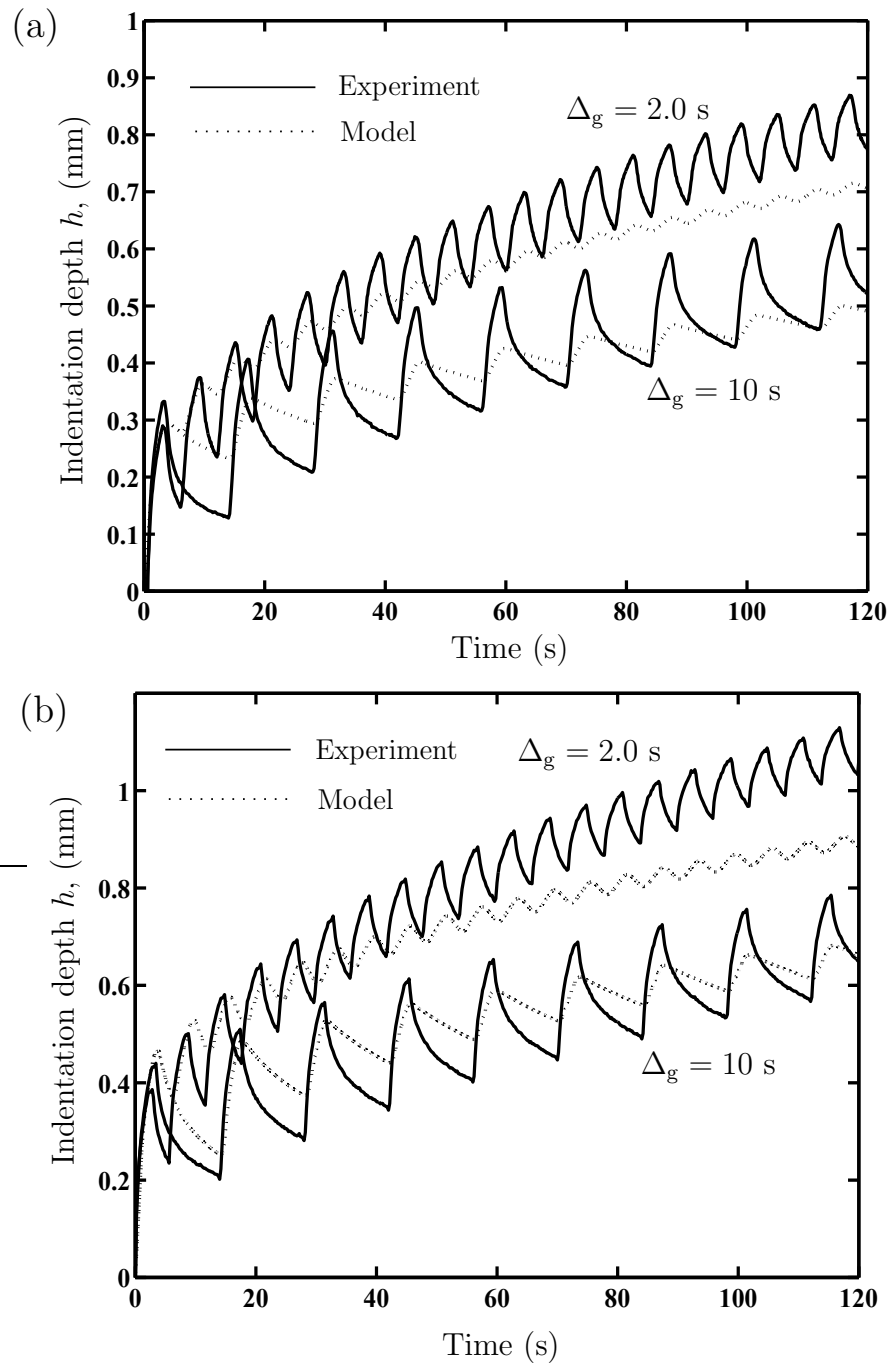


Figure 4.9: Cyclic load controlled pulse train indentation experimental measurements and model predictions with $F_p = 75\text{N}$ and $\Delta_p = 4.0\text{s}$ for two selected values of the pulse gap Δ_g at (a) 0°C and (b) 5°C .

Chapter 5

Review of previous research on bituminous mixes

5.1 Introduction

The most common approaches to modelling bituminous mixes have employed *Continuum Mechanics* theories and more recently *Micro-mechanical Models*. Early models were based on empirical relations due to the complexity of the problem and the limited understanding of the behaviour of heterogeneous materials (Deshpande, 1997).

This chapter presents a brief description of the main research on continuum and micromechanical models of the behaviour of bituminous mixes. Detailed reviews can be found elsewhere (Cheung, 1995; Deshpande, 1997).

5.2 Continuum models of bituminous mixes

5.2.1 Stiffness representation

Van der Poel (1955) extended the *stiffness* concept of bitumen to map the dynamic

behaviour of bituminous mixes under small strains, where linear behaviour is usually found. Van der Poel assumed that the stiffness of the mix is a function of the stiffness of the bitumen and the volume fraction of the aggregate. Later Heukelom and Herrin (1964) proposed the following relationship to model the stiffness of a mix:

$$\frac{S_{mix}}{S_{bit}} = \left\{ 1 + \frac{2.5c}{\kappa(1-c)} \right\}^{\kappa}, \quad (5.1)$$

where S_{mix} , S_{bit} are the stiffness of the mix and bitumen respectively measured in MPa, c is the volume concentration of the aggregate, defined as:

$$c = \frac{\text{Volume of aggregates}}{\text{Volume of (aggregates + bitumen)}}, \quad (5.2)$$

and

$$\kappa = 0.83 \log \left\{ \frac{4 \times 10^4}{S_{bit}} \right\}. \quad (5.3)$$

These equations were obtained from empirical fits to experimental data from dynamic tests on compacted mixes with approximately 3% air voids and c values from 0.7 to 0.9. Brown and Co-workers (1992) modified the above equations to give:

$$\frac{S_{mix}}{S_{bit}} = \left\{ 1 + \frac{257.5 - 2.5 VMA}{\kappa(VMA - 3)} \right\}^{\kappa}, \quad (5.4)$$

where VMA is the percentage of voids in mixed aggregate, and κ is the same as in equation 5.3. Equation 5.4 is valid for VMA values from 12% to 30% and $S_{bit} \geq 5MPa$. For higher values of bitumen stiffness, bitumen behaves as an elastic solid and the stiffness ratio is a measure of the stiffening effect due to rigid inclusions in an elastic matrix. For lower values of S_{bit} , the stiffness ratio becomes a function of the elastic, viscoelastic and viscous responses of the material.

5.2.2 Creep properties

Pavement rutting is a problem associated with high temperatures and repeated load pulses of short duration. Under these circumstances, linear viscoelastic models fail

to predict the behaviour of bituminous mixes. Therefore, mechanistic approaches of pavement design have been developed based on compression creep tests of mixes, either uniaxial or triaxial e.g. (Hills et al., 1974; Van de Loo, 1976; Van de Loo, 1978; Nunn, 1986; Mahboub, 1990; Brown and Co-workers, 1992; Collop et al., 1995; Lu and Wright, 2000). Some of those models showed reasonable agreement with test results or in-situ pavement data. However, large calibration factors are often required to correct the models so that they agree with the results of in-situ measurements.

5.2.3 Linear viscoelastic models

In the 1960's, when Van der Poel's stiffness approach was popular for describing the behaviour of pure bitumen and bituminous mixes at low strain and stress levels, some researchers extended that approach to model the asphalt behaviour, based on uniaxial creep tests and dynamic tests at constant load amplitude (Pagen, 1965; Pagen, 1968). There have been many studies associated with linear viscoelastic models for characterising bituminous mixes and structural analysis of pavements, e.g. (Papazian, 1962; Pagen, 1965; Moavenzadeh and carnaghi, 1966; Sayegh, 1967; Andersson, 1967; Huang, 1967; Ishihara and Kimura, 1967; Pagen, 1968; Pagen, 1972; Thrower, 1975; Pink et al., 1980; Nunn, 1986; Christensen, 1998; Mehta and Christensen, 2000). Most measured model parameters from particular experiments, and a few used mix specification to predict those parameters (Francken and Verstraeten, 1974; Collop, 1994; Collop et al., 1995). Despite the good results of those models at low strain and stress levels, they are unable to model the correct behaviour at high strain and stress levels where the non-linear behaviour is prominent (e.g. (Monosmith and Sekor, 1962; Monosmith et al., 1966)). Linear viscoelastic approaches are still the most popular choice for modelling the deformation of bituminous mixes, because of their ease of implementation.

5.2.4 Non-linear viscoelastic models

As bituminous mixes at large strain or stress levels exhibit non-linear behaviour, some researchers have attempted to extend the linear viscoelastic models to include the non-linear effects e.g. Fitzgerald and Vakili (1973), Lai and Anderson (1973), Vakili (1983) and Vakili (1985). However, these models have not been employed to model the deformation behaviour of real pavement structures due to their complexity, uniaxial nature and number of material constants required. As an attempt to overcome these problems, other more appealing models based on a nonlinear extension of the correspondence principle developed by (Schapery, 1984) were developed to model the behaviour of mixes under large strains or stresses under monotonic or cyclic conditions in the time domain, with reasonable results compared with experimental results (Kim and Dallas, 1989; Kim et al., 1990; Kim et al., 1995; Lee and Kim, 1998; Zhao and Kim, 2003).

Recently, non-linear viscoelastic models have been developed using thermodynamic theories e.g. Saleeb et al. (2003) and Krishnan and Rajagopal (2004). These models also require many calibration constants and complex fitting procedures.

5.2.5 Viscoelastoplastic models

Researchers like Dunhill et al. (2000), Airey et al. (2002), Huang et al. (2002), Airey et al. (2003) and Huang et al. (2004) applied viscoelastoplastic theories for modelling asphalt deformation with reasonably good results. For example, Dunhill et al. (2000) used a constitutive model based on the phenomenological approach proposed by Scarpas and Blaauwendraad (1998) to model materials exhibiting strain rate dependent plastic deformation, in conjunction with the Desai et al. (1986) yield criterion. Huang et al. (2004) used a hierarchical single surface (HiSS) based model (Desai, 1980; Wathugala, 1990; Chia, 1994) to predict triaxial compressive behaviour

of asphalt from the experimentally measured parameters. The main drawback of these models is the many experimentally fitted parameters they require.

5.2.6 The finite element model

During the last decade a popular choice for modelling the deformation behaviour of bituminous mixes has been Finite Element Methods (FE) (Sepehr et al., 1994; Bahia et al., 1999; Weissman et al., 1999; Kose et al., 2000; Long, 2001; Masad and Bahia, 2002; Taciroglu and Hjelmstad, 2002; Papagiannakis et al., 2002; Collop et al., 2003; Sadd et al., 2004; Abbas et al., 2004). These models usually make use of viscoelastic or viscoelastoplastic constitutive models. For instance, Long (2001) used a non-linear viscoelastic extension to the models proposed under the SHRP-A-415 (1994), while Collop et al. (2003) developed a viscoelastoplastic model with damage for asphalt based on the model of Scarpas and Blaauwendraad (1998).

5.2.7 Triaxial models

While most of the models developed for bituminous mixes were developed under uniaxial conditions, triaxial testing has long been recognised as important to understand mix behaviour for more general conditions.

In the late 1940's, Nijboer (1948) and Goetz and Chen (1950) studied the behaviour of various bituminous mixes under triaxial loading using a soil mechanics approach with two parameters, namely, "the angle of internal friction", and the "cohesion". They concluded that the cohesion reflected the binding capacity of bitumen for a particular aggregate. Higher bitumen penetration values decrease the cohesion, whereas higher rates of loading increase the cohesion. The *stability of the mix* (deviatoric stress at failure) was found to increase with hydrostatic pressure and to depend on the other mix parameters in a similar way as the cohesion. On the other hand, the

value of the angle of internal friction reflected the type and gradation of the aggregate. While the angle of internal friction usually decreased with increasing bitumen content, the mechanical properties of bitumen and the loading rate were found to have little effect.

A number of other investigations of the triaxial behaviour of bituminous mixes can be found in the literature e. g. Huang (1967), Hills and Heukelom (1969), Brown and Cooper (1980), Brown and Cooper (1984), Huschek (1985), Brown et al. (1991), Cooper et al. (1991), Low et al. (1993) and Kim et al. (1997).

After triaxial quasi-static and cyclic creep tests, Brown and Snaith (1974), Brown and Cooper (1980) and Brown and Cooper (1984) concluded that the volumetric strain rates depend on hydrostatic stress only, while deviatoric strain rates depend on both the hydrostatic stress and the deviatoric stress. They also found that deformation resistance was greater for continuously graded¹ rolled asphalts than for gap graded² rolled asphalts. This indicates that the effect of aggregate interlock is more important than the viscous properties of the bitumen. From cyclic triaxial results, they observed that a relationship between quasi-static and cyclic behaviour could be found, however, no further attempt was made to establish that relationship.

More recently, Deshpande and Cebon (1999b) and Collop and Khanzada (2001) investigated the monotonic steady-state behaviour of idealised bituminous mixes under triaxial conditions, finding a strong dependence of the deviatoric and hydrostatic stresses on the steady-state deformation behaviour of fully dense mixes (more than 64% volume fraction of aggregate).

¹Mixes with a continuous distribution of small, medium and large aggregate.

²Mixes with only small and large aggregate.

5.3 Micromechanical models for bituminous mixes

The microstructure of bituminous mixes has been used as a qualitative measure of the mix behaviour by various researchers e.g. (Nijboer, 1948; Hills and Heukelom, 1969; Hills, 1973). However, during the last decades there has been an increased interest in modelling the mix behaviour in terms of the microstructure e.g. (Frölich and Sack, 1946; Van der Poel, 1958; Hills, 1973; Christensen and Lo, 1979; Deshpande and Cebon, 2004; Abbas et al., 2004; Krishnan and Rajagopal, 2004). Some of the most representative models will be briefly described in the following sections.

5.3.1 The three phase composite sphere model

Van der Poel (1958) attempted to model the behaviour of bituminous mixes by calculating the rigidity of a concentrated solution of elastic spheres in an elastic medium, using a method developed for dilute dispersions by Frölich and Sack (1946). While the reported results showed good agreement with experiments for volume fractions of aggregate up to 60%, certain errors in the calculation technique were later reported by Christensen and Lo (1979).

5.3.2 The bitumen film creep model

Hills (1973) attempted to develop a theoretical model of the long time creep behaviour of bituminous mixes. His model described the internal structure of the mixes in terms of the bitumen film thickness, and the evolution of this state variable as a function of the macroscopic straining of the material. The macroscopic strain of a mix was assumed to be accommodated on a microscopic scale by displacements of adjacent aggregate particles in both shear and compression. These displacements were assumed

to be independent of each other. It was further proposed that the macroscopic strain of the mix was uniquely related to the shear displacements of adjacent aggregate particles. So, the microscopic shear resistance of the bitumen films was considered to be controlled by its thickness. The bitumen was modelled as an incompressible, linear viscous fluid. Results were given in terms of the stiffness in the region $S_{bit} < 5 \text{ MPa}$.

Hills' model was based on an empirical estimation of the evolution of film thickness under deformation, rather than on a theoretical analysis of thin film deformation of the bitumen³. The model provided the general form of the constitutive equations, but it depended entirely on curve fitting to experimental data. Collop (1994) and Collop et al. (1995) developed a method to obtain the parameters for Hills' model from fundamental mix parameters (e.g. the *VMA*), and used this modified model to estimate the rutting of paving mixtures undergoing accelerated tests, with good agreement.

Following the ideas of Hills, Cheung et al. (1999) used the isolated contact modeling approach, originally developed for the analysis of stage I powder compaction, to analyze the deformation behaviour of an asphalt, idealized as a random distribution of rigid spheres separated by thin films of bitumen. The predictions of the model agreed qualitatively with experimental results but the isolated contact model substantially underpredicted the "stiffening" effect of the aggregate.

5.3.3 The discrete element model (DEM)

Rothenburg et al. (1992) reported a micromechanical model for bituminous mixes in which the material was represented by a set of discrete elastic particles bound by linear viscoelastic bitumen. The model simulated the motion of a large number

³A complete theoretical and experimental study on thin film behaviour of pure bitumen can be found in Cheung (1995) and Cheung and Cebon (1997c).

of individual randomly shaped particles. This motion was constrained either by a viscoelastic film of bitumen or frictional contact between particles. They also proposed a microstructure to model the presence of bitumen and voids to predict the behaviour of particle contacts. Although the proposed microstructure and the constitutive behaviour of bitumen were not rigorous, the simulation yielded many insights concerning the fundamental mechanisms of deformation of bituminous mixes. Other researchers, for example Chang and Meegoda (1993), Sitharam (1999), Buttlar and You (2001), Ullidtz (2001), Collop et al. (2004) have also attempted to model bituminous mixes using DEM. Computational time constraints make the use of these models impractical for simulating deformation in a pavement.

5.4 Review of research on particulate composites

Composite materials are strongly inhomogeneous relative to a small length scale (microscale), but show homogeneous properties relative to a larger scale (macroscale), over which variations in applied loads are significant (Willis, 1982).

Deshpande (1997) performed an extensive literature review of the deformation behaviour of nonlinear viscous materials reinforced by rigid inclusions. He found that the existing models fall into three main categories:

1. Homogenisation formulae for the properties of periodic composites

Examples in this category are the composite sphere model (Hashin, 1962; Hashin, 1985), the three phase model (Van der Poel, 1958; Christensen and Lo, 1979), the concentrated suspension model (Frankel and Acrivos, 1967) and periodic unit cell analysis (Christman et al., 1989; Bao et al., 1991). These models usually assume certain repetitive microstructure to solve the boundary value problem of a representative unit cell by finite element (FE) analysis or other

analytical technique. The main problem of these models arise when modelling composites of high volume fractions of aggregate because of the sensitivity of the results to the defined size and shape of the unit cell, as well as the imposed boundary conditions.

2. Estimates for the effective properties of *ad hoc* models of composites

The most representative models of this category are the dilute suspension model (Frölich and Sack, 1946; Einstein, 1956) and the self-consistent and differential self-consistent models (Hill, 1965; Budiansky, 1965; McLaughlin, 1977; Duva, 1984). The dilute suspension model is based on the solutions for the deformation of a single inclusion in an infinite matrix. These solutions are employed in self-consistent and differential self-consistent schemes to model composites with finite concentrations of inclusions. These models are classified as *ad hoc* because they do not use a definite microstructure. The main disadvantage of these methods is that they neglect the interaction between inclusions and therefore cannot be used to model composites having volume fractions higher than about 40%.

3. Variational boundaries for the properties of random composites

The most representative models of this category are the Voigt and Ruess bounds (Paul, 1960), the general Hashin-Strikman bounds (Hashin and Strikman, 1963; Willis, 1982; Willis, 1983; Ponte Castañeda and Willis, 1988; Ponte Castañeda, 1989; Ponte Castañeda, 1991; Willis, 1991; Willis, 1992; Talbot and Willis, 1992; Ponte Castañeda, 1992a; Ponte Castañeda, 1992b; Ponte Castañeda and deBotton, 1992; Ponte Castañeda and Zaidman, 1994) and bounds for the assemblage of composite spheres (Suquet, 1993). The Voigt and Ruess bounds, which are based on the general assumption that the composite is macroscopically homogeneous, are generally too far apart for typical composites to be of any practical

value. The general Hashin-Strikman bounds give more definitive solutions because of an additional assumption that the composite is isotropic. However, these bounding models are unable to describe the dilation behaviour under deviatoric stresses (which is commonly observed for some high volume fraction composites), anisotropic behaviour and the evolution of the microstructure under various loading conditions.

5.5 Steady-state constitutive relationship for idealised asphalt mixes

Deshpande (1997) performed an extensive experimental study of the steady-state deformation behaviour of idealised bituminous mixes, consisting of pure bitumen mixed with single-sized or multi-sized sub-spherical aggregate, with volume fractions up to 85%. He performed both uniaxial and triaxial experiments and found that the main characteristics of the steady-state deformation of these mixes were:

1. The steady-state uniaxial behaviour of the mixes was found to be linear viscous at low stresses and non linear viscous at high stresses, similar to pure bitumen.
2. The aggregate has a “stiffening” effect on the bitumen (fig.5.1). This stiffening effect was found to be primarily a function of the volume fraction of the aggregate and not strongly dependent on the shape and size of the aggregate particles. Including a stiffening factor S , the steady-state behaviour of the mixes can be obtained by modifying equation 2.14 as:

$$\frac{\sigma}{\sigma_o} = \frac{S\dot{\epsilon}}{\dot{\epsilon}_o} \left(\frac{1}{1 + \left(\frac{S\dot{\epsilon}}{\dot{\epsilon}_o}\right)^m} \right). \quad (5.5)$$

3. The mixes were observed to dilate under compressive triaxial stresses.

4. The volumetric strain varied linearly with the distortional strain and was dependent on the volume fraction of aggregate but independent of the stress state, strain rate or properties of the bitumen.
5. The steady-state behaviour of the mixes was found to be a function of both mean and deviatoric stresses.

Based on these observations about the behaviour of idealised mixes, Deshpande and Cebon (1999b) developed a steady-state constitutive model for idealised asphalt mixes, based on soil mechanics concepts. They used the shear box analogy (Taylor, 1948) and a modified version of the Composite Sphere Model (Hashin, 1962), with Suquet (1993) method used to convert between linear and non-linear viscous behaviour (Deshpande and Cebon, 1999a).

The overall upper bound solution for the steady-state viscous deformation behaviour of idealised bituminous mixes is given by (Deshpande, 1997; Deshpande and Cebon, 1999b):

$$\dot{\mathcal{E}}_e \geq \frac{\dot{\epsilon}_o[\omega s + 1]^n}{\left(\frac{1}{2}k s^2 + \frac{3}{2}\mu\right)^{(n+1)/2}[1 - (c + v)]^{(n-1)/2}} \left(\frac{\Sigma_e}{\sigma_o}\right)^n. \quad (5.6)$$

Where

$\dot{\mathcal{E}}_e = \left(\frac{2}{3}\dot{\mathcal{E}}'_{ij}\dot{\mathcal{E}}'_{ij}\right)^{\frac{1}{2}}$ = is the Von Mises equivalent macroscopic strain rate

$\dot{\mathcal{E}}'_{ij}$ = is the deviatoric macroscopic strain rate tensor

$\omega = \Sigma_m/\Sigma_e$ = mean stress/Von Mises equivalent stress

c, v = Volume fraction of rigid inclusions and voids, respectively

$\dot{\epsilon}_o, \sigma_o, \{n = 1/(1 - m)\}$ = Bitumen parameters from the Modified Cross Model

The dilation gradient s is defined as the slope of the volumetric strain vs distortional strain for uniaxial or triaxial tests on an specific mix as

$$\dot{H} = s|\dot{\mathcal{E}}_e|, \quad (5.7)$$

μ is the upper bound on the shear modulus which can be found using Hashin's composite sphere model according to (Hashin, 1962):

$$\mu = \frac{2}{3} \left\{ 1 + \frac{c}{\frac{2}{5}(1-c) - \frac{c(1-c^{2/3})^2}{-\frac{10}{21}c^{7/3} + \frac{10}{21}}} - \frac{v}{\frac{3}{5} + \frac{2}{5}v + \frac{v(1-v^{2/3})^2}{\frac{95}{168}v^{7/3} + \frac{10}{21}}} \right\}. \quad (5.8)$$

The bulk modulus k is given by:

$$k = \frac{8}{9} \frac{1-v}{v} \frac{1}{1-c}. \quad (5.9)$$

The constitutive law (eq. 5.6) can be applied to uniaxial or triaxial axisymmetric loading. In these cases, the general constitutive law can be written as:

$$\dot{\mathcal{E}} = \frac{\dot{\epsilon}_o [\eta s \text{sign}(\Sigma) + 1]^n}{(\frac{1}{2}k s^2 + \frac{3}{2}\mu)^{(n+1)/2} [1 - (c+v)]^{(n-1)/2}} \left(\frac{|\Sigma|}{\sigma_o} \right)^n \text{sign}(\Sigma), \quad (5.10)$$

where Σ is the deviatoric stress, and $\dot{\mathcal{E}}$ is the distortional macroscopic strain rate. Also note that the sign “ \geq ” in the bounding solution is replaced by the sign “=” for convenience. However, it should be taken into account that this is an upper bound estimate.

The axial macroscopic strain rate $\dot{\mathcal{E}}_{33}$ is given by:

$$\dot{\mathcal{E}}_{33} = \dot{\mathcal{E}} \left(1 + \frac{s \text{sign}(\Sigma)}{3} \right). \quad (5.11)$$

Thus, the axial macroscopic strain rate can be written as:

$$\dot{\mathcal{E}}_{33} = \frac{\dot{\epsilon}_o}{S} \left(\frac{|\Sigma|}{\sigma_o} \right)^n \text{sign}(\Sigma), \quad (5.12)$$

where S is the stiffening factor given by:

$$S = 0.55 \frac{(\frac{1}{2}k s^2 + \frac{3}{2}\mu)^{(n+1)/2} [1 - (c+v)]^{(n-1)/2}}{[\eta s \text{sign}(\Sigma) + 1]^n} \left[1 + \frac{s \text{sign}(\Sigma)}{3} \right], \quad (5.13)$$

and $\eta = \Sigma_m/\Sigma$ is the stress ratio. The constant factor “0.55” in eq. (5.13) follows from a numerical correction added by Deshpande and Cebon (1999b) for values of

$n \approx 2.5$ (see Deshpande and Cebon (1999b) for details). The hydrostatic strain rate is given by the kinematic constraint $\dot{H} = s|\dot{\mathcal{E}}_e|$.

This model showed good agreement with uniaxial and triaxial tests performed on ideal mixes with various volume fractions of aggregate, over a wide range of stresses, strain rates and temperatures (Deshpande, 1997; Deshpande and Cebon, 1999b).

5.6 Quasi-static mechanics of granular assemblages

An important factor in modelling the deformation behaviour of granular assemblies is a phenomenon of *dilatancy*, which causes an increase of volumetric strain with distortional strain (Deshpande and Cebon, 1999b). This phenomenon was first revealed by Reynolds (1885) and later adopted in Rowe's "stress-dilatancy" theory (Rowe, 1962; Rowe, 1972).

Reynolds (1885) stated that for a granular material in a state of maximum density, any contraction in one direction is accompanied by equal extensions in mutual perpendicular directions. Goddard and Bashir (1990) concluded that Reynolds dilatancy must be interpreted as an internal kinematical constraint reflecting the geometrical effects which are operative in the quasi-static motion of nearly rigid granules. In the absence of any such internal constraint, the volume or density of a compressible material is independent of its shape. Using the same notation as in section 5.5, Reynolds dilatancy theory gives:

$$H = s|\mathcal{E}_e|, \quad (5.14)$$

with $s = 0.75$ for triaxial compression of mono-sized spheres (Deshpande, 1997). Through numerical simulations of the deformation of a 2-D system of mono-sized discs, Bashir and Goddard (1991) found a linear dependence of the volumetric strain

on the shear strain with $s = 1.82$. They associated this high value of s to anisotropy in the packing model used in the numerical simulations.

Later, Goddard and Didwania (1998) theoretically studied the dilatancy of 2-D and 3-D assemblies of rigid frictional spheres, with various sphere sizes and gradations. They assigned to a granular assembly, a nearest-neighbour graph consisting of a network of sites or nodes connected by “bonds”. Global fraction f_A of bonds are presumed to be active, and fraction $1 - f_A$ of bonds are assumed to be broken or inactive. The bonds, both active and inactive, are assumed to define the edges of elementary space-filling, volume elements or *simplexes*, which in space dimension d ($d = 2$ for 2-D) represent the minimal cluster of particles for which a d -volume can be assigned (Goddard, 1998).

Each simplex consists of $d + 1$ particles or vertices connected pairwise by $m = d(d + 1)/2$ edges, and the effective kinematic properties of a granular assembly can be calculated from appropriate volume or ensemble averages over simplexes.

Under the assumption of fully dense ($f_A = 1$) random isotropic assemblies, Goddard and Didwania (1998) were able to derive an analytical expression for the dilatancy with $d = 2$ as:

$$\frac{D_v}{K_1} = \frac{4(R_1 + R_2 + R_3)^{\frac{3}{2}}(R_1 R_2 R_3)^{\frac{1}{2}}}{\pi(R_1 + R_2)(R_1 + R_3)(R_2 + R_3)}, \quad (5.15)$$

where K_1 is the major principal value of K and $R_1 + R_2$, $R_2 + R_3$, $R_1 + R_3$ are the sides of the representative triangle of three (nearly) touching disks of radius R_i . K is defined as:

$$K = -dD' = -d \left(D - \frac{D_v}{d} \right), \quad (5.16)$$

where D is the deformation or strain tensor and D_v is defined as $D_v = tr \{D\}$. Note that using the same notation of section 5.5, equation (5.15) can be re-written as:

$$s = \frac{H}{|\mathcal{E}|} = \frac{4(R_1 + R_2 + R_3)^{\frac{3}{2}}(R_1 R_2 R_3)^{\frac{1}{2}}}{\pi(R_1 + R_2)(R_1 + R_3)(R_2 + R_3)}. \quad (5.17)$$

In the special case of dense mono-size assemblies ($R_1 = R_2 = R_3$), eq. (5.17) gives:

$$s = \frac{3^{\frac{3}{2}}}{2\pi} = 0.827, \quad (5.18)$$

which can be compared with the Reynolds type estimate $s = 0.5$ (Deshpande, 1997). According to Goddard and Didwania (1998), the only analytical solution for s when $d = 3$, is for the special case of mono-sized spheres under uniaxial compression, giving:

$$s = \frac{3}{2\pi} \left(1 + \frac{1}{\sqrt{3}} \right) = 0.753. \quad (5.19)$$

Note that the 2-D (5.18) and 3-D (5.19) solutions for s differ by about 10%, which is around the experimental error of the uniaxial and triaxial measured s for mono-sized spheres (Deshpande, 1997).

For arbitrary non-axisymmetric K , Goddard and Didwania (1998) implemented a *Monte Carlo* numerical solution with good results.

Theoretical estimation of dilatancy for assemblies of angular shaped particles is still an unsolved and complex problem.

5.7 Conclusions

1. The most commonly employed approaches to modelling the deformation behaviour of bituminous mixes fall into two main categories: *i*) Continuum Mechanics models, and *ii*) Micromechanical models. Continuum mechanics models are still the most popular choice for analysing mixes in engineering practice.
2. A large amount of literature on the prediction of permanent deformation of bituminous mixes was found. However, most of the models fail to incorporate some of the observed characteristic of the deformation of the material or require an excessive amount of calibration parameters, with complex fitting procedures.

3. A simple model, which predicts the main characteristics of the steady-state compressive deformation of bituminous mixes under various stress and strain rate states, was developed by Deshpande and Cebon (1999b) based on soil mechanics and micro-mechanics theories. It shows good agreement with experimental observations and provides a good understanding of the main characteristics of the steady-state deformation behaviour.
4. A simple analytical solution for the dilation of 2-D fully dense disk assemblies was proposed by Goddard and Didwania (1998). However, the theoretical estimation of 3-D assemblies of spheres require complex numerical methods of solution, while for angular particles dilation is still an unsolved problem.

5.8 Figures

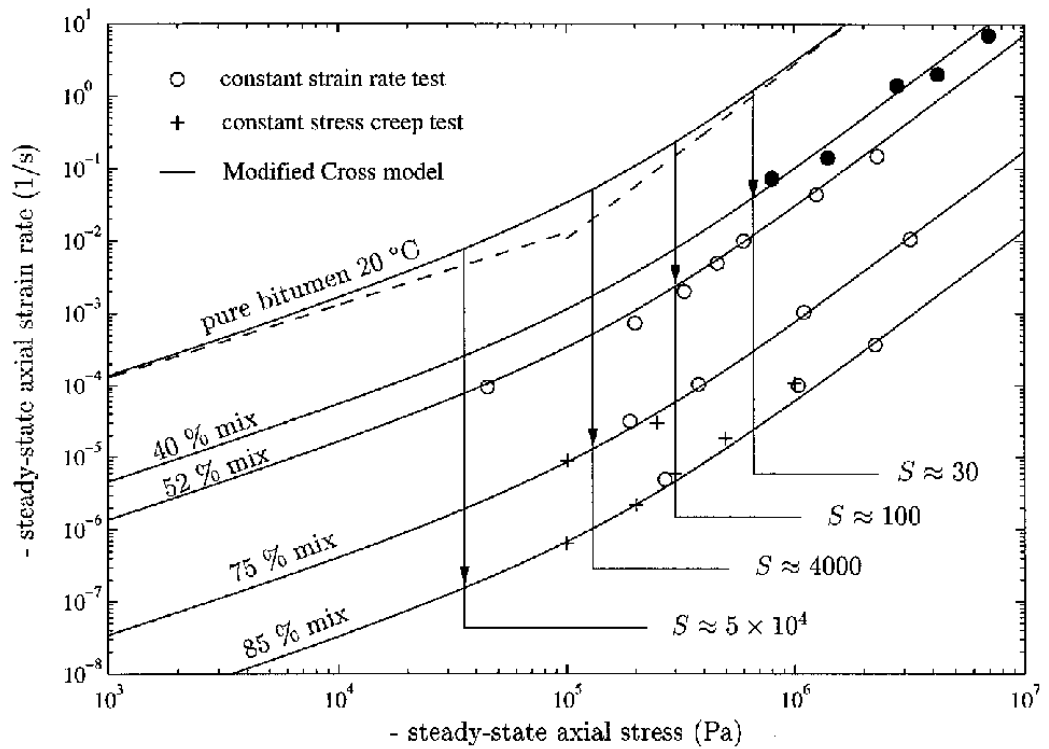


Figure 5.1: Steady-State Deformation Behaviour of idealised mixes with 40, 52, 75, and 85% by Volume Aggregate (Deshpande and Cebon, 2000)

Chapter 6

Uniaxial deformation behaviour of bituminous mixes

6.1 Introduction

Bituminous mixes are complex composite materials consisting of a high volume fraction of aggregate mixed with bitumen and air voids. In order to understand the influence of the mix components and their interactions, various volume fractions of aggregate mixes, ranging from 40% to 85%, with rounded and angular aggregate are studied under uniaxial conditions in this chapter. An extensive experimental study comprising of monotonic, continuous cyclic and pulse loading compressive uniaxial experiments is reported here. Based on these experimental findings a phenomenological model, which is an extension to the model proposed in chapter 3 for bitumen, is proposed. In this model, the total strain-rate is decomposed into rate dependent elastic, permanent and recoverable components.

6.2 Experimental investigation

The experiments measured the uniaxial compressive deformation behaviour of bituminous mixes under monotonic and cyclic loading conditions at various different loading rates and temperatures. Tensile tests were not performed because other mechanisms, such as void nucleation and growth can become dominant (Deshpande and Cebon, 2000; Harvey, 2000; Krishnan and Rajagopal, 2004).

6.2.1 Mix specification

Pure Bitumen

The same 50 pen bitumen studied in chapter 3 was used for the mixes preparation. The material parameters for this 50 pen bitumen are listed in Table 3.1 with the loading calibration curve $\dot{\epsilon}_{oc}(\epsilon)$ and recovery calibration curve $\dot{\epsilon}_{uc}(\epsilon^r)$ plotted in Figs. 3.6 and 3.9, respectively.

Mixes

Following a similar investigation procedure to Deshpande and Cebon (2000), four types of mixes consisting of bitumen and different volume fractions of aggregate were prepared and tested. These are listed in Table 6.1. Mixes AS and BS were low volume fraction dispersions, whereas mixes CS, DS and ES were fully dense mixes (see Finney (1970), German (1989) and Deshpande and Cebon (2000)). The mix preparation and testing procedures are detailed in the following sections.

6.2.2 Mix preparation

Specimen preparation technique has a significant effect on the measured properties of bituminous mixes. The main factors to take into account in specimen preparation are the compaction technique (affecting the density profile and void content, see

Hills (1973) and Wallace and Monismith (1980)) and the surface condition (cut or as-moulded) (Harvey et al., 1994).

Equipment and procedure for specimens of types AS and BS

Bituminous mixes are usually prepared as hot mixes of aggregate and bitumen. Deshpande and Cebon (2000) found that the main problem in the preparation of specimens with an aggregate volume fraction less than the maximum random packing density¹ is that the aggregate settles, leading to poor homogeneity of the specimen. To overcome this problem they prepared these mixes using a “*sintering*” process. That specimen making technique was followed in this study.

A cylindrical mould was manufactured and used to cast and compact the specimens. The diameter of the cylinder was 38.5 mm and the ratio of height to diameter of the specimen was of about 2. A lubricant consisting of a mixture of natural soap and glycerine (see Cheung (1995)) was applied to the inner surface of the mould to avoid sticking of the mix. A piece of non sticking silicone paper was placed in the bottom surface of the plungers to ease removal of the specimen after compaction. Crushed cold bitumen was mixed with the correct amount of sand (40% or 52% volume fraction) and then poured into the mould. The powdered mix was then compacted in a mechanical press (at room temperature) and then heated in a furnace for 1 hour at 55°C². This soft mixture (still in the mould) was further compacted at 5 MPa for 5 min to allow the bitumen to fill the air voids and bond with the sand. The mould was then placed in a freezer to cool down the specimen to about 0°C. Finally, the cold specimen was slowly pushed out of the mould. The final homogeneity of the specimens was checked using the same technique described for mixes CS, DS and ES in the next section, with good results.

¹The maximum random packing density for single sized spheres is about 64% (Finney, 1970).

²This is the approximate *softening point* of the bitumen used.

Equipment and procedure for specimens of types CS, DS and ES

Various compaction procedures are commonly used in the preparation of laboratory asphalt specimens. Fwa et al. (1993) evaluated several techniques based on the density profile of the specimens. The density profile was measured using a twin-probe nuclear density gauge (see Tan and Fwa (1991) for details). Their main conclusion was that single plunger compaction in multiple layers, or double plunger compaction in a single layer, gave homogeneous test specimens.

An evaluation was performed of the following compaction processes: single plunger compaction in one layer, single plunger compaction in three layers and double plunger compaction in one layer, using the bituminous mixes prepared in this study. To measure the density profile of the specimens, an X-ray computed tomography system was used. The advantage of this method of measurement is that it enables the density of the specimen to be measured at different positions along the length.

Figure 6.1 shows the density profiles for the three compaction techniques studied on the center line of mix CS specimens (64% Volume fraction of sand). It can be seen that the density profiles obtained with double plunger compaction and single plunger compaction in three layers are reasonably uniform, as concluded by Fwa et al. (1993). Double plunger compaction in one layer was selected as the compaction technique for mixes CS, DS and ES in this study instead of the three layer compaction technique used by Deshpande and Cebon (2000). This choice was motivated by the possibility that during the preparation of the three layers specimens, traces of the release agent applied to the plunger may be left at the layer interfaces. This could affect the deformation behaviour of the mix.

The same mould used for mixes AS and BS was used to cast the specimens of mixes CS and DS, while a cylindrical mould of internal diameter of 70 mm was used to cast the mix ES (85% volume fraction) specimens.

A mixture of the correct amounts of bitumen and aggregate (64%, 75% or 85% volume fraction) was heated to melt the bitumen. The mixture was then well stirred, poured into the mould, and compacted in a mechanical press at a pressure of approximately 15 MPa. After the mix had cooled down to room temperature, the specimen was slowly pushed out of the mould and stored at sub-zero temperature, following the same procedure described by Deshpande and Cebon (2000).

6.2.3 Test protocol

The test protocol was based on the test program developed in chapter 3 for bitumen. The main difference was the loading direction of the tests. Uniaxial compressive tests on the cylinder shaped specimens were performed in a hydraulic testing machine. The top and bottom surfaces of the loading platens of the testing machine were lubricated with a mixture of soap and glycerine in order to reduce friction between these surfaces and the specimen and thus to reduce bulging. The load was measured with a 20 kN load cell and used to calculate the nominal stress in the specimen. The load line displacement was used to calculate the nominal axial strain. The radial strains were measured by fitting a *Hall effect* radial transducer to the specimens of mixes AS, BS, CS and DS, while a non-contact laser scan micrometer was used to measure the radial strains of mix ES specimens. The test temperature was controlled by an environmental chamber with a resolution of $\pm 0.5^\circ\text{C}$ attached to the hydraulic testing machine. Prior to testing, all specimens were kept in the environmental chamber for about 2 hours to allow them to attain the test temperature. Experimental results from tests at 0°C , 10°C and 20°C are reported here. A number of spot repeat tests confirmed the repeatability of the tests. For the sake of brevity, these results are not presented.

Monotonic tests

Constant strain-rate and constant stress creep tests were employed to characterize the monotonic stress versus strain behaviour of the mixes. In the constant strain-rate tests, a specified uniaxial compressive strain-rate $\dot{\epsilon}$ was applied to the specimen and the resulting nominal compressive stress σ and strain ϵ were recorded. In the constant stress creep tests, a constant nominal compressive stress was applied “instantaneously” to the specimen and the nominal compressive strain ϵ was recorded as a function of time t .

Creep recovery tests

The creep recovery behaviour of the mixes was investigated by performing single load/unload tests as shown in Fig. 3.2a. A compressive stress σ was applied rapidly to the specimen and then held constant. The specimen was allowed to creep to a specified total nominal compressive strain ϵ^T . At this strain, the loading stress was released and the compressive strain monitored until the axial strain rate was zero $\dot{\epsilon} \approx 0$. The strain at this point $\epsilon^{Pl} = \epsilon^T - \epsilon^r$ is the “plastic” or irrecoverable strain, as shown schematically in Fig. 3.2a. Such tests were repeated for a series of strains ϵ^T , creep stresses σ and temperatures.

Cyclic tests

Continuous cyclic and pulse train tests were performed to characterise the cyclic and repeated loading behaviour of the mixtures.

Continuous cyclic tests.

In the continuous cyclic tests, the nominal compressive stress σ was varied between σ_{\min} and σ_{\max} with a triangular wave form as shown schematically in Fig. 3.2b. The

parameters

$$R = \frac{\sigma_{\min}}{\sigma_{\max}} \quad (6.1)$$

and

$$\sigma_m = \frac{\sigma_{\min} + \sigma_{\max}}{2} \quad (6.2)$$

were used to define the load levels, the frequency of the triangular wave was f , giving a loading rate of $\pm(\sigma_{\max} - \sigma_{\min})f/2$. The nominal compressive strain was measured as a function of time and tests were repeated for a series of values of R , σ_m and f .

Pulse train tests.

Tests comprising periodic compressive stress pulses with a trapezoidal shape, as shown in Fig. 3.2c, were performed in order to simulate a load history similar to that experienced in a pavement. The aim here was to investigate the relation between the single load/unload behaviour analysed via the creep and creep recovery tests and the gradual ratcheting of strain due to the application of a continuous train of discrete stress pulses as shown schematically in the bottom half of Fig. 3.2c.

The constant maximum compressive stress σ_p in each trapezoidal stress pulse was applied for a time period $\Delta_p/2$ with a loading and unloading rate $\dot{\sigma} = 4\sigma_p/\Delta_p$. A series of tests was performed at each temperature at fixed σ_p , but with varying time period Δ_g between consecutive trapezoidal pulses.

6.3 Experimental results

6.3.1 Monotonic behaviour

Constant strain-rate tests were performed over a wide range of strain-rates and temperatures. Figure 6.2 shows the nominal stress versus nominal strain response of mix

DS (75% volume fraction of aggregate) at 20°C for two values of the applied strain-rate $\dot{\epsilon}$ (similar results were also obtained at other temperatures). In each test, the compressive stress increases progressively until a maximum value is reached. This value is defined as the steady-state stress σ_{ss} , following the procedure proposed by Ward (1971) and Cheung and Cebon (1997b). With increasing applied strain-rate, the steady-state stress increases.

Constant stress creep tests were also performed over a range of stresses and temperatures. Figure 6.3 shows the monotonic creep response of mix DS at 20°C for two selected stress values. The slope of the secondary creep region, in which the strain varies linearly with time, is defined as the steady-state strain-rate $\dot{\epsilon}_{ss}$ at the prescribed stress, in line with the prescription of Ward (1971) and Cheung and Cebon (1997b).

Figure 6.4 summarises the monotonic steady-state behaviour of mix DS over a range of stresses, strain-rates and temperatures on a log-log scale with axes of $\dot{\epsilon}_{ss}$ and σ_{ss} .

The Modified Cross model (5.5) was fitted to the steady-state experimental data of mix DS in Fig. 6.4. Similar to the observations of Deshpande and Cebon (2000), the mix exhibits power-law viscous behaviour with $\dot{\epsilon}_{ss} \propto \sigma_{ss}^{2.6}$ ($m=0.615$ in eq. 5.5) at high stresses and linear behaviour with $\dot{\epsilon}_{ss} \propto \sigma_{ss}$ at low stress levels. Further, the temperature dependence of the steady-state behaviour of the mix is well characterised by the same Arrhenius relation as for bitumen (eq. 2.16) in the range ($0^\circ\text{C} \leq T \leq 20^\circ\text{C}$). Also shown in fig. 6.4 is the curve obtained in chapter 3 for the bitumen used in these specimens at 20°C, plotted using the Modified Cross Model. It can be seen that the curve for the mix at 20°C has the same shape as that for pure bitumen at 20°C. The main difference, is that the steady-state strain rate for the mix is less than that of pure bitumen at the same stress level by a constant multiplying factor as observed by Deshpande and Cebon (2000). Consequently the monotonic steady state

behaviour of the mix can be described by equation (5.5).

The constant strain-rate and creep tests for any given mix reveal that the steady-state behaviour occurs at a fixed value of strain ($\epsilon_{ss} \approx 0.025$ for mix DS (75%) in fig. 6.2). Thus, as for bitumen, the steady-state Modified Cross model (eq. 5.5) can be viewed as the relation between stress and strain-rate at a strain level $\epsilon = 0.025$ with $\dot{\epsilon}_{pc}$ in eq. (2.16) being a calibration constant for a strain $\epsilon = 0.025$. Thus, it is expected that the Cross model can be extended to give the relation between the stress and strain-rate at any value of strain ϵ by replacing the constant $\dot{\epsilon}_{pc}$ with a reference strain-rate $\dot{\epsilon}_{oc}(\epsilon)$ that is a function of strain ϵ . Equations (5.5) and (2.16) can then be re-written as:

$$\frac{\sigma}{S^l \dot{\epsilon}} = \frac{\sigma_o}{\dot{\epsilon}_o(\epsilon)} \frac{1}{1 + \left(\frac{S^l \dot{\epsilon}}{\dot{\epsilon}_o(\epsilon)} \right)^m}, \quad (6.3)$$

where

$$\dot{\epsilon}_o(\epsilon) = \dot{\epsilon}_{oc}(\epsilon) e^{-k \left(\frac{1}{T} - \frac{1}{273} \right)}, \quad (6.4)$$

where S^l is the loading stiffening factor and k the Arrhenius constant, remaining unchanged from that of bitumen.

The function $\dot{\epsilon}_{oc}(\epsilon)$ can be extracted from one of the monotonic test results, using the procedure described in chapter 3 for bitumen. In this way it is found that the functions obtained from different experimental conditions collapse onto a single master curve. This enables the use of any of the monotonic tests to find the calibration function $\dot{\epsilon}_{oc}(\epsilon)$, as is the case of bitumen.

Similar sets of monotonic tests were also performed on the other four mixes (AS, BS, CS and ES). The steady-state behaviour was again found to be well characterised by the Modified Cross model, with the Arrhenius relation capturing the temperature dependence. Figure 6.5 shows two strain controlled results at the same applied strain rate and temperature for mixes CS (64%) and DS (75%). It can be seen that the

main differences between these mixes are the steady state stresses (stiffening factors) and the strain at which the steady-state (peak) is reached ϵ_{ss} . Similar conclusions can be found for mixes AS (40%) and BS (52%) and ES (85%). Figure 6.6 shows the variation of the loading stiffening factor S^l with volume fraction of aggregate. It can be seen that S^l increases with volume fraction, as observed by Deshpande and Cebon (2000). Conversely, figure 6.7 shows that ϵ_{ss} decreases approximately linearly with the volume fraction of aggregate. The volumetric strain behaviour of the mixes will be discussed in the following sections.

6.3.2 Creep recovery behaviour

Creep recovery tests were performed on the mixes at various temperatures and the recovery behaviour investigated for unloading from various total axial creep strains ϵ^T . The creep recovery response at 20°C for mix DS (75%) with $\sigma = 0.270$ MPa is shown in Fig. 6.8, with axial strain ϵ plotted as a function of time t , for two selected values of ϵ^T (see fig. 3.2a for definitions). In all tests on the mixes studied, the recovered strain ϵ^r was observed to increase with increasing ϵ^T , as for bitumen.

The results of all the uniaxial creep recovery tests performed on mix DS (75%) are summarised in Fig. 6.9, where the recovered strain ϵ^r is plotted as a function of the total strain ϵ^T just before unloading. The figure reveals that, to within experimental error,

$$\epsilon^r = \psi \epsilon^T + \epsilon^{el} , \quad (6.5)$$

with the slope of the line in Fig. 6.9 being independent of temperature for a given mix. Following the same notation adopted for bitumen, this slope will be called “recovery constant” ψ ($0 \leq \psi \leq 1$). This slope was found to be $\psi \approx 0.2$ for mix DS (75%). Contrary to the findings for bitumen, the recovery behaviour of the mixes was found to be dependent on the applied stress, hence the elastic strain ϵ^{el} comes into play

as $\epsilon^{el} = \sigma/E$, and the y-axis intercept in fig 6.9 is not zero. Figure 6.10 shows a reduction in the recovery constant ψ with increasing volume fraction of aggregate.

Following an analogous procedure to that applied to bitumen, the recovery strain versus time history can also be captured by a unique unloading calibration curve. The recovery strain-rate $\dot{\epsilon}^r$ is a maximum immediately after the removal of the stress and reduces to zero as the axial strain $\epsilon \rightarrow \epsilon^{pl}$. Thus, the recoverable strain can be characterised by the parameter $\hat{\epsilon}^r$ which is defined by

$$\hat{\epsilon}^r \equiv \left(\frac{\epsilon}{\epsilon^{pl}} - 1 \right) \frac{1 - \psi}{\psi}, \quad (6.6)$$

with $\hat{\epsilon}^r = 1$ at the instant of unloading and $\hat{\epsilon}^r = 0$ when the strain $\epsilon = \epsilon^{pl}$, ie. when the recoverable strain is zero. The recovery rate $\dot{\epsilon}^r$ at temperature T is described by a unique function $\dot{\epsilon}_{uc}(\hat{\epsilon}^r)$ such that

$$\dot{\epsilon}^r = -\dot{\epsilon}_u(\hat{\epsilon}^r), \quad (6.7)$$

where

$$\dot{\epsilon}_u(\hat{\epsilon}^r) = \dot{\epsilon}_{uc}(\hat{\epsilon}^r) e^{-k\left(\frac{1}{T} - \frac{1}{273}\right)}. \quad (6.8)$$

The recovery rate $\dot{\epsilon}^r$ is (i) a unique function of $\hat{\epsilon}^r$, (ii) independent of loading history, and (iii) scales with temperature according to the same Arrhenius relation that governs the loading temperature dependence. Figure 6.11 shows the recovery calibration curve $\dot{\epsilon}_u(\hat{\epsilon}^r)$ for mix DS (75%). Also in the same figure is plotted the recovery calibration curve found for the 50 pen bitumen used in the mixes. Note that the figures coincide apart from a scale factor. Analogous to the loading case, the scale factor, will be called *recovery stiffening factor* S^r . For the curves plotted in fig. 6.11, $S^r \approx 3000$. Figure 6.12 shows the variation of S^r with volume fraction of aggregate. Also shown in that figure is a re-plot of the data in fig. 6.6. It can be seen that S^l and S^r are equal within the bounds of experimental error.

The radial strains were also measured during the creep recovery tests. For the cylindrical specimens, the volumetric strain H is given by

$$H = 2\mathcal{E}_{11} + \mathcal{E}_{33}, \quad (6.9)$$

where \mathcal{E}_{11} and \mathcal{E}_{33} are the radial and axial strains, respectively. The distortional or Von Mises effective strain \mathcal{E}_e is given by

$$\mathcal{E}_e = \mathcal{E}_{33} - \frac{H}{3} = \frac{2}{3}(\mathcal{E}_{33} - \mathcal{E}_{11}). \quad (6.10)$$

The relationship between distortional and volumetric strain for a selected recovery test on mix DS (75%) is shown in fig. 6.13. The behaviour is similar to that expected for soils (Taylor, 1948). There is an initial reduction in volumetric strain due to compaction of the specimen or lack of parallelism between top and bottom surfaces of the specimen. Then the volumetric strain increases in proportion to the distortional strain with slope s . That slope is called the dilation gradient, and is given approximately by

$$H = s|\mathcal{E}_e|. \quad (6.11)$$

After removal of the load there is a small amount of hysteresis, after which the strains recover with the same slope s as the loading path. Table 6.3 shows the dilation gradient measured for the different mixes. Note that the fully dense mixes CS (64%), DS (75%) and ES (85%) show $s > 0$ while mixes AS (40%) and BS (52%) show $s \approx 0$, in line with the observations of Deshpande and Cebon (2000).

6.3.3 Continuous cyclic response

Stress-controlled, continuous cyclic tests were performed to investigate the effect of the mean stress σ_m , load ratio R , frequency f and temperature on the cyclic strain versus time response of the mixes.

The strain versus time response of mix DS (75%) with $R = 0.5$ at 20°C is shown in Fig. 6.14 for two selected values of the mean stress σ_m . The average cyclic stress-controlled response is seen to be similar in form to the monotonic creep response, with primary, secondary and tertiary regimes of behaviour. The “cyclic steady-state strain-rate” is defined as the mean gradient of the strain versus time history in the secondary regime of behaviour. Fig. 6.14 shows that this steady-state strain-rate increases with increasing mean stress σ_m for a fixed R .

Next, consider the influence of the load ratio R and loading frequency f on the cyclic stress controlled response. The strain versus time history of mix DS (75%) at 20°C with $\sigma_m = 0.245$ MPa and $f = 2.0$ Hz is shown in Fig. 6.15a for three selected values of R and in Fig. 6.15b with $\sigma_m = 0.245$ MPa and $R = 0.7$ for three selected frequencies f . These figures demonstrate that the load ratio³ R and frequency f have a negligible effect on the cyclic stress controlled strain versus time response of the mix, as found for bitumen. A series of similar experiments on the other mixes confirmed this result over the range of temperatures and stresses investigated here.

Given that the cyclic-stress-controlled behaviour of the mixes is governed largely by the mean stress, it is worth examining the relation between the *cyclic* steady-state strain rate and the *monotonic* steady-state creep strain-rate. The cyclic steady-state strain-rate from a series of tests on mix DS (75%) (with varying values of f and R) are also plotted in Fig. 6.4 as a function of the mean stress σ_m , alongside the monotonic steady-state data. It is clear that the cyclic steady-state behaviour follows the monotonic steady-state response, provided the creep stress σ_{ss} is interpreted as the cyclic mean stress σ_m . This is consistent with the results for bitumen described in chapter 3.

³Note that the different slopes on secondary creep regions in the results are due to experimental differences between the specimens and not to the applied values of R .

6.3.4 Results of pulse train tests

Cyclic stress controlled pulse tests were performed for a range of temperatures, pulse stresses σ_p and time period ratios Δ_p/Δ_g (see fig. 3.2c). Representative results for tests on mix DS (75%) at 20°C and 0°C are shown in Figs. 6.16a and 6.16b, respectively. Similar tests on mix CS (64%) at 20°C and 0°C are shown in Figs. 6.17a and 6.17b, and on mix ES (85%) at 20°C in Fig. 6.18a and mix EA (85%) at 20°C in Fig. 6.18b. The results show that for a fixed value of σ_p , the accumulated permanent strain decreases with decreasing Δ_p/Δ_g , because larger fractions of the creep strain are recovered in the zero-load gaps between the pulses. As $\Delta_g \rightarrow 0$, the pulse train tests converge to the continuous cyclic loading tests, with no recovery of the accumulated strain.

6.4 Uniaxial phenomenological model

A uniaxial phenomenological model for a given mix is proposed here. The model contains the key features of the phenomenological model proposed in section 3.5 for bitumen. The main difference is the inclusion of an elastic term which was ignored in the bitumen model. The model attempts to capture the monotonic, creep recovery, continuous cyclic and pulse loading behaviour described in the previous section. It is motivated by the following experimental observations:

1. The monotonic response is adequately described by the extended Cross model with the reference strain-rate $\dot{\epsilon}_{oc}$ a function of the strain ϵ .
2. The recovery response is captured by an unloading reference strain-rate $\dot{\epsilon}_{uc}$ which is a function of the recoverable strain as parametrised by $\tilde{\epsilon}^r$.
3. Elastic effects are considerable for the mixes.

4. The continuous cyclic response follows the monotonic response with the mean stress σ_m interpreted as the creep stress σ . This indicates that recovery is negligible in these continuous cyclic tests.
5. The loading and recovery temperature dependence of the mixes is governed by the temperature dependence of pure bitumen and therefore is adequately described by the Arrhenius relation over the range of temperatures, $0^\circ\text{C} \leq T \leq 20^\circ\text{C}$, investigated here.

The total strain-rate $\dot{\epsilon}$ is written as the sum of the viscous strain-rate $\dot{\epsilon}^v$, which is active during loading ($\sigma \neq 0$), the recovery strain-rate $\dot{\epsilon}^r$, which is only active when the stress $\sigma = 0$ and the elastic strain-rate $\dot{\epsilon}^{\text{el}}$ which is active when $|\dot{\sigma}| > 0$. Thus for an arbitrary loading history,

$$\dot{\epsilon} = \dot{\epsilon}^{\text{el}} + \dot{\epsilon}^v + \dot{\epsilon}^r. \quad (6.12)$$

The elastic response of the mix is given by

$$\dot{\epsilon}^{\text{el}} = \frac{\dot{\sigma}}{E}, \quad (6.13)$$

where E is the Young's modulus of the mix. The viscous response of the mix to an applied load is given by the implicit equation of the extended Cross model

$$\dot{\epsilon}^v = \frac{\dot{\epsilon}^{\text{pl}}}{1 - \psi} = \frac{\sigma \dot{\epsilon}_o(\epsilon)}{\sigma_o} \left[1 + \left(\frac{\dot{\epsilon}^v}{\dot{\epsilon}_o(\epsilon)} \right)^m \right], \quad (6.14)$$

where $\dot{\epsilon}^{\text{pl}}$ is the irrecoverable fraction of the viscous strain-rate and the recovery rate follows from the discussion in Section 6.3.2 as

$$\dot{\epsilon}^r = -\text{sign}(\epsilon) [1 - \text{sign}(|\sigma|)] \dot{\epsilon}_u(\dot{\epsilon}^r). \quad (6.15)$$

Here $\text{sign}(0)$ is defined to be zero and $-\text{sign}(\epsilon)$ ensures that the recovery rate $\dot{\epsilon}^r$ reduces the strain ϵ . Note that the calibration constants $\dot{\epsilon}_o(\epsilon)$ and $\dot{\epsilon}_u(\dot{\epsilon}^r)$ at the temperature T under consideration are given by (6.4) and (6.8), respectively with $\dot{\epsilon}_{oc}$ and $\dot{\epsilon}_{uc}$ the

reference strain-rates. It is worth mentioning here that the stiffening factors S^l and S^r are implicit in the values of the reference strain rates for a given mix (see fig. 6.11).

It is necessary to integrate equations (6.12)-(6.15) with respect to time to obtain the strain resulting from an applied stress history.

An approximate calibration of this model with four uniaxial compressive tests, following a similar procedure to that described for bitumen in section 3.5.3, can be found in Ossa et al. (2004).

Comparison with experimental results

In this section the predictions of the uniaxial phenomenological model are compared with the monotonic, recovery, continuous cyclic and pulse loading experimental results. Detailed comparisons are made for mix DS (75%) while for the sake of brevity, only comparisons for the more realistic pulse loading tests are shown for mixes CS (64%) and ES (85%).

Comparisons between model predictions and experimental data for monotonic constant strain-rate and constant stress creep tests are shown in Figs. 6.2 and 6.3, respectively with the dotted lines corresponding to model predictions. Good agreement is seen with both the constant strain-rate tests and the creep tests over the range of stresses, strain-rates and temperatures studied. Similarly, good agreement is seen between model predictions and the creep-recovery experimental results for mix DS (75%) at 20°C as shown in Fig. 6.8. It is worth emphasising here that the tests used to calibrate $\dot{\epsilon}_{oc}(\epsilon)$ and $\dot{\epsilon}_{uc}(\hat{\epsilon}^r)$ were different from those employed to demonstrate the accuracy of the model in Figs. 6.2, 6.3 and 6.8 : the model is, of-course, in perfect agreement with the calibration tests.

The model captures, to within reasonable accuracy, the continuous cyclic response

of mix DS (75%) as shown in Fig. 6.14.

A key judge of the accuracy of the model lies in its ability to predict the response of the mixes in the pulse loading tests: in these tests both the creep response under load and the recovery behaviour is combined in a complicated manner and the response of the model is integrated over many cycles, enabling modelling errors to build-up. Such comparisons for pulse loading tests on mix DS (75%) at 20°C and 0°C are shown in Fig. 6.16; in fig. 6.17 for mix CS (64%) 20°C and 0°C, and in fig. 6.18a for mix ES (85%) at 20°C. In all these cases the model accurately predicts the total accumulated strains to within reasonable accuracy. The accumulated strain is the relevant parameter in predicting the rutting response of a pavement.

6.5 Effects of particle shape

In order to develop a model to predict the deformation behaviour of any bituminous mix, it is necessary to understand the main effects caused by the components. An increase in volume fraction of aggregate increases the *stiffening effects* on the deformation behaviour and decreases the overall strain of the mix in both loading and recovery. Deshpande and Cebon (2000) found that particle size has no significant effect on the deformation behaviour of spherical and sub-spherical aggregate. Nevertheless, this conclusion cannot necessarily be extended to aggregate with angular particles.

As an initial investigation onto the influence of particle size and shape in the deformation behaviour of mixes, four different mixes were fabricated at a fixed volume fraction of 64% using sand of varying particle shapes and sizes. The specification for those mixes are given in table 6.2. Mixes CA1 and CA2 were made using angular sand with sizes close to those used as filler in asphalt mixes. Mixes CS3 and CS4 were made with sub-spherical sand as those discussed in previous sections. The specimen making

technique employed was the same described in section 6.2.2 for mixes CS, DS and ES. Table 6.4 summarises the main experimental results for these mixes. Note that the stiffening factors S^l and S^r , and the dilation gradient s increase for the angular sand mixes CA1 and CA2 compared with the sub-spherical sand mixes CS3 and CS4 (table 6.3). These considerable increases are due to the increased “interlock” of the sand particles due to the angularity, as well as a reduction in the volume fraction of voids in the mixes. The steady-state strain ϵ_{ss} is seen to decrease for the angular sand mixes.

In order to evaluate the effect of angularity on mixes with higher volume fraction of aggregate, a mix of 85% volume fraction was also studied. Mix EA was made using irregular (angular) stones (see Table 6.2). The stiffening factors for mix EA were lower than the corresponding stiffening factors for mix ES. This difference can be explained due to the increase in the void fraction of mix EA. The dilation gradient s of mix EA increases in comparison with mix ES, as for the sand mixes. The steady state strain ϵ_{ss} of mix EA is similar to the corresponding steady state strain for mix ES.

Surprisingly, the recovery constant ψ remains the same for all the mixes for a fixed volume fraction of aggregate, independent of the angularity of the aggregate.

Figure 6.18b shows the pulse loading behaviour of mix EA. It can be seen that the model described in section 6.4 captures the pulse loading behaviour of the mix reasonably well despite the angularity of the aggregate.

6.6 Concluding Remarks

1. The monotonic constant strain-rate and creep behaviour of bituminous mixes have been measured over a range of temperatures. The monotonic response under both these loading conditions was found to be adequately described by

an extended Cross model wherein the “viscosity” as parametrised by $\dot{\epsilon}_{oc}(\epsilon)$ is a function of strain.

2. The recoverable strain is proportional to the strain prior to unloading with the recovery rate being a unique function of the recoverable strain $\hat{\epsilon}^r$.
3. Both the loading and recovery responses were observed to be temperature dependent with the Arrhenius relation capturing the temperature dependence over the range of temperatures tested, $0^\circ\text{C} \leq T \leq 20^\circ\text{C}$.
4. Two types of cyclic loading tests were conducted, (i) continuous cyclic and (ii) pulse train tests, to simulate vehicle loading in a pavement. While the continuous cyclic response was similar to the monotonic response with only the mean stress governing the behaviour, significant strain recovery was observed during the rest periods in the pulse train experiments.
5. The elastic effects were found to play an important role in modelling the deformation behaviour of mixes, opposite to the results for bitumen.
6. The loading and recovery stiffening factors S^l and S^r have the same values for a given mix and increase with volume fraction of aggregate.
7. The mixes with fully dense aggregate packing ($\geq 64\%$ for spherical aggregate) dilate under uniaxial compressive loading. The volumetric strain varies linearly with distortional strain in both loading and recovery conditions with the same slope s .
8. The main effects of high angularity of the aggregate in the deformation behaviour of the mixes are, (i) an increase in the stiffening factors and dilation gradient and (ii) a reduction in the steady-state strain. However, the recovery constant was found to remain unchanged despite the angularity of the aggregate.

9. An extension to the phenomenological model for bitumen developed in section 3.5, was proposed for mixes. The model is seen to capture the monotonic, continuous cyclic and pulse loading response of the mixtures at different temperatures with reasonable accuracy.

6.7 Tables

Mix	Volume fraction of aggregate	Volume fraction of voids	Type of aggregate
Mix AS	40%	$\approx 3\%$	Subspherical sand particles between 1.18 and 2.36 mm in size
Mix BS	52%	$\approx 3\%$	Subspherical sand particles between 1.18 and 2.36 mm in size
Mix CS	64%	$\approx 4\%$	Subspherical sand particles between 300 and 600 μm in size
Mix DS	75%	$\approx 4\%$	(1) Subspherical sand particles between 300 and 600 μm in size (37.5 %) (2) Subspherical sand particles between 1.8 and 2.36 mm in size (37.5 %)
Mix ES	85%	$\approx 4\%$	(1) Subspherical sand particles between 150 and 300 μm in size (11 %) (2) Subspherical sand particles between 1.8 and 2.36 mm in size (18 %) (3) Rounded stones ~ 10 mm in diameter (56 %)

Table 6.1: Description of mixes studied.

Mix	Volume fraction of aggregate	Volume fraction of voids	Type of aggregate
Mix CA1	64%	$\approx 0.5\%$	Angular sand particles passing 75 μm sieve (filler)
Mix CA2	64%	$\approx 2\%$	Angular sand particles between 150 and 300 μm in size
Mix CS3	64%	$\approx 4\%$	Subspherical sand particles between 300 and 600 μm in size
Mix CS4	64%	$\approx 4\%$	Subspherical sand particles between 1.8 and 2.36 mm in size
Mix EA	85%	$\approx 9\%$	(1) Subspherical sand particles between 150 and 300 μm in size (11 %) (2) Subspherical sand particles between 1.8 and 2.36 mm in size (18 %) (3) Angular stones ~ 10 mm (56 %)

Table 6.2: Description of mixes studied for aggregate shape effects.

Mix	Dilation gradient s
Mix AS (40%)	≈ 0
Mix BS (52%)	≈ 0
Mix CS (64%)	0.7 - 0.9
Mix DS (75%)	0.6 - 0.75
Mix ES (85%)	0.35 - 0.55

Table 6.3: Dilation gradient for the mixes studied

Mix	S^l	S^r	ϵ_{ss}	s	ψ
Mix CA1	7000-30000	5000-10000	0.008-0.016	1.0-1.35	0.2-0.22
Mix CA2	2000-5500	1500-3000	0.012-0.017	1.15-1.45	0.2-0.23
Mix CS3	600-1800	800-1500	0.035-0.07	0.7-0.9	0.2-0.28
Mix CS4	800-2000	800-1700	0.03-0.07	0.7-0.95	0.2-0.25
Mix EA	13000-16000	11000-15000	0.019-0.021	0.8-1.0	0.15-0.17

Table 6.4: Experimental results for mixes studied for aggregate shape effects.

6.8 Figures

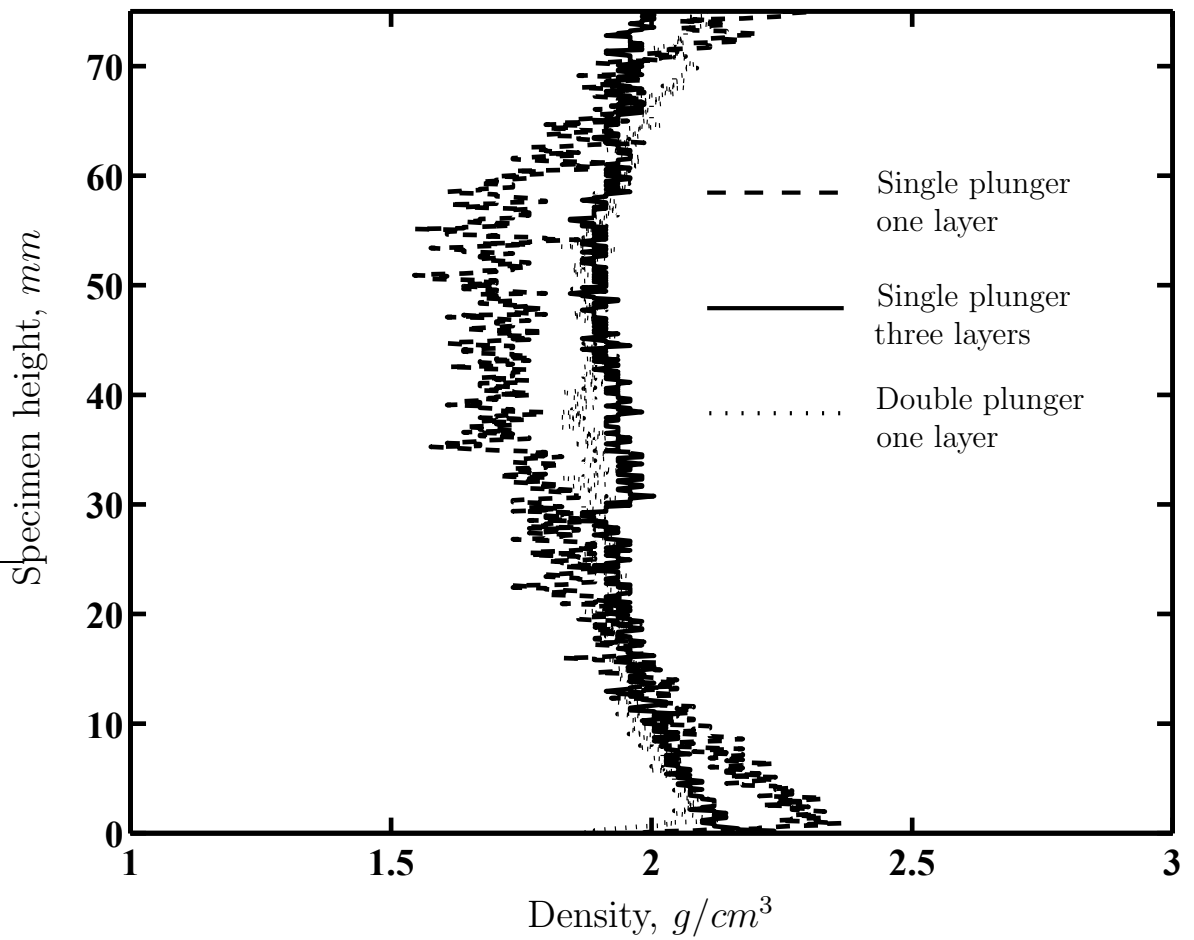


Figure 6.1: Density profiles for three different specimen making techniques studied on mix C (64%).

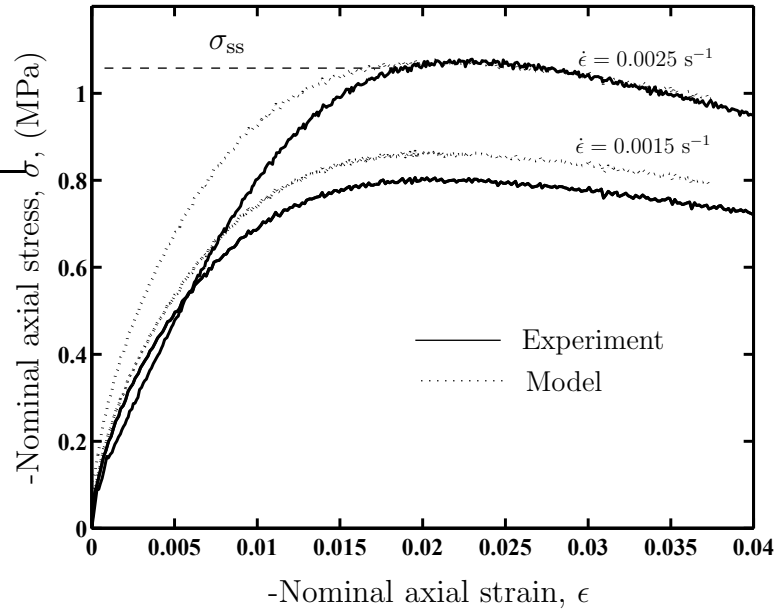


Figure 6.2: Constant strain-rate tests at two selected values of the applied strain-rate for mix DS (75%) at 20°C.

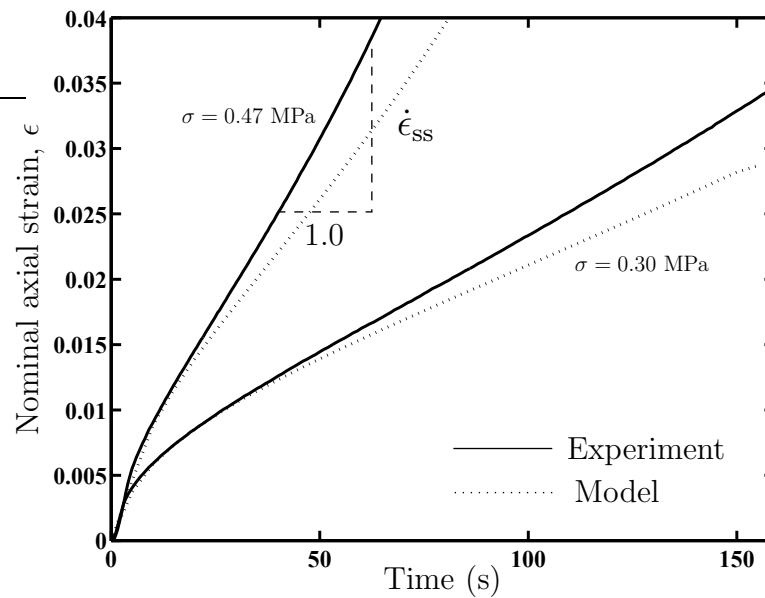


Figure 6.3: Constant stress creep tests at two selected creep stresses on mix DS (75%) at 20°C.

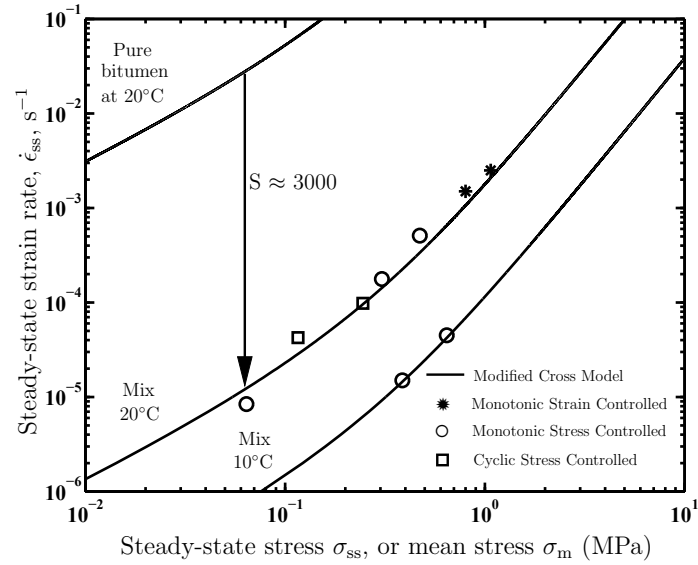


Figure 6.4: Monotonic and continuous cyclic steady-state behaviour at two different temperatures for mix DS (75%). Also shown is the steady-state response of pure bitumen

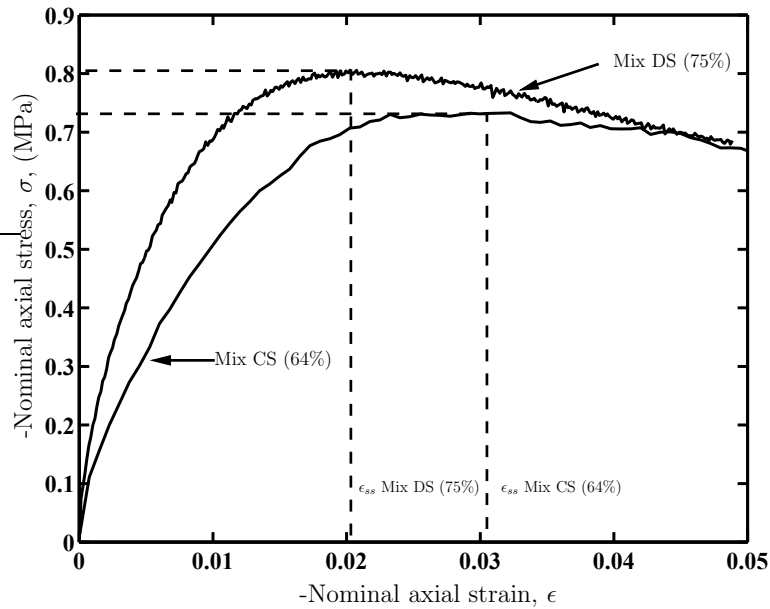


Figure 6.5: Constant strain rate tests for mixes CS (64%) and DS (75%) at 20°C and $0.0015s^{-1}$.

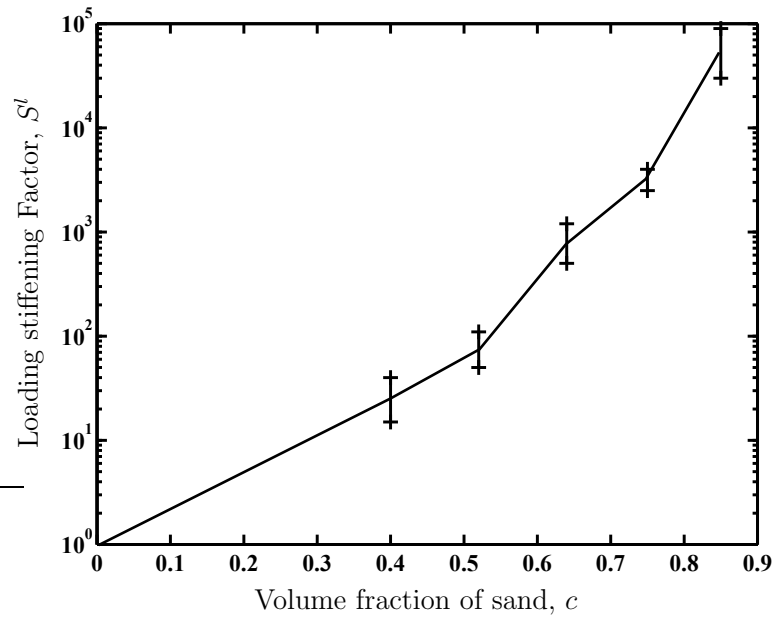


Figure 6.6: Variation of loading stiffening S^l factor with volume fraction of sand. The error bars show the experimental scatter of the results.

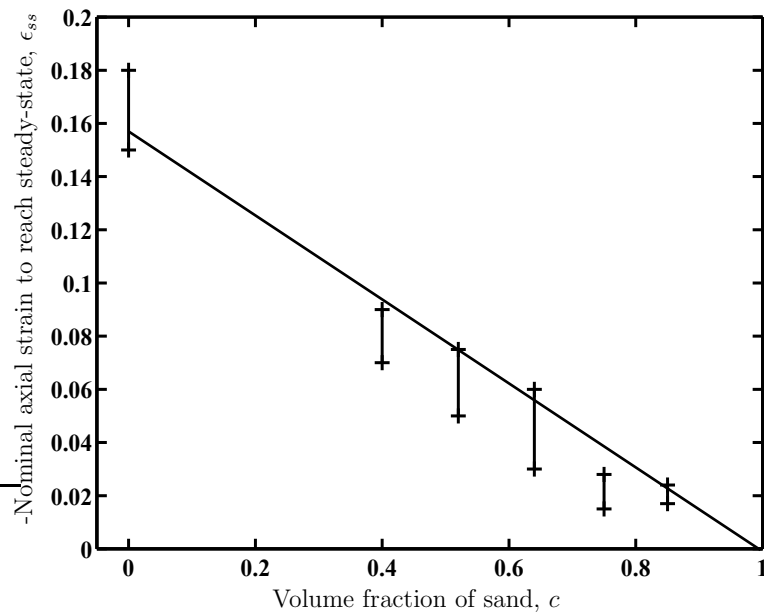


Figure 6.7: Variation of nominal axial strain to reach steady-state with volume fraction of sand. The error bars show the experimental scatter of the results.

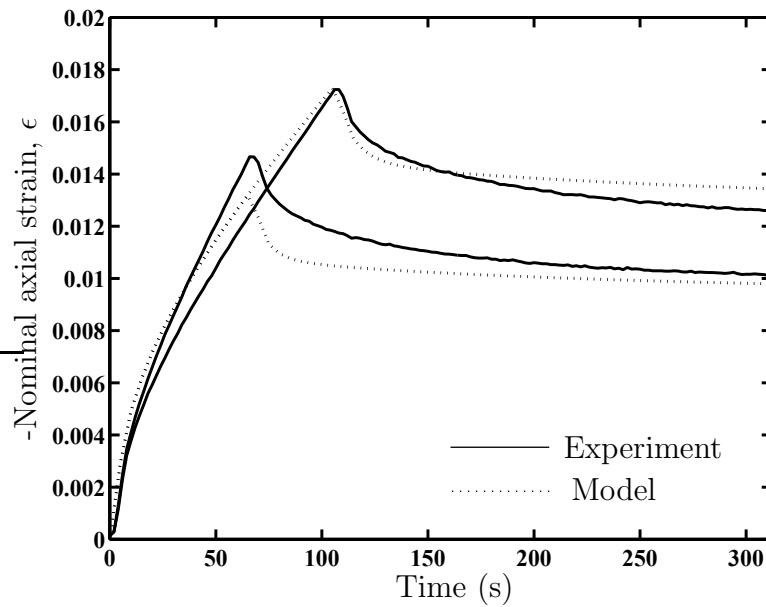


Figure 6.8: Creep recovery test results for mix DS (75%) at 20°C, $\sigma = 0.270 \text{ MPa}$.

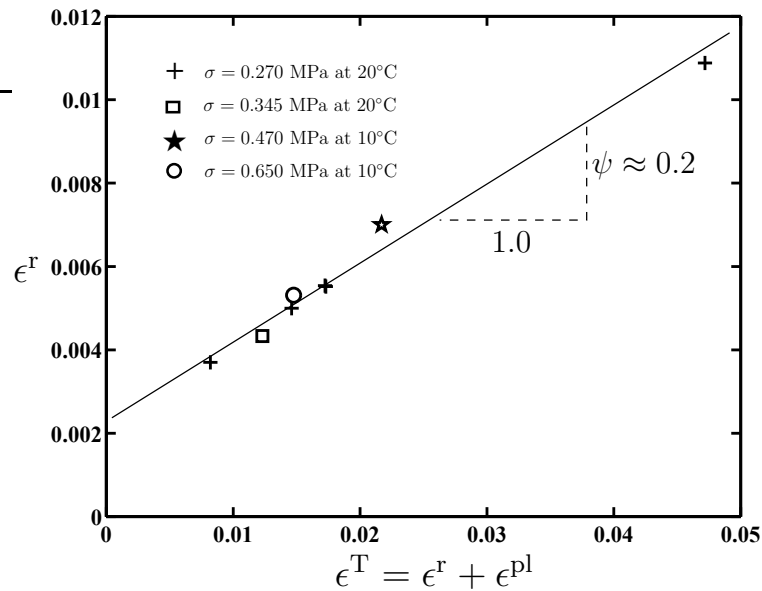


Figure 6.9: Summary of the creep recovery experimental results for mix DS (75%) showing a linear relationship between ϵ^r and ϵ^T .

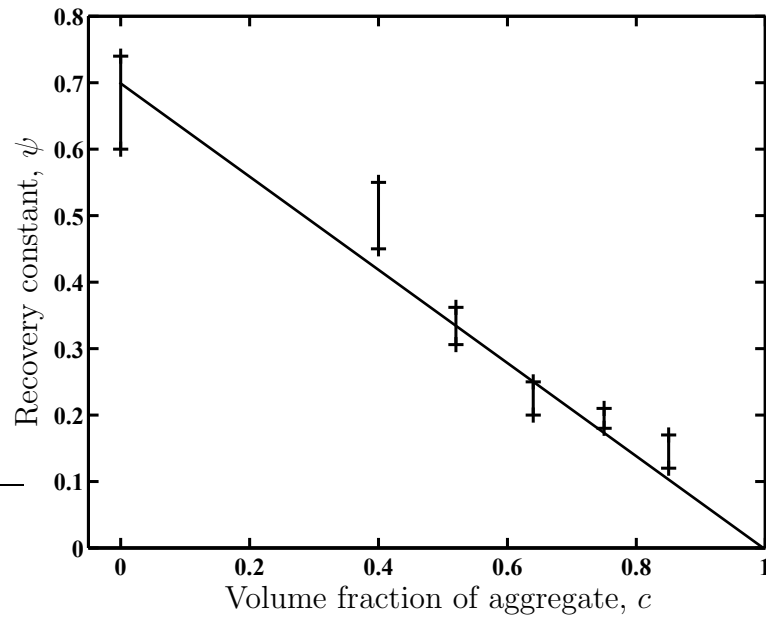


Figure 6.10: Variation of recovery constant with volume fraction of sand. The error bars show the experimental scatter of the results.

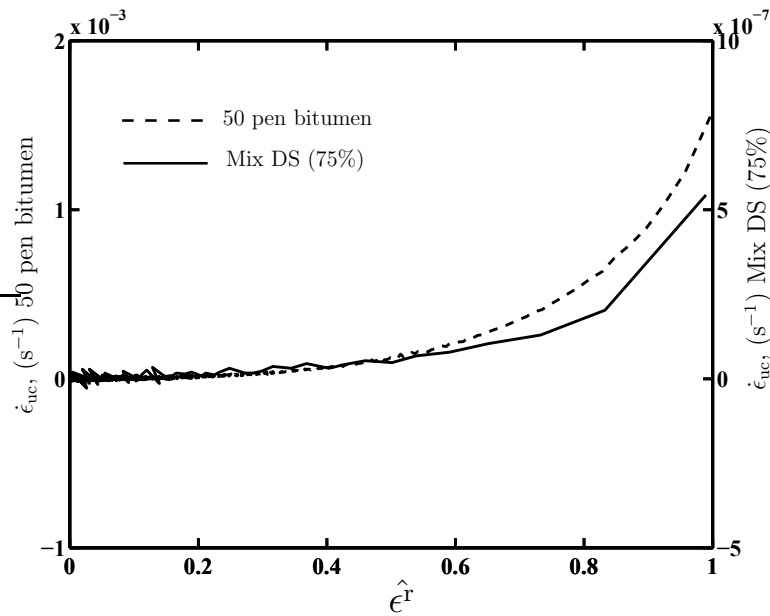


Figure 6.11: Recovery calibration curves $\dot{\epsilon}_{uc}(\hat{\epsilon}^r)$ for 50 pen bitumen and mix DS (75%).

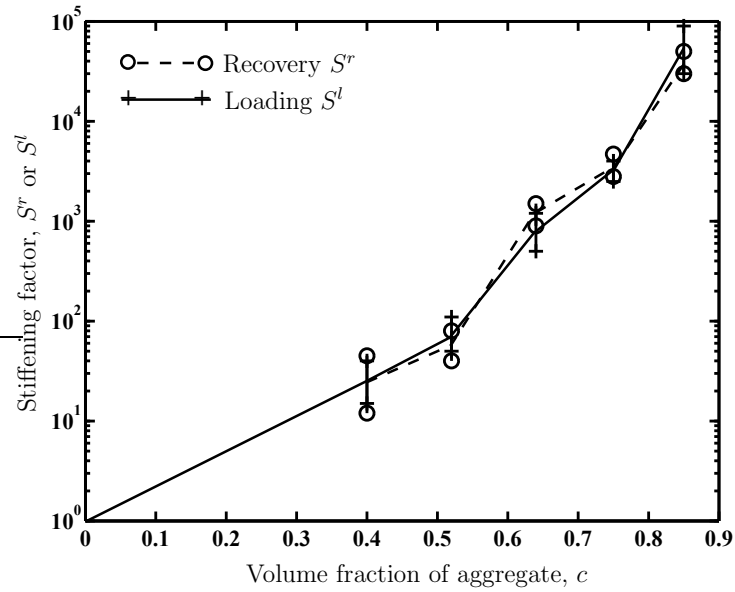


Figure 6.12: Variation of “recovery stiffening factor” with volume fraction of sand. The error bars show the experimental scatter of the results.

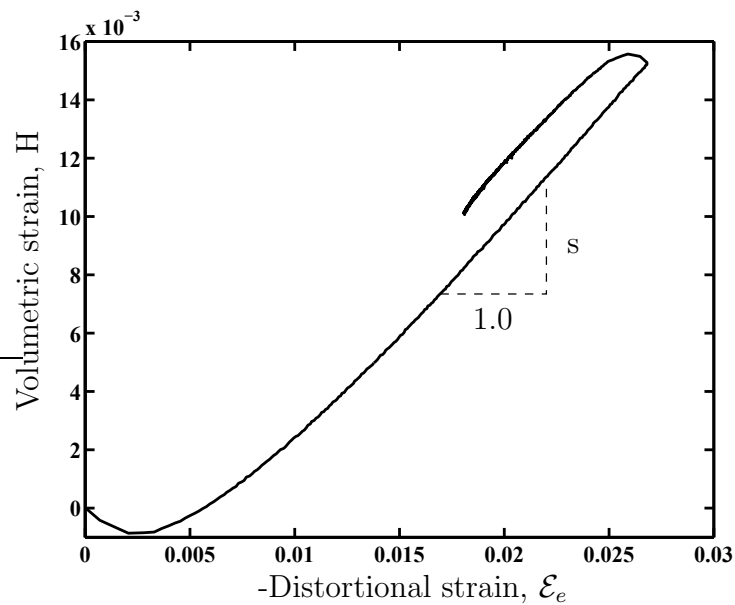


Figure 6.13: Variation of volumetric strain with distortional strain for mix DS (75%). Creep recovery test result, $\sigma = 0.470$ MPa at 10°C .

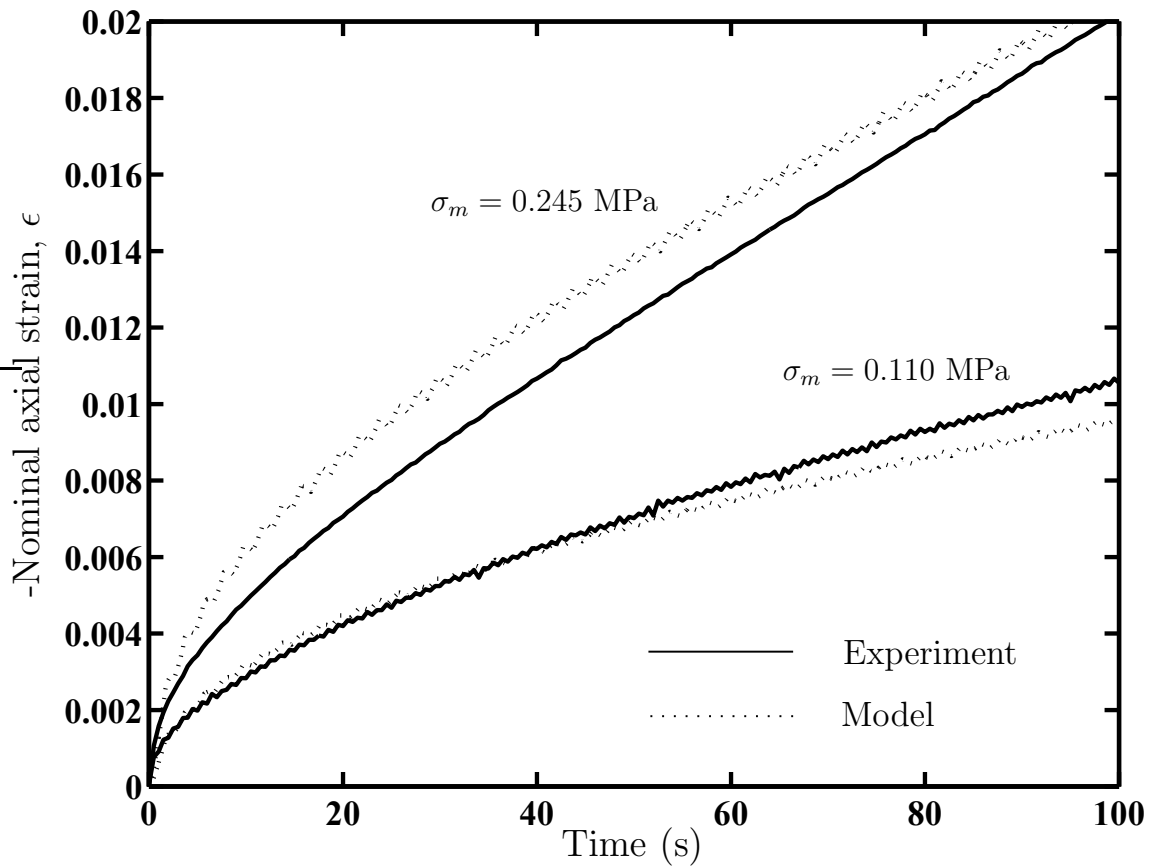


Figure 6.14: Continuous cyclic stress controlled tests for mix DS (75%) at 20°C, $f = 5\text{Hz}$ and $R = 0.5$.

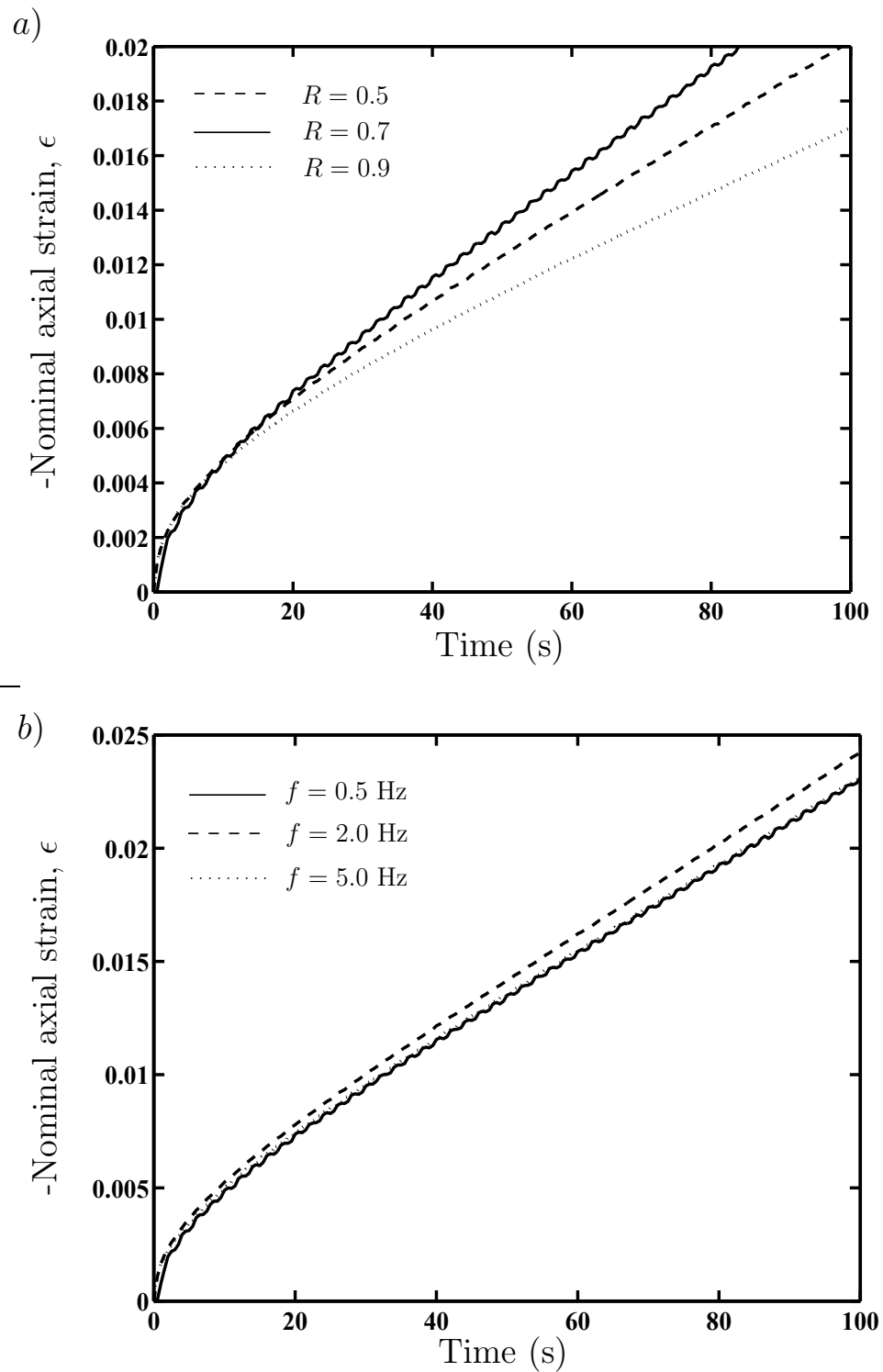


Figure 6.15: Continuous cyclic stress controlled tests at 20° C for mix DS (75%). (a) Results for three selected values of R with $\sigma_m = 0.245$ MPa and $f = 2.0$ Hz. (b) Results for three selected frequencies f with $\sigma_m = 0.245$ MPa and $R = 0.7$.

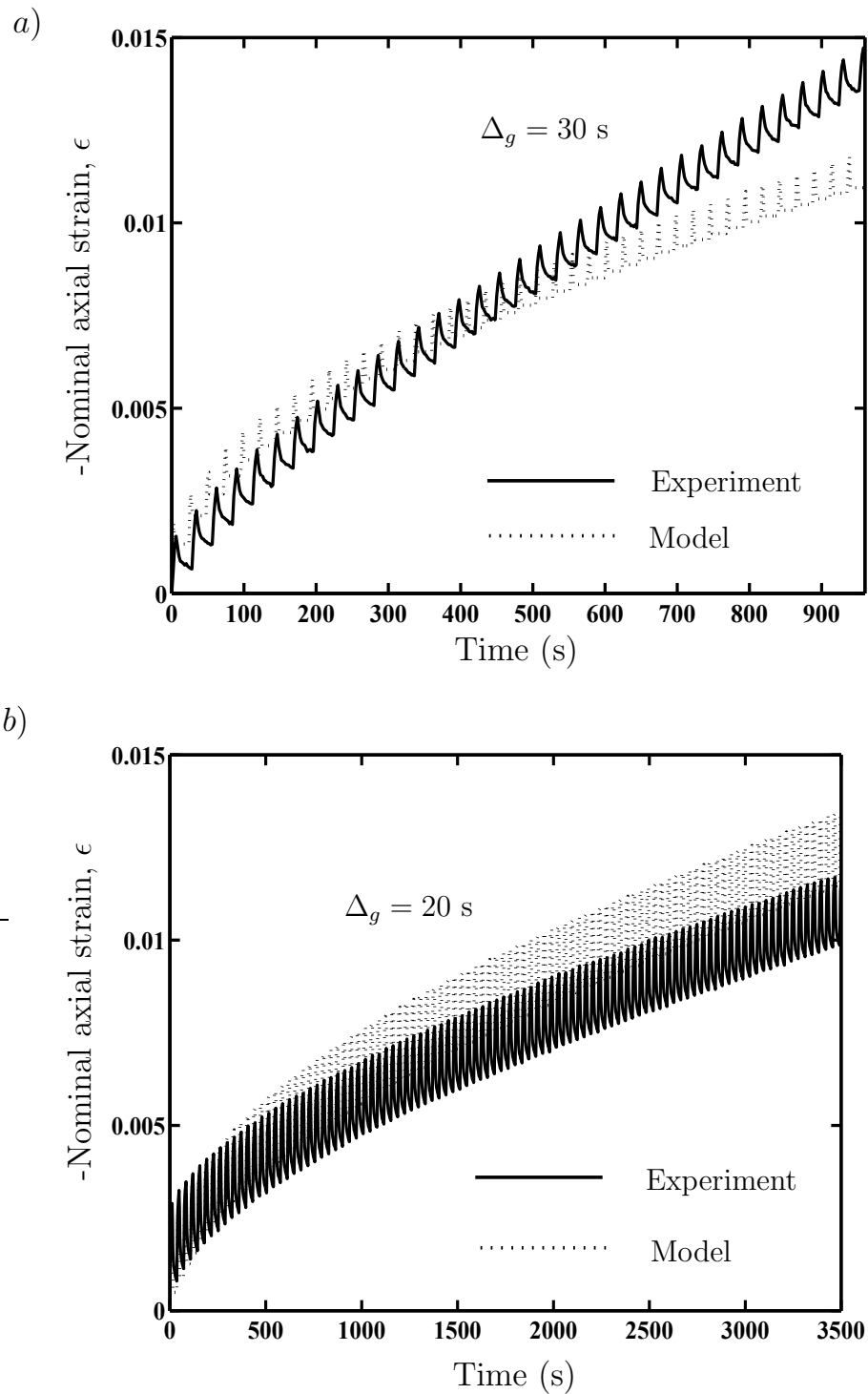


Figure 6.16: Pulse loading tests for mix DS (75%). (a) At 20°C , $\sigma_p = 0.13\text{MPa}$ and $\Delta_p = 4\text{s}$. (b) At 0°C , $\sigma_p = 1.3\text{MPa}$ and $\Delta_p = 16\text{s}$.

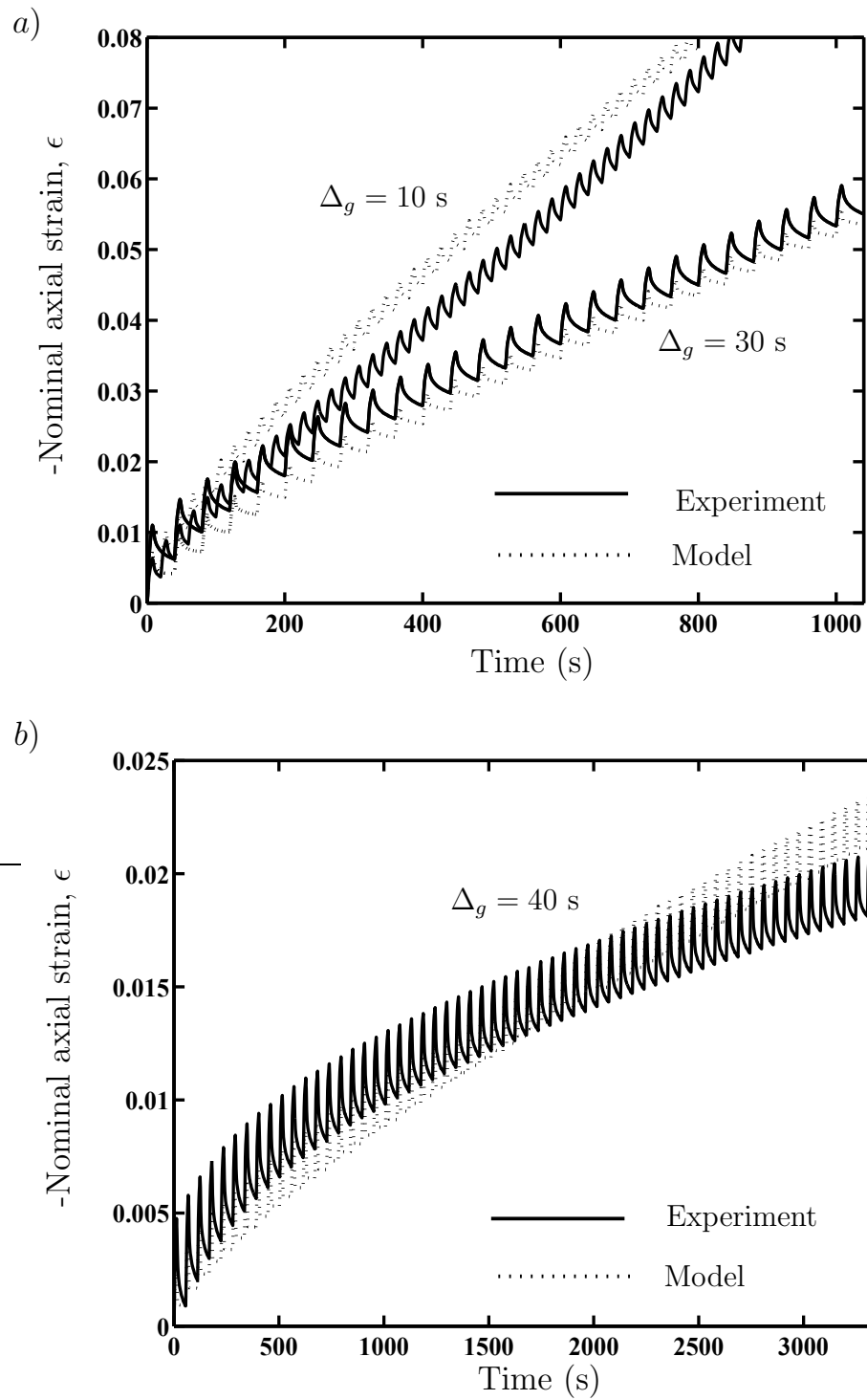


Figure 6.17: Pulse loading tests for mix CS (64%). (a) At 20°C, $\sigma_p = 0.3\text{MPa}$ and $\Delta_p = 10\text{s}$. (b) At 0°C, $\sigma_p = 1.3\text{MPa}$ and $\Delta_p = 16\text{s}$.

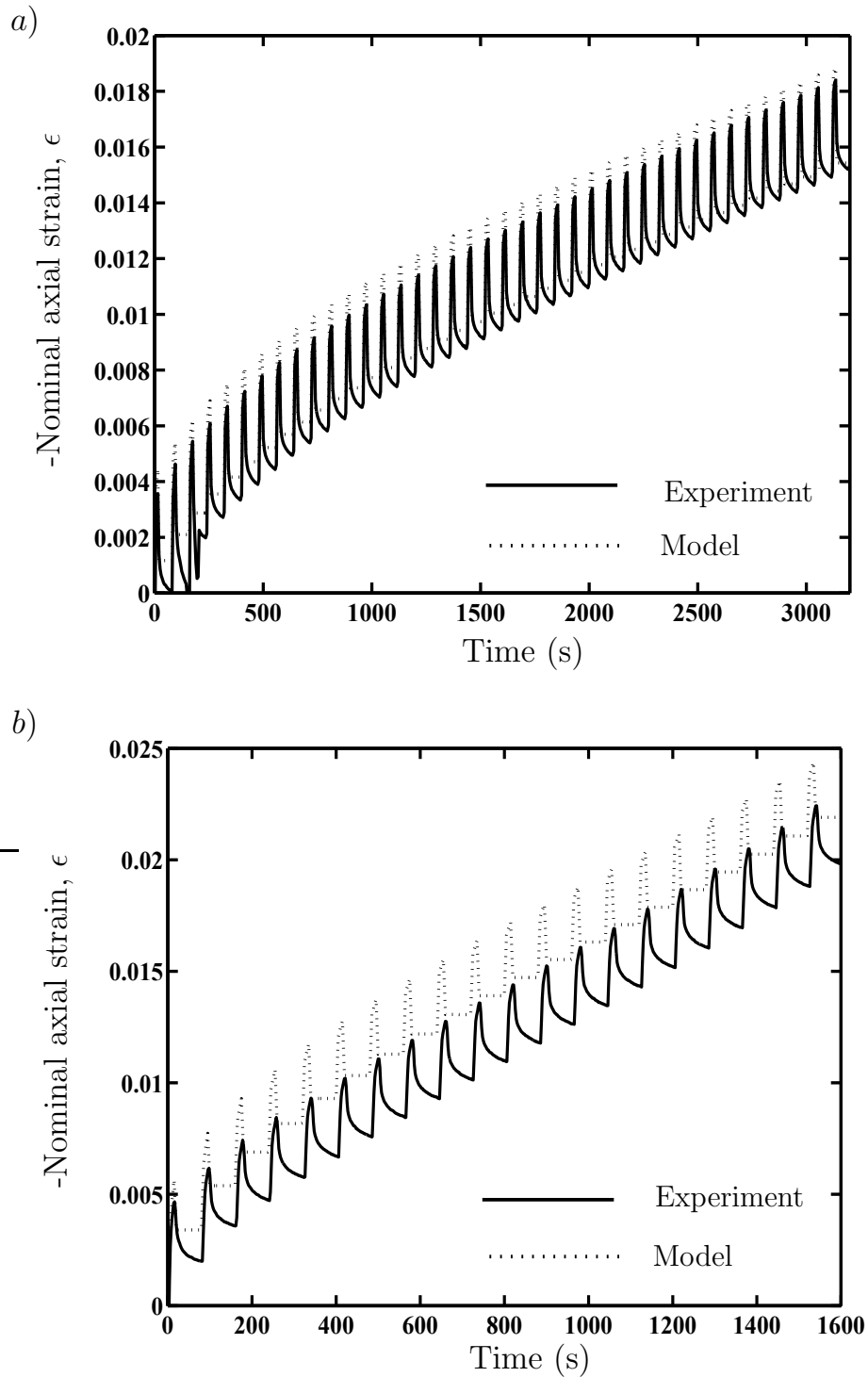


Figure 6.18: Pulse loading tests for mixes with 85% volume fraction of aggregate. (a) Mix ES at 20°C, $\sigma_p = 0.26\text{MPa}$, $\Delta_p = 20\text{s}$ and $\Delta_g = 60\text{s}$. (b) Mix EA at 20°C, $\sigma_p = 0.26\text{MPa}$, $\Delta_p = 20\text{s}$ and $\Delta_g = 60\text{s}$.

Chapter 7

Triaxial deformation behaviour of bituminous mixes

7.1 Introduction

The deformation behaviour of a pavement under a wheel load is highly dependent on the state of triaxial stresses in the asphalt on the upper layers. Hence asphalt need to be tested under various states of stresses (not only uniaxial). The majority of research on the deformation behaviour of asphalt has been done for uniaxial stress states (usually compressive), nevertheless triaxial testing has long been recognised as important to understand the behaviour more generally, as discussed in chapter 5.

Deshpande and Cebon (1999b) and Collop and Khanzada (2001) investigated the monotonic steady state behaviour of idealised bituminous mixes under triaxial conditions finding a strong dependence of the steady-state deformation behaviour of fully dense mixes (more than 64% volume fraction of aggregate) on the deviatoric and hydrostatic stresses.

In this chapter, tests on bituminous mixes under various deviatoric loading condi-

tions (monotonic, recovery, continuous cyclic and pulse train) and hydrostatic stresses are described. The effect of these conditions on the deformation behaviour of varying volume fraction of aggregate mixes will be studied. From these results, a simple constitutive model for mixes will be proposed. This constitutive model simplifies to the uniaxial phenomenological model proposed in chapter 6 under axisymmetric uniaxial conditions.

7.2 Experimental investigation

The main goal of this study was to understand the deformation behaviour of bituminous mixes under compressive monotonic and cyclic triaxial stress states. The micro-structure and behaviour of the low volume fraction dispersions of bitumen and sand are not representative of that of asphalt. Nevertheless in order to have a more broad understanding of the behaviour of different mixes under triaxial state of stresses, a 52% volume fraction sand mix was tested under monotonic triaxial conditions. A full set of triaxial tests was performed on 75% and 85% volume fraction of aggregate mixes. The specimens dimensions and preparation procedures were the same described in section 6.2.2.

Four types of mixes consisting of 50 pen bitumen and different volume fractions of aggregate, similar to those prepared and tested in the uniaxial study (chapter 6), were prepared and tested here. These are mixes BS, DS, ES and EA as listed in Tables 6.1 and 6.2. Mix BS was a low volume fraction dispersion, whereas mixes DS, ES and EA were fully dense mixes. While most of the experimental results are presented for mix DS (75%), the generality of the model developed is demonstrated via the pulse loading triaxial test results on mixes ES and EA (85%).

As the temperature dependence of mixes was found to be governed by the temperature dependence of bitumen (see chapter 6), all the triaxial tests were performed at

room temperature (20°C).

7.2.1 Description of apparatus

A standard axi-symmetric triaxial cell of the type commonly used in soil mechanics was used in the experimental investigation. It had a maximum allowable confining pressure of 1.5 MPa.

The fluid used in the triaxial cell was water and the pressure was applied by a pressure controller supplied by GDS Ltd. The axial load was applied by a standard hydraulic testing machine through a 10 kN submersible load cell. The submersible load cell measured the axial load applied to the specimen and was insensitive to the fluid pressure within the triaxial cell.

As in the uniaxial study, the axial and radial strains of the specimens were measured. The axial strain was measured from the load line displacement of the hydraulic actuator by means of an LVDT. The radial strains of mixes BS and DS were measured using a Hall effect radial transducer. The radial strains of specimens of mixes ES and EA (85% volume fraction) were not measured because the diameter of the specimens was too large for the available transducer.

A pressure transducer was fitted directly to the bottom of the triaxial cell in order to monitor the confining pressure applied to the specimen. The outputs of the radial transducer, LVDT, submersible load cell and pressure transducer were logged by a personal computer through an analogue to digital converter.

7.2.2 Testing procedure

Before testing, the radial strain transducer was attached to the specimens of mixes BS and DS. The specimen was placed between two platens whose surfaces were lubricated with a mixture of glycerine and natural soap to reduce friction and minimise

bulging. Following the same procedure as Deshpande (1997), the specimens were pressurised directly¹. This can be done because of the small void fractions of the asphalt specimens. After filling the triaxial cell with water, the pressure controller was set to maintain a certain hydrostatic pressure. Four different types of triaxial tests were performed on mixes DS (75%) and ES (85%): monotonic, recovery, continuous cyclic and pulse train tests. The procedure followed in these tests is briefly described in the next sections. It is worth mentioning here that a number of spot repeat tests confirmed the repeatability of the test results reported here. For the sake of brevity, these results are not presented here.

Monotonic triaxial tests

The triaxial monotonic test procedure followed is the same as that used by Deshpande (1997), nevertheless a brief description is given here.

After the target hydrostatic pressure was reached and stable, the axial load was applied “instantaneously” and maintained at that constant value. The axial load, axial displacement, radial strain and hydrostatic pressure was logged for the duration of the test. The axial load Q and the hydrostatic pressure P are related to the principal stresses (see fig. 7.1a) by:

$$\begin{aligned}\Sigma_{33} &= Q/A + P \\ \Sigma_{22} &= P \\ \Sigma_{11} &= P,\end{aligned}\tag{7.1}$$

where A is the nominal cross-sectional area of the specimen. Thus,

$$\Sigma_m = \Sigma_{kk}/3 = P + \frac{Q}{3A},\tag{7.2}$$

$$\Sigma = \Sigma_{33} - \Sigma_{11} = \frac{Q}{A},\tag{7.3}$$

¹Soil samples are tested with an impermeable rubber membrane covering the specimen.

are the mean stress and deviatoric stresses respectively. The tests were performed over a range of hydrostatic and deviatoric stresses. The stresses were applied such that for a particular constant stress ratio

$$\eta = \Sigma_m / \Sigma , \quad (7.4)$$

the deviatoric stress Σ was varied over approximately 2 orders of magnitude. The stress ratio η was varied from $\eta = 1/3$ (uniaxial) to $\eta = 1$ ($P = 2Q/3A$).

Triaxial creep recovery tests

The triaxial creep recovery behaviour of the mixes was investigated by performing a series of single load/unload tests, under hydrostatic pressure, as shown in Fig. 7.1b in an analogous way as for the uniaxial tests described in chapter 6. Once the specimen reached the target hydrostatic pressure, a compressive axial load Q was applied rapidly to the specimen and then held constant. The specimen was allowed to creep to a specified total nominal compressive axial strain \mathcal{E}_{33}^T . At this strain, the axial load Q was released (keeping the hydrostatic pressure P constant) and the compressive strain monitored until the axial strain rate was zero $\dot{\mathcal{E}}_{33} \approx 0$. The axial strain at this point

$$\mathcal{E}_{33}^{\text{pl}} = \mathcal{E}_{33}^T - \mathcal{E}_{33}^r \quad (7.5)$$

is the irrecoverable axial strain. Such tests were repeated for a series of axial strains \mathcal{E}_{33}^T , deviatoric stresses Σ and stress ratios η .

Continuous cyclic tests.

In the continuous cyclic triaxial tests, the axial load Q was varied between Q_{\min} and Q_{\max} , while the hydrostatic pressure P was maintained constant. The cyclic deviatoric stress was therefore varied between $\Sigma_{\min} = Q_{\min}/A$ and $\Sigma_{\max} = Q_{\max}/A$ as

shown schematically in Fig. 7.1c, with

$$R = \frac{\Sigma_{\min}}{\Sigma_{\max}}, \quad (7.6)$$

and

$$\Sigma_{\text{mean}} = \frac{\Sigma_{\min} + \Sigma_{\max}}{2}, \quad (7.7)$$

defining the load levels. The loading rate was governed by the frequency f of the triangular waveform. Therefore the stress ratio varied during the test such that:

$$\eta_{\min} = \frac{AP}{Q_{\min}} + \frac{1}{3}, \quad (7.8)$$

$$\eta_{\max} = \frac{AP}{Q_{\max}} + \frac{1}{3}, \quad (7.9)$$

the mean stress ratio is:

$$\eta_m = \frac{\eta_{\min} + \eta_{\max}}{2} = \frac{AP}{2} \left(\frac{1}{Q_{\min}} + \frac{1}{Q_{\max}} \right) + \frac{1}{3}, \quad (7.10)$$

The nominal compressive strain was measured as a function of time and tests repeated for a series of values of R , f , Σ_{mean} and hydrostatic pressures P .

Pulse train tests.

Tests comprising intermittent identical compressive axial stress pulses with a trapezoidal shape in the time domain, as shown in Fig. 7.1d, were performed in order to simulate a load history similar to that experienced in a pavement. The hydrostatic pressure was kept constant as in the other triaxial tests. The aim here was to investigate the relation between the single load/unload behaviour analysed via the triaxial monotonic and triaxial recovery tests, and the gradual ratcheting of strain due to the application of a continuous train of discrete stress pulses.

The constant maximum deviatoric stress Σ_p , due to the applied axial load Q_p , in each trapezoidal stress pulse was applied for a time period $\Delta_p/2$ with a loading and

unloading rate $\dot{\Sigma} = 4\Sigma_p/\Delta_p$ (Fig. 7.1d). The stress ratio of the test was defined as $\eta_p = \Sigma_m/\Sigma_p$. Tests were performed at various stress ratios and various time gaps Δ_g between consecutive trapezoidal pulses at a fixed Σ_p .

7.3 Experimental results

7.3.1 Monotonic behaviour

Figure 7.2 shows the monotonic creep triaxial response of mix DS (75%) for two selected deviatoric stresses with a stress ratio $\eta = 0.6$. The creep curves have a similar form to the uniaxial creep test results (see section 6.3.1), with primary, secondary and tertiary² regions. Following the same procedure as for uniaxial behaviour, the slope of the secondary creep region, is defined as the steady-state strain-rate $\dot{\epsilon}_{ss}$ at the prescribed deviatoric stress Σ and stress ratio η . The steady state strain rate $\dot{\epsilon}_{ss}$ can be seen to increase with the deviatoric stress Σ .

Figure 7.3 summarises the monotonic, triaxial, steady-state behaviour of mix DS (75%) over a range of deviatoric stresses Σ and stress ratios η on a log-log scale with axes of $\dot{\epsilon}_{ss}$ and Σ . Also plotted in fig. 7.3 is the steady state uniaxial behaviour of pure bitumen at the same temperature (see chapter 3). Since bitumen is a von Mises material (Cheung, 1995), this curve will be the same for all compressive axisymmetric stress states. It can be seen that mix curves at a constant stress ratio η , have the same shape as the curve for pure bitumen at the same temperature. The same behaviour was observed for idealised asphalt mixes by Deshpande (1997). Therefore, as for the uniaxial behaviour, the steady state triaxial behaviour can be represented by the

²Not shown in the figure.

Modified Cross Model (Deshpande and Cebon, 1999b):

$$\frac{\Sigma}{S^l \dot{\epsilon}_{ss}} = \frac{\sigma_o}{\dot{\epsilon}_o} \frac{1}{1 + \left(\frac{S^l \dot{\epsilon}_{ss}}{\dot{\epsilon}_o} \right)^m}, \quad (7.11)$$

with the loading stiffening factor S^l a function of the applied stress ratio η . From fig. 7.3 it can be seen that S^l increases with the stress ratio η : $S^l \approx 6000$ for $\eta = 0.6$ to $S^l \approx 44000$ for $\eta = 1$.

Figure 7.4 summarises the effect of the stress ratio η on the steady-state strain rate for the different mixes studied, with

$$\frac{\dot{\epsilon}_{\text{mix}}}{\dot{\epsilon}_{\text{bitumen}}} = \frac{1}{S^l}. \quad (7.12)$$

Note that for the fully dense mixes ($vf > 64\%$)³ the strain rate of the mix decreases with increasing stress ratio η , while for $vf < 64\%$ the mix strain rate is independent of the stress ratio η .

The radial strain was measured and used to determine the distortional or Von Mises effective strain

$$\mathcal{E}_e = \frac{2}{3}(\mathcal{E}_{33} - \mathcal{E}_{11}), \quad (7.13)$$

and the volumetric strain H . The relationship between these strains was observed to be linear and can be represented by :

$$H = s|\mathcal{E}_e|. \quad (7.14)$$

This behaviour is similar to the observations of Deshpande (1997) and to the results of uniaxial tests on the same mix (see 6.3.1), with the dilation factor s unchanged from uniaxial to triaxial experimental results (see Tables 6.3 and 6.4).

The strains to reach steady state in the monotonic triaxial tests were found to be the same as those measured in the uniaxial study. This indicates that they are

³64% vf mixes were not tested under triaxial conditions in this study, nonetheless this conclusion is valid from the work of Deshpande (1997), who tested similar mixes under triaxial stress conditions.

independent of the applied stress ratio η . This, and the fact that the stress ratio η affects only the loading stiffening factor S^l , enables the extension of the Modified Cross Model used for uniaxial behaviour of mixes to be used for triaxial conditions. In the triaxial case, S^l is assumed to be a function of the stress ratio η and the remaining parameters are unchanged. The model is then:

$$\frac{\Sigma}{S^l \dot{\epsilon}} = \frac{\sigma_o}{\dot{\epsilon}_o(\epsilon)} \frac{1}{1 + \left(\frac{S^l \dot{\epsilon}}{\dot{\epsilon}_o(\epsilon)} \right)^m}, \quad (7.15)$$

where

$$\dot{\epsilon}_o(\epsilon) = \dot{\epsilon}_{oc}(\epsilon) e^{-k \left(\frac{1}{T} - \frac{1}{273} \right)}, \quad (7.16)$$

with the Arrhenius constant k remaining unchanged from that of bitumen as for the uniaxial behaviour of mixes.

7.3.2 Creep recovery behaviour

Triaxial creep recovery tests were performed at various deviatoric stresses Σ and stress ratios η , and the recovery behaviour was investigated for unloading from various total creep axial strains \mathcal{E}_{33}^T . The creep recovery response for mix DS (75%) with $\eta = 1.0$ at two selected values of deviatoric stress Σ is shown in Fig. 7.5, with axial strain \mathcal{E}_{33} plotted as a function of time t , for two selected values of \mathcal{E}_{33}^T . The triaxial recovery behaviour is shown to be similar to the uniaxial recovery behaviour with the recovered strain \mathcal{E}_{33}^r increasing as \mathcal{E}_{33}^T is increased.

The results from all the triaxial creep recovery tests performed on mix DS (75%), including uniaxial results from chapter 6, are summarised in Fig. 7.6, where the recovered axial strain \mathcal{E}_{33}^r is plotted as a function of the total axial strain \mathcal{E}_{33}^T prior to unloading. The figure reveals that, to within experimental error, $\mathcal{E}_{33}^r = \psi \mathcal{E}_{33}^T + \mathcal{E}_{33}^{\text{el}}$ with the slope of the line being independent of the applied stress ratio η (from $\eta = \frac{1}{3}$ to $\eta = 1.0$). Following the same notation adopted for bitumen and uniaxial behaviour

of mixes, this slope will be called “recovery constant” ψ ($0 \leq \psi \leq 1$). This slope was found to be $\psi \approx 0.2$ for mix DS (75%).

Following the same procedure as for uniaxial behaviour, the recovery strain versus time history can be captured by a unique unloading calibration curve $\dot{\epsilon}_u(\hat{\mathcal{E}}_{33}^r)$. Figure 7.7 shows the recovery calibration curve $\dot{\epsilon}_u(\hat{\mathcal{E}}_{33}^r)$ for mix DS (75%) with $\eta = 0.6$. Also plotted in the same figure is the recovery calibration curve found for pure bitumen. Note that the two coincide apart from a constant scale factor. That scale factor, as for the uniaxial behaviour, will be called “recovery stiffening factor” S^r . For the curves plotted in fig. 7.7, $S^r \approx 6000$. The variation of S^r with stress ratio η was found to be similar to the variation found for S^l (see fig. 7.3).

The radial strains were also measured during the triaxial creep recovery tests and the volumetric strain was found to vary linearly with the distortional strain, as in the uniaxial case, with a slope s independent of: (i) the applied stress ratio η and (ii) the loading or recovery paths.

7.3.3 Continuous cyclic response

Continuous, triaxial, stress-controlled cyclic tests were performed to investigate the effect of the mean deviatoric stress Σ_{mean} , mean stress ratio η_m , deviatoric load ratio R and frequency f on the cyclic strain versus time response of the mixes.

In order to assess the accuracy of the pressure controller in the highly demanding continuous cyclic triaxial test, preliminary tests were performed under various loading conditions measuring the applied stress ratio η . The maximum deviation from the target confining pressure was found to be around 2%, which is considered satisfactory for this kind of tests.

The strain versus time response of mix DS (75%) with $R = 0.7$ is shown in Fig. 7.8 for two selected values of the mean deviatoric stress Σ_{mean} at $\eta_m = 0.6$ and $f = 0.5 \text{ Hz}$.

The triaxial cyclic stress-controlled response was seen to be similar in form to the monotonic triaxial creep response, with primary, secondary and tertiary⁴ regimes of behaviour. The triaxial cyclic steady-state strain-rate is defined as the mean gradient of the strain versus time history in the secondary regime of behaviour as for the uniaxial case. Fig. 7.8 shows that this steady-state strain-rate increases with increasing mean deviatoric stress Σ_{mean} for fixed R , f and η_m .

Next, consider the influence of the load ratio R and frequency f on the cyclic, triaxial, stress-controlled response, for a given stress ratio η_m . The strain versus time history of mix DS (75%) with $\Sigma_{\text{mean}} = 0.52$ MPa, $R = 0.7$ and $\eta_m = 0.6$ is shown in Fig. 7.9a for 3 selected values of f and in Fig. 7.9b with $\Sigma_{\text{mean}} = 0.18$ MPa, $f = 0.5$ Hz and $\eta_m = 0.6$ for two selected deviatoric stress ratios R . Both these figures demonstrate that the load ratio R and frequency f have a negligible effect on the cyclic triaxial stress-controlled strain versus time response of the mix, as observed for the uniaxial behaviour. A series of similar experiments at different mean stress ratios η_m were also performed. The relationship between the *triaxial cyclic* steady-state strain rate and the *triaxial monotonic* steady-state creep strain-rate for the different stress ratios is shown in fig. 7.3. A comparison between the triaxial cyclic and triaxial monotonic steady-state data reveals that the triaxial cyclic steady-state behaviour follows the triaxial monotonic steady-state response, with the deviatoric stress Σ replaced by the deviatoric cyclic mean stress Σ_{mean} , in line with the results for uniaxial behaviour. Furthermore, the mean stress ratio η_m shows the same loading stiffening factor S^l as for the monotonic triaxial steady state behaviour.

The radial strains were also measured for the continuous cyclic triaxial tests. The volumetric strains showed, once again, a linear variation with the distortional strain, keeping the same slope s as measured for the monotonic recovery tests discussed

⁴Not shown in the figure.

previously.

7.3.4 Pulse train triaxial behaviour

Triaxial, cyclic, stress-controlled pulse tests were performed for a range of deviatoric pulse stresses Σ_p , time period ratios Δ_p/Δ_g (see fig. 7.1d) and stress ratios η_p . Representative results for tests on mix DS (75%) at two selected values of applied stress ratio η_p with constant Δ_p/Δ_g and Σ_p are shown in fig. 7.10. The results show that for fixed values of Σ_p and Δ_p/Δ_g , the accumulated permanent strain decreases with increasing η_p , as expected due to the increase in stiffening factors S^l and S^r with increasing stress ratio η_p . It was also found (not shown) that as $\Delta_g \rightarrow 0$, the pulse train tests converged to the continuous cyclic loading tests, with no recovery of the accumulated strain, as for the uniaxial case (Ossa et al., 2004).

Figure 7.11 shows pulse test results for mixes ES and EA for the same values of applied η_p , Σ_p and Δ_p/Δ_g .

7.4 Phenomenological constitutive model

Based on the experimental observations, a phenomenological constitutive model for a given mix is proposed here. The model retains the key features of the model for uniaxial behaviour of mixes. The main differences with that model are the dependence of the loading and recovery stiffening factors on the applied stress ratio η , and inclusion of the effects of the dilation, the other parameters remaining unchanged.

The Von Mises effective strain-rate $\dot{\mathcal{E}}_e$ for an arbitrary loading history can be written as

$$\dot{\mathcal{E}}_e = \dot{\mathcal{E}}_e^{\text{el}} + \dot{\mathcal{E}}_e^{\text{v}} + \dot{\mathcal{E}}_e^{\text{r}}, \quad (7.17)$$

where the elastic response is given by

$$\dot{\mathcal{E}}_e^{\text{el}} = \sqrt{\frac{2}{3} \dot{\mathcal{E}}_{ij}^{\text{el}} \dot{\mathcal{E}}_{ij}^{\text{el}}}, \quad (7.18)$$

where

$$\dot{\mathcal{E}}_{ij}^{\text{el}} = \frac{1 + \nu}{E} \dot{\Sigma}_{ij} - \frac{\nu}{E} \dot{\Sigma}_{kk} \delta_{ij}. \quad (7.19)$$

Here E is the Young's modulus of the mix, ν is the Poisson ratio, and δ_{ij} is the Kronecker delta.

The viscous response is given by

$$\dot{\mathcal{E}}_e^{\text{v}} = \frac{\dot{\mathcal{E}}_e^{\text{pl}}}{(1 - \psi)} = \frac{\Sigma_e \dot{\epsilon}_o(\mathcal{E}_e)}{S \sigma_o} \left[1 + \left(\frac{S \dot{\mathcal{E}}_e^{\text{v}}}{\dot{\epsilon}_o(\mathcal{E}_e)} \right)^m \right], \quad (7.20)$$

where $\dot{\mathcal{E}}_e^{\text{pl}}$ is the irrecoverable fraction of the viscous effective strain-rate. The recovery effective strain rate is written as

$$\dot{\mathcal{E}}_e^{\text{r}} = -\text{sign}(\mathcal{E}_e) [1 - \text{sign}(|\Sigma|)] \frac{\dot{\epsilon}_u(\hat{\mathcal{E}}_e^{\text{r}})}{S}. \quad (7.21)$$

Here $\text{sign}(0)$ is defined to be zero and $-\text{sign}(\mathcal{E}_e)$ ensures that the recovery effective rate $\dot{\mathcal{E}}_e^{\text{r}}$ reduces the effective strain \mathcal{E}_e . The volumetric strain rate is given by

$$\dot{H} = s \dot{\mathcal{E}}_e. \quad (7.22)$$

It is necessary to integrate equations (7.17)-(7.22) with respect to time to obtain the strain resulting from an applied stress history.

The approximate calibration of the model for uniaxial behaviour of bituminous mixes of Ossa et al. (2004) can be easily extended to obtain the model parameters for the constitutive phenomenological model described. The reader is referred to the work of Ossa et al. (2004) for a complete description of this approximate calibration procedure.

7.5 Comparison with experimental results

In order to compare the predictions of the constitutive phenomenological model with the triaxial experiments described in previous sections, the constitutive model must be rewritten for axisymmetric stress states. The axial and radial strain rates are given by

$$\dot{\mathcal{E}}_{33} = \dot{\mathcal{E}}_{33}^{el} + \dot{\mathcal{E}}_{33}^v + \dot{\mathcal{E}}_{33}^r, \quad (7.23)$$

and

$$\dot{\mathcal{E}}_{11} = \dot{\mathcal{E}}_{22} = \left(\frac{2s \operatorname{sign}(\Sigma) - 3}{2s \operatorname{sign}(\Sigma) + 6} \right) \dot{\mathcal{E}}_{33}, \quad (7.24)$$

respectively, where the axial elastic component is written as

$$\dot{\mathcal{E}}_{33}^{el} = \frac{\dot{\Sigma}}{E}. \quad (7.25)$$

The axial viscous response is given by

$$\dot{\mathcal{E}}_{33}^v = \frac{\Sigma \dot{\mathcal{E}}_o(\mathcal{E}_e)}{S \sigma_o} \left\{ \frac{s \operatorname{sign}(\Sigma) + 3}{3} \right\} \left[1 + \left(\frac{S \dot{\mathcal{E}}_{33}^v}{\dot{\mathcal{E}}_o(\mathcal{E}_e)} \left\{ \frac{3}{s \operatorname{sign}(\Sigma) + 3} \right\} \right)^m \right], \quad (7.26)$$

and the axial recovery rate is given by

$$\dot{\mathcal{E}}_{33}^r = -\operatorname{sign}(\mathcal{E}_{33}) [1 - \operatorname{sign}(|\Sigma|)] \frac{\dot{\mathcal{E}}_u(\hat{\mathcal{E}}_e^r)}{S}. \quad (7.27)$$

where

$$\hat{\mathcal{E}}_{33}^r = \left(\frac{\mathcal{E}_{33}}{\mathcal{E}_{33}^{pl}} - 1 \right) \frac{1 - \psi}{\psi}. \quad (7.28)$$

Comparisons between model predictions and experimental results for triaxial, monotonic, constant-stress creep tests are shown in fig. 7.2, with the dotted lines corresponding to model predictions. Good agreement is seen between experimental results and model predictions within experimental error. The triaxial recovery results are also captured reasonably well by the model as shown in fig. 7.5. The model also captures, to within reasonable accuracy, the triaxial continuous cyclic response as shown in figs. 7.8 and 7.9.

A key judge of the accuracy of the model lies in its ability to predict the response of the mixes in the pulse loading tests: in these tests both the creep response under load and the recovery behaviour is combined in a complicated manner and the response of the model is integrated over many cycles, enabling modelling errors to build-up. Such comparisons for pulse loading tests on mix DS (75%) at two different stress ratios η_p are shown in fig. 7.10 and in fig. 7.11 for mixes ES and EA. The model is seen to accurately predict the total accumulated strains and the steady-state slope (see section 3.5.1) in all the cases. It is important to note that the model predicts the deformation behaviour of mixes to be independent of the aggregate size and shape. See section 6.5 for a discussion of the effect of aggregate size and shape on the deformation behaviour of mixes. The current simple model succeeds in capturing the total accumulated strain to within reasonable accuracy, which is the relevant parameter in predicting the rutting response of a pavement.

It is important to emphasize here that the differences seen between model predictions and experimental results are highly influenced by the experimental scatter, caused by differences in the specimens resulting from their fabrication. Fig. 7.12 shows the error between the “steady-state” slope, measured and predicted, in the pulse loading tests⁵ for all tests performed, including the results for pure and polymer-modified bitumens. Also plotted in the same figure as solid lines is the coefficient of variation of the experimental results derived from the steady-state monotonic tests, giving an indication of the experimental scatter. Note that the modelling error generally falls between the limits of two standard deviations error, indicating that experimental scatter is a reasonable explanation for the differences. Each experimental point is accompanied by a pair of numbers representing the time period ratio Δ_p/Δ_g and the test temperature T . No correlation can be observed between the modelling

⁵Pulse loading tests were not performed for mixes AS and BS, therefore the error in these mixes was measured on the steady-state part of the monotonic curves.

error and Δ_p/Δ_g , T or volume fraction of aggregate for either uniaxial or triaxial tests. This indicates that the accuracy of the model is independent of all these variables, i.e. it captures their effects without any systematic error. Further, the mean modelling error was found to be of approximately 14% (dashed line in fig. 7.12), which is considered between reasonable limits.

7.6 Discussion

A phenomenological constitutive model for bituminous mixes has been developed. The model is capable of predicting the response of a given mix for a variety of monotonic and cyclic triaxial loadings. Most models for the monotonic and cyclic behaviour of asphalt, such as those discussed in chapter 5, treat asphalt as either a linear or nonlinear viscoelastic or viscoplastic solid. By contrast with the simple constitutive model proposed here, an extensive set of experiments is needed to calibrate these models.

It has been discussed by some researchers that void content and its distribution has a significant effect on the deformation behaviour of the mix (see for instance Von Quintus et al. (1991), Krishnan and Rao (2000) and Krishnan and Rajagopal (2004)). In this study, the amount, distribution and evolution of voids on the mix were taken into account implicitly in the loading and recovery calibration curves, which include all the effects of air voids in the deformation. This holds true for a given volume fraction of aggregate and air voids.

The effect of aggregate angularity on the uniaxial deformation behaviour of bituminous mixes was discussed in section 6.5. It was found that the main effect of angularity was an increase of the dilation gradient s . The triaxial behaviour of the 85% volume fraction mix with angular aggregate (mix EA) was studied here. The effect of the confining pressure was seen to be the same as for the rounded aggregate

mixes, with the deformation rate of the mix decreasing with increasing stress ratio η for monotonic and cyclic triaxial conditions.

The constitutive model proposed does not take into account mechanisms like fracture of bitumen and coalescence and growth of voids in the mixes. These mechanisms are expected to be important when the mix is subjected to tensile stresses (Deshpande and Cebon, 1999b; Genin and Cebon, 2000). Therefore, the constitutive model should only be applied to bituminous mixes subjected to compressive stresses (as in all the experiments described).

7.7 Conclusions

1. The triaxial deformation behaviour of the fully dense mixes was found to be a function of the mean and the deviatoric stresses.
2. For a constant stress ratio η , the steady-state axial creep behaviour of the mixes has the same form as that of pure bitumen. The loading stiffening factor S^l is a function of the volume fraction of the aggregate and the stress ratio $\eta = \Sigma_m/\Sigma$, as observed by Deshpande and Cebon (1999b).
3. The triaxial monotonic response was found to be adequately described by a reference strain rate function of the applied strain $\dot{\epsilon}_o(\mathcal{E}_e)$ as for the uniaxial behaviour. This reference function is dependent on the applied stress ratio η .
4. The strain to reach steady state ϵ_{ss} was found to be unaffected by the level of confining pressure.
5. The recovery stiffening factor S^r was found to be a function of the volume fraction of aggregate and the stress ratio η . The effects of these variables on S^r were found to be the same as for the loading stiffening factor S^l . The recovery

constant ψ was found to be unaffected by the stress ratio η , and dependent only on the volume fraction of aggregate.

6. The recovery behaviour of the mixes under triaxial conditions can be described by a reference recovery strain rate which is a function of a parametrised strain $\dot{\epsilon}_u(\hat{\mathcal{E}}_e^r)$ as for the uniaxial case. This function scales with the function found for pure bitumen with the recovery stiffening factor S^r .
7. Two types of triaxial cyclic loading tests were conducted, (i) continuous cyclic and (ii) pulse train tests to simulate vehicle loading in a pavement. While the triaxial continuous cyclic response was similar to the monotonic response with the mean deviatoric stress and mean stress ratio η_m governing the behaviour, significant strain recovery was observed during the rest periods in the pulse train experiments, as also found for the uniaxial behaviour of mixes.
8. The mixes with a high volume fraction of aggregate dilate under triaxial compressive loading. The volumetric strain varies linearly with distortional strain in both loading and recovery conditions with the same slope s . The value of s is not affected by the applied stress ratio η or loading conditions (monotonic or cyclic).

7.8 Figures

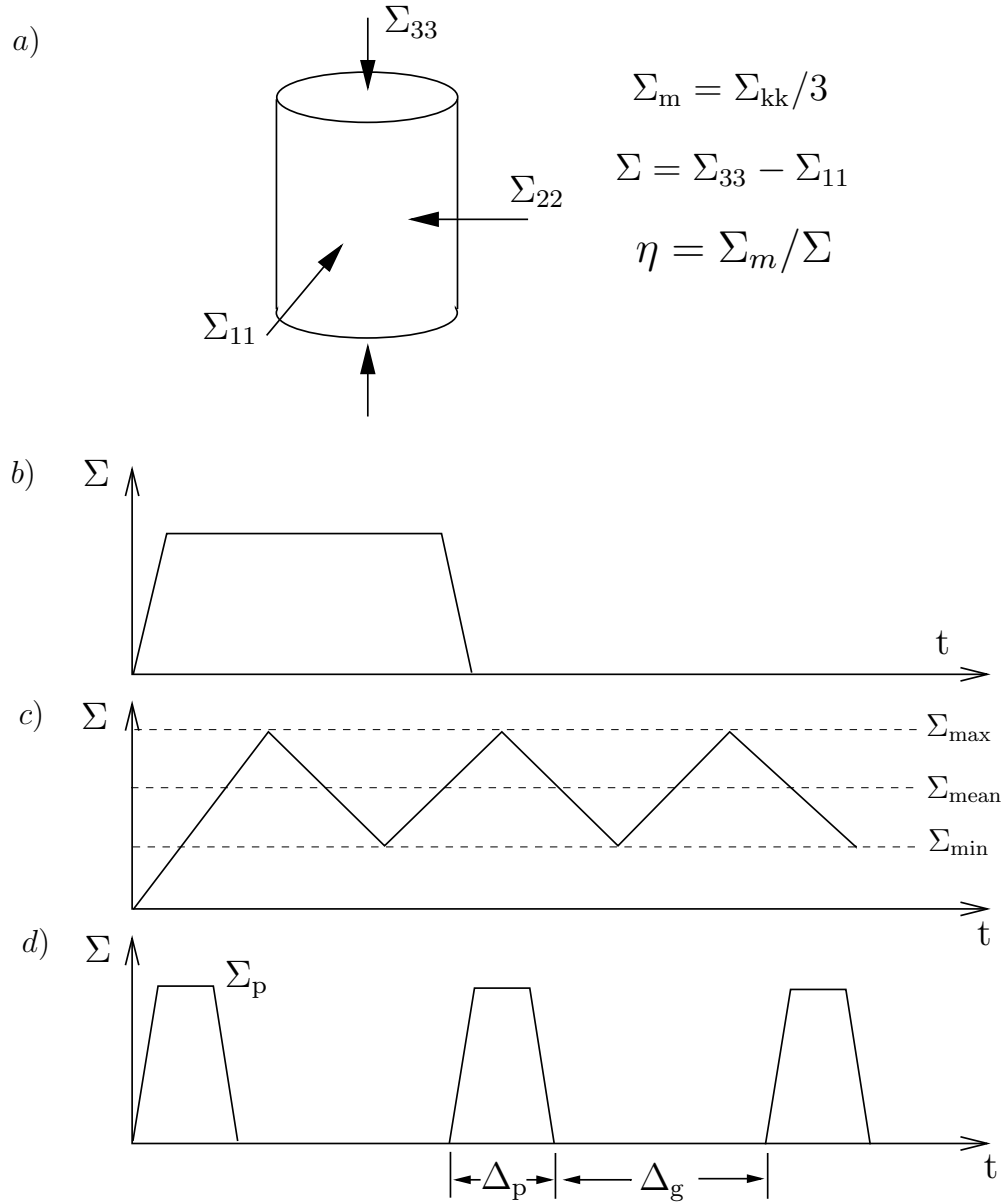


Figure 7.1: Schematic showing the triaxial test coordinate system and test sequences. (a) Stresses on the cylindrical specimen and definition of stress ratio η . (b) Recovery test. (c) Continuous cyclic test sequence. (d) Pulse train test sequence.

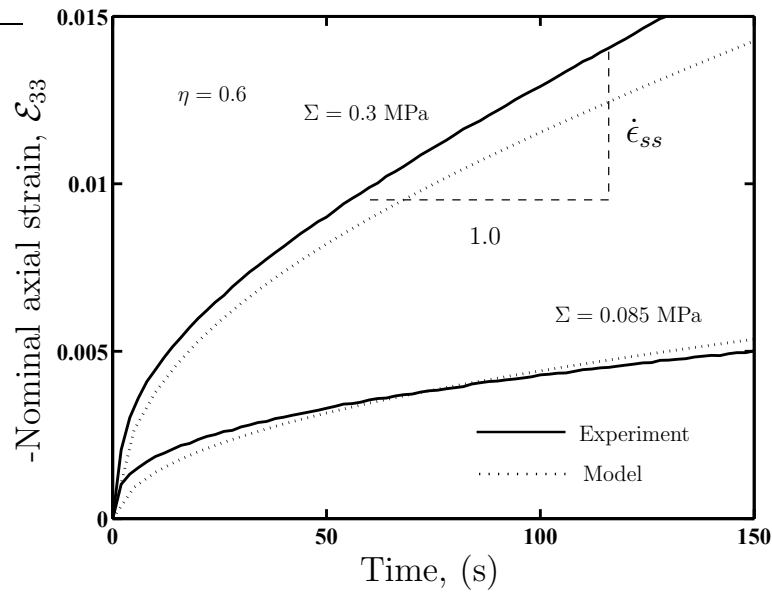


Figure 7.2: Monotonic constant stress creep triaxial tests on mix DS (75%) at two selected values of the applied deviatoric stress, at 20°C with the same stress ratio ($\eta = 0.6$) in both cases.

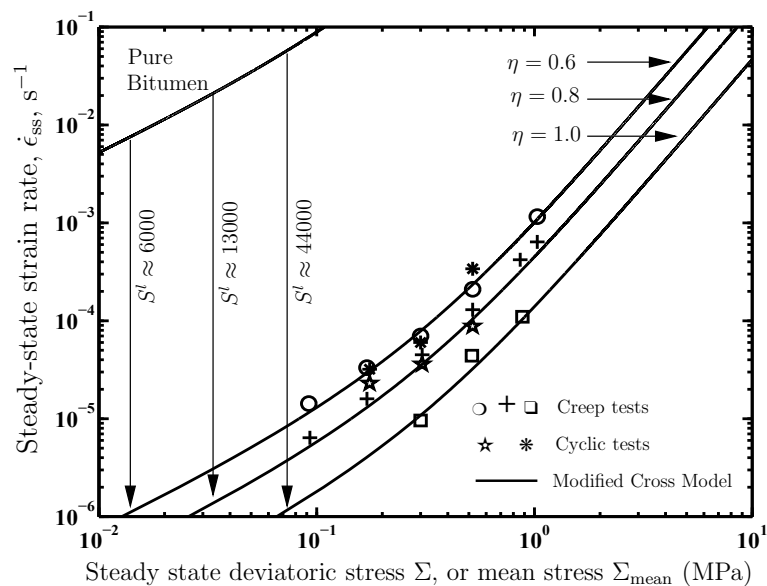


Figure 7.3: Triaxial steady state behaviour on mix DS (75%) at various stress ratios η for monotonic and continuous cyclic loading at 20°C.

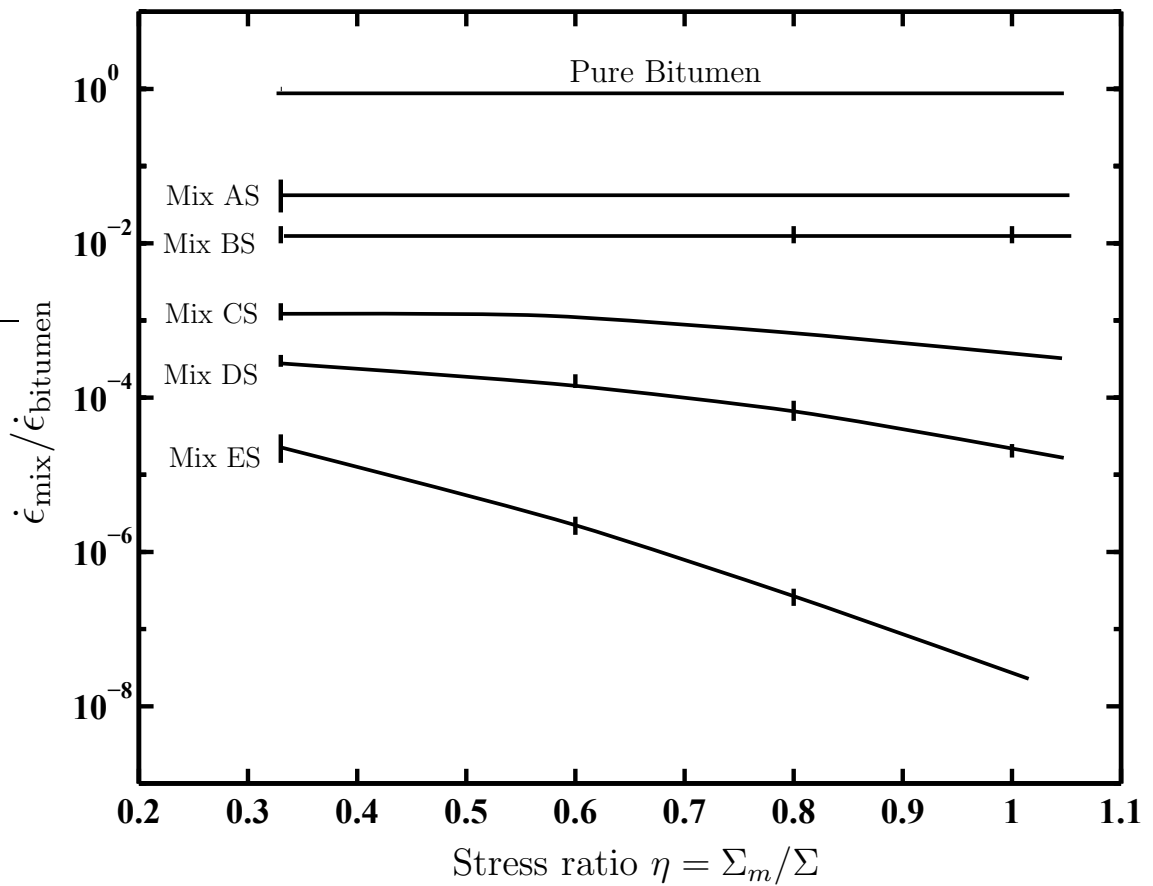


Figure 7.4: Effect of stress ratio on deformation behaviour of mixes with varying volume fractions of aggregate.

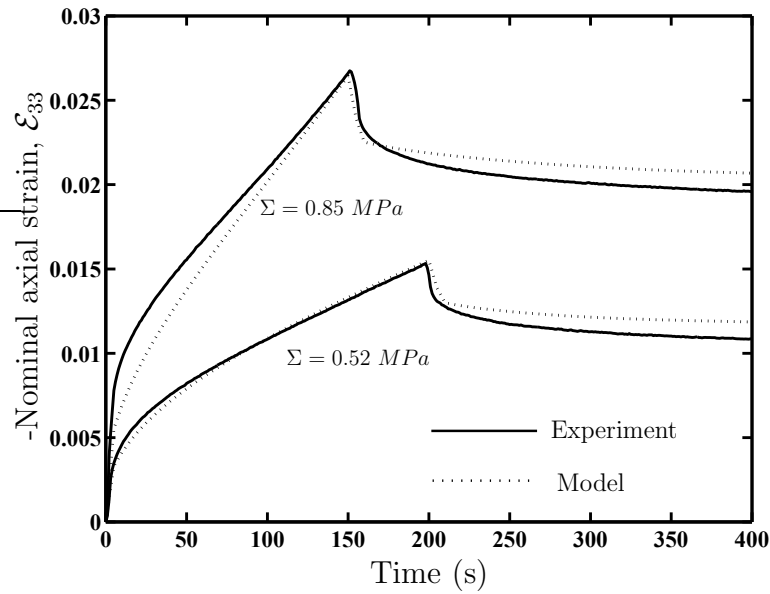


Figure 7.5: Creep recovery triaxial test results for mix DS (75%). Results for two selected values of Σ with $\eta = 1.0$ in both cases.

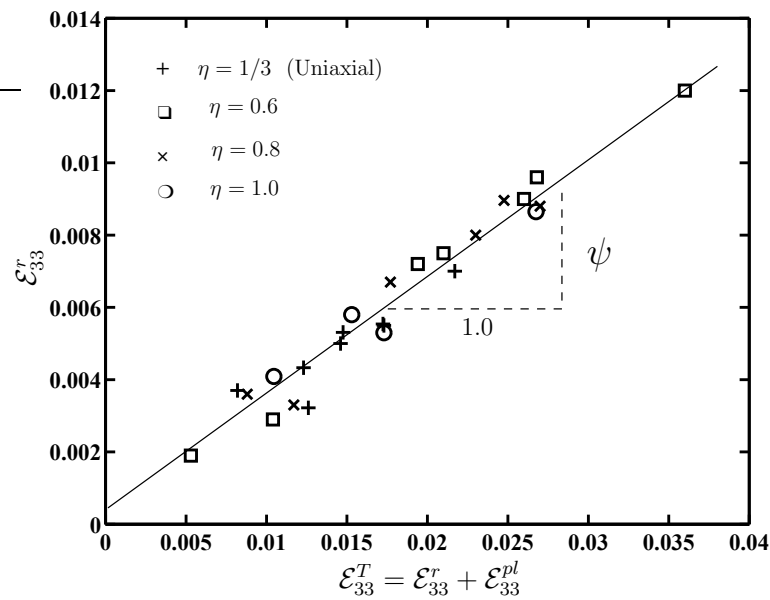


Figure 7.6: Summary of the creep recovery triaxial test results for mix DS (75%) at different stress ratios η .

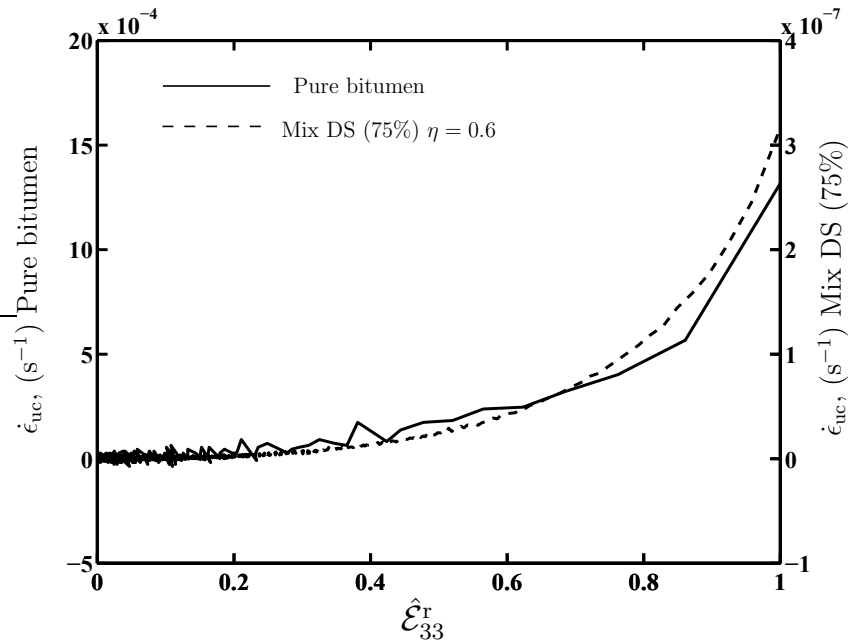


Figure 7.7: Recovery calibration curves $\dot{\epsilon}_{uc}(\hat{\mathcal{E}}_{33}^r)$ for pure bitumen and mix DS (75%) with $\eta = 0.6$.

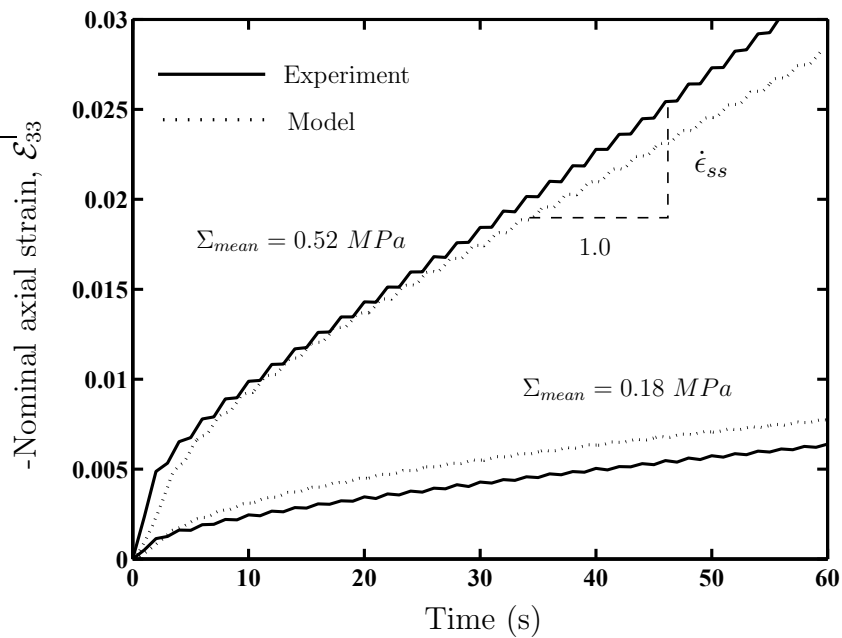


Figure 7.8: Continuous cyclic triaxial tests for mix DS (75%). Results for 2 selected values of Σ_{mean} , with $f = 0.5 \text{ Hz}$, $\eta_m \approx 0.6$ and $R = 0.7$.

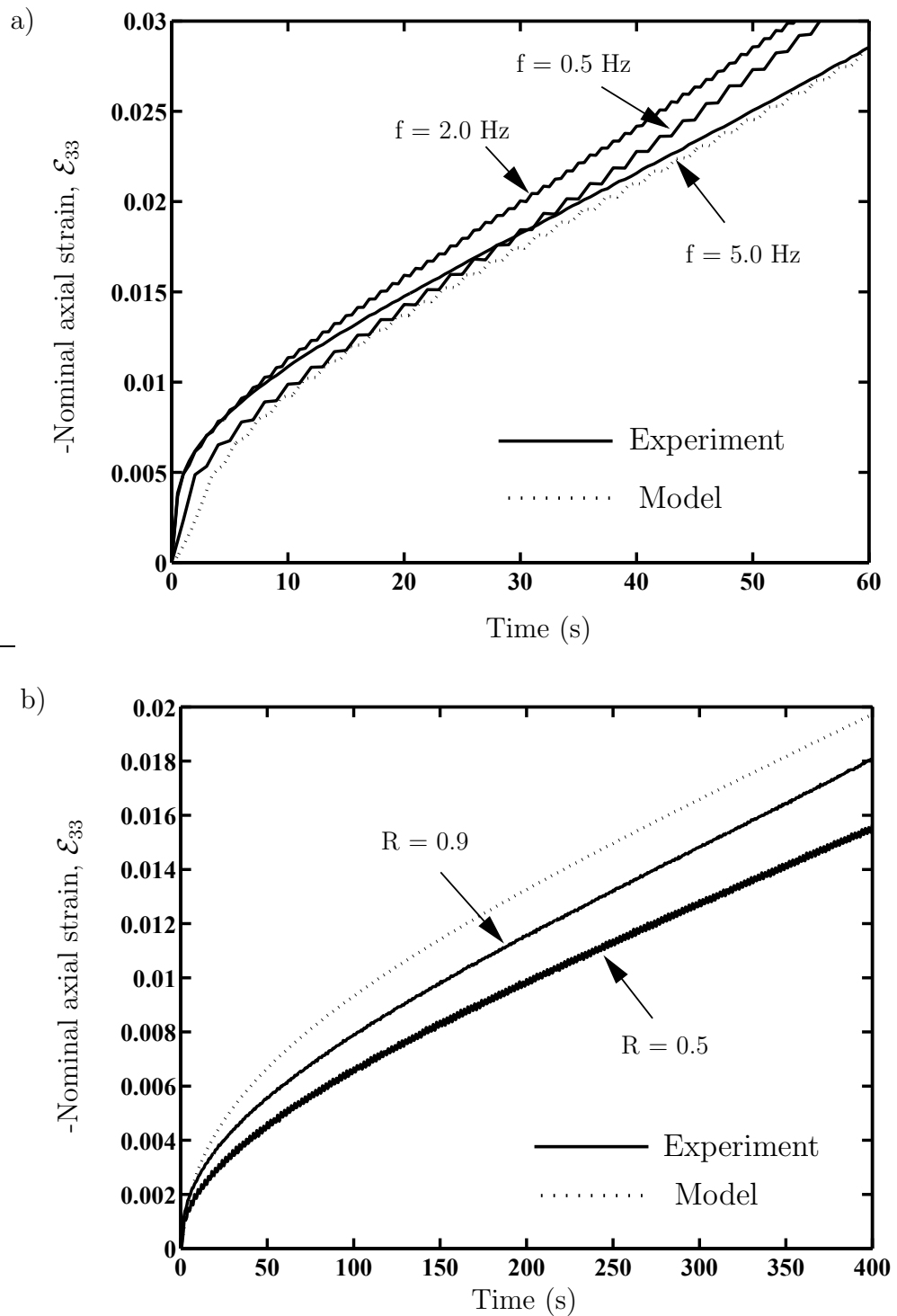


Figure 7.9: Continuous cyclic triaxial tests for mix DS (75%). (a) Results for three selected values of f with $\Sigma_{mean} = 0.52$ MPa, $\eta_m = 0.6$ and $R = 0.7$. (b) Results for three selected values of R with $\Sigma_{mean} = 0.18$ MPa, $\eta_m = 0.6$ and $f = 0.5$ Hz.

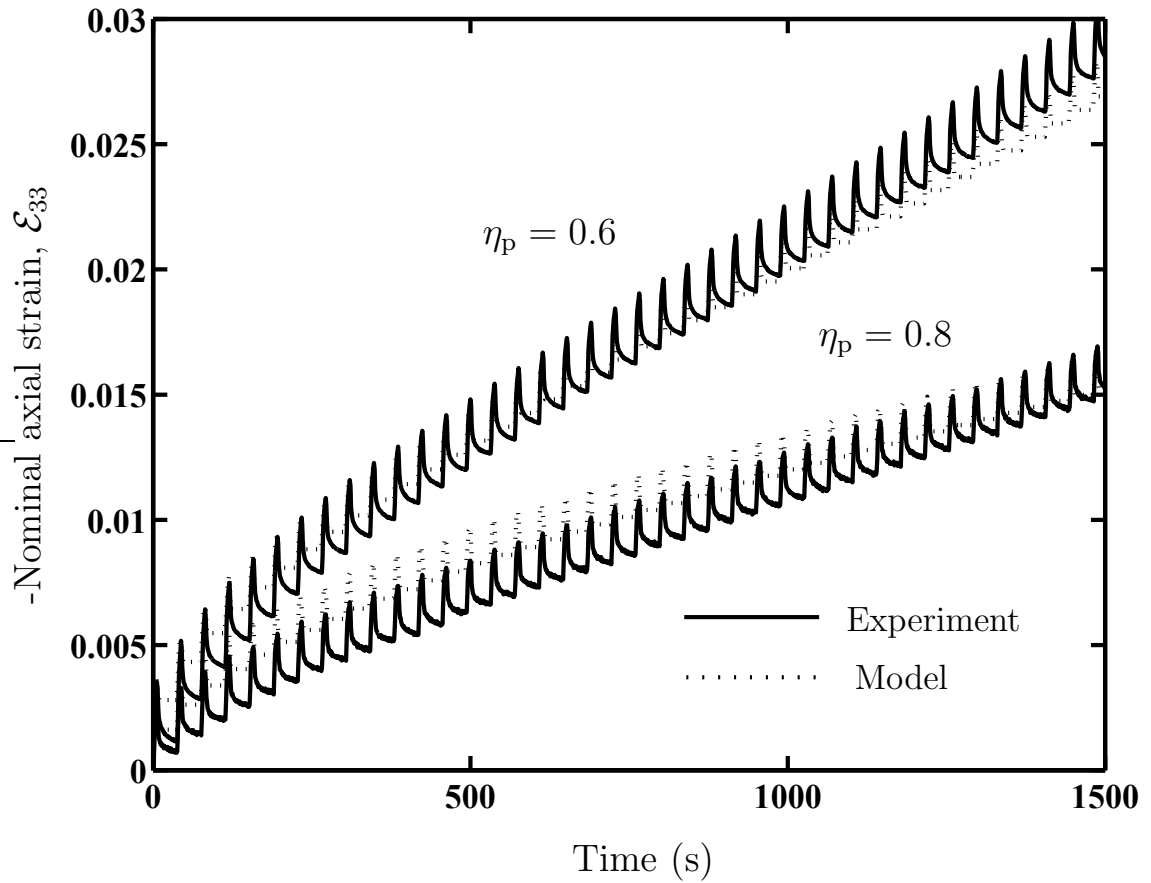


Figure 7.10: Triaxial pulse test results at 20° C for mix DS (75%) with $\Sigma_p = 0.3 \text{ MPa}$, $\Delta_p = 8 \text{ s}$, $\Delta_g = 30 \text{ s}$ at two different stress ratios η_p .

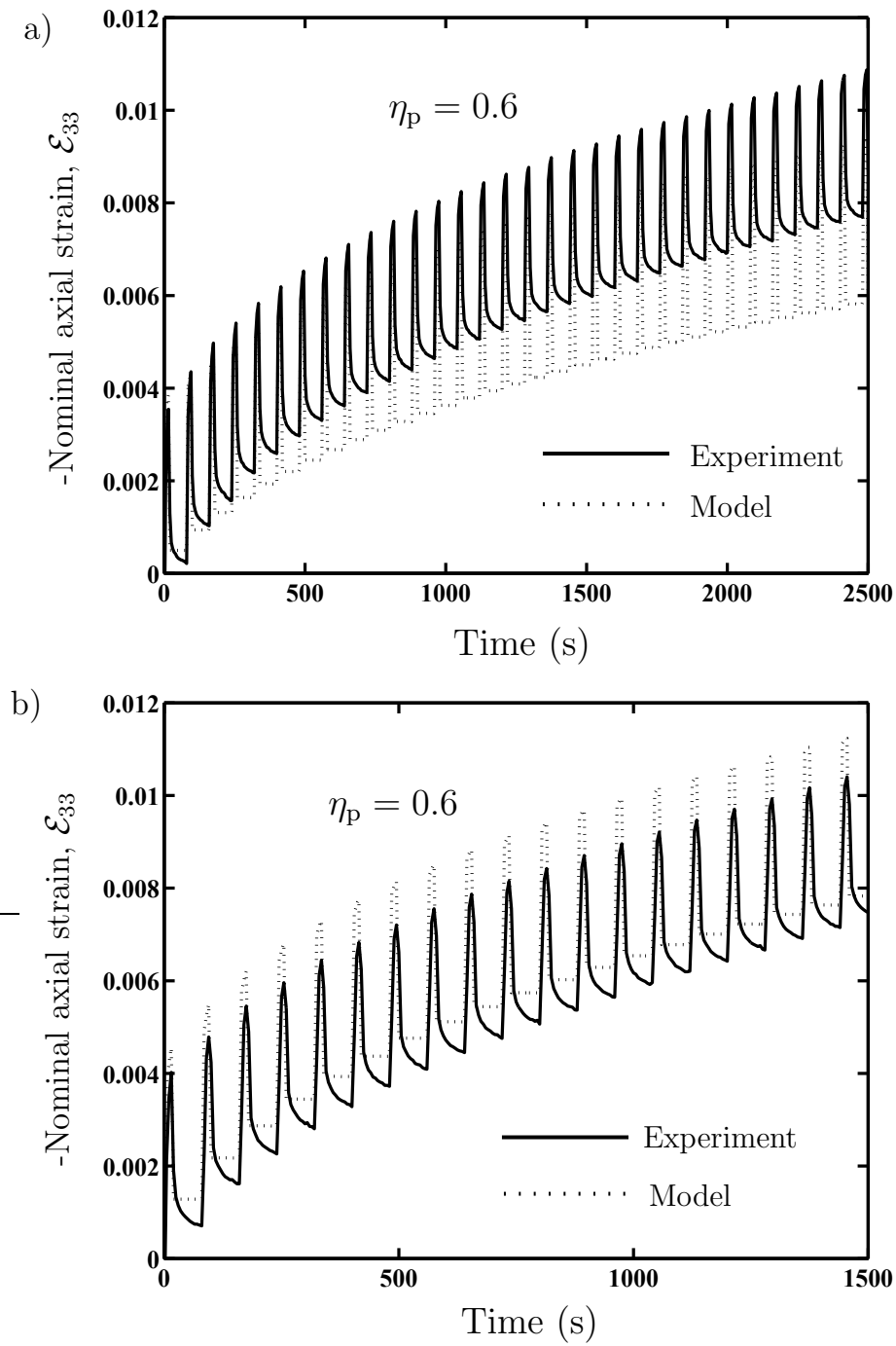


Figure 7.11: Triaxial pulse test results at 20° C for 85% volume fraction of aggregate with round and angular stones. (a) Mix ES (Round stones) with $\Sigma_p = 0.52 \text{ MPa}$, $\Delta_p = 20 \text{ s}$, $\Delta_g = 60 \text{ s}$. (b) Mix EA (Angular stones) with $\Sigma_p = 0.52 \text{ MPa}$, $\Delta_p = 20 \text{ s}$, $\Delta_g = 60 \text{ s}$.

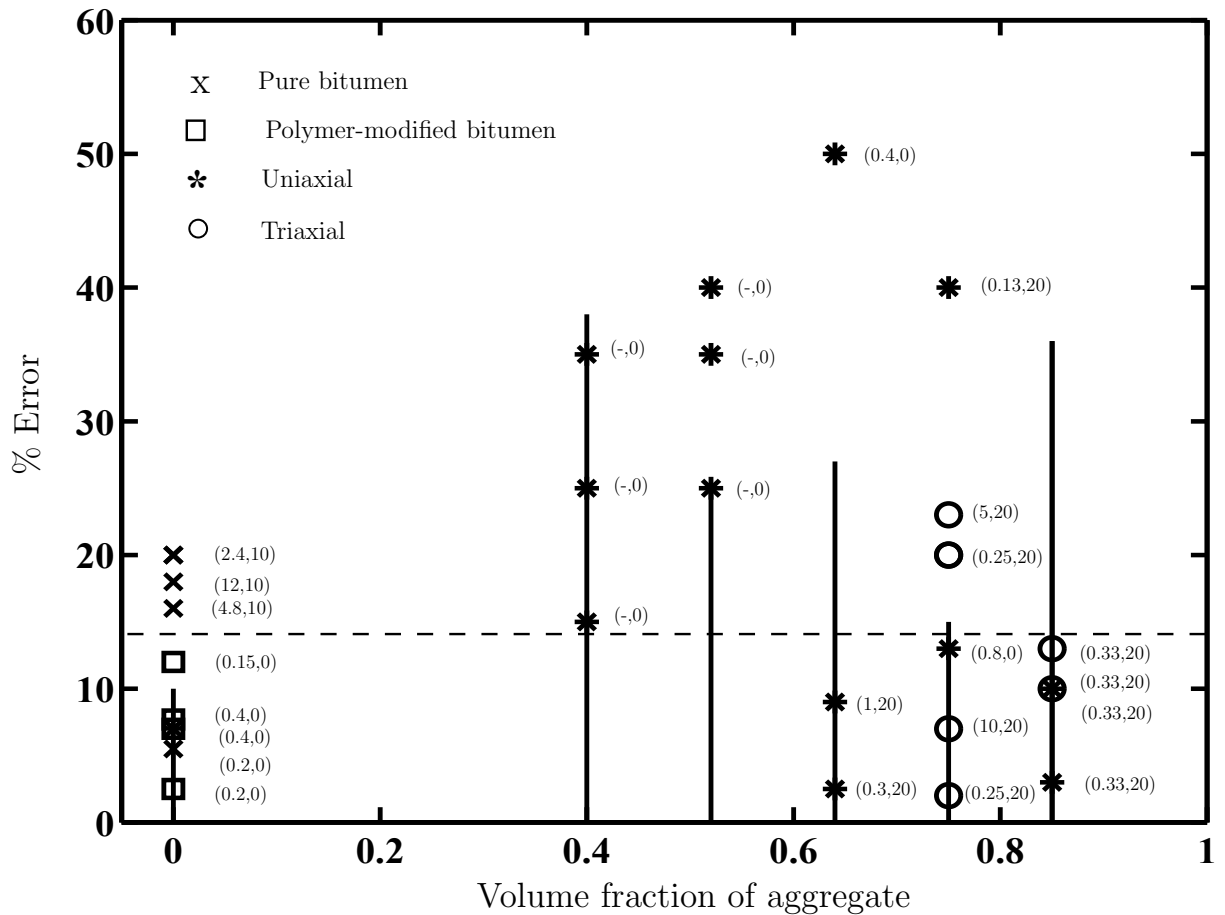


Figure 7.12: Error between experiments and model for pulse loading tests for all specimens tested. The time period ratio and temperature (Δ_p/Δ_g , T) are shown for each experimental point. Solid lines represent the standard deviation error of the steady-state experimental results for each mix. The mean modelling error is represented by dashed line.

Chapter 8

Micro-mechanical modelling of asphalt deformation

8.1 Introduction

The deformation behaviour of bituminous mixes has been studied experimentally in previous chapters. The main characteristics of the deformation behaviour of the mixes were:

1. The steady-state monotonic and continuous cyclic loading behaviour followed the Modified Cross Model, exhibiting linear and non-linear viscous behaviour at low and high stresses, respectively.
2. The mixes were stiffer with lower strains for the same stress levels than pure bitumen.
3. The recoverable strain was proportional to the strain prior to unloading with the recovery rate a unique function of the recoverable strain $\tilde{\epsilon}^r$.
4. The elastic effects were found to play an important role in modelling the defor-

mation behaviour of mixes, unlike the response of pure bitumen.

5. The loading and recovery stiffening factors S^l and S^r have the same values for a given mix and increase with volume fraction of aggregate and stress ratio η .
6. The triaxial deformation behaviour of the fully dense mixes was found to be a function of the mean and deviatoric stresses.
7. The strain to reach steady-state ϵ_{ss} was found to be unaffected by the applied stress ratio η and a function only of volume fraction of aggregate.
8. The recovery constant ψ was found to be unaffected by the stress ratio η and shape of the aggregate, and to be dependent only on the volume fraction of aggregate.
9. The mixes with a high volume fraction of aggregate dilate under compressive loading. The volumetric strain varies linearly with distortional strain in both loading and recovery conditions with the same slope s . The value of s is not affected by the applied stress ratio η or loading conditions (monotonic or cyclic).

In this chapter a “micro-mechanical” model for the deformation behaviour of asphalt under axisymmetric loading conditions will be assembled using some of the micro-mechanical models found in the literature and some of the phenomenological observations from experiments. First, the model will be described, then, model predictions will be compared with uniaxial and triaxial experimental results.

8.2 Description of the model

8.2.1 General loading

The deformation behaviour of a given bituminous mix can be fully described if the fundamental properties of bitumen (k , σ_o , $\dot{\epsilon}_{oc}(\epsilon)$, $\dot{\epsilon}_{uc}(\hat{\epsilon}_{uc})$, ψ and m), aggregate (s , c) and volume fraction of air voids (v) are known.

The macroscopic Von Mises effective strain-rate $\dot{\mathcal{E}}_e$ of a mix for an arbitrary loading history can be written as:

$$\dot{\mathcal{E}}_e = \dot{\mathcal{E}}_e^{\text{el}} + \dot{\mathcal{E}}_e^{\text{v}} + \dot{\mathcal{E}}_e^{\text{r}}, \quad (8.1)$$

where $\dot{\mathcal{E}}_e^{\text{el}}$ is the elastic effective macroscopic strain rate, $\dot{\mathcal{E}}_e^{\text{v}}$ is the viscous effective macroscopic strain rate, and $\dot{\mathcal{E}}_e^{\text{r}}$ is the recovery effective macroscopic strain rate.

Input parameters:

i) Young's modulus In the experiments reported on chapters 6 and 7, the elastic response of mixes was found to be important (unlike the case of pure bitumen, where the elastic response was found to be negligible in comparison to the viscous response).

As discussed in Chapter 5, Heukelom and Herrin (1964) extended the *stiffness* concept of Van der Poel (1955) to model the stiffness of the mix based on the stiffness of the bitumen and volume fraction of aggregate. Noting that for higher values of bitumen stiffness ($S_{bit} > 5 \text{ MPa}$), bitumen behaves as an elastic solid, Heukelom and Herrin's model can be re-written as:

$$E_{mix}^o = E_{bit}^o \left\{ 1 + \frac{2.5c}{\kappa(1-c)} \right\}^{\kappa}, \quad (8.2)$$

where E_{mix}^o and E_{bit}^o are the Young's modulus of the mix and bitumen respectively at 0°C (273 K) expressed in MPa. And

$$\kappa = 0.83 \log \left\{ \frac{4 \times 10^4}{E_{bit}^o} \right\}. \quad (8.3)$$

These equations were obtained from empirical fits to experimental data from dynamic tests on compacted mixes with approximately 3% air voids and c values from [0.7 – 0.9].

Cheung (1995) found experimentally that the Young's modulus of bitumen is strongly affected by temperature. However, due to experimental measurement difficulties, no definitive conclusions were drawn about the temperature dependence of the Young's modulus for bitumen.

As an initial approximation, the temperature dependence of the Young's modulus is assumed here to follow *Arrhenius*-type temperature dependence of bitumen (see equation 2.16) for $T \geq T_g$ as:

$$E_{mix} = E_{mix}^o e^{-k(\frac{1}{T} - \frac{1}{273})}, \quad (8.4)$$

where E_{mix} is the Young's modulus of the mix at the temperature T , and k is the Arrhenius constant of bitumen. This is justified by the experimental results for mixes described in chapter 6, where the temperature dependence of the mixes was well described by the temperature dependence of the bitumen matrix.

Table 8.1 shows a comparison between measured and predicted values of Young's modulus for the fully dense mixes ($c > 0.64$) studied in previous chapters. Equations (8.2) to (8.4) were used to calculate the mix Young's modulus with a value of the bitumen Young's modulus of $E_{bit}^o = 50MPa$. This value of E_{bit}^o was used according to measurements of the Young's modulus for a similar bitumen performed by Cheung (1995). The predicted values of the Young's modulus are strictly valid only for mixes DS, ES and EA as the model developed by Heukelom and Herrin is valid only for volume fractions of aggregate in the range [70% – 90%], which explains the considerable difference between measured and predicted values for mixes with 64% volume fraction of aggregate. The agreement between experimental and predicted results for mixes with $0.7 < c < 0.9$ is considered acceptable for this kind of material where

manufacturing conditions and microstructures vary considerably.

ii) Dilation It was seen from the experimental results that the volumetric strain was related to the distortional strain by (see also Deshpande and Cebon (1999b)):

$$H = s|\mathcal{E}_e|. \quad (8.5)$$

This relation was independent of the stress ratio η , but for the fully dense mixes the value of s depended on the aggregate volume fraction, shape and gradation. This indicates that the dilation of the mix was due to the kinematic constraints imposed by the aggregate similar to that in the deformation of granular assemblies consisting of nearly rigid particles (see section 5.6).

Section 5.6 discussed some studies that have attempted to estimate theoretically the dilation gradient s . The model of Goddard and Didwania (1998) (eq. 5.17) will be used here to calculate the dilation of the mixes. This model assumes the use of rigid circular frictional disks in 2-D. Noting that the 2-D and 3-D solutions of Goddard and Didwania (1998) differ by around 10% for monodisperse gradation, which is around the experimental error of the uniaxial and triaxial measured dilation (see table 8.1), eq. (5.17) is considered as a good approximation to the dilation of 3-D rigid frictional spheres (as asphalt with round aggregate). Table 8.1 shows the measured and predicted values of the dilation s . The values of s predicted by (5.17) agree well with the measured values for mixes with sub-spherical aggregate (specimens CS, DS and ES). However, (5.17) under-predicts s for angular aggregate where the interlocking between aggregate particles is increased (specimens CA1, CA2 and EA).

Elastic response

In order to describe the elastic response, the mix is assumed to be a linear isotropic material with Young's modulus E_{mix} and Poisson's ratio ν . The equivalent elastic

strain-rate $\dot{\mathcal{E}}_e^{\text{el}}$ is then given by

$$\dot{\mathcal{E}}_e^{\text{el}} = \sqrt{\frac{2}{3} \dot{\mathcal{E}}_{ij}^{\text{el}} \dot{\mathcal{E}}_{ij}^{\text{el}}}, \quad (8.6)$$

where

$$\dot{\mathcal{E}}_{ij}^{\text{el}} = \frac{1 + \nu}{E_{\text{mix}}} \dot{\Sigma}_{ij} - \frac{\nu}{E_{\text{mix}}} \dot{\Sigma}_{kk} \delta_{ij}. \quad (8.7)$$

Here $\dot{\Sigma}_{ij}$ is the deviatoric stress rate tensor, $\dot{\Sigma}_{kk}$ is the hydrostatic stress rate and δ_{ij} is the kronecker delta.

Viscous response

The experimental study showed that the transient loading master curve for the mix $\dot{\epsilon}_o(\mathcal{E}_e)$ has the same shape as that for pure bitumen $\dot{\epsilon}_o(\epsilon)$, shifted by a constant factor S in the y-axis and a constant factor function of volume fraction of aggregate c in the x-axis (see sections 6.3.1 and 7.3.1). Therefore, using equation (7.20), the viscous loading response of the mix, which is only active when $|\Sigma| > 0$ can be written as:

$$\dot{\mathcal{E}}_e^{\text{v}} = \frac{\dot{\mathcal{E}}_e^{\text{pl}}}{(1 - \psi)} = \frac{\Sigma_e \dot{\epsilon}_o(\mathcal{E}_e)}{S \sigma_o} \left[1 + \left(\frac{S \dot{\mathcal{E}}_e^{\text{v}}}{\dot{\epsilon}_o(\mathcal{E}_e)} \right)^m \right], \quad (8.8)$$

where $\dot{\mathcal{E}}_e^{\text{pl}}$ is the irrecoverable fraction of the viscous effective strain rate, and σ_o and m are the same values as for the bitumen matrix.

The effective macroscopic mix strain \mathcal{E}_e was observed to decrease with increasing volume fraction of aggregate c (see fig. 6.7). This is consistent with the well known ‘‘rule of mixtures’’ as:

$$\mathcal{E}_e = (1 - c)\epsilon + c\epsilon_{ag}, \quad (8.9)$$

where ϵ and ϵ_{ag} are the Von-Mises effective microscopic strains of bitumen and aggregate, respectively. As the aggregate is stiffer than the bitumen matrix, the second term in (8.9) can be ignored. Therefore, the loading strain rate master curve of pure bitumen $\dot{\epsilon}_o(\epsilon)$ can be used along with eq. (8.9) to obtain the macroscopic loading master curve for the mix $\dot{\epsilon}_o(\mathcal{E}_e)$.

As a first approximation, the stiffening factor S for transient behaviour can be calculated using the non-linear composite-sphere model developed for the steady-state by Deshpande and Cebon (1999b) (see section 5.5) as:

$$S = 0.55 \left\{ \frac{(\frac{1}{2}ks^2 + \frac{3}{2}\mu)^{(n+1)/2} [1 - (c + v)]^{(n-1)/2}}{[1 - s\eta]^n} \right\}, \quad (8.10)$$

where $n = 1/(1 - m)$ and η is the stress ratio. μ is the upper bound on the shear modulus which can be found using Hashin's composite sphere model (Hashin, 1962) according to (Deshpande and Cebon, 1999b):

$$\mu = \frac{2}{3} \left\{ 1 + \frac{c}{\frac{2}{5}(1 - c) - \frac{c(1-c^{2/3})^2}{-\frac{10}{21}c^{7/3} + \frac{10}{21}} - \frac{v}{\frac{3}{5} + \frac{2}{5}v + \frac{v(1-v^{2/3})^2}{\frac{95}{168}v^{7/3} + \frac{10}{21}}} } \right\}, \quad (8.11)$$

and the bulk modulus k is given by:

$$k = \frac{8}{9} \frac{1 - v}{v} \frac{1}{1 - c}. \quad (8.12)$$

This model predicts reasonably well the steady-state stiffening factor of mixes. As the transient stiffening factor was seen to be constant and equal to the steady-state stiffening factor, this approximations is expected to bring good results in the prediction of the transient behaviour of mixes.

Recovery response

Based on equation 7.21, the effective recovery strain rate, which is only active when $\Sigma = 0$ is written as:

$$\dot{\mathcal{E}}_e^r = -\text{sign}(\mathcal{E}_e) [1 - \text{sign}(|\Sigma|)] \frac{\dot{\mathcal{E}}_u(\hat{\mathcal{E}}_e^r)}{S}. \quad (8.13)$$

Here $\text{sign}(0)$ is defined to be zero and $-\text{sign}(\mathcal{E}_e)$ ensures that the recovery effective rate $\dot{\mathcal{E}}_e^r$ reduces the effective strain \mathcal{E}_e . The parametrised strain $\hat{\mathcal{E}}_e^r$ is written as:

$$\hat{\mathcal{E}}_e^r = \left(\frac{\mathcal{E}_e}{\mathcal{E}_e^{\text{pl}}} - 1 \right) \frac{1 - \psi_{mix}}{\psi_{mix}}. \quad (8.14)$$

Similar to the overall loading strain of the mixes, the recovery constant of the mix ψ_{mix} was found to decrease linearly with volume fraction of aggregate c (see fig. 6.10). Therefore, the macroscopic recovery constant of the mixtures (8.9), can be written as:

$$\psi_{mix} = (1 - c)\psi_{bit}, \quad (8.15)$$

where ψ_{bit} is the recovery constant of the bitumen matrix.

From experimental observations (see chapter 6), the recovery strain rate master curve for pure bitumen $\dot{\epsilon}_u(\dot{\epsilon}^r)$ was found to have the same shape as for mixes, with only the stiffening factor S and the recovery constant ψ_{mix} dependent on the volume fraction of aggregate c . Therefore, the master curve for pure bitumen is used to model the recovery behaviour of mixes by combining it with equations (8.10), (8.14) and (8.15).

Mix evolution

Since eq. (8.5) is independent of stress and strain rate, a rate form of this equation can be written as (Deshpande, 1997):

$$\dot{H} = s|\dot{\mathcal{E}}_e|. \quad (8.16)$$

As the mix deforms, it dilates and thus the porosity increases. The evolution law for the porosity is assumed to take a simple form for incompressible matrix behaviour (Gurson, 1977; Deshpande, 1997):

$$\dot{v} = (1 - v)\dot{H}, \quad (8.17)$$

while the volume fraction of the aggregate is assumed to evolve due to the overall volume change according to:

$$\dot{c} = c\dot{H}. \quad (8.18)$$

The evolution of the mix is then given by equation (8.1) along with (8.16), (8.17) and (8.18).

It is worth noting that only the first order effects of the porosity evolution are taken into account here, as discussed by Deshpande (1997). That is, the change in volume fraction of voids is considered, but any anisotropy due to change in aspect ratio of voids is ignored.

8.2.2 Axisymmetric loading

The constitutive model for general loading conditions of bituminous mixes described in the previous sections can be particularized for the case of axisymmetric stress states, like those studied experimentally. Using eq. (7.23) the axial and radial strain rates can be written as:

$$\dot{\mathcal{E}}_{33} = \dot{\mathcal{E}}_{33}^{el} + \dot{\mathcal{E}}_{33}^v + \dot{\mathcal{E}}_{33}^r, \quad (8.19)$$

and

$$\dot{\mathcal{E}}_{11} = \dot{\mathcal{E}}_{22} = \left(\frac{2s \operatorname{sign}(\Sigma) - 3}{2s \operatorname{sign}(\Sigma) + 6} \right) \dot{\mathcal{E}}_{33}, \quad (8.20)$$

respectively. From (7.13), the effective strain rate can be written as:

$$\dot{\mathcal{E}}_e = \dot{\mathcal{E}}_{33} \left(\frac{3}{3 + s \operatorname{sign}(\Sigma)} \right). \quad (8.21)$$

The axial elastic component is given by eq. (7.25) as:

$$\dot{\mathcal{E}}_{33}^{el} = \frac{\dot{\Sigma}}{E_{mix}}. \quad (8.22)$$

The axial viscous response is given by eq. (7.26) as:

$$\dot{\mathcal{E}}_{33}^v = \frac{\Sigma \dot{\mathcal{E}}_o(\mathcal{E}_e)}{S\sigma_o} \left\{ \frac{s \operatorname{sign}(\Sigma) + 3}{3} \right\} \left[1 + \left(\frac{S \dot{\mathcal{E}}_{33}^v}{\dot{\mathcal{E}}_o(\mathcal{E}_e)} \left\{ \frac{3}{s \operatorname{sign}(\Sigma) + 3} \right\} \right)^m \right], \quad (8.23)$$

and the axial recovery rate by eq. (7.27) as:

$$\dot{\mathcal{E}}_{33}^r = -\operatorname{sign}(\mathcal{E}_{33}) [1 - \operatorname{sign}(|\Sigma|)] \frac{\dot{\mathcal{E}}_u(\hat{\mathcal{E}}_{33}^r)}{S}, \quad (8.24)$$

with

$$\hat{\mathcal{E}}_{33}^r = \left(\frac{\mathcal{E}_{33}}{\mathcal{E}_{33}^{pl}} - 1 \right) \frac{1 - \psi_{mix}}{\psi_{mix}}. \quad (8.25)$$

Calculation procedure

Once all input parameters have been obtained, including measured or calculated s and E_{mix} , a flow diagram summarising the procedure to calculate the mix properties as it deforms is shown in figure 8.1. The Young's modulus of the mix can be calculated using eqs. (8.2) to (8.4). From the properties of the bitumen matrix and eqs. (8.9), (8.14) and (8.15) can be obtained the macroscopic reference loading and recovery strain rates for the mix, $\dot{\epsilon}_o(\mathcal{E}_e)$ and $\dot{\epsilon}_u(\hat{\mathcal{E}}_e^r)$, respectively. With the volume fractions of aggregate and voids (c and v) use eqs. (8.11) and (8.12) to calculate μ and k , respectively. Then the stiffening factor S can be calculated using eq. (8.10) for a given stress ratio η . The axial deformation rate can be then estimated using eqs. (8.1), (8.6), (8.8) and (8.13). The volumetric strain rate can be calculated using (8.16). The distortional deformation \mathcal{E}_e is then evaluated by assuming $\dot{\mathcal{E}}_e$ remains constant over a small time interval Δt , and integrating: $\mathcal{E}_e = \dot{\mathcal{E}}_e \Delta t$. The volumetric strain due to the kinematic constraint can be calculated from (8.5). The evolution equations (8.17) and (8.18) are finally integrated to calculate the new volume fractions of voids v and aggregate c . The process can be repeated until the desired macroscopic strain is reached.

8.3 Comparison with experimental results

A comparison between the predictions of the “micro-mechanical” constitutive model described in the previous section and the uniaxial and triaxial test results discussed in previous chapters will be presented in this section.

A detailed comparison between the main model parameters and their evolution

will be presented for mix ES (85% volume fraction of sub-spherical aggregate), while for the sake of brevity, a comparison of the more important parameters in the model will be given for other mixes in order to show the generality of the model.

Figure 8.2 shows a triaxial creep recovery test result for mix ES with $\Sigma = 0.78 \text{ MPa}$ and $\eta = 0.6$. In dotted lines are plotted the model predictions with the two experimentally measured limits of the dilation gradient s (see table 8.1), and in dashed lines the model prediction using s calculated by eq. (5.17). The effect of s in the model predictions is significant, increasing the slope of the loading region ($t < 1000 \text{ s}$) with decreasing s value.

Figure 8.3a shows the evolution of the stiffening factor S predicted by the model for the same results plotted in fig. 8.2, with $s = 0.43$. Figure 8.3b shows the evolution of voids and aggregate volume fractions as the mix deforms. Note that the stiffening factor S decreases during loading ($0 < t < 1000 \text{ s}$) due to the increase of voids and consequently decrease in c . As soon as the load is removed ($t > 1000 \text{ s}$), the void fraction v decreases due to the recovery and consequently decrease in volumetric strain H of the mix, inducing an increase in c and S .

Figure 8.4 shows the predicted variation of the stiffening factor on the steady-state regime for the different mixes studied with sub-spherical aggregate. Also plotted in the same figure are the experimental error bars of the measured steady-state stiffening factors for the same mixes. The model predictions are close to the experimentally measured values for mixes up to 75% volume fraction of aggregate. A significant difference can be seen for the 85% mixes. This error and its influence in predicting permanent deformation will be discussed for the pulse tests.

Figure 8.5a shows the model prediction of a pulse loading test on mix ES (85% sub-spherical aggregate). This type of test is the most demanding in terms of modelling accuracy because of the combination of both loading and recovery conditions for

many cycles. The model predicts reasonably well the “steady-state” slope of this test, however, the initial transient behaviour is under predicted leading to an overall error in the permanent deformation of about 40%. Despite this considerable error, the model is considered as a good approximation taking into account its simplicity and that it captures accurately the “steady-state” slope.

The experimentally measured value of the transient stiffening factor was found to be constant during the deformation (see section 6.3.1), opposite to the model predictions where the stiffening factor is evolving with the mix (figs. 8.3a and 8.5b). To investigate the effect of the evolution of the variables into the model prediction, the model was ran ignoring the evolution of the mix. That is, keeping c and v constant throughout the calculation. This assumption implies a constant value of the stiffening factor S , consistent with experimental observations. Figure 8.6 shows the prediction of the model assuming no evolution. Note that the overall error in permanent deformation of the mix is reduced to about 20%. Despite the improvement in the overall results, the transient deformation is still under estimated.

Figure 8.5b shows pulse loading test results for mix EA at two different stress ratios η . Mix EA was manufactured with angular aggregate, which is closer to the aggregate used in road construction. The model predictions including evolution of variables with $s = 0.9$ (as measured) agree well with experimental results for this mix. Note that the transient deformation in mix EA specimens is small (if any) in comparison with mix ES. This difference is due to the higher dilation and consequently interlocking of mix EA angular particles.

It is worth noting here that the model predictions presented were calculated using the mean values of the experimentally measured values of the void fraction v and temperature T . Variation in these quantities can lead to variation between the results.

8.4 Discussion

A simple constitutive model for predicting the deformation behaviour of bituminous mixes has been proposed in this chapter. The model makes use of some micro-mechanical theories, as well as some phenomenological observations of the behaviour of mixes. Therefore, the model proposed cannot be considered a micro-mechanical model per se. However, as the main parameters of the model are calculated from rigorous micro-mechanical models, the model in its actual form can be understood as a micro-mechanically based model. More theoretical knowledge of some of the parameters taken from phenomenological grounds is required in order to make this a complete micro-mechanical model.

The model proposed uses Deshpande and Cebon's model as a back-bone. That model was developed under the assumption of non-linear (power law) behaviour of the bitumen binder in the mix. After an experimental study of the strain distribution in bituminous mixes, Masad et al. (2001) concluded that the strains experienced in the bitumen matrix during mix deformation are well in the non-linear region inclusive for small deformations. This confirms the assumption of Deshpande and Cebon (1999b) who argued that the microscopic strains in the bitumen films between particles can be large, even though the macroscopic strains are small.

A constitutive phenomenological model for the deformation behaviour of mixes was developed in chapter 7. The predictions of that model were in good agreement with experimental results for a fixed volume fraction of aggregate mix. On the other hand, the model proposed in this chapter is applicable to any volume fraction of aggregate. The generality, few input parameters, and ease implementation, make the model suitable for design of mixes for some applications. Further, the model is amenable to implementation in commercial Finite Element (FE) codes, allowing the study and prediction of the deformation behaviour of bituminous mixes under static

or moving wheel loads.

In the prediction of the permanent deformation or rutting of bituminous mixes, it is expected that the influence of the rate independent elastic term ($\dot{\mathcal{E}}_e^{el}$ in eq. 8.1) is negligible. Therefore, the values calculated of the Young's modulus for the mixes are not expected to make a significant difference to the permanent or plastic behaviour of the mix. Consequently, the differences observed between the calculated and predicted values of E_{mix} (see table 8.1) are considered reasonable.

The dilation gradient s has a critical effect on the deformation behaviour of the mix. It is seen from fig. 8.2 that an increase in the value of the dilation gradient increases the stiffness of the mix and consequently reduces the strain rate. Further, when the stress ratio reaches a critical value given by $\eta = 1/s$, the term $[1-s\eta]^n = 0$ in eq. (8.10) and "lockup" occurs, disabling further deformation of the mix (Deshpande, 1997).

The constitutive model proposed does not take into account mechanisms like fracture of bitumen and coalescence and growth of voids in the mixes. These mechanisms are expected to be important when the mix is subjected to tensile stresses (Deshpande and Cebon, 1999b; Genin and Cebon, 2000). Therefore, the current constitutive model should only be applied to bituminous mixes subjected to compressive stresses (as in all the experiments described).

8.5 Conclusions

1. A simple model of the deformation behaviour of bituminous mixes was assembled using micro-mechanical and phenomenological based theories. The model inputs are the properties of the bitumen matrix and aggregate. The key assumptions of the model are:
 - (a) The Young's modulus of the mix is calculated using Heukelom and Herrin's

model for mixes with volume fractions of aggregate in the range $[0.7 < c < 0.9]$, with the same temperature dependence of bitumen.

- (b) The macroscopic strain \mathcal{E}_e and recovery constant ψ_{mix} of the mix linearly scale with volume fraction of aggregate.
 - (c) The 2-D solution for the dilation of rigid frictional disks of Goddard and Didwania (1998) is approximately equal to the 3-D solution for rigid frictional spheres.
 - (d) The steady-state stiffening factor solution of Deshpande and Cebon (1999b) is assumed to be valid for the calculation of the transient stiffening factor of mixes.
2. The model is capable of predicting the main characteristics of the deformation behaviour of bituminous mixes with various volume fractions, as observed in uniaxial and triaxial tests.
 3. The predicted values of the dilation gradient s for sub-spherical aggregate agree reasonably well with experimentally measured values, while for angular aggregate the difference is significant.
 4. The model is applicable to angular aggregates, provided measured values of the dilation gradient s are used.

8.6 Tables

Mix	E_{mix} measured (20° C)	E_{mix} predicted (20° C)	s measured	s predicted
Mix CS (64% sub-spherical)	60-90	9	0.70-0.90	0.827
Mix CA1 (64% Angular)	60-90	9	1.00-1.35	0.827
Mix CA2 (64% Angular)	55-80	9	1.15-1.45	0.827
Mix CS3 (64% sub-spherical)	65-85	9	0.70-0.90	0.827
Mix CS4 (64% sub-spherical)	70-80	9	0.70-0.95	0.827
Mix DS (75% sub-spherical)	100-150	39	0.60-0.75	0.705
Mix ES (85% sub-spherical)	250-300	380	0.35-0.55	0.43
Mix EA (85% Angular)	250-330	380	0.80 - 1.00	0.43

Table 8.1: Comparison between Young's modulus and dilation gradient measured and predicted by the 2-D model (eq. 5.17) for fully dense mixes. Numbers in bold indicate where models are expected to be valid

8.7 Figures

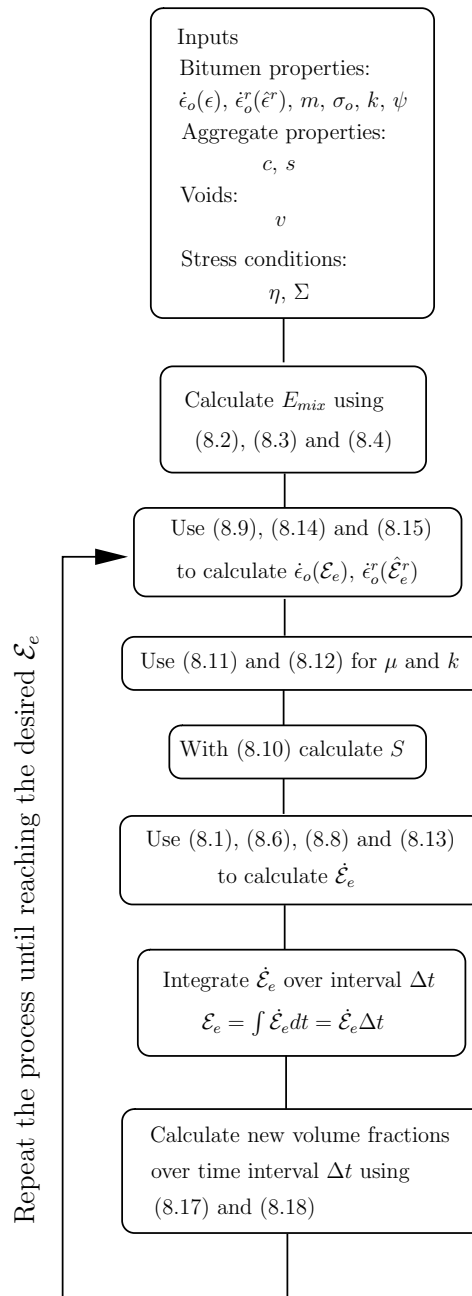


Figure 8.1: Flow diagram showing the procedure of calculation of the deformation behaviour of mixes using the constitutive model.

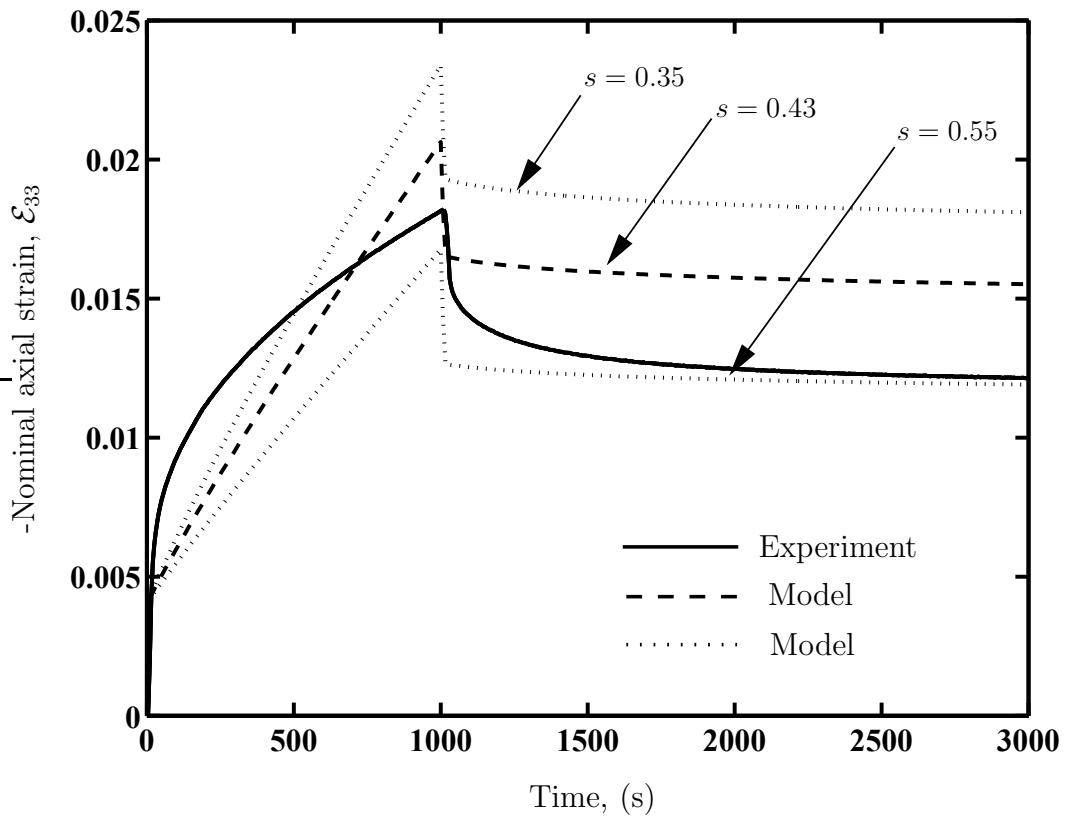


Figure 8.2: Monotonic creep recovery triaxial test on mix ES (85%) at 20°C with $\Sigma = 0.78 \text{ MPa}$ and $\eta = 0.6$. The dotted lines represent the model predictions with the two limits of the experimentally measured dilation gradient s . The dashed line represent the model prediction with $s = 0.43$ calculated using eq. (5.17).

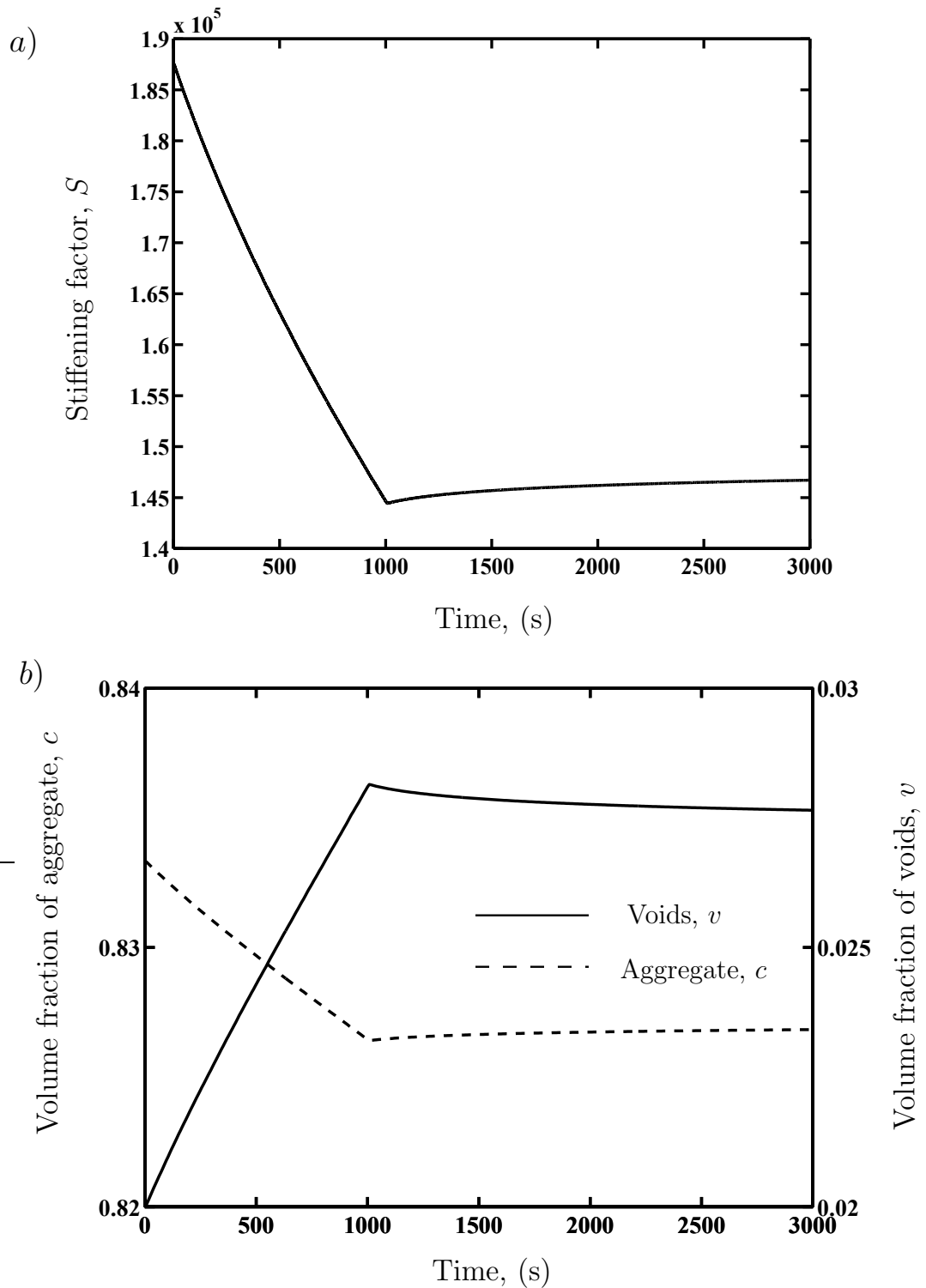


Figure 8.3: Evolution of stiffening factor (a), and volume fractions of aggregate and voids (b), for creep recovery simulation shown in fig. 8.2, with $s = 0.43$.

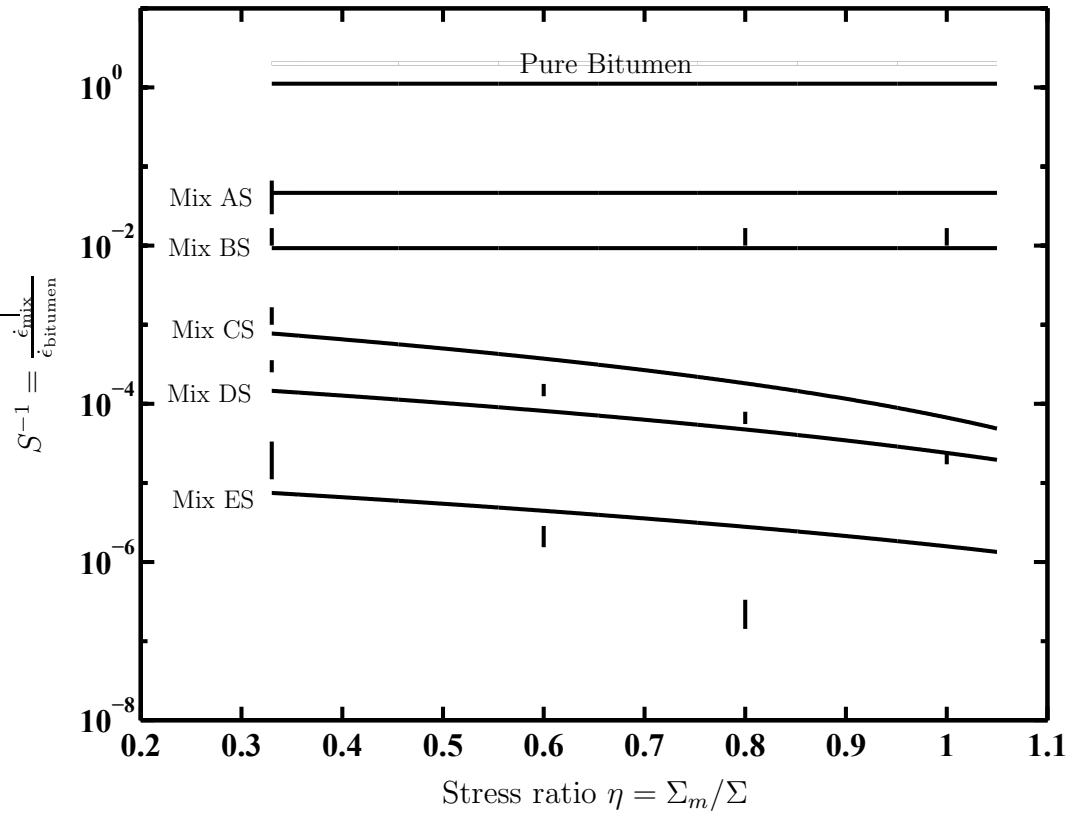


Figure 8.4: Effect of stress ratio on deformation behaviour of mixes with varying volume fractions of sub-spherical aggregate. The values of S^{-1} calculated by the model are plotted along with the experimental error bars of S^{-1} .

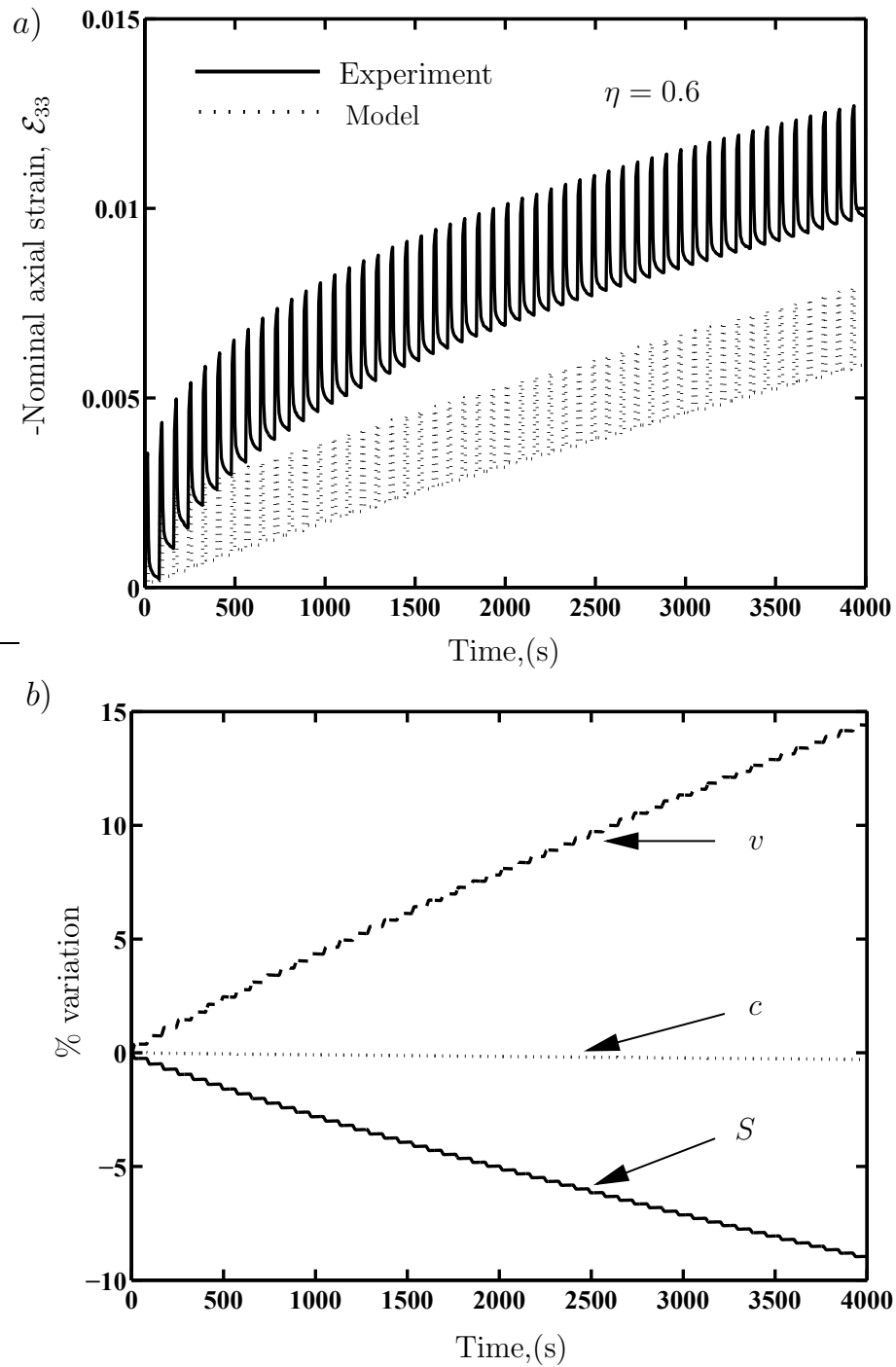


Figure 8.5: Triaxial pulse test results at 20°C for Mix ES (85% volume fraction of sub-spherical aggregate) with $\Sigma_p = 0.52\text{ MPa}$, $\Delta_p = 20\text{ s}$, $\Delta_g = 60\text{ s}$, $s = 0.43$. (a) Model prediction with evolution of c and v . (b) Percentage of variation of c , v and S during mix evolution.

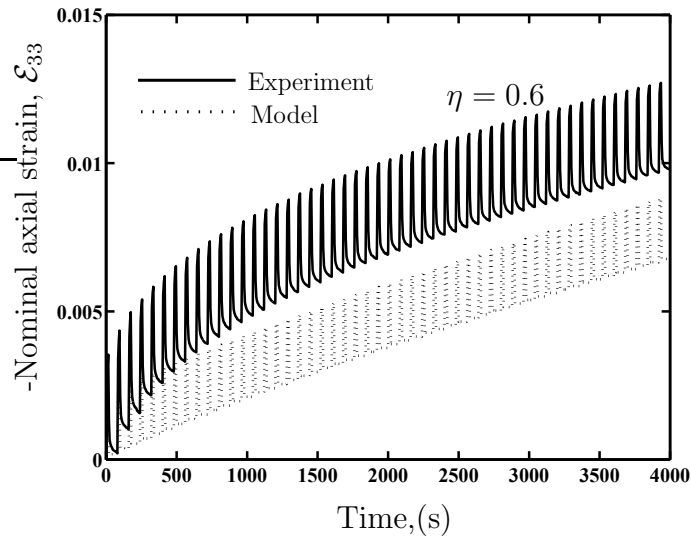


Figure 8.6: Triaxial pulse test results at 20° C for Mix ES (85% volume fraction of sub-spherical aggregate) with $\Sigma_p = 0.52 \text{ MPa}$, $\Delta_p = 20 \text{ s}$, $\Delta_g = 60 \text{ s}$, $s = 0.43$. Model prediction ignoring evolution of the mix.

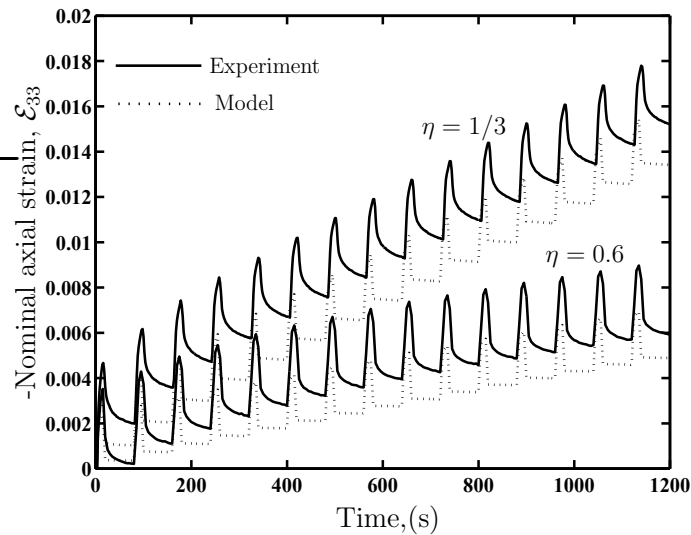


Figure 8.7: Triaxial pulse test results at 20° C for Mix EA (85% volume fraction of angular aggregate) with $\Sigma_p = 0.52 \text{ MPa}$, $\Delta_p = 20 \text{ s}$, $\Delta_g = 60 \text{ s}$, $s = 0.9$ at two different stress ratios. Model prediction with mix evolution.

Chapter 9

Conclusions and Recommendations

This chapter summarises the main conclusions of this dissertation and also provides recommendations for further work.

9.1 Summary of main conclusions

9.1.1 Review of previous research on bitumen: Chapter 2.

A review of the more relevant literature concerned with understanding the deformation behaviour of bitumen was provided in this chapter.

The Modified Cross Model developed by Cheung and Cebon was found to provide a good representation of the steady state behaviour of bitumen at temperatures above the glass transition (T_g). For temperatures below T_g the Eyring Plasticity Model can be used to model bitumen behaviour. Some researchers have attempted to model the transient behaviour of creeping materials based on curve fitting and thermodynamic principles. They have achieved good agreement with experimental results in some cases (usually at small strains). However, these models are complex and usually require specialised software to carry the model fitting with experimental results. The

dynamic behaviour of bitumen at small strains, where the behaviour is nearly linear, is well understood. Nonetheless, the models proposed for the dynamic behaviour in the non-linear regime are prohibitive in terms of the complexity and number of tests needed for calibration. No conclusive information could be found about the indentation behaviour of bitumen for large strains, despite the promising results observed by some researchers for small strains.

9.1.2 Deformation behaviour of bitumen: Chapter 3

The monotonic constant strain-rate and creep behaviour of four bitumens (2 pure and 2 polymer-modified) were measured over a range of temperatures. The monotonic responses were found to be adequately described by an extended Cross model, wherein the “viscosity” is considered to be a function of strain. The recoverable strain was found to be directly proportional to the strain prior to unloading, with the recovery rate being a unique function of the recoverable strain. Both the loading and recovery responses were observed to be temperature dependent, with the Arrhenius relation capturing the temperature dependence over the range of temperatures tested, $-5^{\circ}\text{C} \leq T \leq 20^{\circ}\text{C}$.

Two types of cyclic loading tests were conducted, (i) continuous cyclic and (ii) pulse train tests to simulate vehicle loading in a pavement. The continuous cyclic response was found to be similar to the monotonic response for the same mean stress. However, significant strain recovery was observed during the rest periods in the pulse train experiments.

A simple phenomenological model which can be calibrated by a minimum of four uniaxial tensile experiments was proposed. This model was seen to capture the monotonic, continuous cyclic and pulse loading response of the four bitumens studied with reasonable accuracy. An extension of the model to fully 3D loading is also

proposed based on a von-Mises criterion. This makes the simple model amenable for implementation in a finite element program that could be used to predict the behaviour of bitumen under more complex loading conditions.

9.1.3 Indentation behaviour of bitumen: Chapter 4

The similarity solution for the indentation of a power-law creeping solid developed by Bower et al. (1993), was extended to the constitutive model for the monotonic and cyclic response of bitumen developed in chapter 3. It was assumed that during unloading, the bitumen recovers in a self-similar manner and the effective strain rate under the indenter continues to be related to the indentation depth via Bower's model. Employing this strain relationship in the unloading constitutive relation for bitumen, the indentation behaviour of bitumen was characterised under both monotonic and cyclic loading conditions.

Monotonic, continuous cyclic and cyclic pulse loading indentation experiments were conducted over a range of temperatures. Similar to the uniaxial tensile behaviour of bitumen, the continuous cyclic response was observed to depend mainly on the mean applied indentation load while the cyclic pulse loading behaviour depended strongly on the recovery behaviour of bitumen and hence was affected by the rest periods in the loading history. The proposed indentation model is seen to accurately capture the experimentally observed indentation response over this wide range of loading conditions. The model is also successful in predicting the temperature dependence of the indentation response and the effect of the indenter diameter.

The monotonic and repeated indentation behaviour investigated here is the unit problem for understanding the behaviour of pavements under vehicle loads and is thus of intrinsic interest. Moreover, the indentation study has helped validate the multi-axial constitutive model for bitumen developed in chapter 3.

9.1.4 Review of previous research on bituminous mixes:

Chapter 5

The most commonly employed approaches to modelling the deformation behaviour of bituminous mixes fall into two main categories: *i*) Continuum Mechanics models, and *ii*) Micro-mechanical models. Continuum mechanics models are still the most popular choice for analysing mixes in engineering practice.

A large amount of literature on the prediction of permanent deformation of bituminous mixes was found. However, most of the models fail to incorporate some of the observed characteristic of the deformation of the material or require an excessive number of calibration parameters, with complex fitting procedures.

A simple model, which predicts the main characteristics of the steady-state compressive deformation of bituminous mixes under various stress and strain rate states, was developed by Deshpande and Cebon (1999b), based on soil mechanics and micro-mechanics theories. It shows good agreement with experimental observations and provides a good insight into the main characteristics of the steady-state deformation behaviour.

A simple analytical solution for the dilation of 2-D, fully dense disk assemblies was proposed by Goddard and Didwania (1998). However, theoretical estimation of the dilation of 3-D assemblies of spheres requires complex numerical methods of solution. For angular particles, predicting dilation is still an unsolved problem.

9.1.5 Uniaxial deformation behaviour of bituminous mixes:

Chapter 6

The uniaxial monotonic and cyclic deformation behaviour of asphalt, with varying volume fractions of aggregate, was studied experimentally in this chapter. The main

characteristics of the uniaxial deformation behaviour of bitumen were found to be valid for these mixes. However, elastic effects were found to play an important role in the deformation behaviour of mixes, unlike the case for bitumen.

The loading and recovery stiffening factors S^l and S^r were found to have the same values for a given mix and to increase with volume fraction of aggregate. The mixes with a high volume fraction of aggregate were observed to dilate under uniaxial compressive loading. Consequently, the volumetric strain varied linearly with distortional strain in both loading and recovery conditions with the same gradient s .

The main effects of high angularity of the aggregate on the deformation behaviour of the mixes were, (i) an increase in the stiffening factors and dilation gradient, and (ii) a reduction in the steady-state strain. However, the recovery constant ψ was found to remain unchanged, despite the angularity of the aggregate.

An extension to the phenomenological model for bitumen developed in chapter 3, was proposed for mixes. The model was seen to capture the uniaxial monotonic, continuous cyclic and pulse loading response of the mixtures at different temperatures with reasonable accuracy.

9.1.6 Triaxial deformation behaviour of bituminous mixes:

Chapter 7

The triaxial monotonic and cyclic deformation behaviour of asphalt with varying volume fractions of aggregate were studied experimentally in this chapter. The triaxial deformation behaviour of the fully dense mixes was found to be a function of the mean and the deviatoric stresses. For a constant stress ratio η , the steady-state axial creep behaviour of the mixes has the same form as that of pure bitumen. The loading stiffening factor S^l was a function of the volume fraction of the aggregate and the stress ratio $\eta = \Sigma_m/\Sigma$, as observed by Deshpande and Cebon (1999b).

The triaxial monotonic response was found to be adequately described by a reference strain rate function of the applied macroscopic strain $\dot{\epsilon}_o(\mathcal{E}_e)$ as for the uniaxial behaviour. This reference function is dependent on the applied stress ratio η . The strain to reach steady state ϵ_{ss} was found to remain unaffected by the applied stress ratio η . The recovery stiffening factor S^r was found to be a function of the volume fraction of aggregate and the stress ratio η . Further, the effect of these variables on S^r were found to be the same as for the loading stiffening factor S^l . The recovery constant ψ was found to be unaffected by the stress ratio η , and showed to be only dependent on the volume fraction of aggregate.

The recovery behaviour of the mixes under triaxial conditions was found to be described by a reference recovery strain rate function of a parametrised strain $\dot{\epsilon}_u(\hat{\mathcal{E}}_e^r)$ as for the uniaxial case. This function scales with the function found for pure bitumen using the recovery stiffening factor S^r .

Two types of triaxial cyclic loading tests were conducted, (i) continuous cyclic and (ii) pulse train tests to simulate vehicle loading in a pavement. While the triaxial continuous cyclic response was similar to the monotonic response with the mean deviatoric stress and mean stress ratio η_m governing the behaviour, significant strain recovery was observed during the rest periods in the pulse train experiments, as also found for the uniaxial behaviour of mixes.

The mixes with a high volume fraction of aggregate dilate under triaxial compressive loading. The value of the dilation gradient s is not affected by the applied stress ratio η , the temperature, or loading conditions (monotonic or cyclic).

9.1.7 Micro-mechanical modelling of asphalt deformation: Chapter 8.

A simple model of the deformation behaviour of bituminous mixes was assembled using micro-mechanical and phenomenological based theories. The model inputs are the properties of the bitumen matrix and aggregate. The key assumptions of the model were:

1. The Young's modulus of the mixes is calculated using Heukelom and Herrin's model for mixes with volume fractions of aggregate in the range $[0.7 < c < 0.9]$, with the same temperature dependence of bitumen.
2. The macroscopic strain \mathcal{E}_e and recovery constant ψ_{mix} of the mix linearly scale with volume fraction of aggregate.
3. The 2-D solution for the dilation of rigid frictional disks of Goddard and Didwania (1998) is approximately equal to the 3-D solution for rigid frictional spheres.
4. The steady-state stiffening factor solution of Deshpande and Cebon (1999b) is assumed to be valid for the calculation of the transient stiffening factor of mixes.

The model is capable of predicting the main characteristics of the deformation behaviour of bituminous mixes with various volume fractions, as observed in uniaxial and triaxial tests.

The predicted values of the dilation gradient s for sub-spherical aggregate agree reasonably well with experimentally measured values, while for angular aggregate the difference is significant. The model is applicable to angular aggregate, provided the measured values of the dilation gradient s is used.

9.2 Recommendations for future work

9.2.1 Bitumen

The multiaxial deformation behaviour of bitumen has been studied in this dissertation at temperatures in the range of $-5^{\circ}\text{C} \leq T \leq 20^{\circ}\text{C}$ where the Modified Cross Model is known to be valid. Extension of the proposed models at temperatures below the glass transition temperature T_g , where the Eyring plasticity model applies, is a topic which merits further study.

The indentation behaviour of bitumen at effective strains up to 0.2 were investigated and modelled. In order to study the indentation behaviour at higher effective strains it would be necessary to implement the constitutive model for bitumen in an FE code with a user-defined material model. This is a topic of research proposed for future work.

The adhesive behaviour of bitumen during recovery from indentation is a topic not well understood, so it is necessary to improve the experimental and theoretical knowledge of this subject.

9.2.2 Bituminous mixes

The axisymmetric uniaxial and triaxial behaviour of bituminous mixes with varying volume fractions of aggregate were studied experimentally in this dissertation. From those observations a constitutive model was proposed. This constitutive model should be verified under other loading conditions (e.g. pure shear).

The measured recovery constant ψ for mixes was found to decrease linearly with the volume fraction of aggregate. No theoretical explanation could be found for this behaviour. It is believed that this could be caused by the adhesion of bitumen to the aggregate particles, decreasing the amount of recovered strain for mixes. A unit cell

analysis of a rigid particle embedded in different volume fractions of bitumen could be carried out using special FE elements with the constitutive law for bitumen in order to explain theoretically this recovery behaviour.

The indentation behaviour of mixes is an important topic for further research as it is the unit problem for understanding the rutting of asphalts under moving wheel loads. An experimental study of the indentation behaviour of mixes along with theoretical study using FE analysis is also proposed as a topic of future study.

Once the indentation behaviour of mixes has been understood, the logical next step will be to study the deformation behaviour of asphalt under moving wheel loads by FE analysis.

The theoretical estimation of dilation for angular aggregate is a complex topic which merits research. An initial experimental investigation of the dilation of irregular particles of varying shape, angularity and friction could be carried out in order to bring to light some effects of aggregate selection and pavement durability.

Bibliography

- Abbas, A. R., Papagiannakis, A. T. and Masad, E. A. (2004). Linear and nonlinear viscoelastic analysis of the microstructure of asphalt concretes, *J. of materials in civil engineering* **16**(2): 133–139.
- Abraham, H. (1960). *Asphalt and allied substances*, 6th edn, D Van Nostrand Company Inc.
- Airey, G., Dunhill, S. and Collop, A. (2002). A constitutive material modelling methodology for asphalt mixtures, *Ninth International Conference on Asphalt Pavements*, Copenhagen.
- Airey, G., Dunhill, S., Collop, A. and Scarpas, A. (2003). Determination of constitutive model parameters to simulate asphalt mixture response, *6th International RILEM Symposium on Performance Testing and Evaluation of Bituminous Materials, PTEBM'03*, Zurich.
- Amin, K. E., Mukherjee, A. K. and Dorn, J. E. (1970). A universal law for high temperature diffusion controlled transient creep, *J. of the mechanics and physics of solids* **18**: 413–426.
- Anderson, D. A., Chistensen, D. W. and Bahia, H. (1991). Physical properties of asphalt cement and the development of performance related specifications, *Proceedings of the Association of asphalt paving technologists*, Vol. 60, pp. 437–532.

- Andersson, O. (1967). Rheological behaviour of asphalt pavings under traffic, *Proceedings of the 2nd International Conference on the Structural Design of Asphalt Pavements*, pp. 479–486.
- Atkins, A. G., Silverio, A. and Tabor, D. (1966). Indentation hardness and creep of solids, *Journal Inst. Metals* **94**: 369.
- Bahia, H., Zhai, H., Bonnetti, K. and Kose, S. (1999). Non-linear viscoelastic and fatigue properties of asphalt binders, *Journal of the AAPT* **68**: 1–34.
- Bao, G., Hutchinson, J. W. and McMeeking, R. M. (1991). Particle reinforcement of ductile matrices against plastic flow and creep, *Acta Metallurgica et Materialia* **39(8)**: 1871–1882.
- Bashir, Y. M. and Goddard, J. D. (1991). A novel simulation method for the quasi-static mechanics of granular assemblages, *J. Rheology* **35(5)**: 849–885.
- Bland, D. L. and Lee, E. H. (1956). On the determination of a viscoelastic model for stress analysis of plastics, *Journal of applied mechanics* pp. 416–420.
- Boltzmann, L. (1876). *Pogg. Ann. Phys. U. Chem* **7**: 624.
- Bower, A. F., Fleck, N. A., Needleman, A. and Ogbonna, N. (1993). Indentation of a power law creeping solid, *Proceedings of the Royal Society London. Series A*(441): 97–124.
- Brown, A. B. and Sparks, J. W. (1958). Viscoelastic properties of a penetration grade paving asphalt at winter temperature., *Proceedings of the Association of asphalt Paving Technologists* **27**: 35–51.

- Brown, S. F. and Co-workers, . (1992). Bituminous pavements. materials, design and evaluation. residential course lecture notes. department of civil engineering. university of nottingham.
- Brown, S. F. and Cooper, K. E. (1980). A fundamental study of the stress-strain characteristics of a bituminous material, *Proceedings of the Association of Asphalt Paving Technologists*, Vol. 49, pp. 476–498.
- Brown, S. F. and Cooper, K. E. (1984). The mechanical properties of bituminous materials for road bases and base courses, *Proceedings of the Association of Asphalt Paving Technologists*, Vol. 53, pp. 415–439.
- Brown, S. F., Cooper, K. E. and Preston, J. N. (1991). Application of new concepts in asphalt mix design, *Proceedings of the Association of Asphalt Paving Technologists*, Vol. 60, pp. 264–286.
- Brown, S. F. and Snaith, M. S. (1974). The permanent deformation characteristics of a dense bitumen macadam subjected to repeated loading., *Proceedings of the Association of asphalt Paving Technologists* **45**: 224–252.
- Brule, B., Ramond, G. and Such, C. (1986). Relationships between composition, structure, and properties of road asphalts: state of research at the french public works central laboratory., *Transportation research record* **1096**: 22–34.
- BS2000-49 (1983). *BS 2000: part 49. Penetration of bituminous materials*, British Standards Institution, London.
- BS2000-58 (1983). *BS 2000: part 58. Softening point of bitumen (ring and ball)*, British Standards Institution, London.
- Budiansky, B. (1965). On the elastic moduli of some heterogeneous materials, *J. of the mechanics and physics of solids* **13**: 223–227.

- Buttlar, W. G. and You, Z. (2001). Discrete element modeling of asphalt concrete: Microfabric approach, *Transportation Research Record* **1757**: 111–118.
- Cebon, D. (1993). *Interaction Between Heavy Vehicles and Roads*, SAE International.
- Chang, G. K. and Meegoda, N. J. (1993). Simulation of the behaviour of asphalt concrete using discrete element method, *Proc., 2nd Int. Conf. on discrete element methods*, Massachusetts Institute of Technology Press, Cambridge, Mass., pp. 437–448.
- Chen, J. S., Liao, M. C. and Shiah, M. (2002). Asphalt modified by styrene-butadiene-styrene triblock copolymer: Morphology and model., *J. of Materials in Civil Eng.* **14(3)**: 224–229.
- Cheung, C. Y. (1995). *Mechanical behaviour of bitumens and bituminous mixes*, PhD thesis, Cambridge University Engineering Department.
- Cheung, C. Y. and Cebon, D. (1997a). Deformation mechanisms of pure bitumen, *J. of materials in civil engineering* **9(3)**: 117–129.
- Cheung, C. Y. and Cebon, D. (1997b). Experimental study of pure bitumens in tension, compression, and shear, *J. Rheology* **41(1)**: 45–73.
- Cheung, C. Y. and Cebon, D. (1997c). Thin film deformation behaviour of power-law creeping materials, *J. of engineering mechanics* **123(11)**: 1138–1152.
- Cheung, C. Y., Cocks, A. C. F. and Cebon, D. (1999). Isolated contact model of an idealized asphalt mix, *Int. J. Mechanical Sci.* **41**: 767–792.
- Chia, J. H. (1994). *Constitutive modeling of thermomechanical response of materials in semiconductor devices with emphasis on interface behavior*, PhD thesis, University of Arizona, Tucson, Az.

- Christensen, D. (1998). Analysis of creep data from indirect tension test on asphalt concrete., *Journal of the AAPT* **67**: 458–492.
- Christensen, D. W. and Anderson, D. A. (1992). Interpretation of dynamic mechanical test data for paving grade asphalt, *Proceedings of the Association of asphalt paving technologists*, Vol. 61, pp. 67–116.
- Christensen, R. M. and Lo, K. H. (1979). Solutions for effective shear properties in three phase sphere and cylinder models, *J. of the Mechanics and Physics of Solids* **27(4)**: 1111.
- Christman, T., Needleman, A. and Suresh, S. (1989). An experimental and numerical study of deformation in metal-ceramic composites, *Acta Metallurgica* **37(11)**: 3029–3050.
- Collop, A. C. (1994). *Effects of traffic and temperature on flexible pavement wear*, PhD thesis, University of Cambridge.
- Collop, A. C., Cebon, D. and Hardy, M. S. A. (1995). A viscoelastic approach to rutting in flexible pavements, *J. of transportation engineering* **121(1)**: 82.
- Collop, A. C. and Khanzada, S. (2001). Permanent deformation in idealised “sand asphalt” bituminous mixtures, *Int. Journal of road materials and pavement design* **2(1)**: 7–28.
- Collop, A. C., McDowell, G. and Lee, Y. (2004). Use of the distinct element method to model the behaviour of an idealised asphalt mixture, *International Journal of Road Materials and Pavement Design* **5(1)**: 1–7.
- Collop, A. C., Scarpas, A., Kasbergen, C. and de Bondt, A. (2003). Development and finite element implementation of stress-dependent elastoviscoplastic constitutive model with damage for asphalt., *Transportation Research Record* **1832**: 96–104.

- Cooper, K. E., Brown, S. F., Preston, J. N. and Akeroyd, F. M. L. (1991). Development of a practical method for design of hot-mix asphalt, *Transportation research record* **1317**: 42–51.
- Cross, M. M. (1965). Rheology of non-newtonian fluids: a new flow equation for pseudoplastic systems, *J. of colloid science* **20**: 417–437.
- Derby, B. and Ashby, M. F. (1987). A microstructural model for primary creep, *Acta Metallurgica* **35**(6): 1349–1353.
- Desai, C. S. (1980). A general basis for yield, failure and potential functions in plasticity, *Int. J. for numerical and analytical methods in geomechanics* **4**: 361–375.
- Desai, C. S., Somasundaram, S. and Frantziskonis, G. (1986). A hierarchical approach for the constitutive modelling of geologic materials, *Int. J. for numerical and analytical methods in geomechanics* **10**: 225–257.
- Deshpande, V. S. (1997). *Steady-state deformation behaviour of bituminous mixes*, PhD thesis, Cambridge University Engineering Department.
- Deshpande, V. S. and Cebon, D. (1999a). Models of particle reinforced nonlinear-viscous composite, *J. of engineering mechanics* **125**(3): 255–262.
- Deshpande, V. S. and Cebon, D. (1999b). Steady-state constitutive relationship for idealised asphalt mixes, *Mechanics of materials* **31**: 271–287.
- Deshpande, V. S. and Cebon, D. (2000). Uniaxial experiments on idealised asphalt mixes, *J. of materials in civil engineering* **12**(3): 262–271.
- Deshpande, V. S. and Cebon, D. (2004). Micromechanical modeling of steady-state deformation in asphalt, *J. of materials in civil engineering* **16**(2): 100–106.

- Dickinson, E. J. and Witt, H. P. (1974). The dynamic shear modulus of paving asphalts as a function of frequency, *Transactions of the society of rheology* **18**: 591–606.
- Dietrich, L. and Lekszycki, T. (1998). Problems of identification of mechanical characteristics of viscoelastic composites, *Acta Mechanica* **126**: 153–167.
- Dobson, G. R. (1969). The dynamic mechanical properties of bitumen, *Proceedings of the Association of asphalt paving technologists*, Vol. 38, pp. 123–139.
- Dobson, G. R. (1972). On the development of rational specifications for the rheological properties of bitumens, *J. of the institute of petroleum* **58(559)**: 14–24.
- Dunhill, S., Airey, G., Collop, A. and Brown, S. (2000). An investigation into the deterioration mechanisms of lightly trafficked roads., *Proceedings of the 2nd Euraspalt and Eurobitume Congress*, Vol. 2, Barcelona.
- Duva, J. M. (1984). A self-consistent analysis of the stiffening effect of rigid inclusion on a power law material, *J. of engineering materials and technology* **106**: 317–321.
- Einstein, A. (1956). Eine neue bestimmung der molekuledimensionen, *Annalen der Physik. English translation in investigations on the Theory of Brownian Motions*, Dover Publications.
- Elseifi, M. A., Flintsch, G. W. and Al-Qadi, I. (2003). Quantitative effect of elastomeric modification on binder performance at intermediate and high temperatures, *J. of Materials in Civil Eng.* **15(1)**: 32–40.
- Fafard, M., Boudjelal, M. T., Bissonnette, B. and Cloutier, A. (2001). Three dimensional viscoelastic model with nonconstant coefficients, *J. of engineering mechanics* **127(8)**: 808–815.

- Ferry, J. D. (1980). *Viscoelastic properties of polymers*, 3rd edn, Jhon Wiley and Sons.
- Finney, J. L. (1970). Random packings and the structure of simple liquids. i: The geometry of random close packing, *Proc., Royal Soc., London* **A319**: 479–493.
- Fitzgerald, J. E. and Vakili, J. (1973). Non-linear characterisation of sand-asphalt concrete by means of pavement-memory norms, *Experimental Mechanics* **13**: 504–510.
- Francken, L. (1998). Bituminous binders and mixes, *Technical report*, RILEM.
- Francken, L. and Verstraeten, J. (1974). Methods for predicting moduli and fatigue laws of bituminous road mixes under repeated bending, *Transportation research record* **515**: 114–123.
- Frankel, N. A. and Acrivos, A. (1967). On the viscosity of a concentrated suspension of solid spheres, *Chemical Engineering Science* **22**: 847.
- Frölich, H. and Sack, R. (1946). Theory of the rheological properties of dispersions, *Proceedings of the Royal Society of London*, Vol. A185, pp. 415–430.
- Frost, H. J. and Ashby, M. F. (1982). *Deformation-mechanism maps: The plasticity and creep of metals and ceramics*, Pergamon.
- Fwa, T. F., Low, B. H. and Tan, S. A. (1993). Compaction of asphalt mixtures for laboratory testing: Evaluation based on density profile, *J. Testing and evaluation* **21(5)**: 414–421.
- Garrick, N. W. (1992). Empirical equations for determining the effects of temperature and shear rate on the viscosity of asphalt cements., *Proceedings of the Association of Asphalt Paving Technologists*, Vol. 61, pp. 1–28.

- Gaskins, F. H., Brodnyan, J. G., Philippoff, W. and Thelen, E. (1960). The rheology of asphalt. ii. flow characteristics of asphalt., *Transactions of the society of rheology* **4(435)**: 265–278.
- Geist, R. (1998). Four stage model for predicting creep behaviour, *J. of engineering mechanics* **124(1)**: 118–120.
- Genin, G. M. and Cebon, D. (2000). Fracture mechanisms in asphalt concrete, *Int. J. of Road Materials and Pavement Design* **1(4)**: 419–450.
- German, R. M. (1989). Particle packing characteristics, *Metal Powder Industries Federation, Princeton, N.J.* .
- Gilbert, D. G., Ashby, M. F. and Beaumont, P. W. R. (1986). Modulus maps for amorphous polymers, *J. of materials science* **21**: 3194–3210.
- Goddard, J. D. (1998). *Physiscs of dry granular media*, H. J. Herrmann et al. (eds). Kluwer Academic Publishers, Netherlands, chapter Continuum modeling of granular assemblies, pp. 1–24.
- Goddard, J. D. and Bashir, Y. M. (1990). *Recent developments in structural continua*, Vol. 2, D. De Kee and P.M. Kaloni (eds). Longman Scientific and Technical, London, chapter On Reynolds dilatancy, p. 23.
- Goddard, J. D. and Didwania, A. K. (1998). Computations of dilatancy and yield surfaces for assemblies of rigid frictional spheres, *Q. J. Mech. Appl. Math.* **51(1)**: 15–43.
- Goetz, W. H. and Chen, C. C. (1950). Vacuum triaxial technique applied to bituminous aggregate mixtures, *Proceedings of the Association of Asphalt Paving Technologists*, Vol. 19, pp. 55–81.

- Gurson, A. L. (1977). Continuum theory of ductile rupture by void nucleation and growth: Part i - yield criteria and flow rules for ductile porous media, *J. of Eng. Materials and Technology* p. 2.
- Harvey, J. A. F. (2000). *Bitumen films in tension*, PhD thesis, Cambridge University Engineering Department.
- Harvey, J., Mills, T., Scheffy, C. and Monismith, C. L. (1994). An evaluation of several techniques for measuring air-void content in asphalt specimens, *J. Testing and Evaluation* **22**(5): 424–430.
- Hashin, Z. (1962). The elastic moduli of heterogeneous materials, *J. of Applied Mechanics* **29**: 143.
- Hashin, Z. (1985). Large isotropic elastic deformation of composites and porous media, *International journal of Solids and Structures* **21**(7): 711–720.
- Hashin, Z. and Strikman, S. (1963). A variational approach to the theory of the elastic behaviour of multiphase materials, *J. of the mechanics and physics of solids* **11**: 127–140.
- Heukelom, W. and Herrin, M. (1964). Road design and dynamic loading, *Proceedings of the Association of asphalt paving technologists*, Vol. 33, p. 92.
- Hill, R. (1965). A self consistent mechanics of composite materials, *J. of the mechanics and physics of solids* **13**: 213–222.
- Hill, R., Storakers, B. and Zdunek, A. B. (1989). A theoretical study of the brinell hardness test, *Proceedings of the Royal Society London. Series A*(423): 301.
- Hills, J. F. (1973). The creep of asphalt mixes, *J. of the Institute of Petroleum* **59**(570): 247–262.

- Hills, J. F., Brien, D. and Van de Loo, P. J. (1974). The correlation of rutting and creep tests on asphalt mixes, *J. Inst. Petroleum Paper IP 74-001* .
- Hills, J. F. and Heukelom, W. (1969). The modulus and poisson's ratio of asphalt mixes, *J. of the Institute of Petroleum* **55(541)**: 27–35.
- Houlsby, G. T. and Puzrin, A. M. (2002). Rate-dependent plasticity models derived from potential functions, *J. Rheology* **46(1)**: 113–126.
- Huang, B., Mohammad, L. and Wathugala, G. (2002). development of a thermo-viscoplastic constitutive model for hma mixtures, *J. Ass. Asphalt Paving Technol.* **71**: 594–618.
- Huang, B., Mohammad, L. and Wathugala, G. (2004). Application of a temperature dependent viscoplastic hierarchical single surface model for asphalt mixtures, *J. of Materials in Civil Eng.* **16(2)**: 147–154.
- Huang, Y. H. (1967). Stresses and displacements in viscoelastic layered systems under circular loaded areas, *Proceedings of the 2nd International Conference on the Structural Design of Asphalt Pavements*, pp. 225–244.
- Huschek, S. (1985). The deformation behaviour of asphaltic concrete under triaxial compression, *Proceedings of the Association of Asphalt Paving Technologists*, Vol. 54, pp. 407–431.
- Ishihara, K. and Kimura, T. (1967). The theory of viscoelastic two-layer systems and conception of its application to the pavement design, *Proceedings of the 2nd International Conference on the Structural Design of Asphalt Pavements*, pp. 245–254.
- Jeng, Y. S. and Perng, J. D. (1991). Analysis of crack propagation in asphalt concrete using cohesive crack model, *Transportation research record* **1317**: 90–99.

- Jongepier, R. and Kuilman, B. (1969). Characteristics of the rheology of bitumens, *Proceedings of the Association of asphalt paving technologists*, Vol. 38, pp. 98–122.
- Khong, T. D., Malhotra, S. L. and Blanchard, L. P. (1978). Effect of shear rate, penetration and temperature on the viscosity of asphalts. technical report ip 78-001, *Technical report*, J. of the institution of petroleum.
- Kim, J. R., Drescher, A. and Newcomb, D. E. (1997). Rate sensitivity of asphalt concrete in triaxial compression, *J. of Materials in Civil Eng.* **9(2)**: 76–84.
- Kim, Y. R. and Dallas, N. L. (1989). Evaluation of healing in asphalt concrete by means of the theory of non-linear viscoelasticity, *Transportation Research Record* **1228**: 198–210.
- Kim, Y. R., Dallas, N. L. and Little, D. N. (1990). One dimensional constitutive modelling of asphalt concrete, *J. of engineering mechanics* **116**: 751–772.
- Kim, Y. R., Lee, Y. C. and Lee, H. J. (1995). Correspondence principle for characterisation of asphalt concrete, *J. of Materials in Civil Engineering* **7 (1)**: 59–68.
- Kose, S., Guler, M., Bahia, H. U. and Masad, E. (2000). Distribution of strains within hot-mix asphalt binders, *Transportation Research Record* **1391**: 21–27.
- Krishnan, J. M. and Rajagopal, K. R. (2004). Thermodynamic framework for the constitutive modeling of asphalt concrete: Theory and applications, *J. of materials in civil engineering* **16(2)**: 155–166.
- Krishnan, M. J. and Rao, L. C. (2000). Air void reduction of asphalt concrete using mixture theory, *Int. J. of Engineering Sciences* **38**: 1331–1354.

- Lai, J. S. and Anderson, D. (1973). Irrecoverable and recoverable nonlinear viscoelastic properties of asphalt concrete, *Highway Research Record* **468**: 73–88.
- Lee, A. R. and Warren, J. B. (1940). The flow properties of asphaltic bitumens with reference to road behaviour, *Proceedings of the Association of asphalt paving technologists*, Vol. 11, pp. 340–364.
- Lee, H. and Kim, Y. R. (1998). Viscoelastic constitutive model for asphalt concrete under cyclic loading, *J. of Engineering Mechanics* **124** (1): 32–40.
- Lethersich, W. (1942). The mechanical behaviour of bitumen, *J. of the society of chemical industry, Transactions and communications* **61**: 101–108.
- Lin, H. D. and Wang, C. C. (1998). Stress-strain-time function of clay, *J. of geotechnical and geoenvironmental engineering* **4**: 289–296.
- Long, F. M. (2001). *Permanent deformation of asphalt concrete pavements: A non-linear viscoelastic approach to mix analyses and design*, PhD thesis, University of California, Berkeley.
- Low, B. H., Tan, S. A. and Fwa, T. F. (1993). Analysis of marshall test behaviour with triaxial test determined material properties, *Journal of testing and evaluation* **21**(3): 192–198.
- Lu, Y. and Wright, P. J. (2000). Temperature related visco-elastoplastic properties of asphalt mixtures, *J. of Transportation Engineering* **126**(1): 58–65.
- Mahboub, K. (1990). Asphalt concrete creep as related to rutting, *J. of Materials in Civil Engineering* **2**(3): 147–163.

- Marasteanu, M. O. and Anderson, D. (1999). Improved model for bitumen rheological characterization., *Eurobitume workshop on performance related properties for bituminous binders* **Paper No 133**.
- Martinez-Boza, F., Partal, P., Navarro, F. and Gallegos, C. (2001). Rheology and microstructure of asphalt binders., *Rheol Acta*. **40**: 135–141.
- Masad, E. and Bahia, H. (2002). Effects of loading configuration and material properties on non-linear response of asphalt mixes, *Journal of the AAPT* **71**: 535–558.
- Masad, E., Somadevan, N., Bahia, H. U. and Kose, S. (2001). Modeling and experimental measurements of strain distribution in asphalt mixes, *Journal of Transportation Eng.* **127**(6): 477–485.
- Mayo, M. J. and Nix, W. D. (1988). A micro-indentation study of superplasticity in pb, sn and sn-38 wt% pb., *Acta metall.* **36**: 2183.
- McLaughlin, R. (1977). A study of the differential scheme for composite materials, *International journal of engineering science* **15**: 237–244.
- Mehta, Y. and Christensen, D. (2000). Determination of the linear viscoelastic limits of asphalt concrete at low and intermediate temperatures., *Journal of the AAPT* **69**: 281–312.
- Moavenzadeh, F. and carnaghi, R. A. (1966). Viscoelastic response of sand-asphalt beams on elastic foundations under repeated loading, *In proceedings of the association of asphalt paving technologists* **35**: 514–528.
- Monosmith, C. L., Alexander, R. L. and Sekor, K. E. (1966). Rheological behaviour of asphalt concrete, *Proceedings of the Association of asphalt paving technologists*, Vol. 35, p. 400.

- Monosmith, C. L. and Sekor, K. E. (1962). Viscoelastic behaviour of asphalt concrete pavements, *Proceedings of the 1st International Conference on the Structural Design of Asphalt Pavements*, p. 476.
- Mulhearn, T. O. and Tabor, D. (1960). Creep and hardness of metals: a physical study, *Journal Inst. Metals* **89**: 7–12.
- Nellensteyn, F. J. (1924). The constitution of asphalt, *J. of the institution of petroleum technologists* **10**: 311–325.
- Nellensteyn, F. J. (1927). The relation of the micelle to the medium in asphalt, *J. of the institution of petroleum technologists* **14**: 134–138.
- Nijboer, L. J. (1948). *Plasticity as a factor in the design of dense bituminous road carpets*, Elsevier.
- Nunn, M. E. (1986). Prediction of permanent deformation in bituminous pavement layers, *Technical Report 26*, Transport and Road Research Laboratory.
- Ogbonna, N. (1994). *Indentation and compaction of inelastic solids*, PhD thesis, Cambridge University.
- Ogbonna, N., Fleck, N. A. and Cocks, C. F. (1995). Transient creep analysis of ball indentation, *Int. J. of Mechanical Sciences* **37**(11): 1179–1202.
- Ossa, E. A., Deshpande, V. S. and Cebon, D. (2004). Uniaxial monotonic and cyclic behaviour of bituminous mixes, *Technical report*, CUED/C-MICROMECH/TR.95.
- Pagen, C. A. (1965). Rheological response of bituminous concrete, *Highway Research Record* **67**: 1.

- Pagen, C. A. (1968). Size and thermological relationships of asphaltic concrete, *Proceedings of the Association of asphalt paving technologists*, Vol. 37, p. 228.
- Pagen, C. A. (1972). Dynamic structural properties of asphalt pavement mixtures., *Proceedings of the 3rd International Conference on Structural Design of Asphalt Pavements*, Vol. 1, pp. 290–316.
- Papagiannakis, A. T., Abbas, A. R. and Masad, E. A. (2002). Micromechanical analysis of viscoelastic properties of asphalt concretes, *Transportation Research Record* **1789**: 113–120.
- Papazian, H. S. (1962). The response of linear viscoelastic materials in the frequency domain with emphasis on asphaltic concrete., *Proceedings of the 1st International Conference on Structural Design of Asphalt Pavements*, pp. 454–463.
- Paul, B. (1960). Prediction of elastic constants of multiphase materials, *Transactions of the ASME* **218**: 36.
- Petersen, J. C. (1984). Chemical composition of asphalt as related to asphalt durability: state of the art, *Transportation research record* **999**: 13–30.
- Pink, H. S., Merz, R. E. and Bosniack, D. S. (1980). Asphalt rheology: Experimental determination of dynamic moduli at low temperature, *Proceedings of the Association of Asphalt Paving Technologists*, Vol. 49, pp. 64–94.
- Poh, K. W. (1998). General creep time equation, *J. of materials in civil engineering* **10**(2): 118–120.
- Ponte Castañeda, P. (1989). The overall constitutive behaviour of nonlinearly elastic composites, *Proceedings of the Royal Society of London*, Vol. A422, pp. 45–71.

- Ponte Castañeda, P. (1991). The effective mechanical properties of nonlinear isotropic composites, *J. of the mechanics and physics of solids* **39(1)**: 45–71.
- Ponte Castañeda, P. (1992a). Bounds and estimates for the properties of nonlinear heterogeneous systems, *Philosophical transactions of the Royal Society of London*, Vol. A340, pp. 531–567.
- Ponte Castañeda, P. (1992b). New variational principles in plasticity and their application to composite materials, *J. of the mechanics and physics of solids* **40(8)**: 1757–1788.
- Ponte Castañeda, P. and deBotton, G. (1992). On the homogenized yield strength of two-phase composites, *Proceedings of the Royal Society of London*, Vol. A438, pp. 419–431.
- Ponte Castañeda, P. and Willis, J. R. (1988). On the overall properties of nonlinearly viscous composites, *Proceedings of the Royal Society of London*, pp. 217–244.
- Ponte Castañeda, P. and Zaidman, M. (1994). Constitutive models for porous materials with evolving microstructure, *J. of the mechanics and physics of solids* **42(9)**: 1459–1497.
- Qi, X., Sebaaly, P. and Epps, J. (1995). Evaluation of polymer-modified asphalt concrete mixtures., *J. of Materials in Civil Eng.* **7(2)**: 117–124.
- Reynolds, O. (1885). On the dilatancy of media composed of rigid particles in contact. with experimental observations., *Phil. Mag.* **20**: 469–481.
- Romberg, J. W. and Traxler, R. N. (1947). Rheology of asphalt, *J. of colloid science* **2**: 33–47.

- Rothenburg, L., Bogobowicz, A., Hass, R., Jung, F. W. and Kennepohl, G. (1992). Micromechanical modelling of asphalt concrete in connection with pavement rutting problems, *Proceedings of the 7th International Conference on Structural Design of Asphalt Pavements*.
- Rowe, P. W. (1962). The stress-dilatancy relation for static equilibrium of an assembly of particles in contact, *Proc. Royal Society London A* **269**: 500–529.
- Rowe, P. W. (1972). *Theoretical meaning and observed values of deformation parameters for soil.*, G. T. Foulis & Co., London, chapter pp. 143-194.
- Saal, R. N. J. (1950). *The properties of asphaltic bitumen*, Elsevier publishing company.
- Saal, R. N. J. and Labout, W. A. (1940). Rheological properties of asphaltic bitumens, *J. of physical chemistry* **44**: 149–165.
- Sadd, M. H., Dai, Q., Parameswaran, V. and Shukla, A. (2004). Microstructural simulation of asphalt materials: Modeling and experimental studies, *J. of materials in civil engineering* **16**(2): 107–115.
- Saleeb, A. F., Wilt, T. E., Al-Zoubi, N. R. and Gendy, A. S. (2003). An anisotropic viscoelastoplastic model for composites; sensitivity analysis and parameter estimation, *Composites Part B: Engineering* **34**(1): 21–39.
- Saleeb, A. F., Wilt, T. E., Trowbridge, D. A. and Gendy, A. S. (2002). Effective strategy for automated characterization in complex viscoelastoplastic and damage modeling for isotropic/anisotropic aerospace materials, *J. of Aerospace Engineering* **15**(3): 84–96.
- Sargent, P. M. and Ashby, M. F. (1992). Indentation creep, *Materials science and technology* **8**: 594–601.

- Sayegh, G. (1967). Viscoelastic properties of bituminous mixes., *Proceedings of the 2nd International Conference on Structural Design of Asphalt Pavements*, pp. 743–755.
- Scarpas, A. and Blaauwendraad, J. (1998). Experimental calibration of a constitutive model for asphaltic concrete, *Computational Modelling of Concrete Structures*, Rotterdam, pp. 193–202.
- Schapery, R. A. (1984). Correspondence principles and a generalised j integral for large deformation and fracture analysis of viscoelastic media, *International journal of fracture* **25**: 195–223.
- Sepehr, K., Svec, O. J., Yue, Z. Q. and El Hussein, H. M. (1994). Finite element modeling of asphalt concrete microstructure, *Proc., 3rd Int. Conf. on computer-aided assesment and control localized damage.*, Udine, Italy.
- SHRP-A-369 (1994). *Binder characterisation and evaluation. Volume 3: Physical characterization (A-369)*, Strategic Highway Research Program, Washington DC.
- SHRP-A-415 (1994). *Permanent deformation response of asphalt aggregate mixes*, Strategic Highway Research Program, Washington DC.
- SHRP-A-631 (1993). *Review of relationships between modified asphalt properties and pavement performance*, Strategic Highway Research Program, Washington DC.
- Sisko, A. W. (1965). Determination and treatment of asphalt viscosity data, *Highway research record* **67**: 27–37.
- Sitharam, T. G. (1999). Micromechanical modeling of granular materials: effect of confining pressure on mechanical behaviour, *Mechanics of Materials* **31**: 653–665.

- Suquet, P. M. (1993). Overall potentials and extremal surfaces of power law or ideally plastic composites, *J. of the mechanics and physics of solids* **41(6)**: 981–1002.
- Tabor, D. (1951). *Hardness of metals*, Oxford:Clarendon Press.
- Tacıroglu, E. and Hjelmstad, K. D. (2002). Simple nonlinear model for elastic response of cohesionless granular materials, *J. of Eng. Mechanics* **128(9)**: 969–978.
- Talbot, D. R. S. and Willis, J. R. (1992). Some simple explicit bounds for the overall behaviour of nonlinear composites, *International Journal of solids and structures* **29**: 1981–1987.
- Tan, S. A. and Fwa, T. F. (1991). Non-destructive density measurements of cylindrical specimens by gamma-ray attenuation, *J. Testing and evaluation* **19(2)**: 155–160.
- Taylor, D. W. (1948). *Fundamentals of soil mechanics*, Wiley, New York.
- Thrower, E. N. (1975). Pavement deformation in a linear visco-elastic model of a road pavement., *Transport research laboratory Supplementary report* **184**.
- Toth, S. (1996). A calculation procedure for the determination of the results of the creep and the oscillatory tests from the flow curves, *Eurasphalt and Eurobitume Congress*.
- Traxler, R. N. (1947). A review of the rheology of bituminous materials, *J. of colloid science* **2**: 49–68.
- Traxler, R. N. and Coombs, C. E. (1936). The colloidal nature of asphalt as shown by its flow properties, *J. of physical chemistry* **40**: 1133–1147.
- Traxler, R. N., Schweyer, H. E. and Romberg, J. W. (1944). Rheological properties of asphalt, *Industrial and engineering chemistry* **36**: 823–829.

- Ullidtz, P. (2001). A study of failure in cohesive particulate media using the discrete element method, *Proc., 80th Transportation Research Board Meeting*.
- Vakili, J. (1983). An experimental study of asphalt concrete based on a multiple integral representation of constitutive equation of a nonlinear viscoelastic solid, *J. of Rheology* **27(3)**: 211–222.
- Vakili, J. (1985). Determination of nonlinear viscoelastic properties of asphalt concrete by a simple experimental procedure, *Res. Mechanica* **14**: 145–153.
- Van de Loo, P. J. (1976). A practical approach to the prediction of rutting in asphalt pavements. the shell method, *Proceedings of the Symposium on Predicting Rutting in Asphalt Concrete Pavements*, Transportation research board, Washington.
- Van de Loo, P. J. (1978). The creep test: A key tool in asphalt mix evaluation and in the prediction of pavement rutting, *Proceedings of the Association of Asphalt Paving Technologists*, Vol. 47, pp. 64–94.
- van der Poel, C. (1954a). A general system describing the visco-elastic properties of bitumens and its relation to routine test data, *J. of applied chemistry* **4**: 221–236.
- van der Poel, C. (1954b). Representation of rheological properties of bitumen over a wide range of temperatures and loading times, *Proceedings of the 2nd international congress on rheology*, pp. 331–337.
- Van der Poel, C. (1955). Time and temperature effects on the deformation of asphaltic bitumens and bitumen-mineral mixtures, *J. of the society of petroleum engineers* pp. 47–53.
- Van der Poel, C. (1958). On the rheology of concentrated dispersions, *Acta Rheologica* **1**: 198–205.

- Von Quintus, H. L., Scherocman, J. A., Hughes, C. and Kennedy, T. (1991). Asphalt aggregate mixture analysis system, *Technical Report NCHRP 338*, Transportation Research Board, Washington, D.C.
- Wallace, K. and Monismith, C. L. (1980). Diametral modulus on nonlinear pavement materials, *Proceedings of the Association of asphalt paving technologists*, Vol. 49, pp. 633–644.
- Ward, I. M. (1971). *Mechanical properties of solid polymers*, Wiley Interscience.
- Ward, I. M. and Onat, E. T. (1963). Non-linear mechanical behaviour of oriented polypropylene, *J. of the mechanics and physics of solids* **11**(4): 217–229.
- Wathugala, G. W. (1990). *Finite element dynamic analysis of nonlinear porous media with applications to piles in saturated clays*, PhD thesis, University of Arizona, Tucson, Az.
- Webster, G. A., Cox, A. P. D. and Dorn, J. E. (1969). A relationship between transient and steady state creep at elevated temperatures, *Metal science journal* **3**: 221–225.
- Weissman, S. L., Harvey, J., Sackman, J. L. and Long, F. (1999). Selection of laboratory test specimen dimension for permanent deformation of asphalt concrete pavements, *Transportation Research Record* **1681**: 113–120.
- Welborn, J. Y., Oglio, E. R. and Zenewitz, J. A. (1966). A study of viscosity graded asphalt cements, *Proceedings of the Association of asphalt paving technologists*, Vol. 35, pp. 19–60.
- Whiteoak, D. (1990). *The Shell bitumen handbook*, Shell Bitumen UK.

- Wilkinson, D. S. and Ashby, M. F. (1975). Pressure sintering by power law creep, *Acta metall.* **23**: 1277.
- Williams, M. L. (1972). Continuum mechanics and adhesive fracture, *J. of adhesion* **4**: 327.
- Willis, J. R. (1982). *Elasticity theory of composites*, Vol. The Rodney Hill 60th Anniversary of *Mechanics of solids*, Pergamon Press.
- Willis, J. R. (1983). The overall elastic response of composite materials, *J. of applied mechanics* **50**: 1202–1209.
- Willis, J. R. (1991). On methods for bounding the overall properties of nonlinear composites, *J. of the mechanics and physics of solids* **39(1)**: 73–86.
- Willis, J. R. (1992). On methods for bounding the overall properties of nonlinear composites: correction and addition, *J. of the mechanics and physics of solids* **40(2)**: 441–445.
- Zeng, M., Bahia, H., Zhai, H., Anderson, M. and Turner, P. (2001). Rheological modeling of modified asphalt binders and mixtures., *Journal of the AAPT* **70**: 403–441.
- Zhao, Y. and Kim, Y. R. (2003). Time-temperature superposition for asphalt mixtures with growing damage and permanent deformation in compression, *Transportation Research Record* **1832**: 161–172.